

Photoreduction of Outer Membrane Cytochromes: Solution and Proteoliposome Nanocompartment Studies

Emma Victoria Ainsworth

PhD Thesis

School of Chemistry

University of East Anglia

Norwich Research Park

Norwich, NR4 7TJ

© Emma Victoria Ainsworth, April 2017

This copy of the thesis has been supplied on condition that anyone who consults it is understood to recognise that its copyright rests with the author and that use of any information derived there from must be in accordance with current UK Copyright Law. In addition, any quotation or extract must include full attribution.

This book is dedicated to the memories of Joan and Thomas Howes for being wonderful grandparents who shone with pride; Audrey Plumbly and Sheila Feek for being amazing great aunties who kept the Howes family traits of being kind, loyal and fun-loving alive; and Alison Hill for being a true, loving friend who supported and encouraged me to be myself no matter what anyone else thinks. You may be elsewhere but you all left traces of love and happiness behind. You will never be forgotten.

Table of Contents

Abstract	IX
Acknowledgements	X
Abbreviations	XII
Symbols	XVII
Chapter 1 Introduction	1
1.1 General Introduction	1
1.2 Natural Photosynthesis	2
1.3 Artificial Photosynthesis: Three-Component Systems	4
1.3.1 Photosensitisers	4
1.3.2 Electrocatalysts	8
1.3.3 Sacrificial Electron Donors	9
1.4 Artificial Photosynthesis: Beyond Three-Component Systems	10
1.4.1 Artificial Leaf	10
1.4.2 Light-Driven Whole-Cell Catalysis	12
1.5 Compartmentalised Reaction Vessels	14
1.5.1 Compartments from Membranes, Proteins and Polymers	15
1.5.2 Liposomes	17
1.5.2.1 Phospholipids	18
1.5.2.2 Formation of Liposomes	21
1.6 Light-Driven, Transmembrane Electron Transfer	24
1.6.1 Bacterial Transmembrane Electron Transfer	24
1.6.2 Outer Membrane-Associated Cytochromes	26

1.6.3	Demonstration of Transmembrane Electron Transfer by MtrCAB in Liposomes	29
1.7	Aims of this Study	30
Chapter 2	Materials and Methods	34
2.1	General Reagent Preparations and Characterisations	34
2.1.1	Preparation of Buffer, Photosensitiser and Lipid Stock Solutions	34
2.1.2	Electronic Absorbance Spectroscopy	35
2.1.3	Cyclic Voltammetry	35
2.2	Characterisation and Purification of <i>S. oneidensis</i> MR-1 Outer Membrane Cytochromes	37
2.2.1	SDS-PAGE Analysis	37
2.2.2	Protein Visualisation Following SDS-PAGE Analysis	37
2.2.3	Outer Membrane Cytochrome Purification	39
2.3	Characterisation and Preparation of (Proteo)liposomes	43
2.3.1	Dynamic Light Scattering	43
2.3.2	Bright-Field Microscopy	45
2.3.3	Resolution of Proteoliposome Composition by SDS-PAGE Analysis	45
2.3.4	MtrCAB Incorporation into Preformed Liposomes	45
2.4	Light-Driven Photoreductions of Redox Dyes and Cytochromes	48
2.5	Assessing Changes in (Proteo)liposomes due to the Presence of Photosensitisers	49

Chapter 3	Photoreduction of Outer Membrane Cytochromes from <i>Shewanella oneidensis</i> MR-1 Using Organic and Inorganic Photosensitisers	51
3.1	Introduction to Coupling Photosensitisers to Metalloproteins	51
3.2	Characteristics of Photosensitisers Chosen for this Study	52
3.2.1	Ruthenium Complexes	52
3.2.2	Organic Photosensitisers	55
3.2.2.1	Eosin Y and Fluorescein	56
3.2.2.2	Proflavin	58
3.2.2.3	Flavins	60
3.3	Initial Screening of Photosensitisers for Visible-Light-Driven Reduction of MtrCAB Suspensions	64
3.4	Optimising Conditions for Photoreduction Studies	67
3.4.1	Optimisation of Protein:Photosensitiser Ratios via FMN Photoreduction of MtrC	68
3.4.2	Optimisation of Lamp Power via Eosin Y Photoreduction of MtrC	72
3.4.3	Conditions Selected for Detailed Studies of Cytochrome Photoreduction	74
3.5	Visible-Light-Driven Reduction of MtrC	75
3.5.1	Flavins	75
3.5.2	Eosin Y, Fluorescein and Proflavin	76
3.5.3	Ruthenium Complexes	78
3.5.4	Summary of Visible-Light-Driven Reduction of MtrC	79
3.6	Photoreduction of OmcA and MtrCAB and Comparison to MtrC	83
3.7	Identification of the Sacrificial Electron Donor(s) and Favourable Photoreduction Mechanisms	86

3.8	Discussion	91
3.9	Conclusions	96
Chapter 4	Exploration of Interactions Between Photosensitisers and Methyl Viologen-Containing (Proteo)liposomes: MtrCAB Incorporated in Preformed Liposomes	98
4.1	Possible Interactions Between Photosensitisers and (Proteo)liposomes	98
4.2	Preparation and Characterisation of (Proteo)liposomes via MtrCAB Incorporation into Preformed Liposomes	100
4.3	Assessment of Photosensitiser Association with (Proteo)liposomes	103
4.4	Methyl Viologen as a Probe of Liposome Permeability	109
4.4.1	Propensity of Methyl Viologen for Light-Driven Reduction	111
4.4.1.1	Ruthenium Complexes	111
4.4.1.2	Flavins	112
4.4.1.3	Eosin Y, Fluorescein and Proflavin	113
4.4.2	Irradiation of Liposomes Containing Methyl Viologen	116
4.4.2.1	Ruthenium Complexes	117
4.4.2.2	Flavins	118
4.4.2.3	Eosin Y, Fluorescein and Proflavin	119
4.4.3	Assessment of Methyl Viologen Leakage from Liposomes in Presence of Photosensitisers	120
4.5	Discussion	124
4.6	Conclusions	124

Chapter 5	Photoreduction of MtrCAB in Liposome Bilayers: Proteoliposomes Formed by Simultaneous Protein Incorporation and Liposome Assembly	127
5.1.	Overview of Strategies for Proteoliposome Formation	127
5.1.1	Detergents and Detergent-Mediated (Proteo)liposome Formation	128
5.2	Preparation and Characterisation of MtrCAB Proteoliposomes from Rapid Dilution of MtrCAB-Detergent and Lipid-Detergent Micelles	132
5.3	Possible Interactions Between Photosensitisers and (Proteo)liposomes with Greater MtrCAB Incorporation	137
5.4	Assessment of Photosensitiser Association with Liposomes	138
5.5	Visible-Light-Driven Reduction of Proteoliposome Incorporated MtrCAB and Comparison with that for MtrCAB in Detergent Suspensions	139
5.6	Conclusions	145
Chapter 6	Encapsulation of Redox Indicators within (Proteo)liposomes to Demonstrate Visible-Light-Driven Transmembrane Electron Transfer	147
6.1	Properties Ideal for Redox Indicators within (Proteo)liposomes	147
6.2	Characterisation of Redox Indicators Chosen for Encapsulation within (Proteo)liposomes	148
6.2.1	Resazurin	149
6.2.2	Indigotetrasulfonic Acid	149
6.2.3	Azo Dyes	151
6.3	Redox Indicator Encapsulation within (Proteo)liposomes	153

6.3.1	Redox Indicator Encapsulation within (Proteo)liposomes Prepared from Phosphatidylcholine	154
6.3.2	Redox Indicator Encapsulation within (Proteo)liposomes Prepared from <i>E. coli</i> Total Lipid Extract	157
6.4	Preparation and Characterisation of RR120-Containing (Proteo)liposomes Prepared from <i>E. coli</i> Total Lipid Extract	161
6.5	Possible Interactions Between Photosensitisers and RR120-Containing (Proteo)liposomes Prepared from <i>E. coli</i> Total Lipid Extract	166
6.6	Assessment of Photosensitiser Association with Liposomes	166
6.7	RR120 as a Probe of Liposome Permeability	168
6.7.1	Propensity of RR120 for Light-Driven Reduction	169
6.7.1.1	Eosin Y, Fluorescein and Proflavin	170
6.7.1.2	Flavins	170
6.7.2	Irradiation of Liposomes Containing RR120	171
6.7.2.1	Eosin Y, Fluorescein and Proflavin	172
6.7.2.2	Flavins	173
6.8	Flavin-Dependent Photoreduction of RR120 inside MtrCAB Proteoliposomes by Transmembrane Electron Transfer	174
6.9	Discussion	176
6.10	Conclusions	178
Chapter 7	Summary and Future Perspectives	181
	References	186
	Appendix	205

Abstract

Due to ever increasing global energy demand and depletion of fossil fuels, interest has grown in developing systems which can utilise the near limitless supply of energy provided to the Earth by the sun. Artificial photosynthetic systems mimic natural photosynthesis by using photosensitisers that absorb solar energy to generate high-energy electrons. These photoexcited electrons are passed to catalysts which drive reductive transformations to produce fuels and valued organic compounds. Sacrificial electron donors regenerate photosensitisers to complete the photocatalytic cycle. To date artificial photosynthetic systems are unable to fully mimic and reap the full benefits of natural photosynthesis as they lack spatially separating reaction compartments, and/or compartment-linking transmembrane electron transport chains.

A model for the biochemistry that supports such transmembrane electron transfer is provided by the outer membrane cytochromes of *Shewanella oneidensis* MR-1. In this Gram-negative bacterium, trans-outermembrane electron transfer to extracellular electron acceptors is performed by the extracellular cytochromes MtrC and OmcA acting together with the porin:cytochrome complex (MtrCAB), which provides an outer membrane spanning conduit that moves electrons from the periplasm to the cell surface.

Liposomes offer reaction compartments which are separated from the surrounding external environment by a phospholipid membrane. Incorporation of MtrCAB in the membranes of liposomes containing methyl viologen facilitates transmembrane electron transfer from an external reductant to the compartmentalised electron acceptor. In this study the potential for MtrCAB proteoliposomes to act as a modular artificial photosynthetic system, which performs reductive transformations, was investigated. To explore this potential we have studied the ability of several photosensitisers to photoreduce: i) outer membrane cytochromes of *S. oneidensis*; ii) methyl viologen in solution and within liposomes; iii) MtrCAB in liposome membranes; and iv) reactive red 120 in solution and within (proteo)liposomes. In addition the sacrificial electron donor(s), photoreduction mechanisms and interaction mechanisms used by each photosensitiser have been identified.

Acknowledgements

I would like to first express my appreciation to Prof. Julea Butt for the opportunity to be a part of this exciting area of research and for her continuous support, guidance and enthusiasm. I will always be extremely grateful for all the opportunities that Julea has offered me to boost my career, and to live and work in different universities across the world. If I manage to work half as hard as Julea I know I will do well in the future. I would like to thank Prof. Nick Le Brun and Dr Andy Gates for their time, support and interest towards my studies. I also owe my sincerest gratitude to Nick for suggesting I apply for the position within Julea's lab in the first place.

I would like to thank my many collaborators for all their helpful discussions and support towards this work. Thank you to Dr Erwin Reisner and his group at the University of Cambridge for providing ruthenium photosensitisers and for letting me utilise their photosensitiser expertise. I would like to thank Dr Lars Jeuken and Dr Ee Taek Hwang from the University of Leeds, for their hospitality and their valuable expertise in lipids and proteoliposome preparation. I must thank Anna Stikane and Dr Rebecca Thompson, University of Leeds, for the beautiful cryo-TEM images of (proteo)liposomes developed during this work. I must thank Prof. Moh El-Naggar and Dr Sahand Pirbadian at the University of Southern California, USA, for their generous hospitality, their time spent teaching me microscopy and interesting discussions revolving around MtrCAB nanowires and their formation. I must thank Dr Liang Shi and Dr Matthew Marshall from Pacific Northwest National Laboratory, USA, for providing stains allowing MtrC and OmcA overproduction and antibodies specific to MtrB. Thank you also to the Engineering and Physical Sciences Research Council for sponsoring my PhD studentship.

I would like to share my immense thanks to the other members of Julea's group. Firstly I would like to thank Dr Colin Lockwood for the endless discussions in which we both openly did not understand what was happening in our science; for sharing fun travels to conferences and meetings; and for the many late night presentation practices in our hotels. If an opportunity comes up when Colin actually requires a real PA I hope he remembers me favourably. I must thank future doctor-to-be Sam Rowe for the many nights of unwinding after hard days in the lab and for the numerous discussions over photosensitisers, light sources and mechanisms. I would also like to thank Dr Tony Blake and Dr Jessica van Wonderen for providing new, honest, and funny, opinions about the group's work and the life of being Post Doctorates. I must also thank Jess for performing

liquid chromatography–mass spectrometry of MtrC and OmcA samples. My PhD would not have been the same without you all being such wonderful colleges and friends.

Special thanks must be made towards Dr Gaye White for her time spent teaching me the dark magic behind the preparation of proteoliposomes. Without her vast expertise and help in the early stages of my PhD I know the development of proteoliposomes and the progress of my PhD would have been stunted. Special thanks must also go to Dr Marcus Edwards for being the generous oracle of all *S. oneidensis* knowledge and for always being a quiet inspirational scientist. I would like to thank Verity Lyall for her knowledge in *S. oneidensis* outer membrane protein purification and the training which she provided a chemist entering into a new biological world. Special tribute must also be paid towards Verity and Dr Simone Payne for purifying the proteins that were essential for this work. Thanks must be given to the members of the Chemistry desk room; especially to Dr Justin Bradley, Dr Jason Crack, Dr Krissy Kay and future doctor-to-be Sophie Bennett; for their help and providing a motivating atmosphere where I could openly laugh and moan when things did not go as planned. I would like to thank the many members of BIO 2.30 past and present who openly welcomed a chemist to share their cakes and conversations during numerous coffee breaks. The friends I have found here have been the most valuable gift gained from my PhD.

I cannot express gratitude that I owe to my closest friend, my mum Joanne Ainsworth, for her constant support and limitless faith in my ability; even if she thought and told the rest of our family I was working with potatoes. I would like to thank one of my oldest friends and future doctor-to-be Lisa Cooper for following me to UEA and the school of chemistry - knowing I always had her around for support and normal, fun chats definitely helped me to keep going. I would like to thank my friends; Katie Springham, Beki Ottley-Porter, Becky Evans, Liz Elliot, and Jenny Lovell; for their regular visits and our holidays which never failed to cheer me up. I must also convey my immense gratitude to Katie for being my dearest friend and dedicated proof reader. Without her bubbly attitude and continual encouragement every day would have been a lot harder to deal with. Finally I would like to thank Emma Waters for reminding me that happiness does not have to come from watching spectral changes, and there is much more to life than MtrCAB and proteoliposomes. Without her endless support, beautiful smile and love over the last year and a half I would be a wreck.

Abbreviations

[Ox]	Concentration of oxidised species	Br	Bromine atom
[Red]	Concentration of reduced species	C	Carbon atom
[Ru(bpy)₃]⁺	Reduced species of [Ru(bpy) ₃] ²⁺	Ca	Calcium atom
[Ru(bpy)₃]²⁺	Tris(bipyridine) ruthenium(II)	CaCl₂	Calcium chloride
[Ru(bpy)₃]³⁺	Oxidised species of [Ru(bpy) ₃] ²⁺	Cd	Cadmium
~	Approximately	CdS	Cadmium sulphide
≈	Approximately equal to	Cl	Chloride atom
¹F*	Singlet excited state of flavin	CMC	Critical micelle concentration
¹PFH⁺*	Singlet excited state of proflavin	Co	Cobalt atom
¹[Ru(bpy)₃]²⁺	Singlet excited state of [Ru(bpy) ₃] ²⁺	Co-HER	Cobalt hydrogen evolving catalyst
³F*	Triplet excited state of flavin	Co-OEC	Cobalt oxygen evolving catalyst
³PFH⁺*	Triplet excited state of proflavin	CV	Column volumes
³[Ru(bpy)₃]²⁺	Triplet excited state of [Ru(bpy) ₃] ²⁺	Cys	Cysteine
ADP	Adenosine diphosphate	Cyt	Cytochrome
Ag	Silver	DEAE	Diethylaminoethyl
AgCl	Silver chloride	DLS	Dynamic light scattering
ATP	Adenosine triphosphate	DNA	Deoxyribonucleic acid
Au	Gold atom	d-π*	Metal to ligand charge transfer transition
BCIP	5-bromo-4-chloro-3'-indolyphosphate	E	Energy or Equilibrium potential
bpy	2,2'-bipyridine	e⁻	Electron

E (PS*)	Photosensitiser triplet state energy	FNR	Ferredoxin-NADP ⁺ reductase
<i>E. coli</i>	<i>Escherichia coli</i>	GPC	Glycerophosphocholine
EA	Electron acceptor	GUV	Giant unilamellar vesicles
EA⁻	Reduced electron acceptor	H	Hydrogen atom
EET	Extracellular electron transfer	H⁺	Proton
E_m	Midpoint potential	H[•]	Hydrogen radical
E_m (PS*/PS⁻)	Reduction potential of the triplet state photosensitiser	H₂O	Molecular water
E_m (PS⁰/PS⁻)	Reduction potential of the ground state photosensitiser	H₂O₂	Hydrogen peroxide molecule
E_m (PS⁺/PS*)	Oxidation potential of the triplet state photosensitiser	HCl	Hydrogen chloride
E_m (PS⁺/PS⁰)	Oxidation potential of the ground state photosensitiser	HEPES	4-(2-hydroxyethyl)-piperazine-1-ethane-sulphonic acid
E_p^{ox}	Oxidative peak potential	HER	Hydrogen evolving catalyst
E_p^{red}	Reductive peak potential	His	Histidine
F	Flavin	<i>hν</i>	Light process
FAD	Flavin adenine dinucleotide	I	Intensity of light or Transmitted light intensity
Fd	Ferredoxin	I₀	Incident light intensity
Fe	Iron atom	IC	Internal conversion
FH[•]	Flavin semiquinone	i_p^{ox}	Oxidative peak current
FH₂	Fully reduced flavin (hydroquinone)	i_p^{red}	Reductive peak current
FMF	Formylmethylflavin	ISC	Intersystem crossing
FMN	Flavin mononucleotide	K	Potassium atom

KCl	Potassium chloride	Na	Sodium atom
LB	Lysogeny broth	NADP⁺	Nicotinamide adenine dinucleotide phosphate
LC	Lumichrome	NADPH	Reduced nicotinamide adenine dinucleotide phosphate
LDAO	<i>N,N</i> -dimethyl- <i>n</i> -dodecylamine <i>N</i> -oxide	NaOH	Sodium hydroxide
LF	Lumiflavin	NBT	Nitroblue tetrazolium
LUVs	Large unilamellar vesicles	<i>n</i>hν	Multiple light processes
<i>M. thermoacetica</i>	<i>Moorella thermoacetica</i>	Ni	Nickel
Mg	Magnesium atom	Ni-HER	Nickel hydrogen evolving catalyst
MgCl₂	Magnesium chloride	Ni-NTA	Nickel-nitrilotriacetic acid
MLVs	Multilamellar vesicles	NIR	Near infrared
Mn	Manganese atom	O	Oxygen atom
MR	Metal reducing	O₂	Molecular oxygen
MV	Methyl viologen	OEC	Oxygen evolving complex
MV⁺	Singly reduced methyl viologen	OG	<i>n</i> -octylglucoside
MV⁰	Fully reduced methyl viologen	OMVs	Outer membrane vesicles
MV²⁺	Oxidised methyl viologen	P	Phosphorus atom
N	Nitrogen atom	PA	Phosphatidic acid
N.D.	None detected	PAGE	Polyacrylamide gel electrophoresis
N/A	Non applicable	PC	Phosphatidylcholine
N₂	Molecular nitrogen	Pc	Plastocyanin

Pd	Polydispersity	<i>R. eutropha</i>	<i>Ralstonia eutropha</i>
PDB ID	Protein database identity	RB5	Reactive black 5
PE	Phosphatidylethanolamine	RF	Riboflavin
PF⁻	Reduced species of proflavin or Anionic proflavin radical	RMM	Relative monomer mass
PFH⁺	Proflavin	RNA	Ribonucleic acid
PFH²⁺	Oxidised species of proflavin	RR120	Reactive red 120
PG	Phosphatidylglycerol	Ru	Ruthenium atom
PI	Phosphatidylinositol	RuP	Bis(bipyridine)(bipyridine-4, 4'-bisphosphonic acid) ruthenium(II)
Pi	Phosphate	S	Singlet energy level or Sulphur atom
POPC	1-palmitoyl-2-oleoyl- <i>sn</i> -glycero-3-phosphocholine	<i>S. oneidensis</i>	<i>Shewanella oneidensis</i>
PS	Photosensitiser or Phosphatidylserine	S₀	Singlet ground state
PS⁻	Reduced photosensitiser	S₁	First singlet excited state
PS*	Photosensitiser excited state	S₂	Second singlet excited state
PS⁺	Oxidised photosensitiser	SDS	Sodium dodecyl sulphate
PS⁰	Photosensitiser ground state	SED	Sacrificial electron donor
PSI	Photosystem I	SHE	Standard hydrogen electrode
PSII	Photosystem II	<i>sn</i>	Stereospecific numbering
Q	Plastoquinone or Quaternary	SUVs	Smaller unilamellar vesicles
QH₂	Reduced plastoquinone	T	Triplet state
R	Organic side chain	T₁	First triplet excited state

T₂	Second triplet excited state
TBST	Tris-buffered saline and Tween 20
TEM	Transmission electron microscopy
TEOA	Triethanolamine
Ti	Titanium atom
TiO₂	Titanium dioxide
TMB	3,3',5,5'-tetramethylbenzidine dihydrochloride
Tris	Tris(hydroxymethyl)aminomethane
UV	Ultraviolet
ν	Vibrational energy level
v/v	Volume per volume
VR	Vibrational relaxation
vs	Verses
w/v	Weight per volume (g L ⁻¹)
w/w	Weight per weight
X	Random amino acid
π-π^*	Bonding to antibonding pi orbital transition

Symbols

%	Percent	J	Joules
% min⁻¹	Percent per minute	K	Kelvin
[x]	Concentration of x	k	Boltzmann constant ($1.38 \times 10^{-23} \text{ m}^2 \text{ kg s}^{-2} \text{ K}^{-1}$)
°C	Celsius	kDa	Kilodaltons (10^3 Da)
A	Ampere or Absorbance or Amplitude	kg	Kilograms (10^3 g)
Å	Ångström	kW m⁻²	Kilowatts per meter squared (10^3 W m^{-2})
B	Baseline	L	Litre
c	Concentration or Speed of light ($\sim 3.00 \times 10^8 \text{ m s}^{-1}$)	l	Pathlength
cm	Centimetre (10^{-2} m)	M	Molar
D	Diffusion coefficient	m	Meter
Da	Dalton	m s⁻¹	Meter per second
e	Exponential	mA	Milliampere (10^{-3} A)
eV	Electron volt	mg	Milligrams (10^{-3} g)
F	Faraday constant (96485 J mol^{-1})	mg mL⁻¹	Milligrams per millilitre
g	Grams or Gravitational-force	mins	Minutes
g(t)	Time autocorrelation function	mL	Millilitre (10^{-3} L)
h	Planck's constant ($6.58 \times 10^{-16} \text{ eV s}$)	mM	Millimolar (10^{-3} M)
hr	Hour	mm	Millimetre (10^{-3} m)
hrs	Hours	mM⁻¹ cm⁻¹	Extinction coefficient units
I	Intensity	mV	Millivolt (10^{-3} V)

mV s⁻¹	Millivolt per second	μA	Microampere (10 ⁻⁶ A)
MΩ cm	Electrical resistivity units	μg	Micrograms (10 ⁻⁶ g)
n	Number of electrons	μg mL⁻¹	Micrograms per millilitre
nm	Nanometer (10 ⁻⁹ m)	μL	Microlitre (10 ⁻⁶ L)
psi	Pound per square inch	μm	Micrometer (10 ⁻⁶ m)
ppm	Parts per million	μM	Micromolar (10 ⁻⁶ M)
q	Magnitude of scattering vector		
R	Gas constant (8.31 J K ⁻¹ mol ⁻¹)		
r	Hydrodynamic radius		
s	Second		
T	Temperature		
t	Time		
V	Volts		
W	Watts		
W m⁻²	Watts per meter squared		
ΔAbs	Difference in absorbance		
ε	Extinction coefficient		
η	Solvent viscosity		
λ	Wavelength		
λ_{max}	Wavelength of absorbance maximum		

Chapter 1

Introduction

1.1 General Introduction

Due to rapid population and economic growth, global energy demand is projected to at least double by 2050 relative to the present and be more than triple by the end of this century.^[1-3] Such projections amplify concerns surrounding the depletion of finite fossil reserves; elevation of atmospheric CO₂ levels; and the knock on effects in global environmental and climate change. Therefore focus has grown on developments that aim to enhance the sustainable production of electricity and fuels. Nuclear, geothermal, biomass, solar, wind, tide and wave are all sources of sustainable energy that are abundant, cheap and environmentally clean. Even though there is already technology available to utilise each of these options, most are unable to supply electricity to match the current demand even when taken together. Nuclear energy offers high energy output; however, construction of new reactors is controversial with unresolved significant problems associated with nuclear weapons and long-term radioactive waste storage and disposal. In contrast, our sun is the ultimate energy source, delivering more energy to the earth in one hour (4.3×10^{20} J) than humankind currently uses in a year from fossil, nuclear and all renewable sources (4.1×10^{20} J).^[4] This near inexhaustible energy supply has the greatest potential to meet our future energy needs, and its use is safe for our environment and climate.

The utilisation of solar energy requires solar capture, energy conversion and storage. Photovoltaic technologies that capture and convert sunlight to electricity are well-established; however, they suffer from lower efficiencies and higher costs compared with those of fossil fuels, as well as intermittency issues due to daily and annual variations in light levels. Therefore focus has grown on further developing photovoltaic technologies so the electricity produced can be used to generate fuels such as hydrogen from water splitting or formate from carbon dioxide reduction.^[5, 6] In addition to providing energy-dense fuels that can be stored and selectively used, the generation of carbon-based products provides a new source of chemical feedstocks for the chemical, material and pharmaceutical industries that are derived from precursors other than fossil fuels.^[7] Such methods that produce fuels and more complex carbon-based compounds from solar energy gains inspiration from natural photosynthesis.

Photosynthesis as performed in green plants is outlined below. This provides the context for describing approaches towards artificial photosynthesis that aim to combine biotic and/or abiotic components for light-driven production of useful chemicals. The discussion continues by describing the advantages of compartmentalised systems for nanoreactor design and introduces bilayer-spanning porin:cytochrome complexes as conduits for transmembrane electron transfer. This sets the scene for describing studies, Chapter 3 to 6, that aimed to develop and demonstrate lipid-based nanoreactors where external light capture and charge separation was coupled to internal reductive transformations by electron transfer through a conductive porin:cytochrome complex, MtrCAB.

1.2 Natural Photosynthesis

Life, as we know it, depends on solar energy. Over billions of years Nature has developed methods that capture, transform, and utilise solar energy. Photosynthesis is the vital multistep process that converts solar energy into chemical energy by splitting water to produce oxygen and hydrogen equivalents. The chemical energy within these hydrogen equivalents is then converted and stored as energy-dense sugars which are used to fuel all forms of life.

All photoautotrophic organisms, including plants, algae, purple bacteria and cyanobacteria, contain light absorbing reaction centres which carry out light harvesting within the photosynthetic process. Crucial to the design of all of Nature's photosynthetic reaction centres is the bilayer lipid membrane which allows for the molecular organisation of the proteins, lipids, redox molecules and light-absorbing chemicals that are necessary for light capture and charge separation. Light-driven, transmembrane electron transfer and coupled transport of protons across these membranes are key to driving the synthesis of adenosine triphosphate (ATP) and generating hydrogen equivalents. The stored energy within ATP and the reducing power provided by hydrogen equivalents are then used within the light-independent reactions of the Calvin cycle to convert carbon dioxide into more complex carbon compounds. In plants the photosynthetic membrane, the thylakoid membrane, consists of two photosystems which are arranged in series, as illustrated in Figure 1.1.

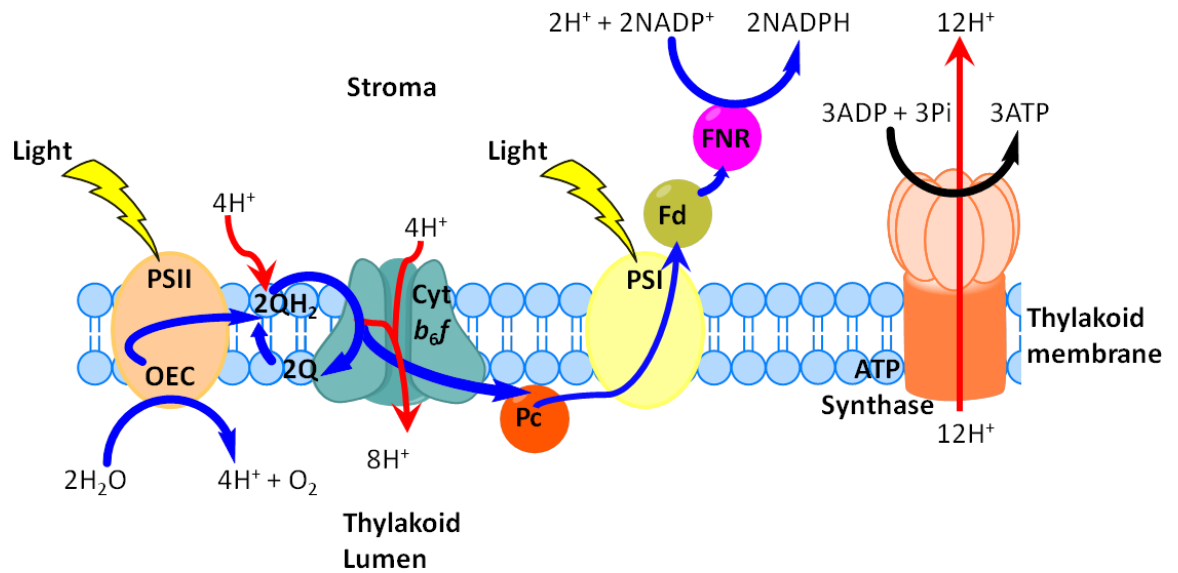


Figure 1.1. Schematic of thylakoid membrane and the electron transfers and proton translocations key to light harvesting within photosynthesis.

Photoexcited electrons within photosystem II (PSII) are transported via plastoquinone (Q), plastocyanin (Pc) and cytochrome *b₆f* to photosystem I (PSI). Ferredoxin (Fd) then mediates the transfer of photoexcited electrons to ferredoxin-NADP⁺ reductase (FNR) which reduces NADP⁺ to NADPH. This electron transport allows the transfer of protons from the stroma into the lumen. This, alongside the oxidation of water by the oxygen evolving complex (OEC), generates a transmembrane proton gradient that powers the synthesis of ATP. Blue arrows represent electron transfers and red arrows represent proton translocations. See text for details.

Firstly sunlight is captured by chlorophylls within photosystem II (PSII), Figure 1.2. Chlorophylls are highly conjugated, magnesium-ion-containing molecules that strongly absorb visible light, which promotes the photoexcitation of an electron which drives the otherwise thermodynamically unfavourable transfer of electrons to photosystem I (PSI). Further light absorption here drives ferredoxin-NADP⁺ reductase (FNR) to produce a reduced hydrogen equivalent in the form of NADPH (reduced form of nicotinamide adenine dinucleotide phosphate, NADP⁺). This transmembrane electron transfer generates a proton gradient across the membrane, which drives the synthesis of ATP by ATP synthase.

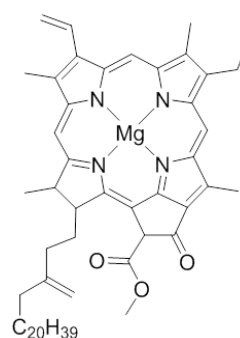


Figure 1.2. Structure of chlorophyll *a*.

The oxidised form of PSII is a highly powerful oxidant which drives the most energetically demanding reaction in biology, the oxidative splitting of water into oxygen and protons by the oxygen evolving complex (OEC). Sacrificial electrons produced as by-products of the OEC water splitting reaction are donated to PSII to regenerate it and complete the cycle of photosynthesis. Therefore H₂O essentially acts as a sacrificial electron donor (SED) to regenerate PSII.

1.3 Artificial Photosynthesis: Three-Component Systems

To completely mimic photosynthesis a system would require five essential modular components: i) a light-absorbing centre to promote the photoexcitation of an electron; ii) a water oxidation catalyst; iii) a catalyst which reduces protons or carbon dioxide to make desirable hydrogen or complex carbon compounds; iv) a membrane which isolates these catalysts, and their reactants and products within different reaction compartments; and v) a transmembrane electron transport chain which electrically links the two compartments whilst preventing unwanted relaxation of the photoexcited electron. Because of the complexity of this idealized system, a fully functional molecular artificial photosynthetic system has yet to be demonstrated.^[8]

To avoid such complexities, and be left with a simpler three-component system, the oxidation and reduction half-reactions are studied in the presence of a sacrificial oxidant or reductant to compensate for the absence of the complementary catalyst. Artificial photosynthesis focuses on the production of fuel or high added-value organic compounds by mimicking reactions of PSI. Therefore artificial photosynthetic systems are traditionally reductive three-component systems that consist of: i) a light-absorbing molecule; ii) an electrocatalyst; and iii) a sacrificial electron donating molecule. The possibilities and mechanisms in which these chemical analogues of PSI operate are discussed in the following subsections.

1.3.1 Photosensitisers

When a molecule absorbs a photon of light the associated energy excites an electron to a higher energy level, Figure 1.3. A molecule will only absorb certain wavelengths of light which correspond to the energy required to promote electrons from the ground state (S_0) to an excited state (S_1 , S_2 , etc). Once photoexcited, the fate of the excited state will depend upon molecular properties, such as the lifetimes of excited states and the relative rates of photophysical processes. Figure 1.3 summarises how an excited state can dissipate the

energy from an absorbed photon where the possible observed outcomes include fluorescence, phosphorescence, and energy or electron transfer to other species.

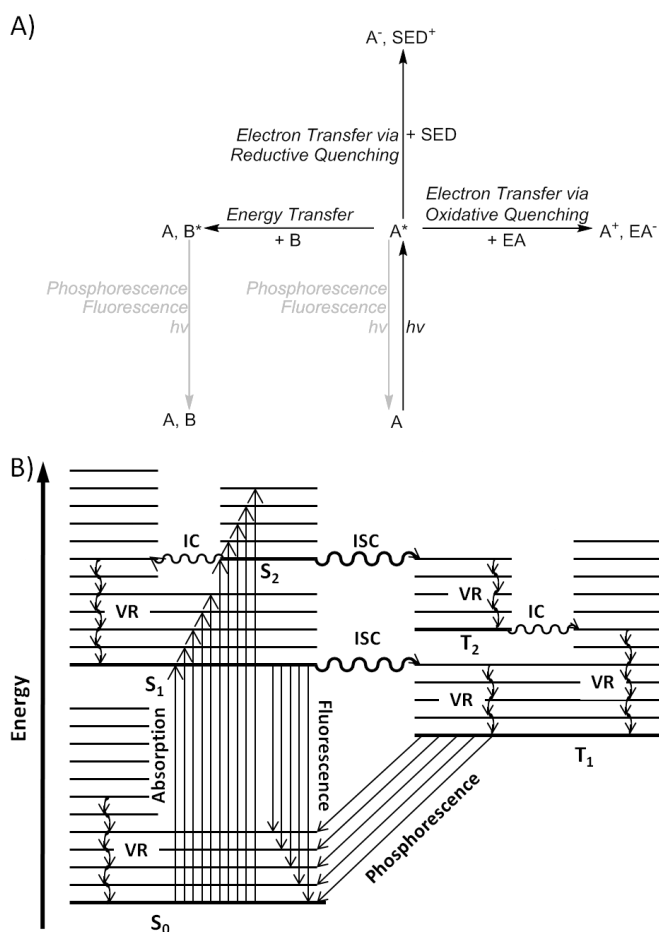


Figure 1.3. Overview of outcomes after photoexcitation of a molecule within multiple and single compound systems.

A) Possible ultimate outcomes after photoexcitation of molecule A. A*, A⁻ and A⁺ corresponds to the photoexcited, one-electron reduced and oxidised states, respectively. EA is the electron acceptor. SED is the sacrificial electron donor. B is a molecule which accepts energy from A to go into an excited state (B*). B) Typical Jablonski diagram of a single compound system. Molecular energy levels are schematically arranged within columns representing different electron spin multiplicities. Within electronic energy states are multiple vibrational energy levels, where bold lines are ground vibrational level of the electronic energy states ($\nu = 0$). Wavy arrows represent radiationless transitions, i.e. energy changes not involving emission of a photon. Straight arrows represent radiative transitions, i.e. energy changes involving absorption or emission of a photon. S₀ is the singlet ground. S₁ and S₂ are the first and second singlet excited states, respectively. T₁ and T₂ are the first and second triplet excited states, respectively. VR is vibrational relaxation. ISC is intersystem crossing. IC is internal conversion.

Immediately after photoexcitation, excess energy is lost to the surroundings as heat via collisions and molecular vibrations. This vibrational relaxation (VR) happens incrementally until the molecule relaxes to the ground vibrational level of the excited electronic state. Internal conversion (IC) is the relaxation from the ground vibrational level of a higher electronic state to a lower electronic state, i.e. S₂ → S₁. IC is quickly followed by VR to the relevant ground vibrational level. Intersystem crossing (ISC) is a transition

between electronic states of different multiplicity, i.e. $S_2 \rightarrow T_2$. Since triplet states have lower energy than the corresponding singlet state, ISC is followed by VR. The majority of energy of a photoexcited state may then be lost through the spontaneous emission of a photon from the lowest vibrational level of an excited electronic state. Fluorescence occurs when the electron spin does not change during the emission, i.e. $S_1 \rightarrow S_0$. Phosphorescence occurs when the spin of the electron changes during the photon emission, i.e. $T_1 \rightarrow S_0$.

The excited state of a molecule can also undergo energy- or electron-transfer with another molecule. Molecular quenching via energy transfer sees the original excited molecule act as an energy donor to a different molecule, which in turn becomes excited so it can perform the same photophysical processes discussed above. Electron transfers occur when an excited molecule acts as an electron donor and/or acceptor to other molecules, Figure 1.4. Molecules which are able to perform such light-driven reductions and oxidations are termed photosensitisers, and it is these that catalyse light-driven electron transfers in photocatalytic applications such as artificial photosynthesis.

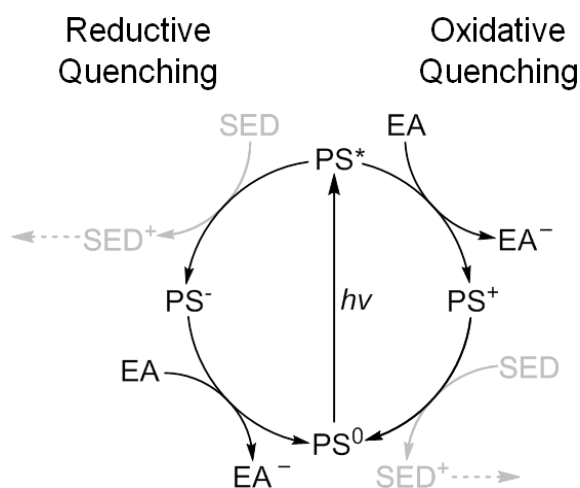


Figure 1.4. Photoreduction via reductive and oxidative quenching mechanisms.

EA is the target electron acceptor. PS^0 , PS^* , PS^- and PS^+ correspond to the ground, photoexcited, one-electron reduced and one-electron oxidised states of a photosensitiser (PS), respectively. SED is the sacrificial electron donor. For simplicity only those steps that positively contribute to photoreduction are shown.

For photocatalytic reduction, net photoreduction of a target electron acceptor (EA) can occur via oxidative and reductive quenching mechanisms, Figure. 1.4. After the photosensitiser absorbs light to promote an electron from the ground state (PS^0) to an excited state (PS^*), photoreduction of EA proceeds by: i) oxidative quenching of PS^* via reduction of target EA before the oxidised photosensitiser (PS^+) is regenerated to PS^0 through oxidation of a SED; or ii) reductive quenching of PS^* by SED oxidation before the reduced photosensitiser (PS^-) reduces the target EA to return to PS^0 and complete the photocatalytic cycle.^[9]

For these electron transfers to be possible, photosensitisers must have long lived excited states to be able to diffuse through solution and collide with another molecule to form a short-lived, photoexcited donor-acceptor complex. Electron transfers proceed by either: i) an inner sphere mechanism, in which a bridging ligand is transferred between the donor and acceptor; or ii) an outer sphere mechanism which relies on the overlap of the electronic orbitals of the donor and acceptor molecules. Electron transfers that are induced by an irradiated photosensitiser are not associated with bond breaking/formation and therefore occur via an outer sphere mechanism. Once a photoexcited donor-acceptor complex is formed, outer sphere electron transfer is only successful if the formed complex results in a significant electronic orbital overlap before complex dissociation.

There are numerous different photosensitisers but they all fall within the classes of: organic photosensitisers (xanthenes, acridines, and flavins, etc); inorganic complexes (ruthenium(II), cobalt(III), chlorins, etc); quantum dots (cadmium selenide, lead sulphide, etc); semiconducting nanoparticles (titanium dioxide, zinc oxide, etc); and dye-sensitised nanoparticles.^[10] All these photosensitisers carry out their photoredox reactions via quenching mechanisms, with their underlying basis outlined in Figure 1.4. Properties that impact on the choice of a photosensitiser for a specific application includes solubility in water; fast electron transfers; high quantum efficiencies; large extinction coefficients; spectral absorption range; sufficiently long excited-state lifetime; favourable oxidation and reduction potentials; and high photochemical stability.^[8] It is common that in choosing a photosensitiser for one particular advantageous property another intrinsic property could hinder the desired photochemical reaction.

The feasibility of reductive and/or oxidative quenching mechanisms to carry out successful photoreduction is determined by relevant photosensitiser (photo)reduction potentials in respect to those of the target electron acceptor, and SED, as exemplified in the following equations. Photosensitiser photoexcited state energy can be calculated from the wavelength of phosphorescence where the triplet excited state decays back to the ground state. The Planck–Einstein relation (Equation 1.1) converts this wavelength, λ , into photon energy, E (PS*), where h is the Planck constant and c is the speed of light.

$$E(\text{PS}^*) = hc/\lambda \quad (1.1)$$

Photoreduction potentials of the excited state, $E_m(\text{PS}^*/\text{PS}^-)$ and $E_m(\text{PS}^+/\text{PS}^*)$, are calculated from photoexcited state energy, $E(\text{PS}^*)$, and the cyclic voltammetry determined standard reduction and oxidation potentials of the ground state photosensitisers, $E_m(\text{PS}^0/\text{PS}^-)$ and $E_m(\text{PS}^+/\text{PS}^0)$ respectively, using Equations 1.2 and 1.3.

$$E_m(\text{PS}^*/\text{PS}^-) = E(\text{PS}^*) + E_m(\text{PS}^0/\text{PS}^-) \quad (1.2)$$

$$E_m(\text{PS}^+/\text{PS}^*) = E_m(\text{PS}^+/\text{PS}^0) - E(\text{PS}^*) \quad (1.3)$$

In some cases photosensitiser triplet state energies have been estimated from the wavelength of fluorescence where the singlet excited state decays back to the ground state. This causes slight over-estimations in both photoexcited state energies and photoreduction potentials of photoexcited states.

Irrespective of the driving force, the extent of photoreduction achieved under a given condition in practice is also determined by the rates of these reactions and those of competing excited electron recombination processes, which are not productive with respect to reduction of the desired target.

1.3.2 Electrocatalysts

There is a vast selection of electrocatalysts to choose from when designing artificial photosynthetic systems to catalyse the reduction of protons or carbon dioxide, as discussed below. These electrocatalysts can be elemental catalysts, purified enzymes or synthetic homologues inspired by these biological electrocatalysts.

Platinum and iridium have been used as catalysts for the reduction of protons during the electrolysis of water; however, their use are limited for large-scale hydrogen production due to these elements being finite, expensive and readily inhibited.^[11] Enzymes which catalyse the inter-conversion between protons and hydrogen under ambient conditions are called hydrogenases. These hydrogenases are divided into three different classes that are based on their catalytic site chemical composition of either: dinuclear Fe, dinuclear Ni-Fe or mononuclear Fe.^[12] The iron-sulphur cluster free [Fe]-hydrogenase is exclusively involved in hydrogen oxidation, during which reduction of the cofactor of methenyltetrahydromethanopterin occurs as an intermediary step in carbon dioxide reduction to methane.^[13] [FeFe]-hydrogenases contain a unique dinuclear [2Fe-2S] cluster which is connected via a cysteine sulphur bridge to a ferredoxin-type [4Fe-4S] cluster. [NiFe]-hydrogenases contain a dinuclear [NiFe] complex in which the two metal atoms are bridged together by two cysteine ligands. The irons within the active site of these hydrogenases are further coordinated by carbon monoxide and cyanide ligands.

These [NiFe]- and [FeFe]-hydrogenases can catalyse the reversible reduction of protons which can be used for sustainable hydrogen production. Hydrogenases have received considerable interest because they use Earth-abundant metals, have high catalytic

activity and also demonstrate a high selectivity towards protons. In addition to this, some hydrogenases can operate with high efficiency in the presence of oxygen and even conventional platinum inhibitors such as carbon monoxide and hydrogen sulphide.^[14] Purified hydrogenases have been coupled with photosensitisers for solar hydrogen production; however, scaling up the application of hydrogenases within artificial photosynthesis is not practical given their oxygen sensitivity, the requirement for large-scale cultivation of organisms and difficulties in purification of active enzyme.^[15, 16]

Considerable efforts have been made to mimic the active sites of hydrogenases with the synthesis of analogous molecular catalysts. Indeed, several functional organo-metallic complexes containing iridium, rhodium, nickel, iron, platinum, palladium and/or cobalt have been prepared that show structural and/or functional features similar to those of the hydrogenases catalytic sites.^[8, 17–19] A number of these have been successfully coupled with photosensitisers to produce catalytic solar hydrogen.

The reduction of carbon dioxide to useful molecules such as carbon monoxide, formic acid, methanol, ethanol, pyruvate, and methane are carried out by an even more diverse range of purified enzymes and synthesised catalysts.^[7, 20] Such purified enzymes include pyruvate synthase and carbon monoxide and formate dehydrogenases.

1.3.3 Sacrificial Electron Donors

To achieve net photoreduction of a desired target electrocatalyst/molecule in artificial photosynthetic systems, sacrificial electron donors (SEDs) are used alongside a photosensitiser. SEDs are simple molecules that readily fuel a photosensitiser with electrons, whilst producing inert waste products which are unable undergo recombination reactions with the photoreduced target electrocatalyst/molecule. Within natural photosynthesis, H₂O can be viewed as the SED that fuels PSII with electrons and O₂ can be viewed as the non-reactive waste product. Theoretically the desired photoreduction will proceed until all SEDs have been oxidised. There are many different SED molecules used in artificial photosynthetic systems including: ascorbic acid; lactic acid; oxalate; thiols; thiolates; triphenylphosphine; phenols; and tertiary amines.^[21]

Triethanolamine (TEOA) is a well described SED employed in photoreductions, with a reduction potential around 1000 mV vs SHE.^[22, 23] Reductive quenching of photosensitiser photoexcited state and regeneration of oxidised photosensitisers occurs via electron donation by the tertiary amine group of TEOA to generate an aminyl radical cation, Figure 1.5.^[24, 25] This aminyl radical cation in theory is a strong oxidant which

could react with any reduced species to cause counterproductive back electron transfer. However, subsequent proton abstraction from the aminyl radical by another TEOA molecule yields a strongly reducing carbon-centered radical which prevents back electron transfer and can donate a second electron.^[24, 25] The iminium species formed here can undergo hydrolysis to further degrade into glycolaldehyde and a secondary amine.

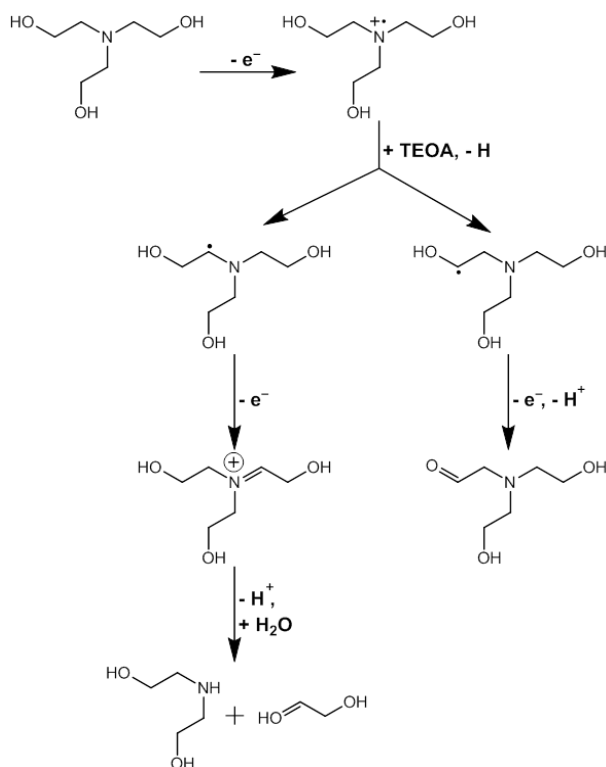


Figure 1.5. Scheme for the oxidation of TEOA.

1.4 Artificial Photosynthesis: Beyond Three-Component Systems

1.4.1 Artificial Leaf

There have been a number of notable successes that extend beyond the three-component artificial photosynthetic systems, heading towards a fully functional molecular artificial photosynthetic system, Figure 1.6. The most notable of these was developed by Nocera *et al.* and is commonly termed the “artificial leaf”, Figure 1.6 A.^[5, 26] This advanced photovoltaic cell comprises earth-abundant elements and consists of a triple junction, amorphous silicon photovoltaic interfaced to a hydrogen-evolving-reaction catalyst (HER) and an oxygen-evolving complex (OEC) made from a nickel-based ternary alloy (Ni-HER) and a cobalt phosphate catalyst (Co-OEC), respectively.^[5, 26] This artificial photosynthetic device was the first to couple a solar cell and both water-oxidising and proton-reducing catalysts into one stand-alone device with no wires in between. When the device was

immersed in water and irradiated, solar energy was converted into stored chemical energy within hydrogen bonds via water splitting, with an overall direct solar-to-fuels efficiency of 2.5 % which is an improvement on that of natural plant leaves that averages at 1 %.^[5, 27]

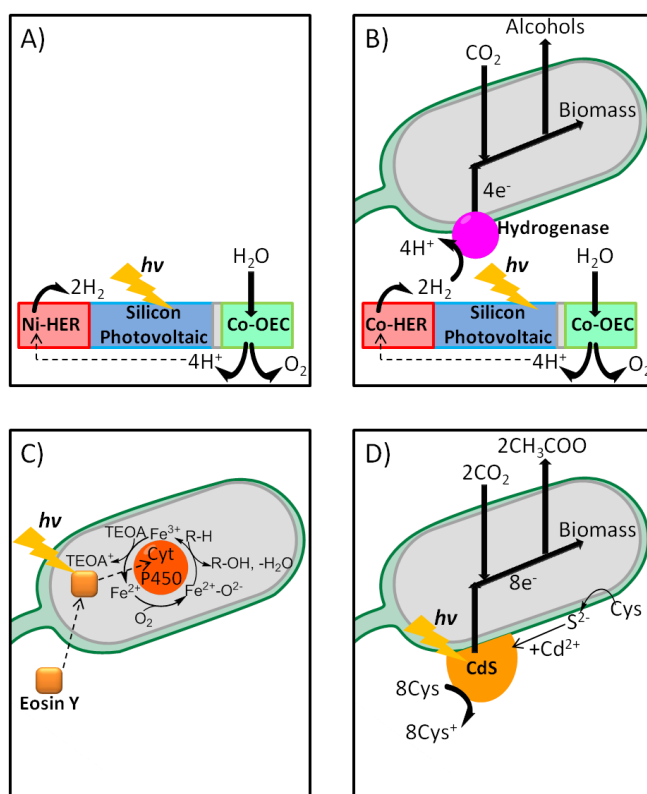


Figure 1.6. Notable successes that head towards fully functional molecular artificial photosynthetic systems.

A) Light-driven water oxidation takes place at the Co-OEC with proton reduction taking place at the Ni-HER.^[5, 26] B) Light-driven water oxidation takes place at the Co-OEC with proton reduction taking place at the Co-HER. *R. eutropha* oxidises hydrogen using a membrane-bound hydrogenases to ultimately reduce carbon dioxide to alcohols via the Calvin cycle.^[28] C) Eosin Y enters the cytoplasm of *E. coli* and binds to cytochrome P450. Subsequent light-driven catalytic turnover of cytochrome P450 is mediated by eosin Y in the presence of TEOA.^[29] D) *M. thermoacetica*-CdS hybrid system forms from the precipitation of CdS nanoparticles. Subsequent light-driven reduction of carbon dioxide to acetic acid, via the Wood-Ljungdahl cycle, is mediated by surface CdS in the presence of cysteine.^[30] Not to scale. See text for further details.

This device offered many attractive features. The Co-OEC self-assembled upon oxidation of Co(II) to Co(III) in aqueous solution at room temperature and was self healing. The oxygen-evolving reaction by the Co-OEC occurred in water at neutral or near-neutral conditions, which allowed the use of the Ni-HER. The conductivity and stability of the silicon was enhanced by coating its surface with a conducting metal oxide. Even with all of these attractive benefits, the scaling up of this device was not pursued as the lack of hydrogen storage infrastructure and the costly photovoltaic framework was considered too expensive in comparison to existing energy sources.^[27, 31]

More recently a hybrid inorganic-biosynthetic system has been developed by Nocera *et al.* that uses the catalysts of the artificial leaf in combination with wild-type and engineered *Ralstonia eutropha* (*R. eutropha*) to synthesise biomass and liquid fuel alcohols, respectively, from the hydrogen produced.^[32] A membrane-bound hydrogenase oxidises the hydrogen to fuel the reduction of carbon dioxide by *R. eutropha*. However, this system required high overpotentials to drive water splitting as low overpotentials favoured the production of toxic reactive oxygen species by the Ni-HER over biological cell growth.^[32] The Ni-HER leached toxic nickel which also inhibited cell growth, therefore it was decided that the cathode of this bionic artificial leaf should be replaced.^[32]

Swapping the Ni-HER with a cobalt-phosphorus alloy (Co-HER) provided a cathode that was not toxic to the bacterium, resistant to reactive oxygen species and allowed the overpotential for water splitting to be lowered, Figure 1.6 B.^[28] Moreover, the activity of the Co-HER surpassed the activity of the Ni-HER, and any toxic cobalt leached from the Co-HER was salvaged by the self healing Co-OEC.^[28] Even though ~ 50 % of the electrons gained by *R. eutropha* went into carbon dioxide reduction, the rate of electrons being fuelled into *R. eutropha* was limited by hydrogen oxidation.^[28] This system was however shown to be scalable without affecting the solar-to-fuels efficiency of ~ 10 %.^[28]

1.4.2 Light-Driven Whole-Cell Catalysis

Being able to couple photosensitisers to the enzymes of microorganisms provides another highly attractive, novel route for the generation of valuable chemicals from solar energy. Such microbial catalysts are inexpensive, easy to grow, scalable, and self-sustaining and long-lived as long as they gain enough energy to perform essential cell maintenance.^[33] Additionally, time-consuming and labour-intensive enzyme purifications are avoided by performing whole-cell catalysis. There are a few notable successes in whole-cell photoredox catalysis.

Park *et al.* were able to show that with the careful selection of an appropriate photosensitiser, photosensitisers can enter within microbial cells to perform *in vivo* light-driven catalysis, Figure 1.6 C.^[29] The organic photosensitiser, eosin Y, was able to enter the cytoplasm of *Escherichia coli* (*E. coli*) and bind specifically to the heme domain of cytochrome P450.^[29] Cytochrome P450 belongs to a family of heme containing monooxygenases that can catalyse various regioselective and stereospecific oxygen insertion reactions of non functionalised hydrocarbons (e.g. deamination, hydroxylation, and dealkylation).^[34] Upon visible-light irradiation, photoexcited electrons from eosin Y

are directly transferred to the heme iron.^[29] This photoactivation of the P450 catalytic cycle successfully was able to carry out the bioconversion of numerous substrates; including chemicals, pharmaceuticals and steroids.^[29]

Yang *et al.* showed non-photosynthetic bacteria can use cadmium sulphide (CdS) quantum dots to harvest electrons from sunlight to reduce carbon dioxide, resulting in the production of acetate, Figure 1.6 D.^[30] Growing an acetogen, *Moorella thermoacetica* (*M. thermoacetica*), in the presence of cadmium and cysteine led to the biological precipitation of CdS nanoparticles that coated the surface of the bacterium.^[30] Upon irradiation, photoexcitation of CdS resulted in electron transfer to *M. thermoacetica* which reduced carbon dioxide to generate acetate.^[30] The exact mechanism of how photoexcited electrons are transferred to *M. thermoacetica* is unknown but could have occurred by: i) hydrogen production at the CdS surface, followed by hydrogen oxidation by membrane-bound hydrogenases; ii) direct electron transfer from CdS to membrane-bound hydrogenases; iii) direct electron transfer to membrane-bound cytochromes; and/or iv) electron transfer by secreted soluble redox mediators.^[30] Either way, growth of this hybrid organism was sustained purely through solar energy and only was limited by the depletion of cysteine.^[30] Notably, this system had a solar-to-fuels efficiency of ~ 20 %, with ~ 90 % of the electrons being directed towards acetate production and the other ~ 10 % going towards biomass production.^[30]

Just like *M. thermoacetica*, there are many bacteria that are able to participate in the synthesis of CdS, and other, quantum dots which could potentially then be used to mediate whole-cell photocatalysis.^[35] Many strains of *Klebsiella* overcome cadmium toxicity through the formation of photoactive, CdS nanoparticles on the cell surface.^[35–37] Cadmium detoxification is also carried out by *Clostridium thermoaceticum* which forms CdS nanoparticles at the cell surface as well as in the extracellular solution.^[38] When *E. coli* is incubated with cadmium chloride and sodium sulphide, intracellular formation of CdS nanoparticles occurs following the uptake of Cd²⁺ and S²⁻ ions.^[39] These are just a few examples of many. Bacteria are able to produce a huge variety of high-valued chemicals; therefore, the direct coupling of photosensitisers to bacteria provides a novel approach to the solar production of chemicals of interest.

The artificial photosynthetic systems discussed here (Figure 1.6) do not include: a membrane which separates the oxidising and reducing reaction compartments; and/or a transmembrane electron transport chain which allows electrical communication between the compartments whilst acting as a reservoir for photoexcited electrons. By not including

these components these systems miss out their benefits which could improve them. The benefits of compartmentalisation and transmembrane electron transfer, and how these can be achieved are discussed in the following sections.

1.5 Compartmentalised Reaction Vessels

Section 1.2 shows how compartmentalisation of multiple enzymes and substrate molecules brings advantages for natural photosynthesis. Such compartmentalisation of catalysts and molecules within spatially separated, nano-scale environments enables a high level of control over reactions and can selectively enhance them. The walls of these nanoreactors serve as scaffolds to stabilise and precisely position numerous catalysts that work together in successful multistep reaction cascades. In addition to facilitating efficient passage of reaction intermediates, nanoreactor boundaries have a semi-permeable nature which minimises opportunities for unwanted reactants to interfere, regulates the flux of molecules in and out of the nanoenvironment, and controls internal conditions (pH, electrolyte concentration, etc) and allows them to differ from external conditions. These compartments can also protect the exterior environment from harmful intermediates or protect the contents from highly reactive external conditions.

Compartmentalisation is crucial to all living cells and is even thought to be instrumental in the origin of life.^[40] Cells have a semi-permeable membrane that allows nutrients to diffuse into the cell, where they are processed. Cells are essentially micro-sized compartments where the cell membrane regulates external stimuli and allows correct internal response. Multicompartmentalisation within cells allows for positional assembly and spatial separation of molecules, enzymes and processes within different compartments. This allows cells to perform many different metabolic reactions simultaneously in a controllable manner, so they do not affect each other in an uncontrolled way.^[41]

Recently increased attention has been given to the elegant compartmentalisation strategies found in Nature and mimicking these nanoreactors.^[41-43] Additional benefits can be envisioned for catalytic reactions performed in compartmentalised nanoreactors when compared to those performed in bulk solutions. Compartmentalisation can simplify the separation of the catalyst from the reaction mixture and thus improves the possibilities for catalyst reuse. As reaction efficiency, selectivity and separation of products are improved by compartmentalisation, reactant concentration need not be as high as those used in bulk solutions. Compartment walls and internal volume provide both hydrophobic and hydrophilic environments, respectively, removing the possible need for organic solvents.

By developing artificial nanocompartments it is hoped the numerous benefits of compartmentalisation can be utilised for compound encapsulation and/or novel (bio-)chemical reactors for desired complex catalytic reactions. In order to mimic Nature's compartments, scientists have taken inspiration from natural systems to design a variety of different nano- or micro-capsules, Figure 1.7.

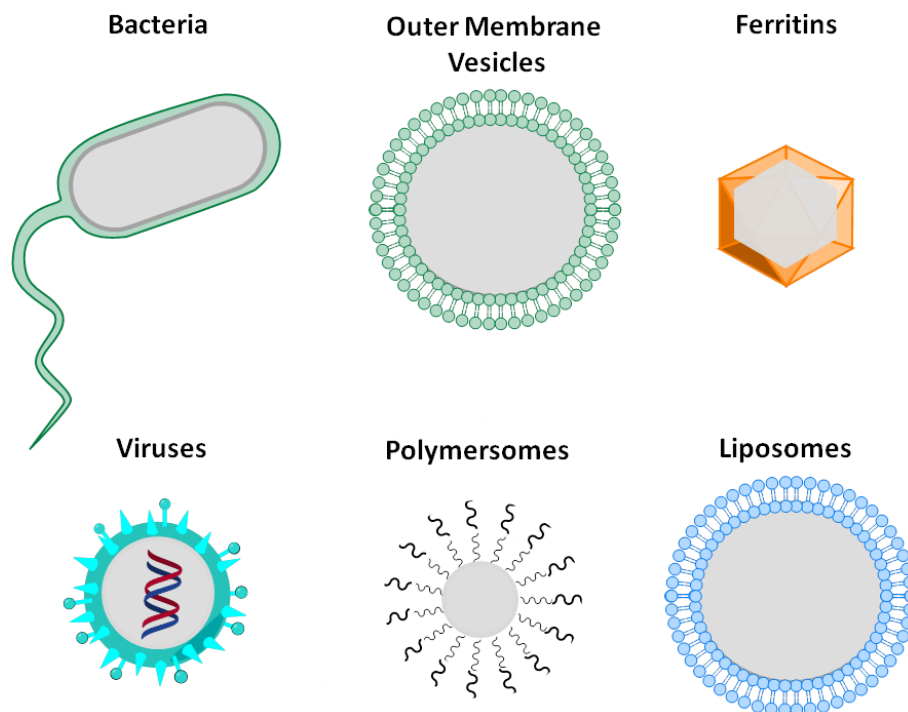


Figure 1.7. Overview of bio-inspired compartmentalised reaction vesicles.

Vesicles are not to scale. Grey areas represent internal aqueous compartments.

These bio-inspired reaction vesicles have been assembled from various components but they share the common features of: i) an internal aqueous volume where the reaction occurs; ii) a semi-permeable shell that allows only desired molecules to enter/exit but prohibits the passage of other molecules; and iii) a catalyst for the desired reaction which is selectively located either internally, externally or actually within the walls of the compartments.

1.5.1 Compartments from Membranes, Proteins and Polymers

To prepare nanoreactors some have taken a top-down approach in which they directly utilise Nature's compartments and adapt them so they encapsulate selected compounds and perform desired reactions. Bacteria are completely natural nanocompartments, Figure 1.7. Bacteria are able to produce a huge variety of high-valued chemicals, e.g. proteins, amino acids, organics, fuels, antibiotics, metabolites and promising chemical precursors for industry and therapeutics.^[44] Therefore, the optimisation of such reaction pathways within

bacteria is of interest to industry. Genetic engineering (inactivation, overexpression, redox engineering, introduction, etc) informed by biochemical, genetic and regulatory studies allows optimisation of existing, or introduction of new, cellular processes and reaction pathways within target bacteria to achieve optimised desired compound production.^[44–46] Even though engineering is informed, it is vastly complex and sometimes gene manipulation can result in unpredicted results which affect the cell viability.

Another approach to manipulating bacterial compartments involves outer membrane vesicles (OMVs), Figure 1.7. OMVs are nano-sized spherical, phospholipid bilayered structures that are produced during the growth of some gram-negative bacteria, via parts of the outer membrane budding to entrap some periplasm before being extruded from the cell surface.^[47] These vesicles have similar compositions to those of the outer membranes, possessing phospholipids, lipopolysaccharides, and outer membrane proteins.^[47] Genetic fusion of a recombinant polypeptide with outer membrane proteins already present allows new fusion partner proteins to be introduced to OMVs.^[48, 49] Genetic engineering towards novel OMVs is even more complex than that of whole cells, due to the more unpredictable influences that gene manipulation may have on the production of OMVs. Purification of OMVs from bacterial cultures can be complex and tricky. The inability to encapsulate any desired compound internally within OMVs, and even whole cells, is a reason why some would avoid using these as nanoreactors.

Other naturally occurring nanocapsules include those consisting of a protein shell, e.g. ferritins, viruses, etc. Ferritins are nano-sized icosahedral cages which naturally store and transport iron ions as compact iron minerals, Figure 1.7. Iron ions, other metal ions, metal complexes and small organic molecules pass into the ferritin interior via three-fold channels within the protein shell.^[50] Unlike ferritin, viruses have a variety of shapes and sizes and provide larger interior spaces for the natural storage of genomic materials such as DNA/RNA, Figure 1.7.^[50] The size and shape of such robust protein cages, and the number and nature of the functional groups on their surface, are precisely defined as they are gene products.^[51–53] Natural cargos within these self-assembled protein cages can be replaced with larger artificial cargos such as molecular catalysts, enzymes, and other interesting chemicals.^[50–54] The proteins cages are conveniently disassembled and reassembled via partial chemical protein denaturing by pH, salt concentration, etc.^[53] The small pores within the protein cages allow substrates and products to freely diffuse in and out of these compartments making them ideal nanoreactors.^[50] In addition, the surface of these nanocompartments can be modified chemically or genetically via covalent linkers and/or

site-specific modification to incorporate new surface functional groups or proteins.^[53] Prior to using such compartments they have to be expressed in host cells and purified.

Another method of preparing nanoreactors is to take a bottom-up approach in which purified or synthesised amphiphilic molecules self-assemble into compartments and simultaneously encapsulate selected compounds for desired reactions.

Polymersomes are vesicles that have polymer membranes and have recently attracted a lot of attention. When amphiphilic block copolymers come into contact with water they spontaneously form bilayered vesicles, whilst encapsulating the aqueous medium, Figure 1.7.^[43] This vesicle formation is similar to those of other amphiphilic molecules but, due to the nature of polymers, forms vesicles that are more stable, less permeable, easier to chemically modify surface functionality and can be tailor-made with respect to size and shape.^[55] Due to long carbon chains of polymers, the thicker bilayers of polymersomes consist of a large hydrophobic domain.^[55] The resulting low bilayer permeability, even to water, is a drawback for nanoreactors relying on internally captured catalysts, as transport of substrates and products across the polymer membrane would be vastly hindered.^[55, 56] The large chemical versatility possible in block copolymer synthesis allows the properties of polymersomes to be selectively tuned.^[57] In some cases, copolymers have been reported to form porous vesicles due to imperfect carbon chain stacking within the bilayer, which allows diffusion of small molecules across the membrane.^[41, 55, 57] In a majority of cases, membrane proteins have been inserted into the polymeric bilayer to induce permeability and allow the diffusion of solvent and substrate molecules.^[58-61] In contrast to polymers, the use of lipids to form vesicles is long-established as discussed in the next sections.

1.5.2 Liposomes

The first, and most widely studied, nanocompartments consisted of a phospholipid bilayer, which made their membranes rather similar to those of cells, Figure 1.7.^[57] These liposomes may be more fragile than their polymersomes counterparts, but they have had much interest since the first protein was incorporated in liposome membranes in 1970.^[62] These lipid vesicles have the advantage that they are more likely to be compatible with membrane proteins. Also reconstitution of purified proteins into liposomes, systems hereafter referred to as proteoliposomes, allows the study of their biochemical and biophysical properties in a model membrane environment, instead of within detergent suspensions. The study of proteins biochemical and biophysical properties can be affected,

complicated or unobservable within the natural cell environment due to the presence of other proteins and chemicals. A detailed discussion of the properties of liposomes follows.

1.5.2.1 Phospholipids

Biological membranes may be complex, but the major component of any membrane is a bilayer formed by phospholipids. These amphiphilic molecules self-assemble so their polar, hydrophilic phosphate groups form two surfaces which interact with the surrounding aqueous environment, while their hydrophobic acyl chains form a nonpolar region in between the two layers.

All natural phospholipids are derived from *sn*-glycerol-3-phosphate, where acyl chains are bound to C-1 and C-2 of the glycerol backbone via ester bonds, as illustrated in Figure 1.8. Esterification of the phosphate group of phosphatidic acid (PA), the simplest phospholipid, with various alcohols (choline, ethanolamine, serine, glycerol or inositol) creates the other naturally occurring phospholipids: phosphatidylcholine (PC), phosphatidylethanolamine (PE), phosphatidylserine (PS), phosphatidylglycerol (PG) and phosphatidylinositol (PI). The major phospholipids found within mammalian and bacterial membranes are PC and PE, respectively. At physiological pH these zwitterionic phospholipids have an overall neutral charge which dilutes the negative charge caused by the anionic phospholipids PS, PG and PI.

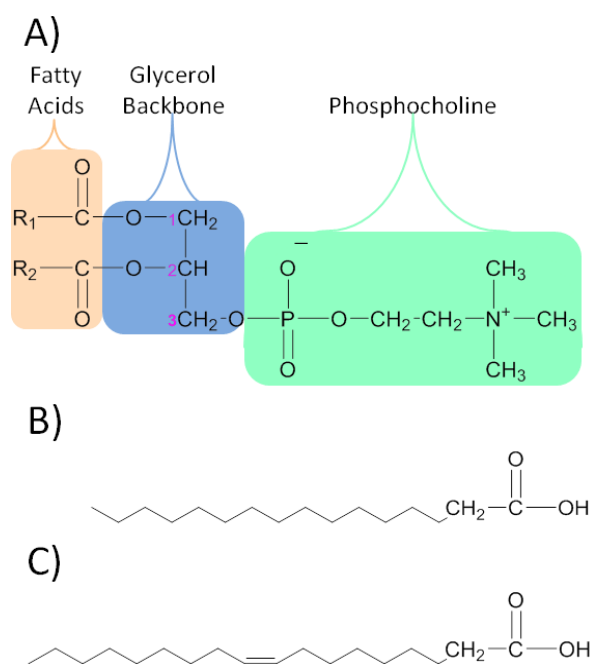


Figure 1.8. Structures of A) phosphatidylcholine, B) palmitoleic acid and C) oleic acid at pH 7. Numeric labels for the glycerol carbons are included in purple. R₁ and R₂ represent the different acyl side chains of PC.

In addition to phospholipids being classified by their phosphate headgroup, they are further identified and subcategorised via the length and saturation of their hydrophobic acyl chains. Acyl chains are typically between 10 to 24 carbons long, with an even number of carbons due to their biosynthesis, and are either saturated or contain one, or more, carbon-carbon double bonds so that they are referred to as unsaturated. For many membrane phospholipids frequently the R-1 acyl chain is saturated while R-2 is unsaturated. The fatty acid common names are used when naming acyl chains as this indicates their chain length and degree of saturation. For example palmitoyl is a saturated 16 carbon chain and oleoyl is a monounsaturated 18 carbon chain with a double bond between carbons 9 and 10, as shown in Figure 1.8.

When it comes to (proteo)liposome preparation, the choice of phospholipid/s plays a vital role in the membrane composition, introduction of unknown impurities, and efficiencies of encapsulation and protein incorporation. It is therefore important to consider which phospholipid/s would best suit the requirements of the (proteo)liposomes.

The best mimic of a cell membrane is achieved by utilising a total lipid cell extract, as this would contain all components, at similar relative abundances, to those naturally found within a lipid bilayer. For example, the major components within *E. coli* total lipid extract (Avanti Polar Lipids Incorporation Product Number 100500) are PE (57.5 %), PG (15.1 %), and the diphosphatidylglycerol cardiolipin (9.8 %), Figure 1.9. A relatively large proportion of this extract is classified as unknown (17.6 %), indicating the presence of other membrane components such as porin proteins and all inner membrane components, including those of the quinone pool. Even though making bilayers from natural membrane extracts would provide the closest comparison to cell membranes these unknown components could interfere with the incorporation and study of a desired purified protein.

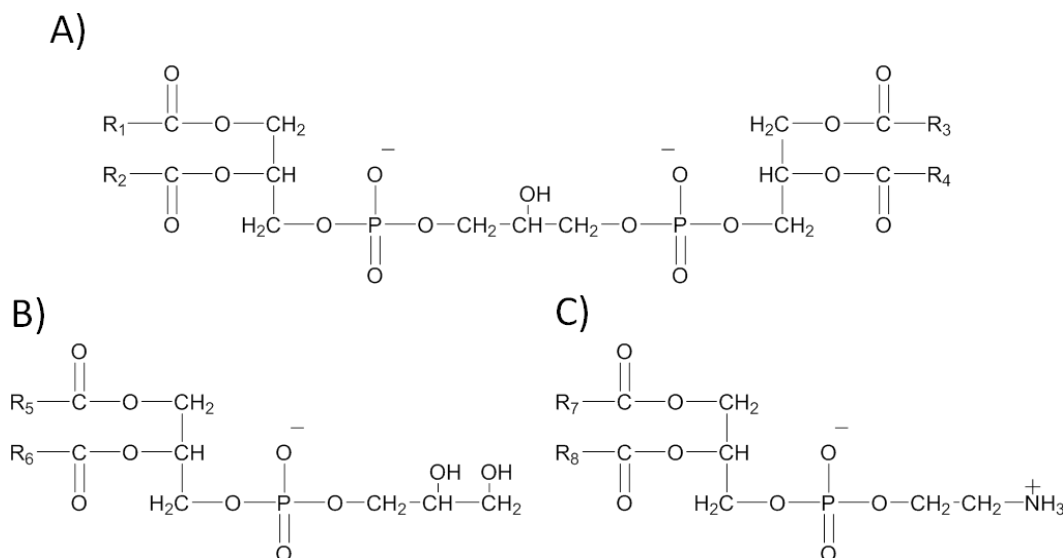


Figure 1.9. Structures of A) cardiolipin, B) phosphatidylglycerol (PG) and C) phosphatidylethanolamine (PE) found within *E. coli* total lipid extract.
 R_1 to R_8 represent the acyl side chains of these phospholipids.

To remove this unknown, phospholipids can be selectively extracted and purified from cell membranes. Acyl chain positions of phospholipids are unaffected upon purification so final purified phospholipids should have a fatty acid distribution similar to that of the natural membrane. For example, PC extracted from mammalian cell membranes and purified by chromatography contains a composition of numerous fatty acids where the major component is 1-palmitoyl-2-oleoyl-*sn*-glycero-3-phosphocholine (POPC), Table 1.1. As POPC molecular length is ~ 2.5 nm, and POPC is the major component, it is assumed bilayers prepared using PC would have a cross sectional length of ~ 5 nm.^[63] POPC, and other phospholipids with defined R_1 and R_2 groups, can also be chemically synthesised as pure lipids, Figure 1.10. Synthetic phospholipids with specific polar head group, fatty acid compositions are synthesised using acylation and enzyme catalysed reactions of *sn*-glycerol-3-phosphocholine, obtained via deacylation of purified phospholipids.^[64]

Fatty Acid (R_1 and R_2)	(Chain Length: Saturation Degree)	Distribution (%)
Myristic Acid	(14: 0)	0.2
Palmitic Acid	(16: 0)	32.7
Palmitoleic Acid	(16: 1)	1.1
Stearic Acid	(18: 0)	12.3
Oleic Acid	(18: 1)	32.0
Linoleic Acid	(18: 2)	17.1
Dihomo- γ -linolenic Acid	(20: 2)	0.2
Mead Acid	(20: 3)	0.3
Arachidonic Acid	(20: 4)	2.7
Docosahexaenoic Acid	(22: 6)	0.4
Unknown	-	1.0

Table 1.1. Fatty acid distribution of chicken egg phosphatidylcholine.
 Details from Avanti Polar Lipids Incorporation Product Number 840051.

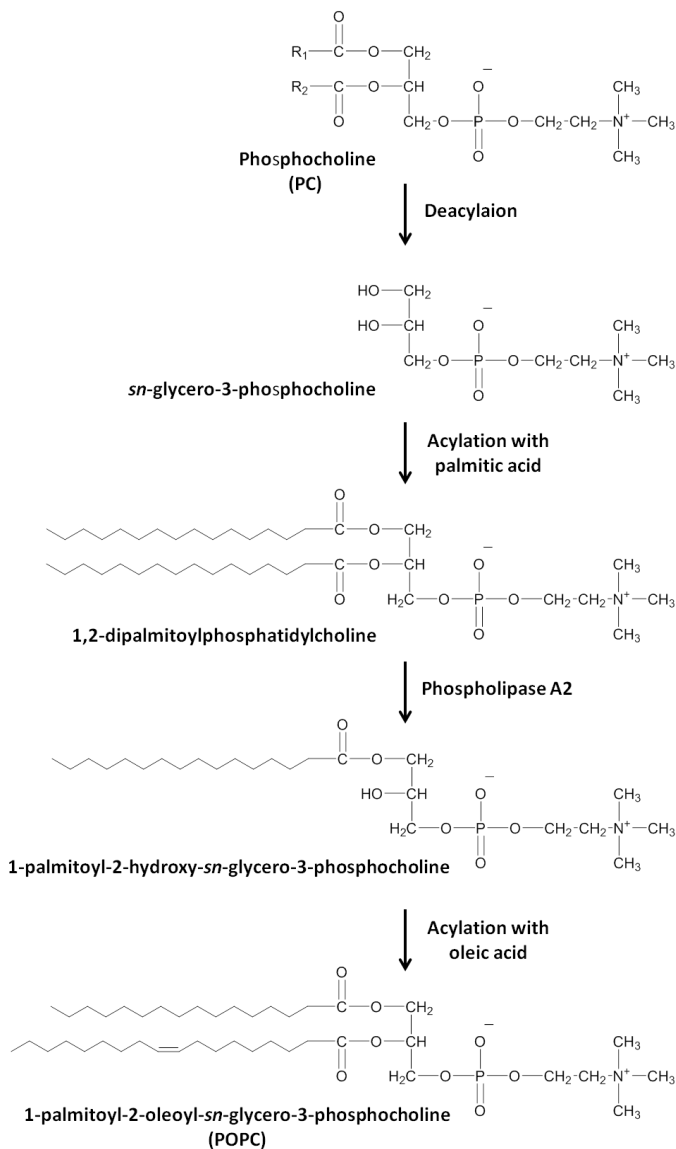


Figure 1.10. Synthesis of POPC from purified natural PC.

Firstly purified natural PC is deacylated to form *sn*-glycero-3-phosphocholine, which is esterified with palmitic acid to yield dipalmitoylphosphatidylcholine. Selective hydrolysis of the palmitic acid at position two of the glycerol backbone is then carried out enzymatically with phospholipase A2 to form 1-palmitic-2-hydroxy-*sn*-glycero-3-phosphocholine. The hydroxyl group can then be esterified with oleic acid.

Such choice in lipid and fatty acid variability allows for complete control in defining the phospholipid composition of prepared membrane bilayers. Preparing an exact mimic of a cell membrane with identical composition via the mixing of purified and synthesised lipids would be extremely difficult; however, due to the vast number of different components.

1.5.2.2 Formation of Liposomes

Aqueous phospholipid suspensions arrange themselves into bilayers, whose edges seal to ensure hydrophobic acyl chains are not exposed to water. This leads to the formation of

approximately-spherical liposomes, where a small aqueous internal environment is enclosed and separated from the external environment during their formation, Figure 1.7. Once formed, liposomes are quite stable and can be purified by dialysis, gel filtration or centrifugation, which allows the external environment to be different to that of the internal environment. These liposome systems closely resemble living cells, as materials such as DNA, proteins, drugs, or other chemicals of interest can be encapsulated by the lipid bilayer.^[64, 65] Spontaneous formation of liposomes with defined membrane compositions occurs upon hydration of lipids, which is advantageous as there is no need to include any other reagents to make liposomes.

Liposomes can be classified by size and number of bilayers of which the membrane is composed, which is highly dependent upon the preparation method used, Figure 1.11.^[63] A liposome membrane composed of a single bilayer is unilamellar, while a membrane composed of multiple concentric bilayers is multilamellar. Multilamellar vesicles (MLVs) are usually formed upon rehydrating dried lipid films with aqueous solutions. MLVs are highly polydisperse with relatively large radii that are greater than 500 nm, but small encapsulated volumes due to their multilamellar structures. Similar to MLVs are multivesicular vesicles where smaller vesicles are encapsulated within one larger vesicle. Giant unilamellar vesicles (GUVs) are extremely fragile due to their relatively large radii of 2.5 to 150 μm . GUVs can be formed by slowly hydrating lipids at high lipid concentrations, before eliminating MLVs via sedimentation through sucrose.^[66] Larger vesicles can be converted into smaller unilamellar vesicles (SUVs) with radii less than 50 nm by extensive sonication, french pressing or extrusion through polycarbonate filters with a defined pore size. Large unilamellar vesicles (LUVs) with radii from 50 to 2500 nm can be made by the fusion of SUVs via freeze-thawing. LUVs have the advantage of having larger encapsulated volumes, but are more fragile due to their larger size and more heterogeneous in size due to freeze-thawing. Repeated extrusion through polycarbonate filters of defined pore sizes provide more uniform LUV sizes.

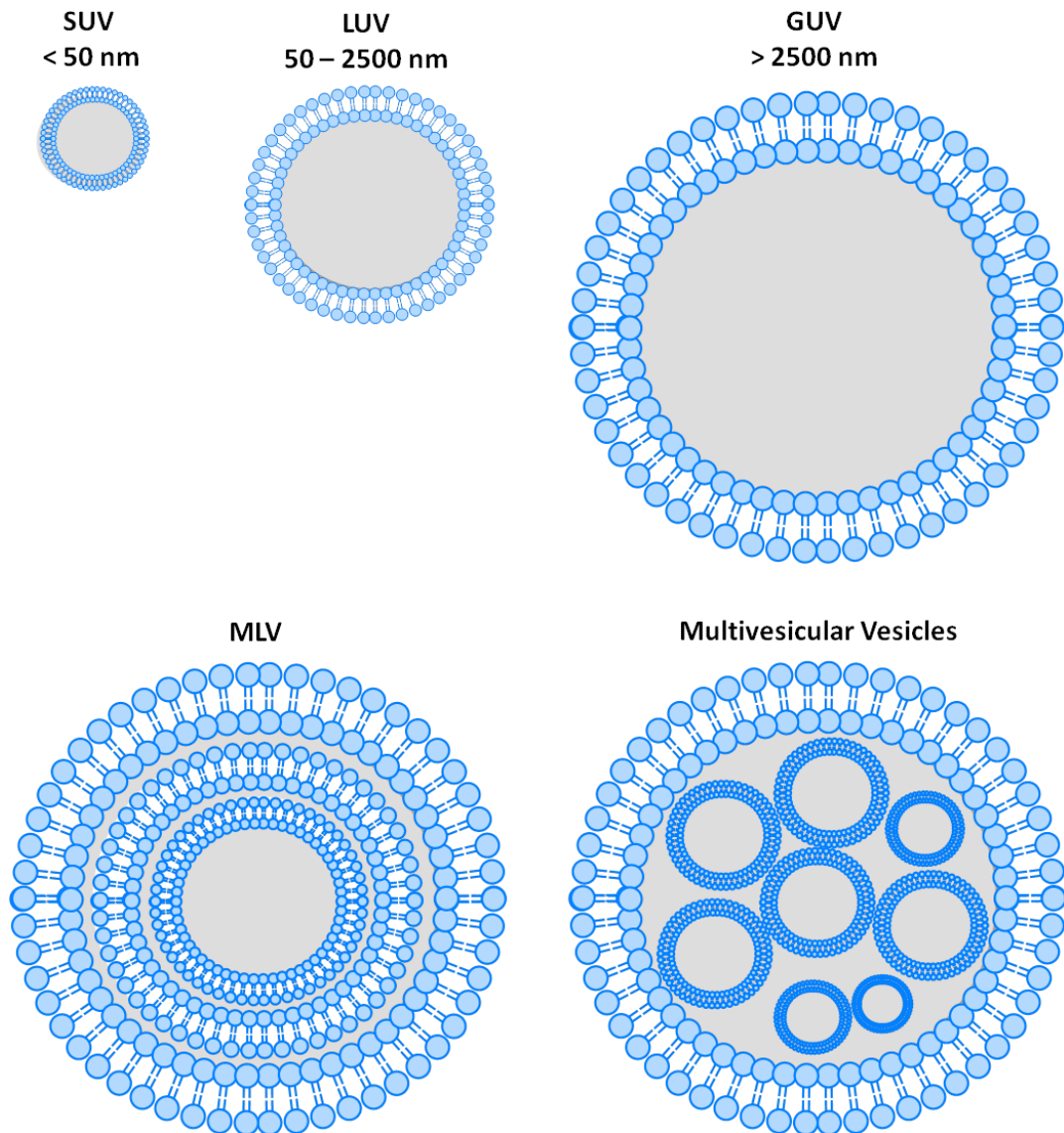


Figure 1.11. Cartoon of the common size and lamellar classification system of vesicles.

SUV represents small unilamellar vesicle; LUV represents large unilamellar vesicle; GUV represents giant unilamellar vesicle; and MLV represents multilamellar vesicle. MLVs have many membrane layers, and multivesicular vesicles encapsulate smaller vesicles. Sizes represent radii of vesicles. Lipid bilayers (blue structures) and vesicles are not to scale. Internal aqueous compartments (grey) can be different from external aqueous surroundings.

In addition to internal encapsulation of desirable reagents within liposomes of known compositions and sizes, purified membrane proteins can be incorporated within the membranes. Like liposomes, proteoliposomes are judged by the same criteria of polydispersity, size and number of lamellae. Additional information about proteins within liposome bilayers are useful for defining proteoliposome systems; such as reconstitution efficiency, homogeneity of distribution, spread of biological activity, protein orientation and whether this is homo- or heterogeneous.^[66]

1.6 Light-Driven, Transmembrane Electron Transfer

Previous sections described how light-driven, transmembrane electron transfer is advantageous for photosynthesis, as it offers better charge separations after photoexcitation and improved efficiency for light-driven reactions. To date, externally located photosensitisers have only been able to carry out transmembrane electron transfers to nanoreactors via the use of soluble electron mediators that pass through the compartment walls.^[29, 67, 68] To truly mimic and perhaps reap the full benefits seen within photosynthesis, photosensitisers and nanoreactors have to electronically communicate via transmembrane electron transfers by biological-nanowires like that of PSI.

1.6.1 Bacterial Transmembrane Electron Transfer

Some bacteria have evolved an ability to harness energy from their environment through transmembrane electron-transfer-driven redox transformations of solid minerals on the outsides of their cellular structures.^[69] Unlike other respiratory substrates such as oxygen or nitrite, such metal (hydr)oxide minerals are highly insoluble at neutral pH and thus are unable to freely diffuse into the bacterial cell to be reduced within. Metal oxide respiring bacteria therefore have to overcome physical limitations associated with transporting electrons generated during cytoplasmic metabolism across the cell envelope to extracellular terminal electron acceptors, Figure 1.12. For electrons to cross the periplasm and outer membrane to reach the cell surface there is distance of at least 300 Å; a distance that is too great to be covered by electron tunnelling alone which is limited to 14 Å.^[70, 71]

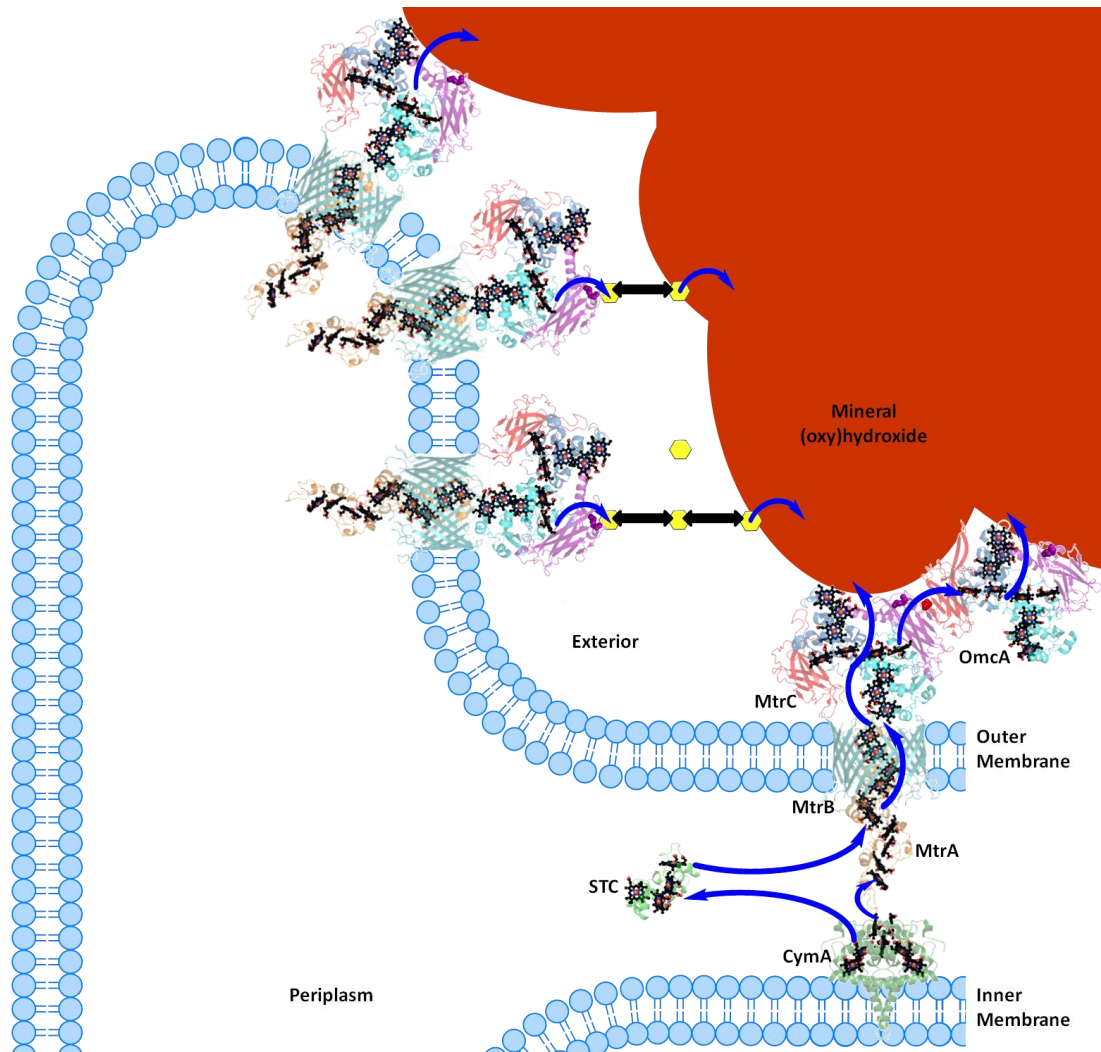


Figure 1.12. Schematic to indicate structures and cellular locations of cytochromes and electron transfers mechanisms key to *S. oneidensis* MR-1 mineral respiration.

High-resolution protein structures of *S. oneidensis* STC (PDB ID: 1M1Q), MtrC (4LM8) and OmcA (4LMH). Structures of CymA and MtrA are unavailable so structures of their homologues; NrfH (2J7A) and NrfB (2OZY); are included. Predicted structure and one possible arrangement of proteins within the membrane spanning MtrCAB complex is shown as no overall structure is available. Electrons from the oxidation of organic substrates pass through the inner membrane to CymA. Electrons cross the periplasm to the outer membrane directly or indirectly via periplasmic mediators like STC. MtrAB moves electrons across the outer membrane, and are ultimately transferred from the cell surface by: i) flavin mediators (yellow hexagons); ii) directly from extracellular cytochromes; iii) or via outer membrane appendages called nanowires. Hemes as spheres (C, black; O, red; N, blue, Fe, orange). Decaheme disulfide bond cysteines as spheres coloured for the corresponding domain. Blue arrows represent electron transfers and black arrows represent flavin electron shuttling.

Shewanella oneidensis MR-1 is a highly versatile, Gram-negative, facultative, anaerobic bacterium that can utilise metal oxide minerals containing Fe(III) and Mn(IV) as extracellular respiratory electron acceptors, Figure 1.12.^[72–74] This bacterium is rich in respiratory electron transport *c*-type cytochromes, that underpin electron transfer from the inner membrane to the cell surface via a chain of heme *c* cofactors.^[75–77] Heme *c* comprises an iron ion coordinated in the centre of a large heterocyclic porphyrin ring via four pyrrole

nitrogens, Figure 1.13. These redox centres are covalently attached to polypeptides via thioether bonds between the heme *c* vinyl groups and the thiol groups of two cysteine residues, located in the Cys-X-X-Cys-His binding motif. The planar heme structure allows for tight packing of two or more heme groups within multiheme cytochromes. The heme iron is axially coordinated by histidine located in the heme *c* binding motif and can be coordinated by a second axial ligand, which is typically another histidine or methionine. Such low-spin, hexa-coordinated hemes allow rapid electron transfers, as the iron can cycle between oxidised Fe(III) (ferric) and reduced Fe(II) (ferrous) oxidation states. In contrast, high-spin, penta-coordinated hemes have a vacant coordination site to which exogenous substrates can bind for redox transformation in enzymes.

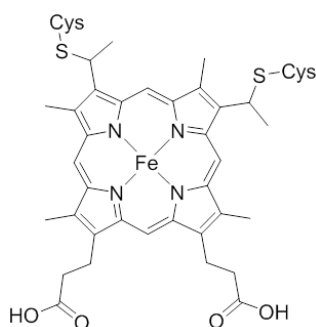


Figure 1.13. Structure of heme *c*.

The network of multiheme cytochromes within *S. oneidensis* MR-1 provide the structural and electrochemical means to mediate electron transfer from the quinone pool of the inner membrane all the way to the extracellular terminal electron acceptors outside the cell, Figure 1.12. At the cell surface, electrons can be transferred either: i) directly following contact between the mineral and surface outer membrane cytochromes; ii) indirectly through cell-secreted flavin shuttles; or iii) along extracellular appendages, termed as nanowires, which are up to 100 Å extensions of the outer membrane that contain outer membrane decaheme cytochromes.^[76, 78–81] There is currently a lot of debate which of these, singly or combined, provide the true mechanism for microbe-to-mineral electron transfer because there is firm evidence to support them all.^[82] However, general consensus states that the outer membrane porin:cytochrome complex MtrCAB and the outer membrane decaheme cytochrome MtrC, and the related homologues OmcA, MtrF and UndA, are vital in microbe-to-mineral electron transfer mechanisms.

1.6.2 Outer Membrane-Associated Cytochromes

MtrCAB spans the ~ 40 Å-wide outer membrane of *S. oneidensis*, providing a conduit electron passage across an otherwise nonconductive barrier.^[83] MtrCAB comprises of three

proteins including a periplasm-exposed decaheme cytochrome (MtrA) and an extracellular-associated decaheme cytochrome (MtrC), which are close enough to form a heme wire insulated inside a β -barrel transmembrane porin (MtrB), Figure 1.12.^[83]

MtrA (39 kDa) consists of two pentaheme domains which both share significant sequence homology with the pentaheme cytochrome *E. coli* NrfB, shown in Figure 1.14.^[84] Sequence alignments of NrfB and the N-terminal half of MtrA suggests positions and orientations of five heme cofactors in MtrA and many of the bishistidine axial ligands are conserved despite the different arrangements of the polypeptide chains.^[84] The five hemes of NrfB are within 6 Å of their nearest neighbour and therefore would facilitate rapid electron transfer across this 4 nm molecular wire.^[84] If MtrA consisted of an end-to-end NrfB homodimer, this suggests the 10 hemes of MtrA would be close enough to facilitate electron transfer across its entire length of ~ 104 Å.^[85] MtrA forms a tight complex with MtrB (76 kDa), a predicted 28-strand β -barrel protein.^[83] Comparisons with the slightly smaller 22-stranded β -barrel protein, FepA, suggests MtrB would have a pore size of at least 40 Å and, as MtrA is approximately 25 Å \times 50 Å at its largest cross-section, it is proposed that MtrA would be partially inserted within the β -barrel of MtrB.^[85, 86]

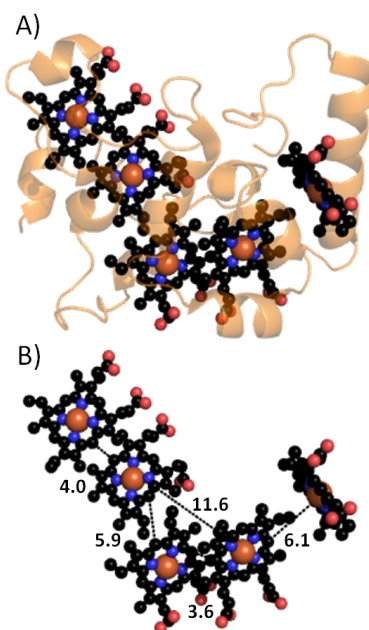


Figure 1.14. Structure of NrfB, a MtrA homologue.

A) High-resolution structure of NrfB (PDB ID: 2OZY). B) Heme arrangement within NrfB, where the distances between the heme iron ions are indicated (Ångströms). Hemes as spheres (C, black; O, red; N, blue, Fe, orange).

MtrC (75 kDa) copurifies with MtrAB in a 1:1:1 ratio to form an extracellular cytochrome terminus.^[83] It is thought the size of MtrC, approximately 80 Å \times 60 Å \times 30 Å, is too large to fit into the MtrB barrel and would mostly be exposed to the extracellular environment.^[87] OmcA (86 kDa) is a bigger extracellular decaheme cytochrome,

approximately $95 \text{ \AA} \times 60 \text{ \AA} \times 50 \text{ \AA}$, that is thought to bind and exchange electrons with MtrC to support extracellular electron transfer.^[88] MtrC and OmcA are homologous decaheme cytochromes, as shown in Figure 1.15, that were found to have overlapping roles in mineral reduction.^[87–89]

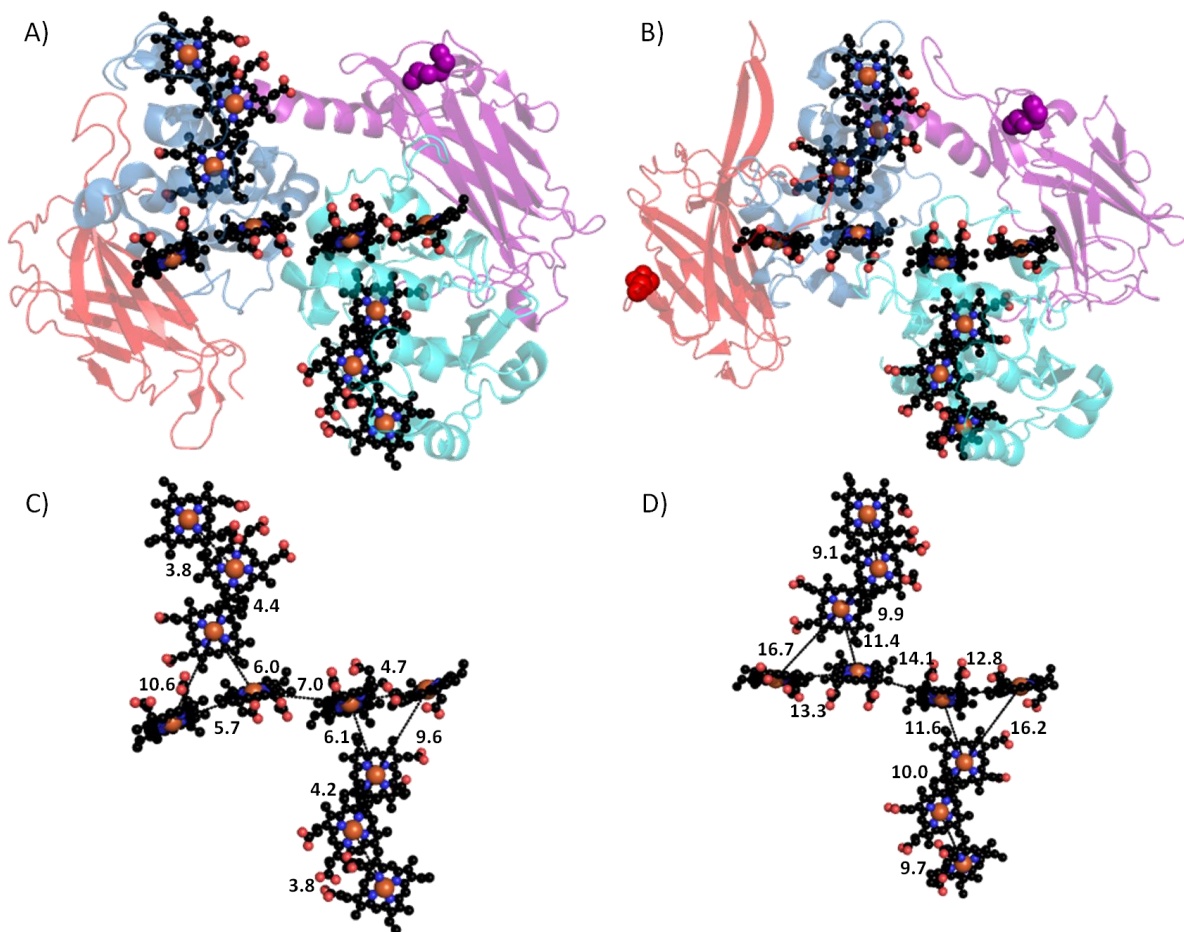


Figure 1.15. Structures of MtrC and OmcA from *S. oneidensis* MR-1.

High-resolution structures of A) MtrC (PDB ID: 4LM8) and B) OmcA (4LMH), with their four domains coloured red, blue, purple and cyan from the N termini to the C termini. Heme arrangements within C) MtrC and D) OmcA, where the distances between the heme iron ions are indicated (Ångströms). Hemes as spheres (C, black; O, red; N, blue; Fe, orange). Disulfide bond cysteines as spheres coloured for the corresponding domain.

Both comprise four domains, two split β -barrel domains and two heme domains.^[87, 88] Domains II and IV coordinate ten bis-histidine hemes in a significantly conserved staggered cross formation, with each heme in sufficient proximity to its nearest neighbour to facilitate rapid intramolecular electron transfer.^[87, 88] A disulfide bond is located in domain III and for OmcA a second disulfide bond is in domain I.^[87, 88] *In vitro* reduction of these disulphides triggers tight binding of flavin mononucleotide (FMN) and riboflavin (RF) to both proteins, which supports evidence from *in vivo* studies suggesting MtrC and OmcA are flavocytochromes during anaerobic respiration.^[87, 90] The four terminal points of the staggered heme cross are suggested to be possible sites for electron

exchange between MtrA, each other and with soluble substrates or electron shuttles; however, their relative orientations with each other and MtrAB is unknown.^[88, 91]

Evidence supporting predictions of locations of MtrCAB, and orientation of MtrB, with respect to the outer membrane is supported by proteinase K experiments revealing the complete digestion of MtrC, followed by partial digestion of MtrB, from MtrCAB embedded in liposomes or cell membranes.^[87, 92]

1.6.3 Demonstration of Transmembrane Electron Transfer by MtrCAB in Liposomes

Evidence supporting the role of MtrCAB in trans-outer membrane electron transfer comes from the ability of this complex to support transmembrane electron transfer when incorporated in a liposome.^[83, 92, 93] MtrCAB, purified from *S. oneidensis* MR-1, was incorporated into preformed liposomes made from chicken egg PC via a mixed reconstitution method that uses both freeze-thawing and slow, gentle removal of detergent by adsorption to Biobeads.^[83, 92, 93] The redox dye methyl viologen (MV) was encapsulated within these liposomes. As shown in Figure 1.16, MV has three oxidation states: i) the oxidised, colourless dication (MV^{2+}); ii) the deeply blue coloured radical cation (MV^+) which has associated an absorbance peak at 606 nm; and iii) the very pale yellow doubly reduced species (MV^0).^[94] From here onwards the oxidation state of methyl viologen will only be included when it is specifically known and being discussed; and otherwise this molecule will be described generally as MV. Only the first one-electron reduction of MV^{2+} is observable upon the addition of the membrane-impermeable reductant dithionite ($E_m \approx -500$ mV).^[94, 95]

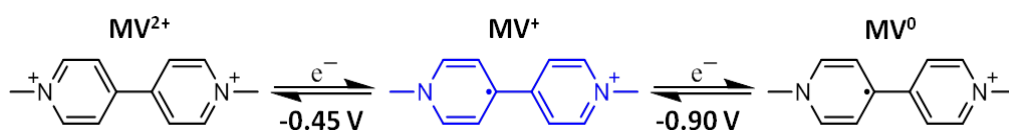


Figure 1.16. Methyl viologen redox reactions at pH 7
All reduction potentials are reported versus SHE.^[95]

Parallel dithionite additions made to MV^{2+} -containing MtrCAB proteoliposomes and liposomes demonstrated MtrCAB acts as a nanowire, allowing transmembrane electron transfer to MV^{2+} , Figure 1.17.^[83, 92, 93] In the timescale of this experiment reduction of MV^{2+} to MV^+ was not observed in liposomes without MtrCAB incorporated, as phospholipid membranes are nonconductive and MV^{2+} , MV^+ and dithionite are membrane-impermeable.^[83, 92, 93] Addition of externally located soluble and insoluble

Fe(III) to dithionite-reduced proteoliposomes showed MtrCAB supported bidirectional transmembrane electron transfer as encapsulated MV^+ was reoxidised, in a similar manner to that observed *in vivo* during mineral respiration.^[83, 92]

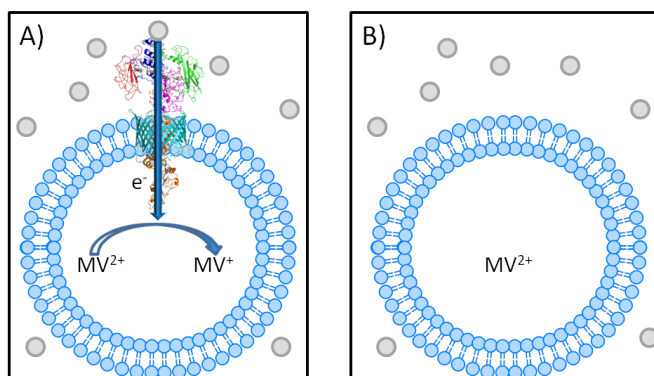


Figure 1.17. Cartoons representing events following additions of dithionite to MV^{2+} -containing (proteo)liposomes.

A) Dithionite addition to MV^{2+} -containing proteoliposomes results in reduction of colourless MV^{2+} to blue MV^+ . B) No reduction is observed in liposomes without MtrCAB incorporated. Dithionite is represented by grey circles.

Physical characterisations of MtrCAB proteoliposomes were obtained by transmission electron microscopy, dynamic light scattering and western blots with MtrC-specific antibodies.^[93] These showed MtrCAB proteoliposomes were large unilamellar vesicles with an average radius of 250 nm, and between 0 to 200 MtrCAB molecules per liposome.^[93] Solubilisation of reduced (proteo)liposomes with anaerobic Triton X-100 released $\sim 30 \mu\text{M}$ MV from 1 mg mL^{-1} (proteo)liposome suspensions, of which $\sim 80 \%$ was redox addressable in proteoliposomes.^[93] Additionally, the topology of MtrCAB within these proteoliposomes has been studied with proteinase K susceptibility alongside hybridisation with gold-labelled MtrC and MtrA antibodies.^[92] These results established that MtrCAB inserts into these liposome bilayers with MtrA facing the interior and MtrC exposed on the outer surface of the phospholipid bilayer, which matches the established *in vivo* orientation of MtrCAB.^[92]

1.7 Aims of this Study

Due to increasing global energy demand and depletion of fossil fuels, scientists look towards photosynthesis for inspiration in developing methods to capture and transform abundant solar energy into high energy fuels and valued organic compounds. Artificial photosynthetic systems mimic natural photosynthesis by having photosensitisers which capture the energy from sunlight and deliver photoexcited electrons to electrocatalysts, before they are regenerated by a SED. To date all artificial photosynthetic systems are

unable to fully mimic and reap the full benefits of natural photosynthesis as they lack spatially separating reaction compartments, and/or a compartment-linking transmembrane electron transport chain. Artificial photosynthetic systems which include these components, and thus completely mimic natural photosynthesis, are of great interest.

There are many different approaches to obtain nanoreaction compartments; however, liposomes are the most studied and well established compartments within the current literature. Liposomes are novel as they offer a phospholipid membrane which self-assemble with desirable reagents internally encapsulated and proteins incorporated into the membrane. Incorporation of MtrCAB in liposome bilayers allows an externally located reductant to reduce internally encapsulated MV^{2+} . The porin:cytochrome complex MtrCAB is novel due to the transmembrane spanning heme constellation that is inserted within a protein porin sheath. This property allows MtrCAB to act as an electrical wire between the interior and exterior of membrane compartments. MtrCAB performs “dark” electron transfers with cell-secreted flavins; however, flavins are able to act as photosensitisers. This suggests that it may be possible to pass photoexcited electrons from flavins to MtrCAB, where the twenty hemes could potentially act as a reservoir for photoexcited electrons and thus provide longer charge separations that are desirable for artificial photosynthetic systems.

In this study the potential for MtrCAB proteoliposomes to serve as nanoreaction compartments for light-induced, transmembrane electron transfer driven redox reactions was investigated in a stepwise manner, as summarised in Figure 1.18. A stepwise approach to exploring photoreduction of MtrCAB proteoliposomes allowed the behaviour of a given photosensitiser towards each component of the proteoliposome system to be explored. Firstly photoreductions of the outer membrane proteins of *S. oneidensis* MR-1 in solution, by a range of soluble photosensitisers, in the presence of TEOA as a SED, were investigated to establish optimal conditions for photoreduction studies, Figure 1.18 A. The photosensitisers chosen were flavin adenine dinucleotide, flavin mononucleotide, riboflavin, eosin Y, fluorescein, proflavin, tris(bipyridine) ruthenium(II) and bis(bipyridine) (bipyridine-4,4'-bisphosphonic acid) ruthenium(II); and the basis for their selection is described in Chapter 3. Chapter 3 also describes the process by which the optimal conditions for outer membrane protein photoreduction were obtained and establishes the effects that photosensitiser and protein identity had upon the rate and extent of outer membrane cytochrome photoreduction. That chapter finishes by characterising the identity of the SED(s) and the photoreduction mechanisms used by each of the investigated photosensitisers.

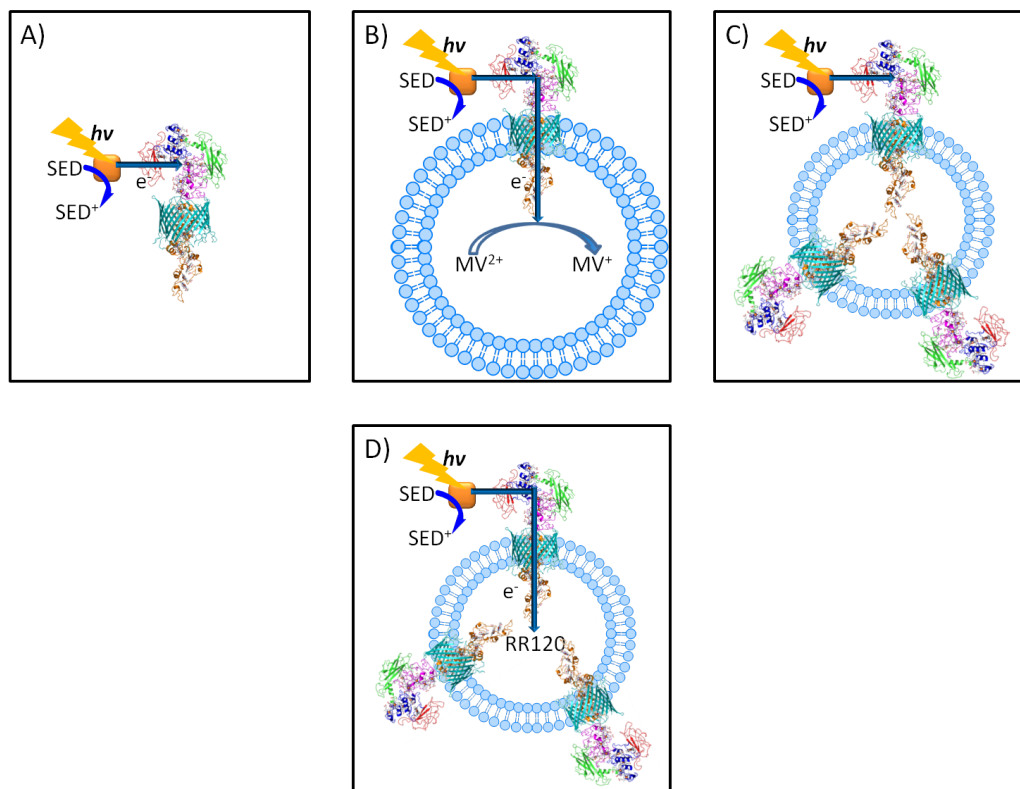


Figure 1.18. Cartoons representing the stepwise investigation into light-induced, transmembrane electron transfer of MtrCAB proteoliposomes.

A) Photoreduction of outer membrane cytochromes in solution. B) Photoreduction of MV^{2+} -containing MtrCAB proteoliposomes. C) Photoreduction of MtrCAB in liposome bilayers. D) Photoreduction of MtrCAB in liposome bilayers and subsequent reduction of redox dye, reactive red 120 (RR120). See text for details. Photosensitisers are represented by orange squares. Please note detergent molecules which solubilise MtrCAB are omitted for clarity.

As MtrCAB proteoliposomes containing MV^{2+} are well-developed and thoroughly characterised, the preparation methods previously reported were used to prepare MtrCAB (proteo)liposomes to study light-driven, transmembrane electron transfers by the investigated photosensitisers in the presence of TEOA, Figure 1.18 B. Chapter 4 describes experiments which investigated whether presence of the chosen photosensitisers resulted in changes to MtrCAB (proteo)liposomes. These assessments established if photosensitisers associated with lipid membranes of (proteo)liposomes and/or caused leakage of internally encapsulated MV. Additionally, the possibility for chosen photosensitisers to photoreduce MV^{2+} in aqueous solution and encapsulated in liposomes with no MtrCAB incorporated was explored. This work established whether the chosen photosensitisers were able to photoreduce encapsulated MV^{2+} without the need of MtrCAB as an electron conduit.

These studies revealed unforeseen complications from use of MV^{2+} -containing (proteo)liposomes. As a consequence an alternative method of proteoliposome preparation was selected for study as described in Chapter 5. With this method it proved possible to incorporate sufficient MtrCAB into proteoliposomes to use spectroscopy of the heme

cofactors as a direct probe of heme oxidation state. This made it possible to cleanly assess the ability of the chosen photosensitisers to photoreduce MtrCAB within the liposome bilayer and the mechanisms by which these occurred. That work identified flavins as photosensitisers with desired properties of MtrCAB reduction without permeating, lysing or associating with the liposome membrane, Figure 1.18 C.

Chapter 6 identified reactive red 120 (RR120) as a redox reporter that could be encapsulated within a (proteo)liposome-based nanoreactor. Photoreductions of these RR120-containing (proteo)liposomes performed by flavin photosensitisers, in the presence of TEOA as a SED, demonstrated photoexcited flavin delivers electrons to internalised RR120 via MtrCAB acting as a transmembrane electron nanowire, Figure 1.18 D. This demonstrates that light capture and charge separation of externally located flavin photosensitisers can be successfully coupled with reductive transformations within proteoliposome nanoreactors by electron transfer through MtrCAB acting as a bilayer-spanning electron conduct.

Chapter 7 discusses the future possibilities for MtrCAB proteoliposomes and *S. oneidensis* as modular components within artificial photosynthetic systems. Discussion of the other possibilities for MtrCAB proteoliposomes to be used to help determine the structure of membrane-bound MtrCAB and understand nanowires of *S. oneidensis* is also included.

Chapter 2

Materials and Methods

2.1 General Reagent Preparations and Characterisations

Flavin mononucleotide (FMN, sodium salt), flavin adenine dinucleotide (FAD, disodium salt hydrate), riboflavin (RF), 2',4',5',7'-tetrabromofluorescein (eosin Y), 3,6-diaminoacridine (proflavin, hemisulfate salt), ruthenium-tris(2,2'-bipyridyl) ($[\text{Ru}(\text{bpy})_3]^{2+}$, dichloride salt), triethanolamine (TEOA), 1,1'-dimethyl-4,4'-bipyridinium (methyl viologen, MV, dichloride salt), 4-(2-hydroxyethyl)piperazine-1-ethanesulfonic acid (HEPES), Triton X-100 (100 % [v/v]), *n*-octylglucoside (OG), valinomycin ready-made solution, sodium D,L-lactate solution syrup (60 % [w/w]), 5,5',7,7'-indigotetrasulfonic acid (indigotetrasulfonic acid, tetrapotassium salt), resazurin (sodium salt), reactive black 5 (RB5), amaranth and reactive red 120 (RR120) were all from Sigma-Aldrich. Fluorescein was from Alfa Aesar. These purchased reagents were used without further purification. $[\text{Ru}(\text{bpy})_2(4,4'-(\text{PO}_3\text{H}_2)_2\text{bpy})]\text{Br}_2$ (RuP) was a kind gift from Dr Manuela Gross, University of Cambridge, and prepared as previously described.^[96] All other reagents were Analar quality or equivalent.

2.1.1 Preparation of Buffer, Photosensitiser and Lipid Stock Solutions

Aqueous solutions were prepared using Millipore water (18.2 M Ω cm). The pH of all solutions was measured using a pH meter, which was calibrated prior to each use using pH standards (4.0, 7.0 and 9.2). When required, solutions were adjusted to the correct pH by adding aliquots of concentrated NaOH or HCl.

Stock solutions of 2 mM photosensitisers and 50 mM TEOA were prepared by dissolving appropriate masses or volume, respectively, in 50 mM HEPES, 2 mM CaCl₂, 10 mM KCl, pH 7 or in 50 mM phosphate, pH 7. Photosensitiser solutions were stored in the dark and their integrity confirmed by electronic absorbance spectroscopy prior to use.

Chicken egg phosphatidylcholine powder (PC, product number 840051P) and *E. coli* total lipid extract dissolved in chloroform (25 mg mL⁻¹, product number 100500C) were from Avanti Polar Lipids Incorporation. PC was stored frozen as supplied under a N₂ atmosphere and used immediately upon exposure to air without further purification. *E. coli* total lipid extract was stored frozen under a N₂ atmosphere after complete

evaporation of the chloroform using a flow of N₂. *E. coli* total lipid extract was then used immediately upon exposure to air without further purification.

Anaerobic buffer solutions were prepared by bubbling with N₂. Other anaerobic solutions were typically prepared by replacing container headspace with a N₂ atmosphere, before placement in N₂ filled, anaerobic chamber (Belle Technology, atmospheric O₂ < 10 ppm) and overnight stirring to equilibrate with atmosphere.

2.1.2 Electronic Absorbance Spectroscopy

Ultraviolet-visible absorbance spectroscopy was performed using either a Jasco V650 UV-visible spectrophotometer for aerobic measurements or a Biochrom WPA Biowave II diode array spectrophotometer for anaerobic measurements made within a N₂ filled, anaerobic chamber. The Beer-Lambert Law relates light absorption by a sample to the concentration of the light-absorbing chemical in the sample (Equation 2.1). Concentrations of samples were calculated using the Beer-Lambert Law (Equation 2.1) where A is the absorbance of light by the sample, c is the concentration, l is the sample path length, and ε is the molecular extinction coefficient. Absorbance is defined via the logarithm of the ratio of the incident light intensity (I₀) to the transmitted light intensity (I) after it passes through the sample (Equation 2.1).

$$\log_{10} \frac{I_0}{I} = A = \epsilon cl \quad (2.1)$$

Protein concentrations were calculated using electronic absorbance spectroscopy of air-oxidised proteins at 410 nm alongside estimated extinction coefficients (mM⁻¹ cm⁻¹) of 1000, 1000 and 2000 for MtrC, OmcA and MtrCAB respectively. Concentrations of MV were calculated using the extinction coefficient of 13.7 mM⁻¹ cm⁻¹ at 606 nm for the one-electron reduced form.^[97] Photosensitiser and other redox dye concentrations were calculated using extinction coefficients given in Tables 3.1 to 3.3 and 5.1, respectively.

2.1.3 Cyclic Voltammetry

Cyclic voltammetry is an electrochemical technique where the current produced or used by an electrochemical redox reaction is measured as a function of applied potential. Electrochemical cells measure current as an applied potential is linearly cycled between two chosen potentials, one oxidising and one reducing. A current-potential profile is recorded when a constant scan-rate is applied, Figure 2.1 A. These cyclic voltammograms

contain important information about the redox reaction. The reversibility of a redox couple is reflected in the height similarity of the oxidative and reductive peaks, and the midpoint reduction potential, E_m , is obtained from the mean of the oxidative and reduction peak potentials, E_p^{ox} and E_p^{red} respectively. Additionally the potential separation between these peaks indicates the number of electrons involved in a redox reaction, where a separation of approximately 59 mV is indicative of a one-electron process while a separation of 29 mV is typical of a two-electron process.

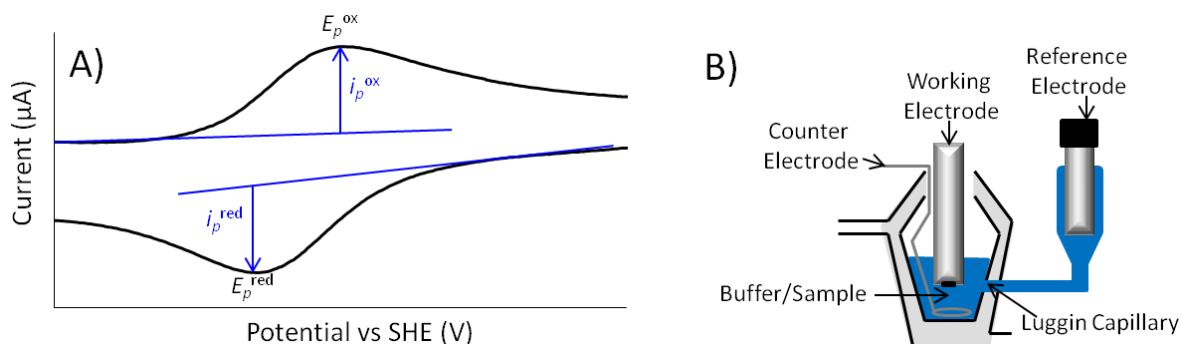


Figure 2.1 A) Typical current-potential profile measured for a reversible redox process by B) three electrode electrochemical cell setup.

The oxidative and reductive peak currents (i_p^{ox} and i_p^{red} , respectively) are given by heights of the peaks as represented with blue arrows.

Solution electrochemistry of redox dyes and photosensitisers was carried out in a three electrode chemical cell configuration, as depicted in Figure 2.1 B. The working electrode was a pyrolytic graphite edge electrode. The counter electrode was provided by a platinum wire. The reference electrode was an Ag/AgCl Russell electrode saturated with KCl solution, positioned in the reference side-arm filled with buffer. Potentials recorded by the Ag/AgCl reference electrode were converted to SHE by the addition of 197 mV. All potentials in this work are quoted versus SHE. Cyclic voltammograms reported within this work are an average of five scans recorded at 20 °C in 50 mM HEPES, 2 mM CaCl₂, 10 mM KCl, pH 7.0 using a scan rate of 20 mV s⁻¹.

The working electrode was prepared by polishing with 0.3 µm aluminium oxide slurry to reveal a fresh graphite layer and then sonication in Millipore water to remove traces of alumina from the surface. This process was repeated thrice. The polished working electrode was then immersed within buffer/sample solution within the electrochemical cell so the electrode surface was level with the luggin capillary tip of the reference side arm. The electrochemical cell was located inside a Faraday cage placed inside a N₂ filled, anaerobic chamber (Belle Technology, atmospheric O₂ < 10 ppm). The three electrodes of the electrochemical cell were linked to an Autolab PGSTAT 30 potentiostat controlled by General Purpose Electrochemical System software.

2.2 Characterisation and Purification of *S. oneidensis* MR-1 Outer Membrane Cytochromes

2.2.1 SDS-PAGE Analysis

During purifications, the presence and purity of respective outer membrane cytochromes were routinely assessed following resolution by sodium dodecyl sulphate polyacrylamide gel electrophoresis (SDS-PAGE) analysis.^[98] SDS is an anionic detergent that denatures the secondary, tertiary and quaternary structures of proteins whilst making them negatively charged. Subsequent gel electrophoresis of SDS-treated samples causes proteins to separate according to their mass. The predicted masses of mature proteins used in this work, that are calculated from combined mass of the peptide and ten hemes where relevant, are as follows: MtrA 38.6 kDa; MtrB 75.5 kDa; soluble MtrC 75.0 kDa; and soluble OmcA 82.8 kDa.

SDS-PAGE gels typically consisted of a resolving layer of 12.5 % acrylamide (v/v), 1.5 M Tris-HCl, pH 8.8 and a stacking layer of 4 % acrylamide, 0.5 M Tris-HCl, pH 6.8. In some cases TruPAGE precast SDS-PAGE gels from Sigma-Aldrich were used that consisted of an acrylamide gradient of 4 - 20 %. Running buffer used contained 2.5 mM Tris-HCl, 19.2 mM glycine, 0.01 % SDS, pH 8.8. Protein samples were mixed in a 1:1 volume ratio with loading buffer containing 6 M urea, 5 % SDS (w/v), 0.1 % glycerol (v/v) and 0.05 % bromophenol blue (w/v), and incubated at 80 °C for 20 mins. 10 - 15 µL of protein sample was loaded alongside 8 µL of dual colour molecular weight marker (BIO-RAD) which helped to estimate protein weights within the range of 10 - 250 kDa. Gels were run at 30 mA for approximately 2 hrs prior to protein visualisation.

2.2.2 Protein Visualisation Following SDS-PAGE Analysis

SDS-PAGE gels were run as described above and proteins were subsequently visualised using Coomassie and heme stains, and Western blot analysis. SDS-PAGE gels were analysed for protein purity using Instant Blue Coomassie stain (Expendeon). This stain visualises proteins by forming ionic interactions between positively charged groups in the proteins and negatively charged sulphonic acid groups of the blue Coomassie dyes. Protein bands developed after being immersed in staining solution for 1 hr.

As covalent bonds are left intact while proteins denature in SDS, SDS-PAGE gels can be also used to specifically identify *c*-type cytochromes using a heme-associated

peroxidase activity stain.^[99] After resolution by SDS-PAGE, gels were incubated in 70 mL of 0.25 M sodium acetate, pH 5.0 for 15 mins, before addition of 30 mL of methanol containing 1 mg mL⁻¹ of 3,3',5,5'-tetramethylbenzidine dihydrochloride monohydrate (TMB). Gels were incubated in this for 30 mins, to allow TMB to soak into the gel, before 300 µL of 30 % hydrogen peroxide (v/v) was added. TMB acts as the reductant in the reduction of hydrogen peroxide which is catalysed by penta-coordinated *c*-type hemes, Figure 2.2. The resulting semiquinone imine radical cation subsequently formed a dark blue charge-transfer complex with the parent TMB, and revealed heme protein bands over 30 mins. The gel was developed in the dark as TMB is light sensitive.

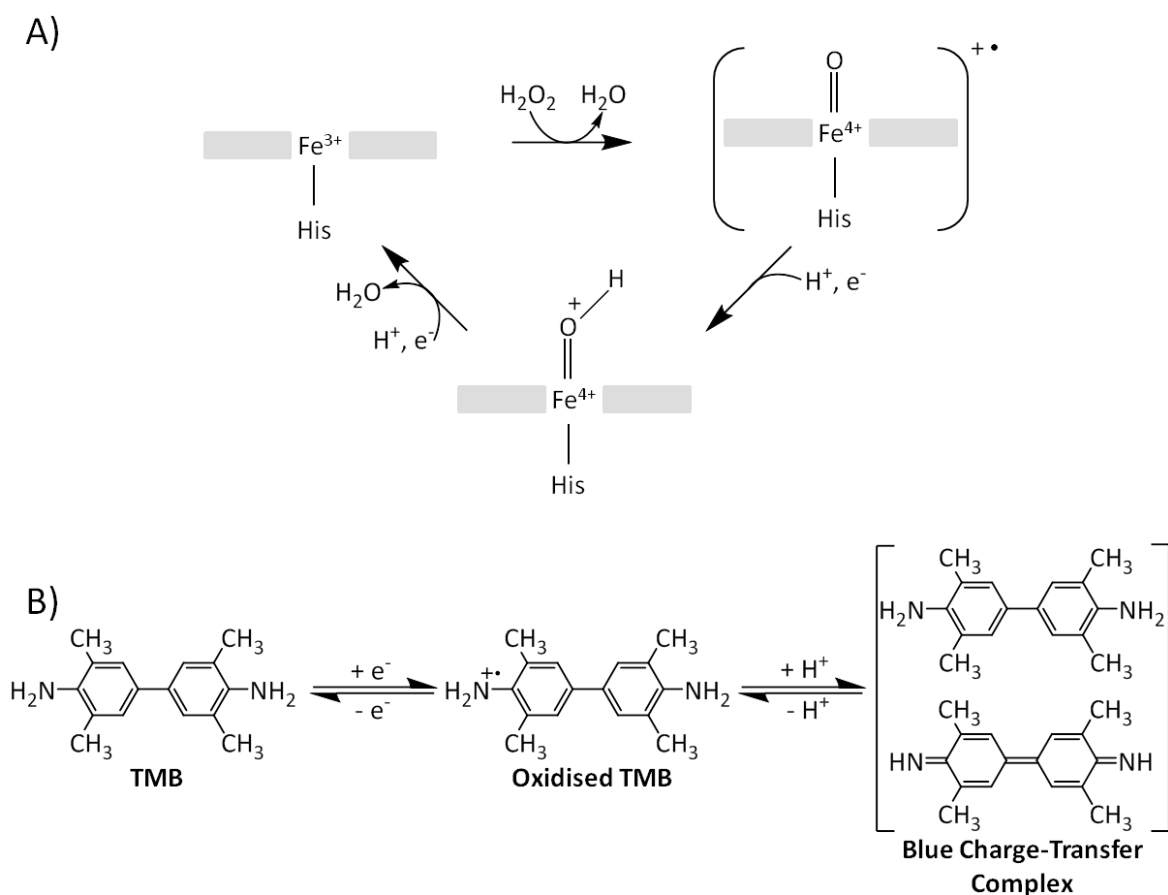


Figure 2.2 Reactions during heme staining.

A) Catalytic reduction of hydrogen peroxide to water by penta-coordinated *c*-type hemes. Grey boxes represent the heme porphyrin ring.^[100] B) Redox reaction of TMB which acts as a hydrogen donor during heme-associated peroxide reduction.^[101]

When required, additional confirmation of the presence of MtrB in MtrCAB samples was obtained by Western blot analysis using an antibody specific to MtrB (residues 23 - 42) that was provided by Dr Matthew Marshall, Pacific Northwest National Laboratory.^[102] Proteins resolved by SDS-PAGE were transferred to a polyvinylidene difluoride membrane which was incubated overnight in 5 % skimmed milk (w/v) in TBST (20 mM Tris-HCl, 140 mM NaCl, 0.1 % Tween 20 (v/v), pH 7.5). The membrane was

incubated for 1 hr with $0.6 \mu\text{g mL}^{-1}$ of MtrB specific, primary antibody in 1 % skimmed milk in TBST. The membrane was then incubated for 1 hr with $0.15 \mu\text{g mL}^{-1}$ of alkaline phosphatase conjugated secondary antibody (anti-rabbit) in 1 % skimmed milk in TBST. Excess antibodies were removed from the membrane via one wash with 1 % skimmed milk in TBST and five washes with TBST. The membrane was then incubated for 1 hr with the enzyme substrate 5-bromo-4-chloro-3'-indolylphosphate (BCIP) and nitroblue tetrazolium (NBT) in 100 mM Tris-HCl, 100 mM NaCl, 5 mM MgCl_2 , pH 9.5. During this time NBT was reduced to an insoluble purple compound which develops as MtrB protein bands, Figure 2.3. Incubations and washes were performed at 4 °C.

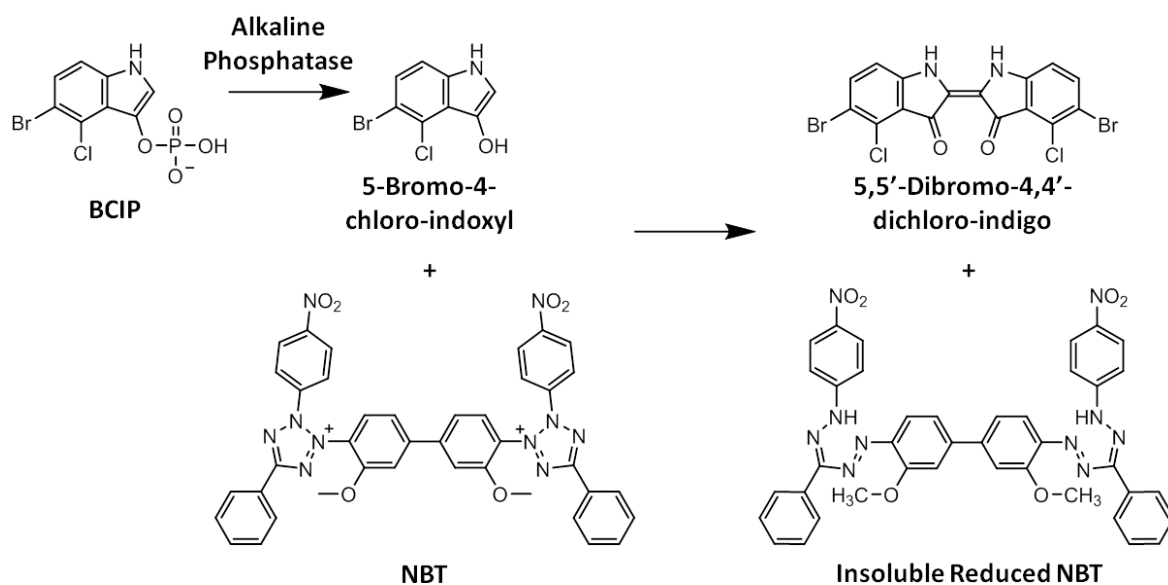


Figure 2.3 Reactions of BCIP and NBT during Western blot analysis.

Alkaline phosphatase converts BCIP into an indoxyl intermediate which undergoes dimerisation and oxidation and subsequently causes the reduction of NBT.

2.2.3 Outer Membrane Cytochrome Purification

Soluble forms of MtrC and OmcA from *S. oneidensis* MR-1, purified with minor modifications of previously described procedures, were kindly provided by Miss Verity Lyall or Dr Simone Payne, University of East Anglia.^[87, 88] In brief, to obtain either soluble MtrC or OmcA the respective encoding genes were amplified from *S. oneidensis* MR-1 and cloned into a pBAD 202 plasmid (Invitrogen). Solubilised proteins were achieved by replacing the 25 amino acids of the N-terminal signal peptides and lipid anchor sites with the N-terminal signal peptide of MtrB of *S. oneidensis* MR-1 and adding a 45 amino acid C-terminal extension including a V5-epitope and a His-tag. *S. oneidensis* MR-1 strains containing these plasmids were grown aerobically at 30 °C in Terrific broth media containing $30 \mu\text{g mL}^{-1}$ kanamycin. Protein expression was induced by addition of 1 mM L-arabinose at mid-log growth phase. Cells were grown overnight and removed by

centrifugation. The media was concentrated using a stirred Amicon pressure cell (30 kDa cutoff filter) before being dialysed into buffer containing 20mM HEPES, pH 7.8 to remove the media components. The dialysed solution was centrifuged to remove any precipitate before loading onto a DEAE-sepharose column pre-equilibrated with 20mM HEPES, pH 7.8. The protein was eluted with a gradient of 0 - 500 mM NaCl over 4.5 column volumes (CV). Fractions containing OmcA/MtrC were pooled and dialysed into 20 mM HEPES pH 7.8. Then, because both proteins were expected to contain a His-tag, the samples were passed through a Ni-NTA column in 20 mM HEPES, 100 mM NaCl, pH 7.6. Majority of protein in samples of MtrC and OmcA failed to bind to the column and eluted in the void volume and these, after buffer exchange, was used for experiments reported here.

Liquid chromatography–mass spectrometry, kindly performed by Dr Jessica van Wonderen at the University of East Anglia, revealed molecular weights for the proteins that were consistent with the absence of the His-tag; MtrC observed mass 75047 Da (predicted 75047 Da without the C-terminal extension), OmcA observed mass 82847 Da (predicted 86319 and 82279 Da, with and without the C-terminal extension). Absence of the C-terminal extensions was most likely due to proteolytic cleavage.

Some samples of MtrCAB used within this study were also kindly provided by Miss Verity Lyall or Dr Simone Payne. For MtrCAB purification, *S. oneidensis* MR-1 was grown microaerobically at 30 °C as by previously published method.^[75, 103] Single *S. oneidensis* MR-1 colonies were picked from lysogeny broth (LB) agar plates and used to inoculate 10 mL sterilised LB media, which were incubated with shaking overnight. 50 mL of sterilised LB media were inoculated (1 %) with resulting cultures before being incubated with shaking for ~ 6 hrs. Resulting cultures were used to inoculate (5 %) baffled flasks containing 1 L of sterilised LB media supplemented with 20 mM ferric citrate and 50 mM sodium D,L-lactate (pH ~ 7.6). These were incubated with gentle shaking overnight (~ 18 hrs). Resulting deep red coloured cells were harvested by centrifugation at 9000 g, 4 °C for 20 mins and stored as cell pellets at -80 °C until purification.

Cell pellets were resuspended in 20 mM HEPES, pH 7.6. DNase (100 mg L⁻¹) was added prior to cells being ruptured using a continuous French Press (1000 psi). Cell debris was removed by centrifugation at 17000 g, 4 °C for 15 mins and the dark red supernatant was ultracentrifuged at 138000 g, 4 °C for 2 hrs to pellet cell membranes. Membrane pellets were resuspended in 20 mM HEPES, 5 % Triton X-100 (v/v), 100 mM NaCl, pH 7.6 and were stirred overnight at 4 °C to solubilise membrane-bound proteins. Please

note all percentages of Triton X-100 in this work are quoted as volume per volume (v/v). Detergent insoluble material was collected by 2 hrs ultracentrifugation at 138000 g, 4 °C and discarded.

The dark red supernatant containing Triton X-100-soluble membrane proteins were loaded onto a DEAE-Sepharose column pre-equilibrated with 20 mM HEPES, 5 % Triton X-100, 100 mM NaCl, pH 7.6. Unbound and weakly bound proteins were removed by washing the column with 2 CV of 20 mM HEPES, 5 % Triton X-100, 100 mM NaCl, pH 7.6. Proteins were eluted with a gradient of 100 - 600 mM NaCl over 6 CV. Elution of MtrCAB was assessed by SDS-PAGE analysis and occurred over NaCl concentration of 200 - 270 mM. MtrCAB containing fractions were pooled and dialysed into 20 mM HEPES, 2 % Triton X-100, 100 mM NaCl, pH 7.6 prior to being loaded onto a Q-sepharose column. A buffer of 20 mM HEPES, 2 % Triton X-100, 100 mM NaCl, pH 7.6 was used to pre-equilibrate and remove unbound or weakly bound proteins from the column with 3 CV. A step 200 - 500 mM NaCl gradient, in 50 mM increments over 2 CV, was applied to elute MtrCAB. Elution of MtrCAB occurred at 250 and 300 mM NaCl as identified by SDS-PAGE analysis. MtrCAB fractions were pooled and concentrated using a stirred Amicon pressure cell (30 kDa cutoff filter), prior to further resolution using a HiPrep 26/60 Sephacryl S-300 HR gel filtration column eluted with 20 mM HEPES, 2 % Triton X-100, 100 mM NaCl, pH 7.6. Elution of MtrCAB occurred over a large volume of ~ 100 mL; however, was confirmed to be pure by SDS-PAGE analysis.

Concentration and, if required, detergent exchange of MtrCAB purified in Triton X-100 was performed using a HiTrap Q-sepharose column, pre-equilibrated with 100 mM NaCl in the desired buffer. Detergent exchanges were performed by washing the column with 50 CV of 100 mM NaCl in the desired buffer. Concentrated MtrCAB was eluted with 1 M NaCl in the desired buffer over 1 CV, before the salt concentration was lowered to 100 mM NaCl in the desired buffer using a stirred Amicon pressure cell (30 kDa cutoff filter).

The amount of Triton X-100 present within MtrCAB samples was assessed using the absorbance peaks of Triton X-100 that are located within the UV spectral region, Figure 2.4 A. A quantifiable relationship between Triton X-100 percentage and absorbance at 245 nm was determined from UV-visible spectra of 5, 4, 3, 2, 1 and 0 % of Triton X-100 in 20 mM HEPES, 100 mM NaCl pH 7.6, Figure 2.4 B.

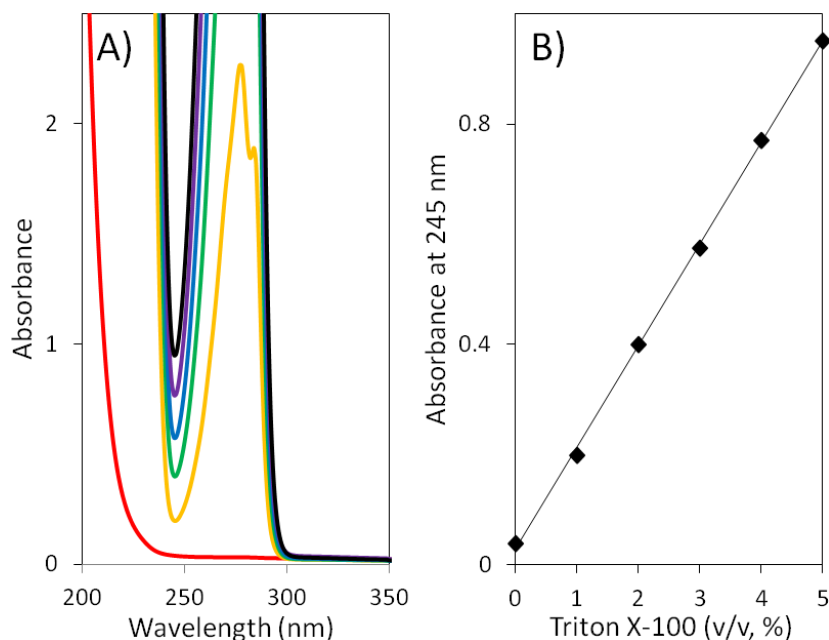


Figure 2.4. Quantification of Triton X-100 in MtrCAB samples.

A) Spectra of 0 % (red line), 1 % (yellow line), 2 % (green line), 3 % (blue line), 4 % (purple line) and 5 % (black line) Triton X-100 (v/v) in 20 mM HEPES, 100 mM NaCl, pH 7.6. Path length 1 mm. B) Percentage of Triton X-100 plotted against the corresponding absorbance at 245 nm. The linear trendline has an equation of $y = (x - 0.028) / 0.184$ and a R^2 value of 0.999.

Within this percentage range absorbance was proportional to Triton X-100 percentage, which allowed percentages of Triton X-100 (v/v) present in samples of MtrCAB to be calculated using Equation 2.2 where A_{245} is the absorbance at 245 nm.

$$\text{Triton X-100 (v/v, \%)} = (A_{245} - 0.028) / 0.184 \quad (2.2)$$

Purified OmcA and MtrC were buffer exchanged using a stirred Amicon pressure cell (30 kDa cutoff filter) into buffer of choice prior to use in the experiments reported here. Purified proteins were stored at $-80\text{ }^{\circ}\text{C}$ after being flash frozen in liquid nitrogen.

SDS-PAGE analysis alongside protein visualisation by Coomassie and heme staining shows the typical quality of samples used throughout this study, Figure 2.5. Typically purified samples of OmcA, MtrC and MtrCAB were heme and protein pure. Purified OmcA migrated as a single band at ~ 75 kDa that could be visualised by both Coomassie and heme staining, Figure 2.5 lanes 1 and 7. Purified MtrC also migrated as a single band at ~ 70 kDa that could be visualised by both Coomassie and heme staining, Figure 2.5 lanes 2 and 8. Heme staining of purified MtrCAB showed the presence of two dominant bands at ~ 70 kDa and ~ 32 kDa corresponding to MtrC and MtrA respectively, Figure 2.5 lane 9. MtrB (~ 75 kDa) was only visualised during Coomassie staining due to the absence of hemes in this protein, Figure 2.5 lanes 3 and 5.

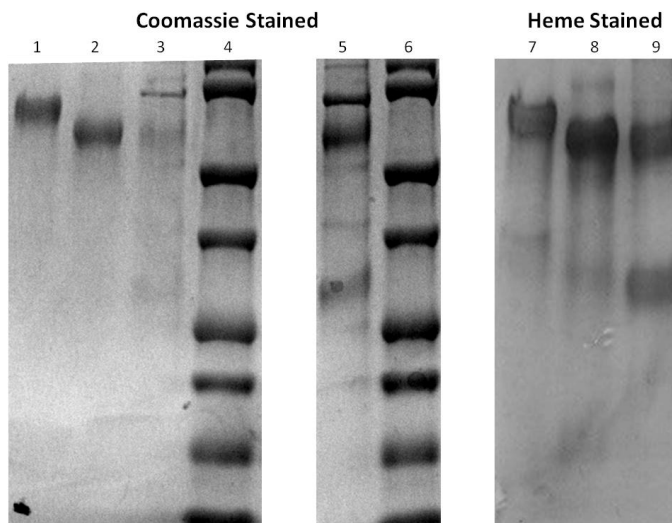


Figure 2.5. SDS-PAGE analysis of purified outer membrane cytochromes of *S. oneidensis* MR-1.

Purified proteins were resolved using 4 - 20 % TruPAGE precast SDS-PAGE gels and were subsequently visualised by Coomassie staining (lanes 1 - 6) and by heme staining (lanes 7 - 9). Lanes 1 and 7, ~ 1 μ g OmcA; lanes 2 and 8, ~ 1 μ g MtrC; lanes 3 and 9, ~ 1 μ g MtrCAB containing approximately 0.2 μ g MtrA, 0.4 μ g MtrB and 0.4 μ g MtrC; lanes 4 and 6, protein molecular weight markers of 100, 75, 50, 37, 25, 20, 15, and 10 kDa; lane 5, ~ 5 μ g MtrCAB containing approximately 1 μ g MtrA, 2 μ g MtrB and 2 μ g MtrC.

2.3 Characterisation and Preparation of (Proteo)liposomes

2.3.1 Dynamic Light Scattering

Dynamic light scattering (DLS) is a technique where the intensity of light scattered by molecules, and/or particles, in solution is measured over time. The intensity of scattered light would be constant if molecules were stationary; however, Brownian motion caused by random collisions with neighbouring molecules results in changes of intensity of scattered light. By detecting these changes over time within a 10 - 15 μ L sample held in a quartz DLS cuvette, DLS essentially measures the speed of Brownian motion and ultimately provides information regarding the average size and size distribution of molecules in a sample. DLS measurements were performed at 20 $^{\circ}$ C using a ProteinSolutions DynaPro-99-E-50 dynamic light scattering module with a TC-100-830 temperature control micro sampler.

The speed of Brownian motion is defined by the relevant diffusion coefficient and is influenced by particle size, solvent viscosity and temperature. This is shown in the Stokes-Einstein equation (Equation 2.3) where k is the Boltzmann's constant, T is the absolute temperature, D is the diffusion coefficient of the particle, η is the solvent viscosity, and r is the hydrodynamic radius of the particle.

$$r = \frac{kT}{6\pi\eta D} \quad (2.3)$$

If the temperature and solvent are constant and known, variations in the intensity of scattered light is directly related to the hydrodynamic radius of particles. The hydrodynamic radius is the radius of a hard sphere that diffuses at the same speed as the species being measured; therefore determined hydrodynamic radii are averaged to account for species not being perfect spheres.

Fluctuations in light intensity were quantified by the DYNAMICS software via a second order, time autocorrelation function (Equation 2.4) where I is the intensity of scattered light and t is time.

$$g(t) = \left(\frac{I(t=0) \times I(t)}{[I(t=0)]^2} \right) \quad (2.4)$$

This correlation function is then modelled using an exponential equation (Equation 2.5) which determines the diffusion coefficient (D); where B is the baseline of the correlation function at an infinite time delay, A is the amplitude of the correlation function at t = 0, q is the magnitude of the scattering vector, and t is time.

$$g(t) = B + A \sum e^{-2q^2 D t} \quad (2.5)$$

The determined diffusion coefficients and autocorrelation data were analysed by the software in several ways to summarise the average hydrodynamic radii and spread of radii of species within the sample.

Typically DLS software was used to obtain size distribution histograms, as illustrated in Figure 2.6. Each peak within a size distribution histogram represents a different species present and their average hydrodynamic radius and size distribution, shown by the width of the peak. Histograms with one peak, and therefore one species present, have a monomodal size distribution, Figure 2.6 A. Samples with multimodal size distributions have multiple species present, and their histograms have more than one peak, Figure 2.6 B. Polydispersity (Pd) describes the level of size homogeneity of a species as a percentage. A species was considered homogenous in size when Pd was less than 15 %. Otherwise the size distribution was considered to be polydisperse. Such terms and average hydrodynamic radii are used to characterise (proteo)liposomes used within this work.

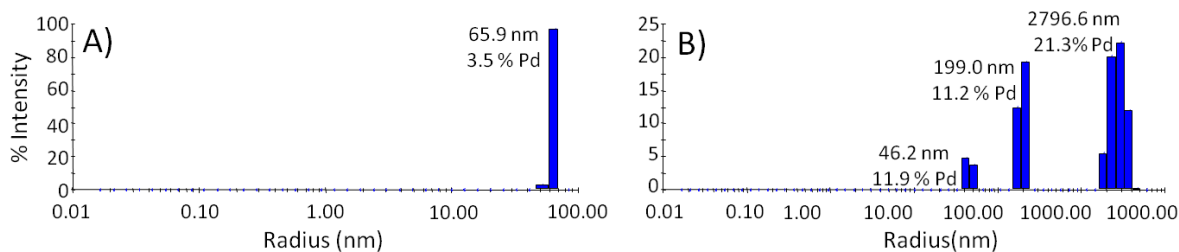


Figure 2.6. Example size distribution histograms from DLS measurements.

Size distribution histograms of: A) a monomodal, homogenously sized sample; and B) a multimodal sample containing different sized species, of which two are homogenous in size with Pd less than 15 % and one has a highly polydisperse size distribution with Pd greater than 15 %. Intensity is based upon the number of contributions by each species. Average hydrodynamic radii and polydispersity (Pd) of different species are included as labels.

2.3.2 Bright-Field Microscopy

Bright-field microscopy is the simplest of all optical microscopy illumination techniques. When white light is shone upon a sample some light is absorbed by species and causes a contrast in the bright field. Bright-field microscopy, performed in the lab of Prof. Moh El-Naggar at the University of Southern California, was used to confirm the sizes and size disruptions of (proteo)liposomes. Bright-field microscopy images were obtained using a Nikon Eclipse Ti-E inverted microscope, equipped with NIS-Elements imaging software and a drift correction unit (Nikon Perfect Focus System) for maintaining focus at the coverslip-medium interface during time-lapse imaging. (Proteo)liposome samples were placed on ethanol cleaned, 43 mm × 50 mm, No. 1 coverslips 30 mins prior to imaging.

2.3.3 Resolution of Proteoliposome Composition by SDS-PAGE Analysis

SDS-PAGE analysis was used to confirm the insertion and presence of MtrCAB within proteoliposomes.^[92] Prior to SDS-PAGE analysis, (proteo)liposome samples were incubated with ice-cold ethanol for 30 mins at -80 °C then centrifuged at 16000 g, 4 °C for 15 mins. The ethanol was removed and the precipitated protein dried before being analysed by SDS-PAGE gels as described in Section 2.2.1. Proteins were subsequently visualised as previously described in Section 2.2.2.

2.3.4 MtrCAB Incorporation into Preformed Liposomes

Mechanically mediated reconstitution of MtrCAB into preformed liposomes has previously been reported.^[92, 93] Preparations of (proteo)liposomes with and without MV²⁺ encapsulated, as illustrated in Figure 2.7, were performed by minor modifications of the previously published method.^[92, 93] DLS was used to monitor average hydrodynamic radii

of lipid vesicles and their polydispersity, Figure 2.7. Proposals about the nature of lipid vesicles structures have been made throughout by comparison of radii reported here with observations from literature, as outlined in Section 1.5.2.2.

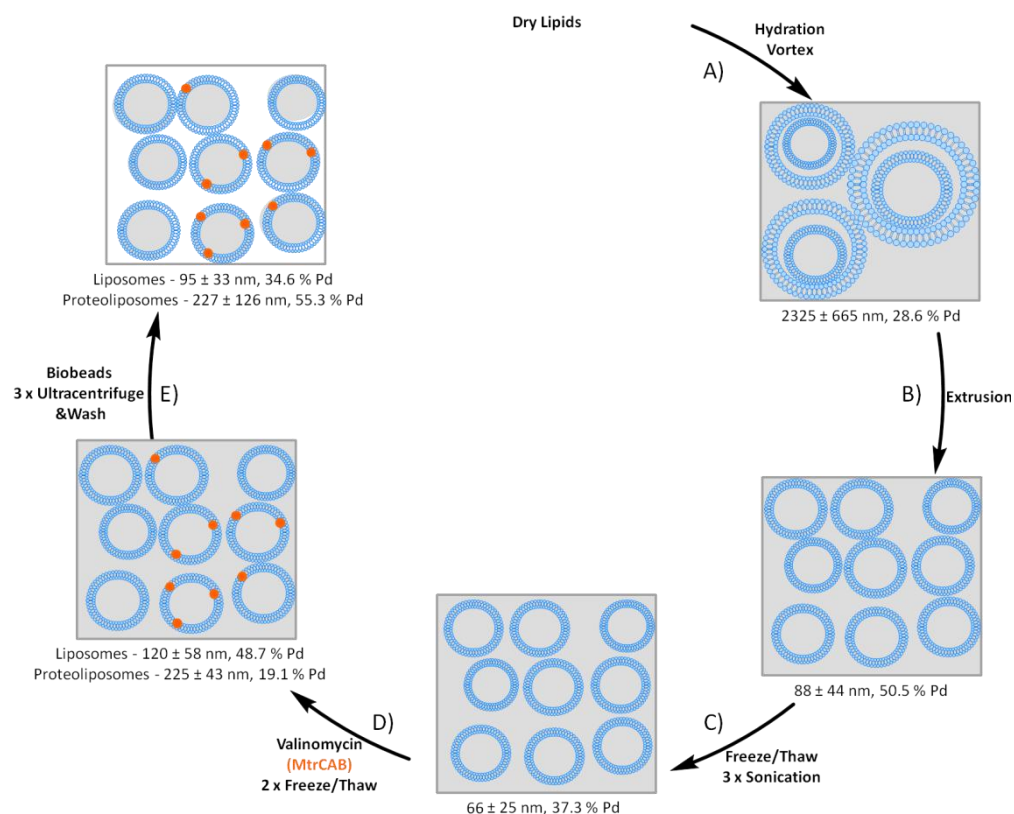


Figure 2.7 Summary of (proteo)liposome preparation via preformed liposomes, with average hydrodynamic radii after key steps.

Average hydrodynamic radii and polydispersity (Pd) determined from DLS. Data are representative of that from several preparations of (proteo)liposomes with and without MV^{2+} encapsulated. Orange circles represent MtrCAB. Structures of MLVs and LUVs indicated are proposed from literature of similar systems, as described in Sections 1.5.2.2 and 1.6.3.^[63, 66, 93]

Suspensions of 10 mg mL^{-1} chicken egg PC (details in Table 1.1) were prepared via vortexing in 50 mM HEPES, 2 mM CaCl_2 , pH 7, with or without 10 mM MV^{2+} , Figure 2.7 A. The resulting highly polydisperse MLVs, with an average radius of $2300 \pm 600 \text{ nm}$, were extruded by 11 passes through polycarbonate membranes with a defined pore size of $0.2 \mu\text{m}$ to generate smaller LUVs with a more uniform radius of $88 \pm 44 \text{ nm}$, Figure 2.7 B. Mini extruder, polycarbonate membranes and membrane supports were supplied and used as instructed by Avanti Polar Lipids Incorporation. Suspensions were slowly frozen at $-80 \text{ }^\circ\text{C}$, prior to being gradually thawed. These suspensions were sonicated for 40 s three times to produce smaller LUVs with a radius of $66 \pm 25 \text{ nm}$, Figure 2.7 C.

At this point valinomycin (1 mg mL^{-1} in dimethyl sulfoxide stock) was added to give a final concentration of 100 nM, Figure 2.7 D. Valinomycin inserts in lipid bilayers,

forming channels that can selectively transport potassium ions.^[104] This, alongside the presence of potassium ions included later, was demonstrated to be essential for extensive transmembrane electron transfers into and out of MV-containing proteoliposomes as these avoid the build up of charge differences across the membrane.^[93] When making proteoliposomes purified MtrCAB in 20 mM HEPES, 100 mM NaCl, ~ 2 % Triton X-100, pH 7 was added at this stage to give a MtrCAB concentration of ~ 10 nM. When making liposomes an equivalent addition of 20 mM HEPES, 100 mM NaCl, ~ 2 % Triton X-100, pH 7 was made.

Proteoliposome and liposome suspensions were both subjected to two further slow freeze/thaw cycles, Figure 2.7 D. DLS showed resulting proteoliposomes and liposomes had distinctly different radii of 225 ± 43 and 120 ± 58 nm, respectively. This difference, alongside minimal changes observed during the remainder of the preparations, suggests that the freeze/thaw cycles are key to reconstitution of MtrCAB in liposomes to make proteoliposomes. During these cycles ice crystals are likely to form cracks within the bilayers that might allow for MtrCAB insertion, with the smaller MtrAB complex (~ 40 Å diameter pore size for MtrB) being the favourable smaller wedge point over the larger MtrC (~ 80 Å × 60 Å × 30 Å) MtrC, Section 1.6.2 - Figures 1.14 and 1.15.^[86, 87] This theory would help to explain why the orientation of MtrCAB in proteoliposomes prepared in this manner is uniform with MtrC being located outside of proteoliposomes, and thus adopting the orientation seen within *S. oneidensis* cells.^[92]

250 mg mL⁻¹ Biobeads SM-2 (BIO-RAD) were added to (proteo)liposome suspensions that were gently shaken overnight at 4 °C to slowly remove detergent. The duration of Biobead incubation with (proteo)liposome suspensions, which was originally 1 hr, was the only deliberate modification to the previously published protocol.^[92, 93] This change was made to ensure sufficient time for complete detergent removal. Biobeads were then allowed to settle before suspensions were removed and ultracentrifuged at 227000 g, 4 °C for 40 mins. The resulting (proteo)liposome pellets were resuspended in 50 mM HEPES, 2 mM CaCl₂, 10 mM KCl, 50 mM TEOA, pH 7 (Figure 2.7 E). This ultracentrifugation was performed thrice to aim to ensure any non-encapsulated MV²⁺ was removed. The final (proteo)liposome suspensions were stored at 4 °C and used within 2 weeks.

2.4 Light-Driven Photoreductions of Redox Dyes and Cytochromes

Irradiation was performed using a KL5125 cold light source (Krüss) fitted with a 150 W (15 V) high-quality, UV-filter quartz halogen glass lamp (Osram). The spectral output from this lamp was measured using a HR2000CG-UV-NIR series high-resolution fiber optic spectrometer (Ocean Optics). The detector of this counted the number of photons emitted from the lamp at each wavelength to provide the lamp spectral output, Figure 2.8 A black line. The integration time was adjusted until the maximum intensity was ~ 3500 counts. A comparative solar spectrum was obtained by performing similar measurements after the detector was placed in direct sunlight, Figure 2.8 A grey line. The spectral distribution of the lamp was similar to that of natural sunlight; however, relatively more photons were emitted between the wavelengths of 550 - 800 nm and the UV-filter only allowed the emission of visible light from the lamp, i.e. wavelengths greater than 350 nm.

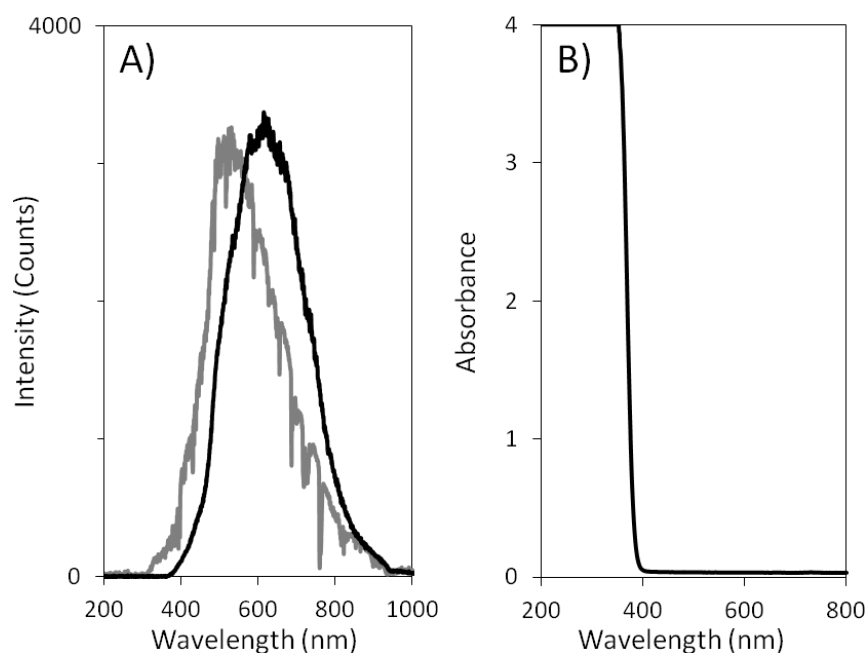


Figure 2.8. Spectral distribution and wavelengths emitted by lamp during photoreductions.

A) Spectral distributions of lamp used in this work (black line) and natural sunlight (grey line).

B) Wavelengths absorbed by acrylic plastic of the anaerobic chamber.

All photoreductions were performed with anaerobic samples within a N_2 filled, anaerobic chamber (Belle Technology, atmospheric $O_2 < 10$ ppm). Light intensity at the anaerobic samples was assessed using a SOLAR-100 amprobe solar power meter (sensor wavelength 400 - 1100 nm) and adjusted to desired intensity by adjusting the distances between light source and sample. As samples were irradiated with the lamp outside the anaerobic chamber, the impact the clear acrylic plastic had upon the lamp spectral output

was assessed by measuring the absorbance spectrum of the plastic using a Hitachi U4100 spectrophotometer. The resulting spectrum indicates that the plastic of the anaerobic chamber absorbed and filtered any UV-light radiation produced by the halogen lamp, Figure 2.8 B.

Solutions of photosensitisers and redox dyes or outer membrane cytochromes were irradiated in stirred, 1 cm pathlength, reduced volume cuvettes. The high optical densities and quantities of outer membrane cytochromes required for experiments with more than 100 μM total heme required the use of 1 mm path length cuvettes and were unstirred. All cuvettes (Starna Scientific) were made from special optical glass with greater than 75 % transmission above 320 nm.

Typically photoreductions were performed in 50 mM HEPES, 2 mM CaCl_2 , 10 mM KCl, 50 mM TEOA, pH 7. Experiments that investigated the identity of the SED(s) and mechanism of OmcA photoreduction by soluble photosensitisers were performed at pH 7 in solutions of three compositions: 50 mM phosphate; 50 mM phosphate, 50 mM TEOA; and 50 mM HEPES, 2 mM CaCl_2 , 10 mM KCl. After irradiations excess anaerobic dithionite was added to cause full reduction of cytochrome or redox dye.

Photoreductions of (proteo)liposomes were performed in an identical manner to those described above. Typically after photoreduction and addition of dithionite a further addition of anaerobic Triton X-100 (~ 0.4 %) was made to (proteo)liposome suspensions, which resulted in lysis of (proteo)liposomes and the release and reduction of any cargo due to the presence of excess dithionite.

2.5 Assessing Changes in (Proteo)liposomes due to the Presence of Photosensitisers

The changes, if any, caused to (proteo)liposomes by the presence of a photosensitiser under dark and irradiation conditions were investigated by monitoring electronic absorbance spectra of (proteo)liposomes before and after incubation with a soluble photosensitiser. These were also compared with electronic absorbance spectra of sample mixture after centrifugation and separation of (proteo)liposome from supernatant to ascertain if the soluble photosensitisers remained in the external solutions or had associated with the (proteo)liposomes.

Stirred, anaerobic incubations were carried out in 1 cm pathlength cuvettes containing 1 mg mL^{-1} (proteo)liposome suspensions in 50 mM HEPES, 2 mM CaCl_2 ,

10 mM KCl, 50 mM TEOA, pH 7, in the absence or presence of a photosensitiser. The solution was incubated for 90 mins either in the dark or under irradiation, to investigate the effects of the photosensitisers' ground states and the photo-excited, -reduced and -oxidised states upon (proteo)liposomes. After this time (proteo)liposome suspensions were collected via ultracentrifugation at 227000 g, 4 °C for 40 mins. The supernatant was separated and the (proteo)liposome pellet was resuspended in an identical volume of buffer which gave a concentration of 1 mg mL⁻¹ lipid. The supernatant and the resuspended (proteo)liposomes were placed in separate cuvettes to obtain their absorbance spectra.

When investigating whether the presence of a photosensitiser resulted in the release of encapsulated MV from (proteo)liposomes, a few changes to this method was included. These changes were included to avoid the production of the colourless redox-inactive species which formed mostly after 30 mins photoreduction of MV²⁺ with some of the investigated photosensitisers. Stirred, anaerobic incubations were carried out in 1 cm pathlength cuvettes containing 1 mg mL⁻¹ lipid suspension of MV²⁺-containing (proteo)liposomes in 50 mM HEPES, 2 mM CaCl₂, 10 mM KCl, 50 mM TEOA, pH 7, in the absence or presence of photosensitiser. The solution was incubated for 30 mins either in the dark or under irradiation performed at 2 kW m⁻². After this time (proteo)liposome suspensions were collected via centrifugation at 16000 g, 4 °C for 15 mins. This low speed centrifugation caused a minor percentage of (proteo)liposomes to remain in the supernatant but the majority were located in the pellet. The supernatant was separated and (proteo)liposome pellet was resuspended in an identical volume of buffer which gave a concentration of 1 mg mL⁻¹ lipid. The supernatant and the resuspended (proteo)liposomes were placed in separate cuvettes to obtain their electronic absorbance spectra before and after the addition of excess anaerobic dithionite to cause reduction of MV²⁺ in the external solution. Further additions of anaerobic Triton X-100 (~ 0.4 %) resulted in complete lysis of (proteo)liposomes and allowed the full reduction of MV²⁺.

Chapter 3

Photoreduction of Outer Membrane Cytochromes from *Shewanella oneidensis* MR-1 Using Organic & Inorganic Photosensitisers

3.1 Introduction to Coupling Photosensitisers to Metalloproteins

Many metalloproteins such as hydrogenases, carbon monoxide dehydrogenases, and formate dehydrogenases, have been previously electronically linked to photosensitisers.^[105–108] Such systems demonstrate the ability to trap photoexcited electrons which can initiate light-driven redox reactions when the protein possesses an active site that catalyses redox reactions. Various strategies have been employed to integrate metalloproteins with light-harvesting compounds, including: i) non-specific interaction between protein and photosensitiser; ii) covalent attachment of photosensitiser to protein; or iii) immobilisation of protein on photoconductor nanoparticles or electrodes. Non-specific systems depend upon short-lived, diffusion-controlled encounters where the orientations of photosensitiser and protein favour desired photoreactions, instead of unfavourable recombination reactions.

This chapter describes the screening of various photosensitisers for their ability to photoreduce outer membrane cytochromes of *S. oneidensis* MR-1 using visible light as the stimulus. Even though alternative strategies would overcome diffusion limitations seen with non-specific linkages, it was decided to investigate photosensitisers which would only interact with the cytochromes via diffusion collisions. This strategy was chosen as the structure for the entire MtrCAB complex, and how this would ultimately be positioned within the membrane of proteoliposomes, is unknown and therefore inappropriate selection of a linkage site may actually hinder the desired photoreductions.

Additionally within this chapter the SED(s) key for photoreductions of the outer membrane cytochromes are identified and the optimal experimental conditions are explored in detail within cytochrome solutions instead of within proteoliposome suspensions. This initial and most simplified system allows investigations into how photosensitiser identity directly impacts the reduction of the proteins and oxidation of the SED(s), without the presence of other complexities and components required for light-driven transmembrane electron transfers.

3.2 Characteristics of Photosensitisers Chosen for this Study

Eight water-soluble photosensitisers, with electronic absorptions within the visible region of the electromagnetic spectrum, were investigated to explore the possibility of visible-light-driven reduction of *S. oneidensis* MR-1 outer membrane cytochromes. The flavin molecules, flavin adenine dinucleotide (FAD), flavin mononucleotide (FMN) and riboflavin (RF), were of particular interest to this study as they are photosensitisers which are naturally produced by *S. oneidensis* MR-1, and the later two are involved in respiratory extracellular electron transfer (EET).^[78, 79, 90] Eosin Y, fluorescein and proflavin were selected as well-studied, light-harvesting analogs of organic molecules that can stimulate EET in microbial fuel cells.^[109–111] The extensively studied inorganic photosensitisers tris(bipyridine) ruthenium(II) ($[\text{Ru}(\text{bpy})_3]^{2+}$) and bis(bipyridine) (bipyridine-4,4'-bisphosphonic acid) ruthenium(II) (RuP) were also chosen for this study as they are employed within dye-sensitised titanium dioxide (TiO_2) solar cells and for visible-light-driven enzyme catalysis.^[112–114] The structures, photoreduction mechanisms, photodegradation reactions and spectral, electrochemical and photophysical properties of these photosensitisers are discussed in the next sections.

3.2.1 Ruthenium Complexes

The transition metal complex $[\text{Ru}(\text{bpy})_3]^{2+}$ consists of Ru(II) bound by three 2,2'-bipyridine bidentate chelating ligands which facilitate the photochemistry chemistry via metal to ligand charge transfers, Table 3.1. $[\text{Ru}(\text{bpy})_3]^{2+}$ is an extensively studied photosensitiser that possesses a unique combination of high chemical stability, relatively long excited state lifetime and strong (photo)redox potentials for driving a variety of photoredox reactions.^[115] Modification of bipyridine ligands alters the spectral, redox and photochemistry of the corresponding Ru(II) dye; however, the beneficial photostability, long lived-triplet excited state and photoredox mechanism associated with $[\text{Ru}(\text{bpy})_3]^{2+}$ (Table 3.1) remain.^[116] As a consequence ligand substituted Ru(II)-bipyridine dyes have also been extensively studied. RuP is a diphosphonate-derivate of $[\text{Ru}(\text{bpy})_3]^{2+}$, Table 3.1. The inclusion of the phosphate substituents, which are in the anionic form at neutral to alkaline pH, allows RuP to strongly adsorb on TiO_2 nanoparticles and electrodes.^[112, 114, 117] RuP-sensitised TiO_2 benefits from being able to utilise visible light for photoexcitation, which TiO_2 is normally unable to absorb.^[112, 114, 117] The covalent coupling allows photoexcited RuP (RuP^*) to inject electrons directly into the conduction band of TiO_2 ($E_m = -700$ mV at pH 7) where recombination of the electron to oxidised RuP is slow in

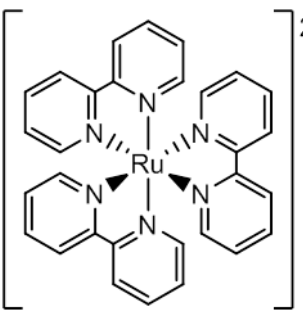
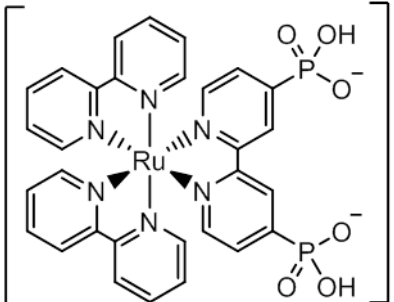
Photosensitisers	Structure	λ_{\max} (nm)	ϵ at λ_{\max} (mM ⁻¹ cm ⁻¹)	E (PS*) (eV)	E_m (PS ⁺ /PS ⁰) (V)	E_m (PS ⁺ /PS*) (V)	E_m (PS ⁰ /PS ⁻) (V)	E_m (PS*/PS ⁻) (V)
[Ru(bpy)₃]²⁺ (Tris(bipyridine) ruthenium(II))		452	14.4 ^[112]	2.10 ^[118]	+1.26 ^[118]	-0.84 ^[118]	-1.26 ^[118]	+0.84 ^[118]
RuP (Bis(bipyridine) (bipyridine-4,4'- bisphosphonic acid) ruthenium(II))		455	10.2 ^[112]	2.21 ^[112]	+1.26 ^[112]	-0.95 ^[112, 119]	-1.09 ^[120]	+1.12 ^a

Table 3.1. Structural, spectroscopic and electrochemical properties of ruthenium photosensitisers at pH 7.

a. Calculated using Equation 1.2, see Section 1.3.1 for details. All (photo)reduction potentials are reported versus SHE.

comparison to regeneration of the ground state by phosphorescence.^[120, 121] These principles and benefits are utilised in dye-sensitised solar cells and dye-sensitised particles with co-adsorbed proteins.

The relevant structures, spectral and electrochemical properties of $[\text{Ru}(\text{bpy})_3]^{2+}$ and RuP are summarised in Table 3.1 and Figure 3.1. The electronic absorption spectra of $[\text{Ru}(\text{bpy})_3]^{2+}$ and RuP in aqueous solution exhibit broad peaks centred at ~ 445 nm with molar extinction coefficients of $\sim 10 \text{ mM}^{-1} \text{ cm}^{-1}$, which are characteristic of metal to ligand charge transfer associated with a $d-\pi^*$ transition.

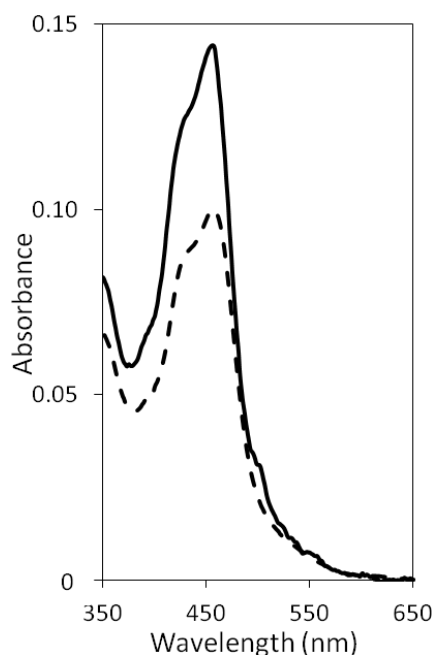


Figure 3.1. Electronic absorbance spectra of ruthenium photosensitisers.

Spectra of $10 \mu\text{M}$ of either $[\text{Ru}(\text{bpy})_3]^{2+}$ (continuous line) or RuP (dashed line) in 50 mM HEPES, 2 mM CaCl_2 , 10 mM KCl, 50 mM TEOA, pH 7. Path length 1 cm.

Photoredox mechanisms, summarised for $[\text{Ru}(\text{bpy})_3]^{2+}$ in Figure 3.2, follow the simple photocatalytic cycle as presented previously in Figure 1.4. Blue light absorption causes metal to ligand charge transfer, producing an excited singlet state which rapidly produces an excited triplet state by ISC. $[\text{Ru}(\text{bpy})_3]^{2+}$ and RuP both exhibit a moderately intense, broad fluorescence peak with maxima at 610 and 620 nm, respectively, which corresponds to an approximate triplet state energy of 2.1 - 2.2 eV.^[8, 122] Oxidative or reductive quenching of this excited triplet state can occur, in which both quenching mechanisms ultimately result in the oxidation of a SED, the reduction of an electron accepting species and the regeneration of ruthenium complex ground state.^[24, 120] Photoreduction by either of these Ru(II) complexes is driven by photoredox couples which

have reductive potentials below -840 mV (Table 3.1.) irrespective of the mechanism, i.e. oxidative or reductive.^[112, 118–120]

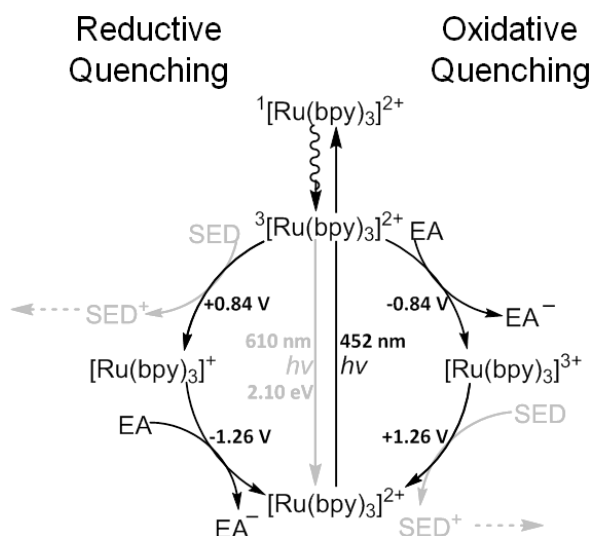


Figure 3.2. Overview of $[\text{Ru}(\text{bpy})_3]^{2+}$ photochemistry and (photo)reduction potentials.

EA is the target electron acceptor. SED is the sacrificial electron donor. For simplicity only those steps that positively contribute to photoreduction are shown.^[118] All (photo)reduction potentials are reported versus SHE.

Even with their high chemical stability, it is favourable for Ru(II) complex photoreductions to be performed in anaerobic solutions as the corresponding long lived excited triplet state is able to generate highly reactive singlet oxygen species upon reacting with the triplet state of ground state oxygen.^[10]

3.2.2 Organic Photosensitisers

The photochemistry of organic photosensitisers is often more complex than that of ruthenium complexes. Organic photosensitisers contain highly conjugated ring systems and the associated π - π^* transitions facilitate their photoredox chemistry. In contrast to Ru(II)-dyes, the one-electron reduced and/or oxidised species formed upon quenching of long-lived photoexcited states of organic dyes are highly reactive radicals. Consequently organic photosensitisers do not always follow the simple descriptions of oxidative and reductive quenching that have been presented so far.

In addition to photoredox reactions, photodegradation and associated photobleaching of highly conjugated organic photosensitisers are often observed.^[10, 123] These lead to absorption bands and photoredox activity to decrease during prolonged irradiation with an intense light source or under aerobic conditions.^[10, 123] In aerobic conditions, the excited triplet state of organic photosensitisers can collide with the triplet

state of ground state oxygen to generate singlet oxygen which destroys conjugated systems and with it their ability to absorb visible light.^[10] Therefore, for photoredox reactions to dominate those of photodegradation, it is favourable to use anaerobic conditions with organic photosensitisers.

3.2.2.1 Eosin Y and Fluorescein

Eosin Y and fluorescein are both xanthene compounds with predominant dianionic forms at pH 7, Table 3.2.^[124] The structures, spectral and electrochemical properties of eosin Y and fluorescein are summarised in Table 3.2 and Figure 3.3.

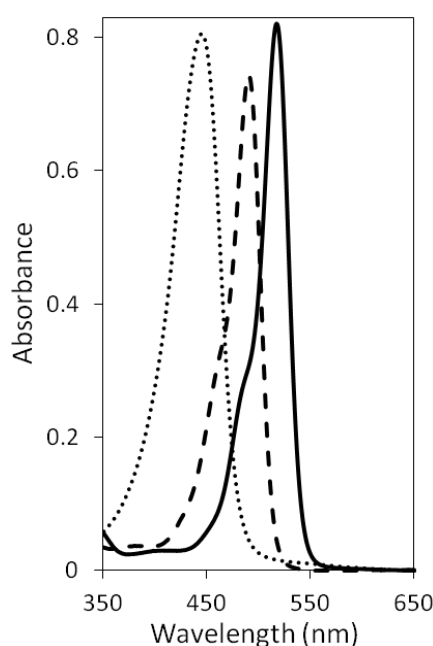


Figure 3.3. Electronic absorbance spectra of eosin Y, fluorescein and proflavin. Spectra of 10 μM eosin Y (continuous line), 12 μM fluorescein (dashed line), and 11 μM proflavin (dotted line) in 50 mM HEPES, 2 mM CaCl_2 , 10 mM KCl, 50 mM TEOA, pH 7. Path length 1 cm.

Fluorescein is one of the most widely used dyes, employed in numerous fields as a fluorescent probe, due to its high absorption and high fluorescent yield.^[124] Eosin Y, a tetrabromo-derivative of fluorescein, is most often used as a cell cytoplasm counterstain in hematoxylin and eosin histological staining but has recently received a lot of attention as a photosensitiser within organic synthesis.^[125, 126]

The electronic absorption spectra of eosin Y and fluorescein in aqueous solution both possess one peak with an absorbance maximum at 520 and 490 nm, respectively. These peaks have large molar extinction coefficients which are characteristic of $\pi\text{-}\pi^*$ transitions that originate from their tricyclic ring system. The absorbance peaks of eosin Y

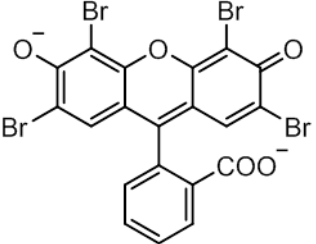
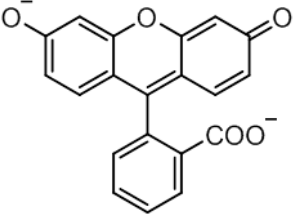
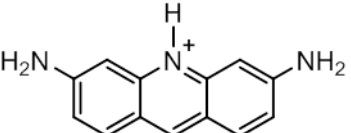
Photosensitisers	Structure	λ_{\max} (nm)	ϵ at λ_{\max} ($\text{mM}^{-1} \text{cm}^{-1}$)	$E(\text{PS}^*)$ (eV)	$E_m(\text{PS}^+/\text{PS}^0)$ (V)	$E_m(\text{PS}^+/\text{PS}^*)$ (V)	$E_m(\text{PS}/\text{PS}^-)$ (V)	$E_m(\text{PS}^*/\text{PS}^-)$ (V)
Eosin Y		520	80.4	1.89 ^[127]	+1.02 ^[9]	-0.87 ^[9]	-0.82 ^[9]	+1.07 ^[9]
Fluorescein		490	64.6	1.96 ^[127]	+0.94 ^[9]	-1.02 ^[9]	-0.98 ^[9]	+0.98 ^[9]
Proflavin		445	76.1	2.17 ^[128]	+1.31 ^[128]	N/A	-0.78 ^[129]	+1.39 ^[129]

Table 3.2. Structural, spectroscopic and electrochemical properties of eosin Y, fluorescein and proflavin photosensitisers at pH 7.

λ_{\max} and ϵ for these photosensitisers were determined from UV-visible spectra of 40, 20, 10, 5, 2.5 and 1.25 μM of dye in 50 mM HEPES, 2 mM CaCl_2 10 mM KCl, pH 7 using the Beer-Lambert law. Within this concentration range absorbance was proportional to photosensitiser concentration. Above 40 μM spectra obtained showed photosensitiser aggregation, and therefore data from these spectra were not included in calculations to determine molar extinction coefficients. See text for details. All (photo)reduction potentials are reported versus SHE.

and fluorescein both have shoulders at approximately 490 and 460 nm, respectively, which are attributed to dimers, Figure 3.3.^[130] The aggregation state of these dyes depends on their concentrations. Above dye concentrations of $\sim 100 \mu\text{M}$ higher aggregates are formed and this is accompanied by additional broad absorbance peaks at $\sim 390 \text{ nm}$, which leads to the absorbance spectra deviating from the simplest description of the Beer-Lambert law (Equation 2.1).^[130] Photoexcitation of eosin Y and fluorescein aggregates is possible; however, the geometry of the aggregate can affect the preferred transition from the ground state to the excited state leading to blue or red shifts in absorption and excitation spectra.^[130]

The photochemistry of eosin Y and fluorescein both occur via the photocatalytic cycles previously presented in Figure 3.2. Blue light absorption causes photoexcitation of an electron to an excited singlet state which then relaxes by ISC into an excited triplet state. Eosin Y and fluorescein both exhibit a strong broad fluorescence peak for their monomer forms with maxima at 535 and 515 nm, respectively, which correspond to an approximate triplet state energy of 1.9 eV.^[130] Photoredox reactions then occur by either reductive or oxidative quenching of the corresponding excited triplet state.^[9] Eosin Y and fluorescein photoreductions are driven by redox couples which have reductive potentials below -820 mV irrespective of the mechanism route undertaken, Table 3.2.^[9] Photodegradations of eosin Y and fluorescein can occur but these reactions are not well characterised.

3.2.2.2 Proflavin

Proflavin, the 3,6-diamino derivative of acridine, may be cytotoxic to many gram-positive bacteria due to its ability to intercalate with DNA but it is also a highly stable photosensitiser with a promising potential for solar hydrogen production from water.^[131–133] At physiological pH, the predominant form of proflavin is protonated at the central nitrogen atom, Table 3.2.^[129, 134]

The electronic absorption spectrum of proflavin in aqueous solution has one peak at 445 nm with a molar extinction coefficient of $76.1 \text{ mM}^{-1} \text{ cm}^{-1}$, which is characteristic of a $\pi\text{-}\pi^*$ transition originating from the tricyclic ring system, as shown in Figure 3.3 and Table 3.2. Proflavin aggregation is observed with concentrations greater than approximately $100 \mu\text{M}$, which leads to absorbance maximum shifts to shorter wavelengths and its molar extinction coefficient to be concentration dependant.^[135]

Proflavin photoredox mechanisms, summarised in Figure 3.4, are complex and extend beyond the simple photocatalytic cycles presented so far. Absorption of blue light excites an electron from the ground state (PFH^+) to an excited singlet state ($^1\text{PFH}^{+*}$). ISC gives an excited triplet state ($^3\text{PFH}^{+*}$) which is reductively quenched on acceptance of an electron from a SED to yield a neutral proflavin radical. [128] Rapid deprotonation produces an anionic proflavin radical ($\text{PF}^{\bullet-}$), which can reduce a desired electron acceptor to regenerate PFH^+ after protonation. [128, 129]

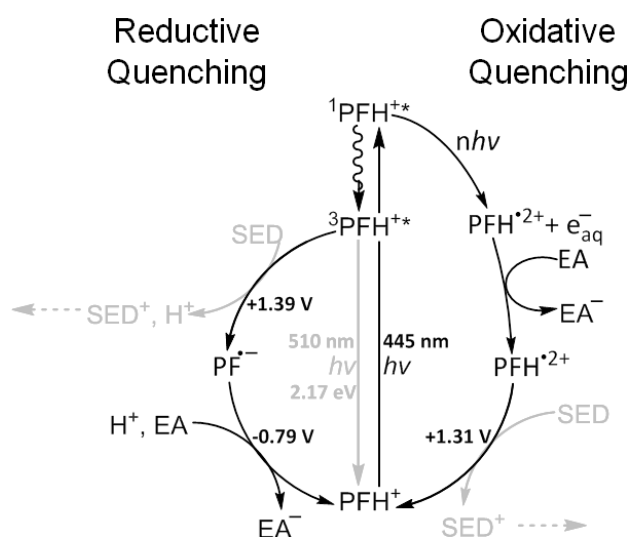


Figure 3.4. Summary of proflavin photochemistry and (photo)reduction potentials.

EA is the target electron acceptor. SED is the sacrificial electron donor. For simplicity only steps that positively contribute to photoreduction are shown. [128, 129, 133] All (photo)reduction potentials are reported versus SHE.

Oxidative quenching of proflavin occurs via photoionisation of $^1\text{PFH}^{+*}$ which absorbs multiple photons to produce an oxidised dication proflavin radical ($\text{PFH}^{\bullet 2+}$) and solvated electrons which reduce a desired EA. [129, 133] PFH^+ is then regenerated by SED oxidation. Proflavin photoreduction via either mechanism likely has a high thermodynamic driving force with reductive potentials below or equal to -780 mV , Figure 3.4 and Table 3.2. [129]

The irradiation of degassed solutions of proflavin in the presence of a SED can result in two known photodegradation products: diacridine and leuco-proflavin. [128] Diacridine, formally known as 3,6,3',6'-diaminobiacridine, possesses an absorbance peak at 424 nm and is formed by dimerisation of two molecules of $\text{PFH}^{\bullet 2+}$. [128] The colourless leuco-proflavin, 3,6,3',6'-diaminobiacridane, is thought to be formed by a reaction between PFH^+ and $\text{PF}^{\bullet-}$. [128] Disproportionation of $\text{PF}^{\bullet-}$ molecules also allows the formation of a fully, two-electron reduced version of proflavin. [128]

3.2.2.3 Flavins

Molecules containing the 7, 8-dimethyl-10-alkylisoalloxazine moiety are generally termed flavins. These molecules are widely utilised in nature to shuttle electrons and act as cofactors within flavoenzymes and photoreceptors. The structures and electrochemical properties of the flavins used in this work are summarised in Table 3.3 and Figure 3.5. RF is the biological precursor for all naturally occurring flavin compounds, including FMN and FAD. Phosphorylation of the ribityl side chain located at the N-10 position on the isoalloxazine ring system of RF results in the formation of FMN, and subsequent addition of adenosine monophosphate produces FAD.

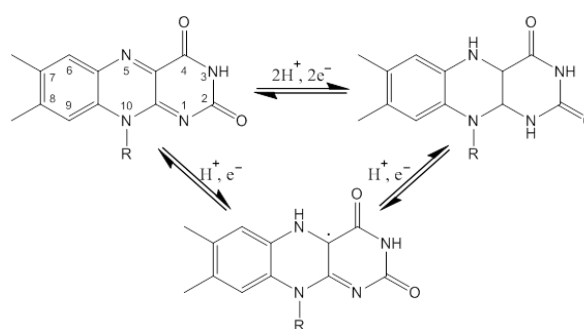


Figure 3.5. Flavin redox reactions at pH 7.

Numeric labels for the flavin moiety carbons are shown on the oxidised state. R is the flavin ribityl side chain. See Table 3.3 for details.

Nitrogen atoms within the tricyclic isoalloxazine ring system facilitate the redox chemistry of flavin compounds, which are able to participate in both one- and two-electron transfers as shown in Figure 3.5. This results in flavins being able to exist in three possible oxidation states: oxidised (quinone), one-electron reduced (semiquinone radical) or two-electron reduced (hydroquinone).

In free solution, the positions of equilibrium linking different flavin species and the preferred electron transfer mechanisms are pH-dependent.^[136, 137] The two-electron reduction, with a reduction potential of about -220 mV, is favoured at neutral pH as the flavin semiquinone is highly unstable with only ~ 5 % being present in an equimolar mixture of oxidised and reduced flavin.^[137, 138] At this pH the flavin moiety is predominately found in the neutral form and the phosphate groups of FMN and FAD are all fully deprotonated.^[137] Upon binding to a protein, the reduction potential(s) and the pK_a values describing a flavin can change drastically.^[138] As it is the flavin moiety which determines spectral, electrochemical and photochemical reactions of FAD, FMN, and RF which only differ by their ribityl side chain, the following points apply to all three.

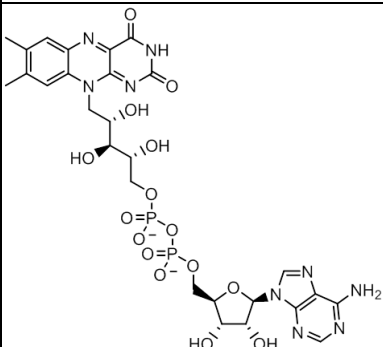
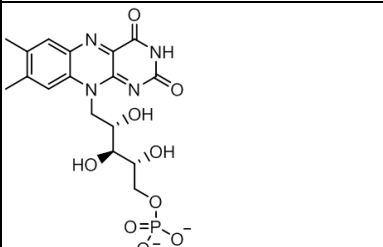
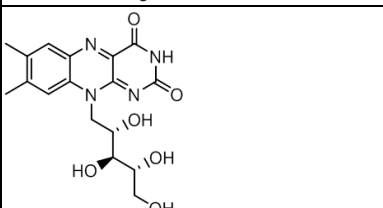
Photosensitisers	Structure	λ_{\max} (nm)	ϵ at λ_{\max} ($\text{mM}^{-1} \text{cm}^{-1}$)	E (PS*) (eV)	E_m (PS/PS ⁻) (V)	E_m (PS*/PS ⁻) (V)
FAD (Flavin Adenine Dinucleotide)		450 (370)	11.3 ^[139]	2.07 ^[136]	-0.22 ^[140]	+1.85
FMN (Flavin Mononucleotide)		445 (370)	12.5 ^[139]	2.07 ^[136]	-0.22 ^[90, 140]	+1.85
RF (Riboflavin)		445 (370)	12.5 ^[139]	2.07 ^[136]	-0.21 ^[141]	+1.86

Table 3.3. Structural, spectroscopic and electrochemical properties of flavin photosensitisers at pH 7.

All (photo)reduction potentials are reported versus SHE.

As shown in Figure 3.6, the electronic absorption spectrum of a flavin in aqueous solution exhibits two broad peaks centred at ~ 445 and 370 nm. These peaks exhibit strong absorbances with molar extinction coefficients greater than $10 \text{ mM}^{-1} \text{ cm}^{-1}$, which are characteristic of π - π^* transitions. These transitions originating from the isoalloxazine ring system gives the characteristic yellow colour to oxidised flavin, which is in contrast to the colourless fully reduced flavin form.^[142]

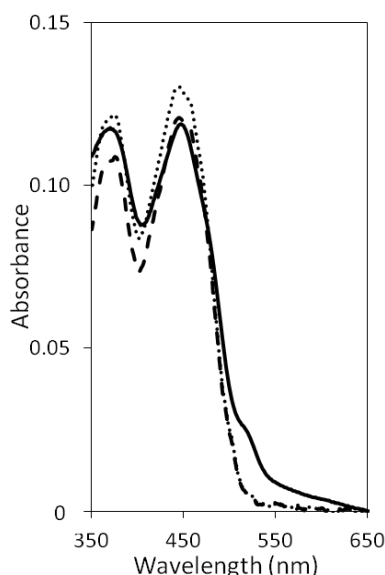


Figure 3.6. Electronic absorbance spectra of flavin photosensitisers.

Spectra of $10 \mu\text{M}$ of either FAD (continuous line), FMN (dashed line) or RF (dotted line) in 50 mM HEPES, 2 mM CaCl_2 , 10 mM KCl, 50 mM TEOA, pH 7. Path length 1 cm .

Flavins can be reduced via a chemical reductant or via visible-light irradiation. Reduction of flavins via visible light, as summarised in Figure 3.7, begins upon absorption of a blue photon. This causes excitation of an electron from the ground state (F) to an excited singlet state ($^1\text{F}^*$) which then relaxes by ISC to populate an excited triplet state ($^3\text{F}^*$). Flavine photoreduction is thought to proceed via $^3\text{F}^*$ being reductively quenched by semiquinone (FH^\bullet) formation and subsequent fast FH^\bullet disproportionation leading to hydroquinone (FH_2) formation.^[143] In the presence of a SED, an electron is donated to $^3\text{F}^*$ from that donor to generate an anionic semiquinone which is protonated below pH 8.^[136] In the absence of a SED, the N-10 ribityl side chain of flavins can act as a hydrogen donor for semiquinone formation.^[142, 144, 145] In support of the ribityl chain being able to assist in intramolecular photoreduction, no photoreduction is observed in phosphate buffer for lumiflavin where identity of the N-10 side chain is a methyl group.^[142] Ultimately, in both cases, FH^\bullet then undergoes a radical disproportionation to form fully reduced flavin (FH_2). The photoreduced flavin can then in turn reduce a target EA via a two-electron reduction ($E_m \approx -220 \text{ mV}$) to regenerate the oxidised flavin.^[90, 140, 141]

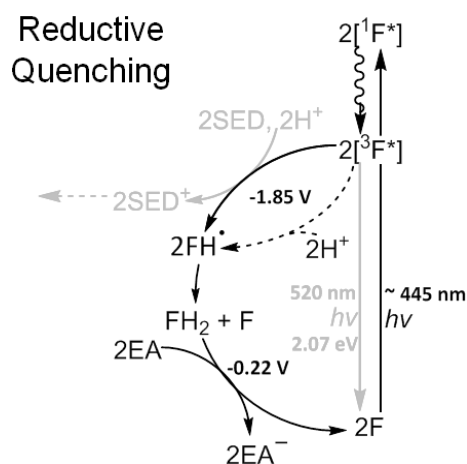


Figure 3.7. Summary of flavin photochemistry and (photo)reduction potentials.

EA is the target electron acceptor. SED is the sacrificial electron donor. For simplicity only steps that positively contribute to photoreduction are shown.^[128, 129, 133] Dashed line represents reductive quenching in absence of a SED. (Photo)reduction potentials are reported versus SHE.

When the ribityl side chain serves as a SED for flavin photoreduction the resulting molecule is unstable and can undergo photodegradation reactions to produce several photoproducts, as illustrated in Figure 3.8. Intermolecular photoaddition of solvent molecules to C-6 or C-9 positions of the flavin group results in the formation of hydroxyl- or alkoxy-dihydroflavins. Intramolecular addition occurs between a ribityl side chain hydroxyl group and the flavin C-9 position to yield a cyclodehydroflavin, where the formation of a 6 membered ring is favourable.^[146] Photodehydrogenation involves the abstraction of a hydrogen atom leading to the ultimate formation of a ketone within the ribityl chain.^[147] When photoreduction of the flavin moiety precedes this side chain oxidation then formation of formylmethylflavin (FMF) occurs, where subsequent photolysis within the ribityl side chain yields lumichrome (LC) and lumiflavin (LF).^[148, 149]

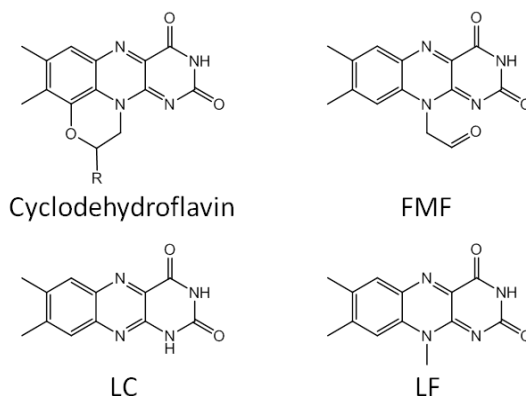


Figure 3.8. Structures of flavin photodegradation products.

R is the flavin ribityl side chain. See Table 3.3 for details.

The rates and magnitudes of these photodegradation reactions depend upon the identity and SED concentration of and on the light intensity and wavelengths of

irradiation.^[150] In aerobic conditions, in the absence of SEDs, photodegradation of flavins dominates over their photoreduction.^[143]

3.3 Initial Screening of Photosensitisers for Visible-Light-Driven Reduction of MtrCAB Suspensions

Initial experiments involving MtrCAB, the key transmembrane cytochrome complex, and the eight photosensitisers described above were performed to explore the possibility of visible-light-driven reduction of *S. oneidensis* outer membrane cytochromes. The absorbance spectrum of oxidised MtrCAB exhibits an intense absorption in the Soret region with a maximum at 410 nm and a broad lower-intensity feature in the α/β -region between 500 and 600 nm, Figure 3.9 continuous black line. These spectral features are characteristic of fully oxidised, low-spin, ferric heme *c*-containing proteins, including MtrC and OmcA.^[151, 152] Addition of the reductant sodium dithionite ($E_m \approx -500$ mV) causes the Soret band to intensify and shift to 420 nm, and the appearance of sharp peaks at 523 and 552 nm in accordance with complete reduction to form ferrous hemes, Figure 3.9 dotted line.^[95] By following changes in intensity at 552 nm, or 420 nm, the oxidation state of cytochromes can be monitored. Assuming that each heme of MtrCAB, OmcA and MtrC equally contributes to the total absorbance change, extent of (photo)reduction can be determined with reference to absorbance of oxidised and dithionite-reduced samples.

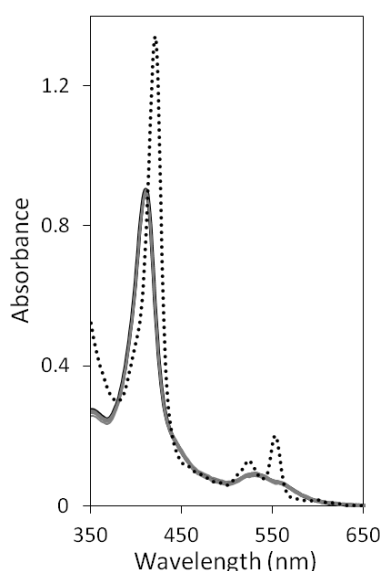


Figure 3.9. No reduction of MtrCAB during irradiations with photosensitisers absent. 0.45 μ M MtrCAB (continuous black line) was irradiated for 5, 15, 30, 60 and 90 mins at 2 kW m^{-2} (grey lines) prior to the addition of dithionite (dotted line). Stirred anaerobic sample in 50 mM HEPES, 2 mM CaCl_2 , 10 mM KCl, 50 mM TEOA, pH 7 in the presence of ~ 0.06 % Triton X-100 (v/v) at 20 $^\circ\text{C}$. Path length 1 cm.

Initial irradiations of anaerobic solutions of $\sim 0.5 \mu\text{M}$ MtrCAB were carried out in the presence of excess TEOA over 90 mins (Krüss KL5125 cold light source fitted with a 150 W halogen lamp, $\lambda > 390 \text{ nm}$, power $\approx 2 \text{ kW m}^{-2}$, see Section 2.4 for details) and electronic absorbance spectroscopy was used to monitor the oxidation state of MtrCAB. Use of this light source was chosen over single-wavelength light source(s) to mimic natural visible-light and avoid photosensitiser excitation bias by selecting one particular wavelength, Figure 2.8 A. Solutions of $\sim 0.5 \mu\text{M}$ MtrCAB after additions of $\sim 10 \mu\text{M}$ of one of the above photosensitisers displayed spectral features that were typical of fully oxidised MtrCAB, Figure 3.10 continuous black lines. Irradiation of these solutions resulted in the appearance of peaks with maxima at 523 nm and 552 nm, as well as a Soret shift to higher wavelengths, indicative of ferrous hemes formation, Figure 3.10 grey lines. The amplitude of these peaks arising from heme reduction increased over the course of the 90 min irradiations, Figure 3.10. Similar irradiation of MtrCAB in the absence of any of the above mentioned photosensitisers provided no indication of heme reduction, Figure 3.9. Thus it can be concluded that all eight photosensitisers are effective at visible-light-driven reduction of hemes within MtrCAB.

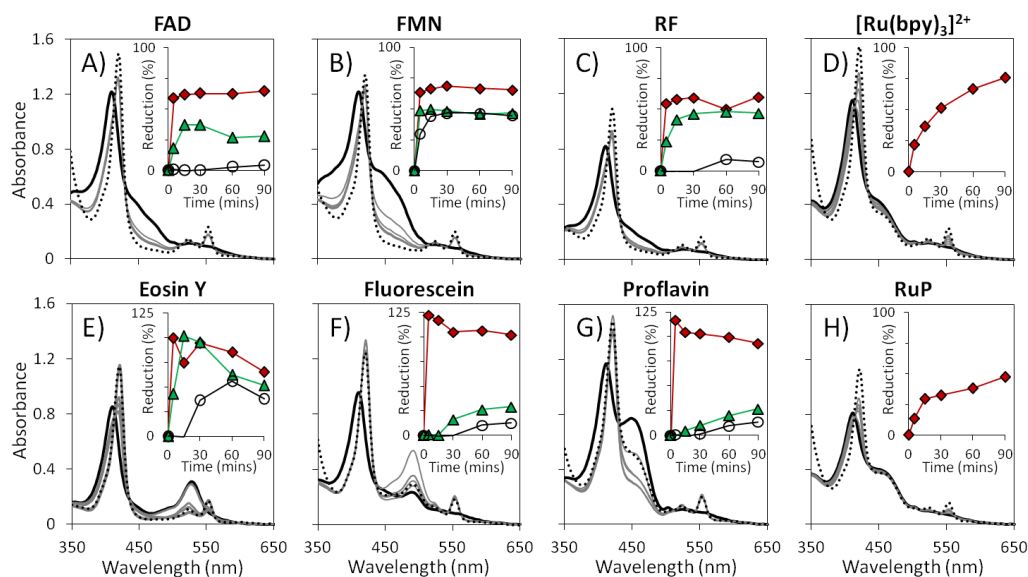


Figure 3.10. MtrCAB photoreduction is observed with all chosen photosensitisers.

A) $0.55 \mu\text{M}$ MtrCAB and $20 \mu\text{M}$ FAD. B) $0.45 \mu\text{M}$ MtrCAB and $40 \mu\text{M}$ FMN. C) $0.40 \mu\text{M}$ MtrCAB and $10 \mu\text{M}$ RF. D) $0.35 \mu\text{M}$ MtrCAB and $20 \mu\text{M}$ $[\text{Ru}(\text{bpy})_3]^{2+}$. E) $0.55 \mu\text{M}$ MtrCAB and $1 \mu\text{M}$ eosin Y. F) $0.45 \mu\text{M}$ MtrCAB and $1 \mu\text{M}$ fluorescein. G) $0.50 \mu\text{M}$ MtrCAB and $10 \mu\text{M}$ proflavin. H) $0.35 \mu\text{M}$ MtrCAB and $30 \mu\text{M}$ RuP. As prepared samples (continuous black lines) were irradiated for 5, 15, 30, 60 and 90 mins at 2 kW m^{-2} (grey lines) prior to addition of excess dithionite (dotted lines). Inserts show extent of MtrCAB reduction during Irradiation, monitored via 552 nm absorbance for all except eosin Y (420 nm), for MtrCAB:PS ratios of $\sim 1:20$ (red diamonds, $\sim 10 \mu\text{M}$ PS), $1:2$ (green triangles, $\sim 1 \mu\text{M}$ PS) and $1:0.2$ (open circles, $\sim 0.1 \mu\text{M}$ PS) with $\sim 0.5 \mu\text{M}$ MtrCAB. Stirred samples in anaerobic 50 mM HEPES, 2 mM CaCl_2 , 10 mM KCl, 50 mM TEOA, pH 7 in presence of $\sim 0.06 \%$ Triton X-100 at 20°C . Path length 1 cm.

At the approximate MtrCAB:PS ratio of 1:20 where photosensitisers are in excess over MtrCAB, most of the photosensitisers' spectral features overlapped significantly with the Soret peak of MtrCAB, with the exception of eosin Y. However, there were negligible changes to the α/β -region, again with exception of eosin Y. Eosin Y possesses an absorbance peak at 520 nm which significantly overlaps with the α/β -region of a heme spectrum but has less spectral impact on the Soret peak, Figure 3.10 E. By adding an excess of dithionite after 90 mins irradiation, the extents of heme photoreduction could be calculated and followed by the 552 nm peak for all photosensitisers aside from eosin Y which was monitored at 420 nm, Figure 3.10 inserts. Inspection of the spectral changes during irradiation confirmed they were dominated by contributions from MtrCAB photoreduction with minimal photosensitiser contributions.

Further experiments were performed with approximate MtrCAB:PS ratios of 1:2 and 1:0.2, Figure 3.10 inserts. Detailed inspection of data with flavins showed that after 5 mins irradiation the flavin spectral features had decreased, in accordance with the production of fully reduced flavin species, and mostly heme spectral contributions remained.^[142] There were no further detectable changes to the MtrCAB spectra during the remaining 90 mins irradiation at all of the MtrCAB:flavin ratios except the catalytic ratio of 1:0.2, where FAD and RF caused very little MtrCAB reduction. Variable extents of MtrCAB reduction were produced with different MtrCAB:flavin ratios.

Inspection of the xanthenes and proflavin experiments showed that after 15 mins irradiation for the MtrCAB:PS ratio of 1:20, MtrCAB had become fully photoreduced. No further detectable changes occurred to the MtrCAB spectra during the remaining 90 mins for fluorescein and proflavin, but eosin Y timecourse data shows the Soret peak began to decrease after 15 mins in accordance with heme reoxidation. Heme reoxidation would generally only be expected when samples were introduced to air or an oxidant, or gradually after irradiation was stopped. It was also notable that catalytic photosensitiser concentrations caused minimal heme reduction over 90 mins irradiation, even though they are meant to effectively carry out catalytic photoreduction. Closer inspection of photosensitiser spectral peaks showed photobleaching occurred during irradiation. This was most striking for eosin Y where the 90 min irradiated spectrum only exhibits heme spectral contributions, Figure 3.10 E. These observations suggest that photosensitiser photodegradation reactions dominate over the desired photoreduction reaction under these strong visible-light irradiations, especially at lower photosensitiser concentrations. During

irradiation, sample condensation was also observed on the sides of the cuvettes suggesting sample temperature increased due to the high irradiation power.

When MtrCAB was irradiated in the presence of the ruthenium complexes, photoreduction gradually occurred over the course of 90 mins irradiation. During irradiation all spectral changes are associated with heme reduction with negligible changes in the ruthenium complex spectral features, confirming their high photochemical stability. Ruthenium complexes were only trialled in excess over protein as complete photoreduction was not observed under these conditions, Figure 3.10 D and H.

These experimental initial results illustrate that all eight chosen photosensitisers can photoreduce MtrCAB. However, the data indicated that experimental conditions needed to be carefully chosen to minimise sample heating, photodegradation and photobleaching during irradiation and identify conditions in which reproducible and catalytic photoreductions could successfully occur. These conditions were established using the experiments described below.

3.4 Optimising Conditions for Photoreduction Studies

In experiments to explore optimal conditions for photoreductions it was decided to use MtrC as the terminal electron acceptor instead of MtrCAB to see if there was any obvious difference that was caused by Triton X-100 that is required to solubilise MtrCAB.

To explore why variable extents of MtrCAB photoreduction were observed by different MtrCAB:flavin ratios, it was decided to trial MtrC photoreduction at varying ratios of MtrC:flavin when the MtrC concentration was constant and then when the flavin concentration was kept constant. FMN was chosen as the flavin representative to perform these reactions, as described in Section 3.4.1.

Initial photoreduction experiments showed eosin Y was a promising but problematic photosensitiser as: i) fast, full reduction of the MtrCAB hemes was followed by their slow reoxidation during irradiation; ii) eosin Y was unable to perform catalytic photoreduction; and iii) eosin Y suffered from photobleaching the most out of all photosensitisers. To explore if these observations were caused by intense visible-light irradiations, and in turn if photodegradation dominated photoreduction, it was decided to trial eosin Y photoreduction of MtrC at a fixed MtrC:eosin Y ratio with varying lamp powers, as described in Section 3.4.2.

3.4.1 Optimisation of Protein:Photosensitiser Ratios via FMN Photoreduction of MtrC

Solutions of $\sim 0.5 \mu\text{M}$ MtrC were prepared to contain approximate MtrC:FMN ratios spanning from 1:2000 to 1:0.2 in the presence of excess TEOA. These samples were then irradiated with visible light at a power of 1 kW m^{-2} over 90 mins with spectra collected periodically, Figure 3.11. Prior to FMN additions all spectra were typical of fully oxidised MtrC and there were negligible changes to the 552 nm peak upon all FMN additions, Figure 3.11 continuous black lines. The only exception to this is the ratio of 1:2000 where the high flavin concentration causes the 552 nm peak to sit on the shoulder of the flavin absorbance feature at 445 nm. Extent of MtrC photoreduction was monitored via 552 nm absorbance at all ratios, Figure 3.11 E.

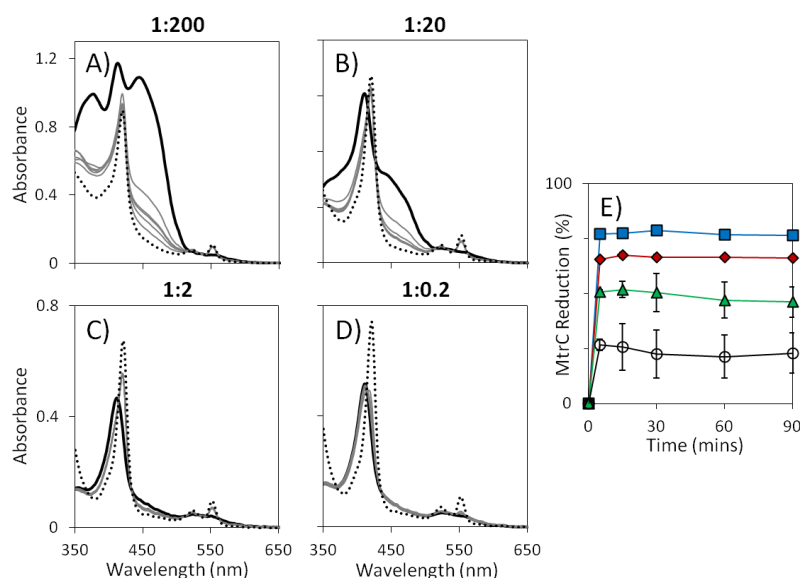


Figure 3.11. Maximum extent of MtrC photoreduction depends on FMN concentration.

$0.5 \pm 0.05 \mu\text{M}$ MtrC with $100 \mu\text{M}$ (A), $10 \mu\text{M}$ (B), $1 \mu\text{M}$ (C), and $0.1 \mu\text{M}$ FMN (D). As prepared samples (continuous black lines) were irradiated for 5, 15, 30, 60 and 90 mins at 1 kW m^{-2} (grey lines) prior to addition of excess dithionite (dotted lines). E) Extent of MtrC reduction during irradiation, monitored via 552 nm absorbance, for MtrC:FMN ratios of approximately 1:200 (blue squares, $100 \mu\text{M}$ FMN), 1:20 (red diamonds, $10 \mu\text{M}$ FMN), 1:2 (green triangles, $1 \mu\text{M}$ FMN) and 1:0.2 (open circles, $0.1 \mu\text{M}$ FMN), with $\sim 0.5 \mu\text{M}$ MtrC. Extent of reduction; and max and min observed values; represent the average of two independent, stirred experiments performed in anaerobic 50 mM HEPES, 2 mM CaCl_2 , 10 mM KCl, 50 mM TEOA, pH 7 at 20°C . Path length 1 cm .

After 5 mins irradiation, the FMN spectral features mostly disappeared due to the formation of fully reduced FMN and the maximum extent of photoreduction by each of these ratios was achieved with no further detectable increases in the 552 nm peak during the remainder of the irradiation, Figure 3.11 E. After irradiation an excess of dithionite was

added to all samples to completely reduce MtrC, Figure 3.11 dotted lines. Inspection of the spectral changes confirmed that the absorbance changes at 552 nm were dominated by contributions from MtrC photoreduction with minimal FMN spectral interference with all ratios of MtrC:FMN, except 1:2000. At the latter ratio the highly intense 445 nm spectral feature of 1000 μM FMN, which constantly decreased during the course of irradiation, interfered too much with the absorbance at 552 nm. This MtrC:FMN ratio resulted in unreliable quantisation of extents of reduction and ultimately it was decided to not include a 1:2000 ratio of any protein:PS combination in any future part of this study.

Figure 3.11 E shows the maximum extent of MtrC photoreduction is dependent upon the initial FMN concentration, with the largest extent of reduction ($77 \pm 1\%$) being achieved by the MtrC:FMN ratio of 1:200. Experiments carried out with catalytic and near stoichiometric FMN concentrations caused lesser extents of photoreduction and had greater associated errors, $48 \pm 10\%$ and $22 \pm 11\%$ respectively. This observation of irreproducibility between experiments at lower initial FMN concentrations suggested that the variable extents of protein photoreduction seen at different protein:flavin ratios may be due to different levels of flavin photodegradation. The behaviour noted here confirmed that observed in previous study with MtrCAB, Figure 3.10.

Similar experiments to those described above were performed with 5 and 36 μM MtrC in the presence of 10 μM FMN, Figure 3.12. This fixed 10 μM concentration of FMN was chosen as it was the lowest FMN concentration that achieved an extent of reduction with a small associated error ($66 \pm 1\%$) in the previous set of experiments.

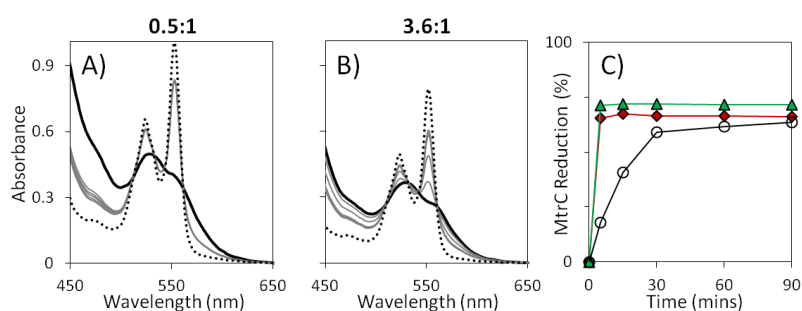


Figure 3.12. Maximum possible MtrC photoreduction is independent of MtrC:FMN ratio.

A) 5 μM MtrC and 10 μM FMN, stirred in a 1 cm cuvette. B) 36 μM MtrC and 10 μM FMN, unstirred in a 1 mm cuvette. As prepared samples (continuous black lines), were irradiated for 5, 15, 30, 60 and 90 mins at 1 kW m^{-2} (grey lines) prior to addition of excess dithionite (dotted lines). C) Extent of MtrC reduction during irradiation, monitored via 552 nm absorbance, for MtrC:FMN ratios of 0.05:1 (red diamonds, 0.5 μM MtrC), 0.5:1 (green triangles, 5 μM MtrC) and 3.6:1 (open circles, 36 μM MtrC), with 10 μM FMN. Experiments performed in anaerobic 50 mM HEPES, 2 mM CaCl_2 , 10 mM KCl, 50 mM TEOA, pH 7 at 20 $^\circ\text{C}$.

Prior to and following FMN additions spectra in the α/β -region were typical of fully oxidised MtrC, Figure 3.12 continuous black lines. Due to the high MtrC concentrations used here the Soret region of the heme spectra swamped any FMN spectral contributions and was above the detection limit of the spectrometer; therefore it has not been mentioned any further in this discussion. Furthermore the highest MtrC concentration required the use of an unstirred, 1 mm pathlength cuvette to resolve the α/β -region. The 552 nm absorbance feature was used to follow photoreduction of MtrC, Figure 3.12 C.

With the stirred solution of 5 μM MtrC with 10 μM FMN (1 cm pathlength), the maximum extent of MtrC photoreduction was achieved after 5 mins irradiation with no further detectable changes in the heme spectra during the remaining 90 mins of irradiation. The 552 nm absorbance of the unstirred solution of 36 μM MtrC with 10 μM FMN continuously increased during the 90 mins irradiation, quickly at first but then slowly over the final hour of irradiation. Even though the final extent of photoreduction can be compared, timecourses cannot be directly compared to that of other experiments as this reaction could not be stirred.

Figure 3.12 C compares timecourses of MtrC photoreductions performed in the presence of 10 μM FMN, and highlights similar final extents of reduction were achieved across the different MtrC:FMN ratios. The maximum extents of photoreduction achieved when FMN was in catalytic and near stoichiometric amounts to MtrC, $63 \pm 1 \%$ and $72 \pm 1 \%$ respectively, were similar to the $66 \pm 1 \%$ reduction that was achieved with excess FMN. Maximum extents of MtrC photoreduction at different ratios of MtrC:FMN, prepared using different concentrations of MtrC and FMN are compared in Figure 3.13.

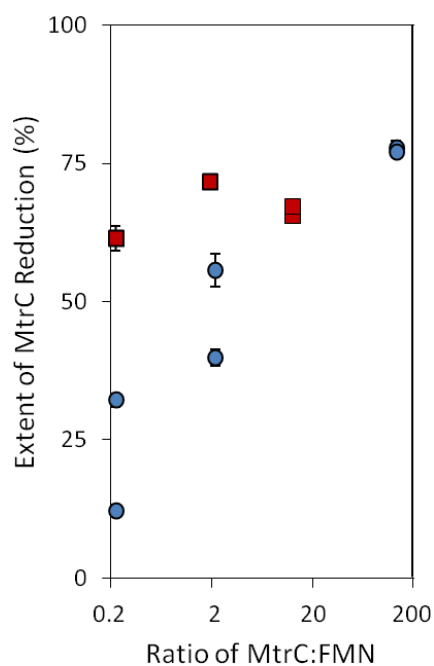


Figure 3.13. Extent of MtrC photoreduction versus ratio of MtrC:FMN.

Blue circles represent the extent of $\sim 0.5 \mu\text{M}$ MtrC photoreduction achieved using varying FMN concentrations, as shown in Figure 3.11. Red squares represent the extent of MtrC photoreduction achieved by $10 \mu\text{M}$ FMN, as shown in Figure 3.12. Extent of reduction; and max and min observed values; are based upon an average of three readings taken at 30, 60 and 90 mins for each experiment.

This summary highlights that when different MtrC:FMN ratios were prepared using an initial FMN concentration equal to or greater than $10 \mu\text{M}$, the maximum extent of MtrC photoreduction achieved was greater than 60 % in all cases. Deviations from this maximum percentage of MtrC photoreduction by FMN were only seen when the initial FMN concentration was less than $10 \mu\text{M}$. Although fast initial MtrC photoreductions were obtained by FMN concentrations below $10 \mu\text{M}$, Figure 3.11, flavin photodegradation reactions subsequently caused these photoreductions to fall short of their maximum possible extents of reduction.

Because flavin photodegradation is more favourable than flavin photoreduction when low initial FMN concentrations are used, it was decided to use only initial photosensitiser concentrations of $10 \mu\text{M}$ or greater in further work. As a consequence, protein concentrations were varied in order to obtain near stoichiometric and catalytic concentration of photosensitiser in relation to that of protein. These considerations should help to ensure protein photoreduction dominates over any photosensitiser photodegradation reactions occurring during irradiation.

3.4.2 Optimisation of Lamp Power via Eosin Y Photoreduction of MtrC

To investigate optimal lamp powers for photoreduction experiments, solutions containing $\sim 0.5 \mu\text{M}$ MtrC and $1 \mu\text{M}$ eosin Y, in the presence of excess TEOA, were prepared. These were then exposed for 90 mins to visible light with a power of 1, 0.5, 0.4 or 0.1 kW m^{-2} , before an excess of dithionite was added to obtain fully reduced samples, Figure 3.14.

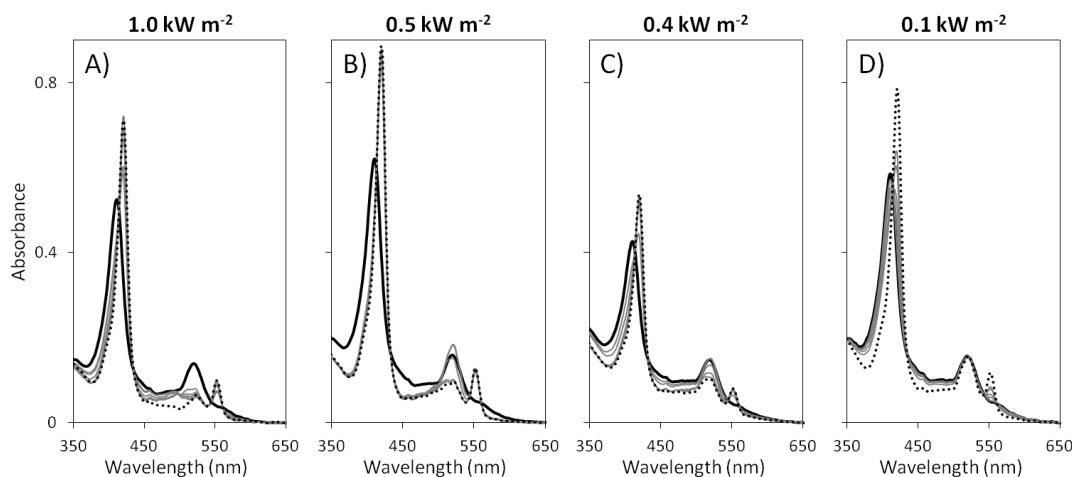


Figure 3.14. MtrC photoreduction by eosin Y at different lamp powers.

Samples of $\sim 0.5 \mu\text{M}$ MtrC and $1 \mu\text{M}$ eosin Y (continuous black lines) irradiated at 1 kW m^{-2} (A), 0.5 kW m^{-2} (B), 0.4 kW m^{-2} (C) or 0.1 kW m^{-2} (D) with spectra recorded at 5, 15, 30, 60 and 90 mins (grey lines) prior to addition of excess dithionite (dotted lines). Stirred in anaerobic 50 mM HEPES, 2 mM CaCl_2 , 10 mM KCl, 50 mM TEOA, pH 7 at 20°C . Path length 1 cm.

An eosin Y concentration of $1 \mu\text{M}$ was chosen for these experiments as this concentration had minimal spectral overlap with α/β -region of MtrC and allowed the 552 nm peak to be used to monitor the oxidation state of MtrC during the course of irradiation, Figure 3.15 A. The eosin Y absorbance peak at 520 nm was also monitored during irradiations and compared with the absorbance prior to irradiation to assess the extent of eosin Y photobleaching, Figure 3.15 B. Inspection of the spectral changes confirmed that the absorbance changes at 520 and 552 nm were dominated by contributions from eosin Y photobleaching and photoreduction of MtrC, respectively.

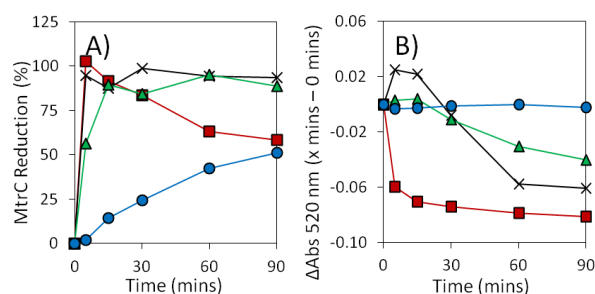


Figure 3.15. Affect of lamp power on MtrC photoreduction and eosin Y photobleaching.

A) Extent of MtrC reduction during irradiation with different lamp powers, monitored via 552 nm absorbance. B) Eosin Y photobleaching, determined by differences between absorbances at 520 nm at x mins and 0 mins irradiation, at different lamp powers. This comparison is representative of samples of $\sim 0.5 \mu\text{M}$ MtrC and $1 \mu\text{M}$ eosin Y irradiated with 1 kW m^{-2} (red squares), 0.5 kW m^{-2} (crosses), 0.4 kW m^{-2} (green triangles) or 0.1 kW m^{-2} (blue circles), as shown in Figure 3.14.

When irradiated at the highest power of 1 kW m^{-2} , MtrC was fully photoreduced and the eosin Y absorbance peak had mostly become photobleached after 5 mins irradiation. Further irradiation resulted in heme reoxidation associated with decrease in absorbance at the 552 nm and the loss of the remaining eosin Y spectral feature, Figures 3.14 A and 3.15 red squares. This MtrC heme reoxidation could possibly be explained by the loss of a reducing environment provided by eosin Y, or by the generation of photodegradation products acting as oxidising agents.

Figures 3.14 B and 3.15 crosses, and Figures 3.14 C and 3.15 green triangles respectively show that irradiation at 0.5 and 0.4 kW m^{-2} were both able to fully reduce MtrC within 15 mins of irradiation, as evidenced by an absorbance increase at 520 nm due to the appearance of the sharp reduced heme peak at 523 nm. The onset of eosin Y photobleaching occurred in both cases after 15 mins. The rate of photobleaching was however much greater for 0.5 kW m^{-2} irradiation where the eosin Y spectral feature was completely lost within 60 mins irradiation. The eosin Y absorbance feature decreased over the remainder of the course of the 0.4 kW m^{-2} irradiation but the dithionite spectra still contained some contributions from eosin Y, Figure 3.14 C dotted line. In comparison using a light power of 0.1 kW m^{-2} caused a slow, steady photoreduction of MtrC, achieving $\sim 50\%$ reduction after 90 mins irradiation, and produced no detectable photobleaching of eosin Y, Figure 3.14 D and 3.15 blue circles.

The temperatures of these solutions were also recorded before and after irradiation with the different lamp powers. In the case of 1 kW m^{-2} , condensation and a temperature change of $5 \text{ }^\circ\text{C}$ was seen during 90 mins irradiation. For other lamp powers, temperature changes were minimal ($< 1 \text{ }^\circ\text{C}$) and no condensation was observed.

These observations suggest rates of photoreduction initially exceed those of eosin Y photodegradation reactions, thus reduction of MtrC occurred prior to any photobleaching of eosin Y. It appears that once the electron acceptor of MtrC had been fully utilised, photobleaching occurred as long-lived, high-energy electrons of photoexcited eosin Y were then more likely to be accepted by the conjugated ring system of eosin Y. The radicals formed would then cause photodegradation of eosin Y. This investigation into an optimal experimental lamp power confirmed eosin Y photobleaching occurs at high lamp powers, even if protein photoreduction is initially more favourable. This investigation also highlighted that irradiation using a low lamp power caused minimal photobleaching but affected the rate of protein photoreduction. It was therefore decided that future photoreductions would be performed at a power of 0.4 kW m^{-2} . This power provided fast protein photoreduction alongside minimal temperature change and photosensitiser photobleaching, and associated photodegradation, during 90 mins visible-light irradiation.

3.4.3 Conditions Selected for Detailed Studies of Cytochrome Photoreduction

Experiments above used FMN and eosin Y, photosensitisers prone to photodamage, to establish conditions for photoreduction with minimal contribution from unwanted photodegradation reactions. These conditions were then used for side by side comparison of photoreduction by various combinations of photosensitisers and proteins.

Experiments were performed with anaerobic samples in a N_2 -filled chamber and irradiated by an external light source ($\lambda > 390 \text{ nm}$) at a power of 0.4 kW m^{-2} for 90 mins, or until photoreduction was complete. All samples contained 50 mM HEPES, 2 mM CaCl_2 , 10 mM KCl, 50 mM TEOA, pH 7. This ensured minimal photodamage and temperature change, in a well buffered system with an excess of SED. MtrCAB photoreductions were performed with Triton X-100 present to ensure this membrane protein remains soluble.

Cytochrome photoreductions were performed across a range of heme:PS ratios spanning from 1:20 (5 μM heme: 100 μM PS) to $\sim 1:0.02$ ($\sim 500 \mu\text{M}$ heme: 10 μM PS). In exception to this, photoreductions by ruthenium complexes were only carried out in excess (1:20) because complete photoreduction was not observed when using a higher lamp power, Figure 3.10 D and H. For heme:PS ratios between 1:2 to $\sim 1:0.02$, solutions of 10 μM PS with different protein concentrations were prepared. To give comparable data, protein concentrations were checked prior to photosensitiser additions, which were also

checked, using electronic absorbance spectroscopy. Due to high optical densities and quantities of proteins required, catalytic cytochrome photoreduction (~ 1:0.02) required the use of a 1 mm pathlength cuvette to monitor heme oxidation state. Due to the inability to stir in such a cuvette, it was decided that these reactions were only performed once to confirm that the photosensitisers could perform catalytic photoreductions of cytochromes. All other photoreductions were performed in duplicate, whilst being stirred in 1 cm pathlength cuvettes.

3.5 Visible-Light-Driven Reduction of MtrC

Photoreduction of MtrC by all photosensitisers under the conditions described above is presented by photosensitiser groups within the following sections. This is followed by a comparison of the photoreduction behaviours in Section 3.5.4.

3.5.1 Flavins

Irradiations of MtrC in the presence of FMN were performed using MtrC:FMN ratios spanning from 1:200 to ~ 1:0.33, with MtrC concentration of 0.5, 5, or 32 μM as appropriate, Figure 3.16. There were negligible spectral changes in the α/β -region upon addition of FMN to the solutions of MtrC, except when 100 μM FMN was added to a solution of 0.5 μM MtrC, Figure 3.16 A. With FMN in such excess, MtrC was prone to ambient light photoreduction prior to irradiation which consequently prevented quantitative analysis of MtrC photoreduction, Figure 3.16 A. Nevertheless irradiation of all MtrC:FMN ratios resulted in the red shift of the Soret peak and the appearance of peaks with maxima at 523 and 552 nm in accordance with the formation of ferrous hemes. Thus, FMN was confirmed as effective at driving visible light reduction of MtrC under these conditions. Inspection of the spectral changes confirmed the absorbance changes at 552 nm were dominated by contributions from MtrC photoreduction and with minimal FMN spectral changes. The spectral features of oxidised FMN decreased during the irradiations in accordance with the formation of fully reduced FMN.

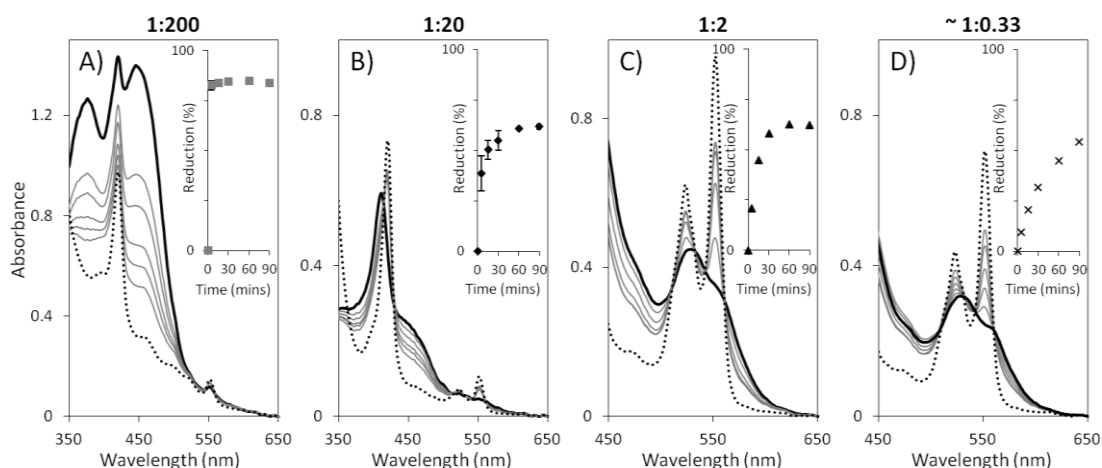


Figure 3.16. MtrC photoreduction with FMN at MtrC:FMN ratios of 1:200 (A), 1:20 (B), 1:2 (C) and ~ 1:0.33 (D).

A) 0.5 μM MtrC and 100 μM FMN. B) 0.5 μM MtrC and 10 μM FMN. C) 5 μM MtrC and 10 μM FMN. D) 32 μM MtrC and 10 μM FMN, unstirred in a 1 mm cuvette (Soret region absorbance above detection limit). As prepared samples (continuous black lines) were irradiated for 5, 15, 30, 60 and 90 mins at 0.4 kW m^{-2} (grey lines) prior to addition of excess of dithionite (dotted lines). Inserts show extent of MtrC reduction during irradiation, monitored via 552 nm absorbance. For experiments containing 0.5 μM MtrC extent of reduction; and max and min observed values; represent average of two independent experiments. Grey symbols show biased extents of reductions - see text for details. Samples in anaerobic 50 mM HEPES, 2 mM CaCl_2 , 10 mM KCl, 50 mM TEOA, pH 7 at 20 $^\circ\text{C}$.

For MtrC:FMN ratios of 1:20 and 1:2 the maximum extent of photoreduction was achieved after 30 mins irradiation, with no further detectable increases in the 552 nm peak after this. Irradiation of the catalytic ratio of ~ 1:0.33 tended towards, but did not reach, a plateau during 90 mins irradiation, Figure 3.16 D. The extent of photoreduction achieved was independent of whether FMN was present in excess or in sub-stoichiometric amounts with respect to MtrC, with an average photoreduction extent of $61 \pm 3 \%$ being observed. It is notable that the extents of photoreduction achieved under these irradiation conditions were similar to those achieved when a lamp power of 1 kW m^{-2} was used, as discussed in Section 3.4.1. Very similar results were obtained in parallel experiments performed with FAD or RF in place of FMN, Appendix 1 and 2 respectively. Identical analysis showed extents of photoreduction achieved by FAD and RF were independent to the ratio of MtrC:flavin used, $62 \pm 3 \%$ and $60 \pm 6 \%$ respectively.

3.5.2 Eosin Y, Fluorescein and Proflavin

Irradiations of MtrC in the presence of eosin Y were performed using MtrC:eosin Y ratios spanning from 1:200 to 1:0.5, with MtrC concentration of 0.5 or 26 μM as appropriate, Figure 3.17. With eosin Y in high excess, MtrC was prone to ambient light photoreduction

prior to irradiation which consequently prevented confident quantitative analysis of MtrC photoreduction, Figure 3.17 A. Nevertheless irradiation of all MtrC:eosin Y ratios resulted in the red shift of the Soret peak and the appearance of a peak with maxima at 552 nm, confirming that eosin Y was effective at reducing MtrC with visible light under these experimental conditions. Inspection of the spectral changes confirmed the absorbance changes at 420 nm, or 552 nm (1:0.5), were dominated by contributions from MtrC photoreduction, with minimal eosin Y spectral changes.

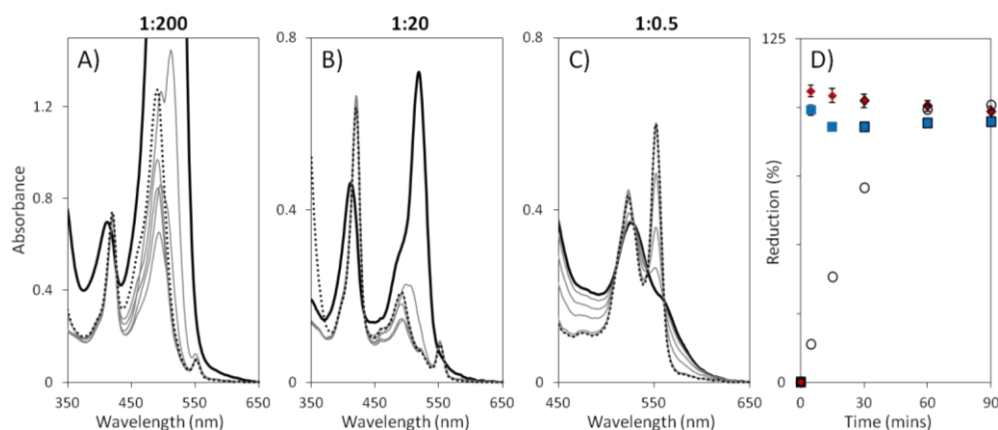


Figure 3.17. MtrC photoreduction with eosin Y at MtrC:eosin Y ratios of 1:200 (A), 1:20 (B) and 1:0.5 (C).

A) 0.5 μM MtrC and 100 μM eosin Y. B) 0.5 μM MtrC and 10 μM eosin Y. C) 26 μM MtrC and 14 μM eosin Y, unstirred within a 1 mm cuvette (Soret region absorbance above detection limit). As prepared samples (continuous black lines) were irradiated for 5, 15, 30, 60 and 90 mins at 0.4 kW m^{-2} (grey lines) prior to addition of excess of dithionite (dotted lines). D) Extent of MtrC reduction during irradiation, monitored via 420 nm absorbance for all except 1:0.5 (552 nm), for MtrC:eosin Y ratios of 1:200 (blue squares, 0.5 μM MtrC), 1:20 (red diamonds, 0.5 μM MtrC) and 1:0.5 (open circles, 26 μM MtrC). For experiments containing 0.5 μM MtrC extent of reduction; and max and min observed values; represent the average of two independent experiments. Stirred samples in anaerobic 50 mM HEPES, 2 mM CaCl_2 , 10 mM KCl, 50 mM TEOA, pH 7 at 20 $^\circ\text{C}$.

Complete and rapid photoreductions of MtrC were induced by eosin Y during these experiments independent of whether eosin Y was present in excess or in catalytic amounts with respect to MtrC. It is key to note that even though photobleaching and photodamage of eosin Y were observed during these irradiations, reoxidation of MtrC hemes was not observed. Complete and catalytic photoreductions of MtrC were observed in similar experiments performed with fluorescein or proflavin in place of eosin Y, as shown in Appendix 3 and 4 respectively. Identical analysis showed fluorescein or proflavin also produced essentially 100 % photoreductions irrespective to the MtrC:PS ratio used. It is also notable that photobleaching of fluorescein and proflavin were observed during these irradiations; however, these spectral decreases were not as striking as those of eosin Y and none caused heme reoxidation.

3.5.3 Ruthenium Complexes

Irradiations of MtrC in the presence of ruthenium complexes were performed using an excess of ruthenium complex to give a MtrC:PS ratio of $\sim 1:200$, Figure 3.18. The absorbance in the α/β -region increased upon addition of either $\sim 100 \mu\text{M}$ $[\text{Ru}(\text{bpy})_3]^{2+}$ or RuP to a solution of $0.5 \mu\text{M}$ MtrC due the spectral features associated with these photosensitisers. Formation of ferrous MtrC occurred slowly over the course of 5 hrs irradiations. All spectral changes were associated with heme redox transformations with no changes in the spectral features of the ruthenium complexes.

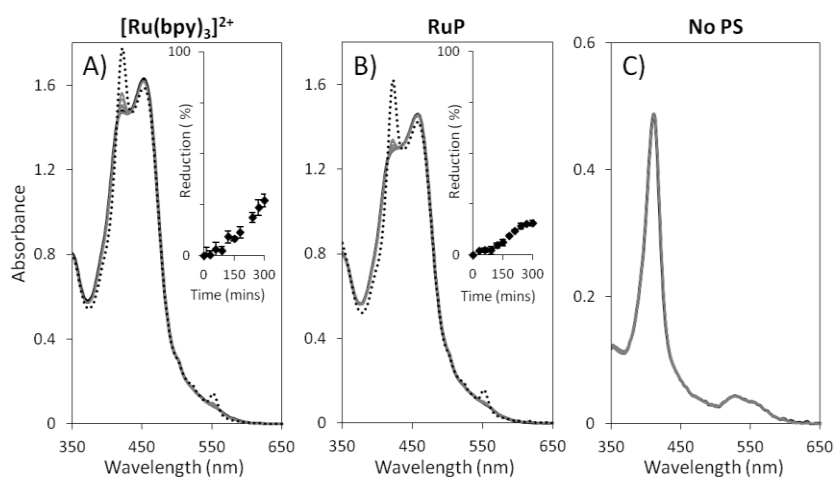


Figure 3.18. Irradiation of MtrC in the presence of $[\text{Ru}(\text{bpy})_3]^{2+}$ (A), RuP (B) and absence of photosensitisers (C).

$0.5 \mu\text{M}$ MtrC with either $110 \mu\text{M}$ $[\text{Ru}(\text{bpy})_3]^{2+}$ (A), $140 \mu\text{M}$ RuP (B) or no photosensitiser (PS) (C). As prepared samples (continuous black lines) were irradiated for 5, 15, 30 mins and every subsequent 30 mins for the remainder of 5 hrs at 0.4 kW m^{-2} (grey lines) prior to addition of excess of dithionite (dotted lines). Inserts show extent of MtrC reduction during irradiation, monitored via 552 nm absorbance. Extent of reduction; and max and min observed values; represent the average of two independent experiments. Stirred samples in anaerobic 50 mM HEPES, 2 mM CaCl_2 , 10 mM KCl, 50 mM TEOA, pH 7 at 20°C . Path length 1 cm .

After 5 hrs of irradiation, $[\text{Ru}(\text{bpy})_3]^{2+}$ was able to achieve $27 \pm 3 \%$ photoreduction of MtrC, whereas RuP was able to photoreduce $15 \pm 1 \%$ of MtrC. Neither of these photoreductions plateaued during the 5 hr irradiations or upon any further irradiation.

To confirm that these slow gradual photoreductions were caused by the presence of the ruthenium photosensitisers and were not due to self photoreduction of MtrC, irradiations of $0.5 \mu\text{M}$ MtrC were performed, Figure 3.18 C. In the absence of any photosensitisers there was no change to the MtrC spectrum during 5 hrs irradiation, and thus no indication of heme reduction. This confirms that the ruthenium complexes are able to perform slow, reproducible photoreductions of MtrC under these conditions.

3.5.4 Summary of Visible-Light-Driven Reduction of MtrC

Detailed photoreductions of MtrC were performed to initialise exploration into the visible-light-driven photoreductions of *S. oneidensis* MR-1 outer membrane cytochromes. These experiments produced successful, reproducible photoreductions of MtrC by all eight photosensitisers using the photoreduction conditions selected from experiments described in Section 3.4.3. Using these conditions catalytic photoreductions of MtrC were obtained from all organic photosensitisers.

The extents of MtrC photoreduction that were achieved from these photosensitisers, as summarised in Table 3.4, can be explained by comparing their (photo)reduction potentials to those of the protein and SED, Figure 3.19. The redox chemistry of MtrC has been resolved by protein film cyclic voltammetry and potentiometric titrations monitored by the electronic absorbance spectra of the hemes.^[83, 153, 154] MtrC hemes display reduction potentials that are reasonably well distributed across a broad, electrochemical potential window spanning ~ 500 mV, from +50 to -450 mV vs SHE at pH 7.^[83, 153, 154] Neither technique was able to resolve the contribution from individual heme reduction potentials as this broad potential range of MtrC is indicative of multiple reversible redox centers with overlapping redox potentials. Comparison of the relevant photosensitiser (photo)reduction potentials with the reduction potential window of MtrC show all eight photosensitisers are thermodynamically able to carry out heme photoreduction, Figure 3.19.

Photosensitiser	Extent of MtrC Reduction (%)
RF	60 ± 6
FMN^[a]	61 ± 3
FAD	62 ± 3
Fluorescein	100 ± 2
Proflavin	100 ± 2
Eosin Y	100 ± 2
[Ru(bpy)₃]²⁺[a]	N.D.
RuP^[a]	N.D.
No Photosensitiser	N.D.

Table 3.4. Extent of 0.5 μM MtrC photoreduction achieved with photosensitisers at 90 mins irradiation.

Values represent the average of at least two independent experiments performed in anaerobic 50 mM HEPES, 2 mM CaCl₂, 10 mM KCl, 50 mM TEOA, pH 7 at 20 °C with 90 mins of irradiation at 0.4 kW m⁻². N.D. denotes where no photoreduction is detected after this time. ^[a] Results are obtained from experiments performed in the presence of 10 μM and 100 μM photosensitiser, except for FMN and ruthenium complexes where values are only obtained from experiments performed in the presence of 10 μM or 100 μM photosensitiser, respectively. See text for details.

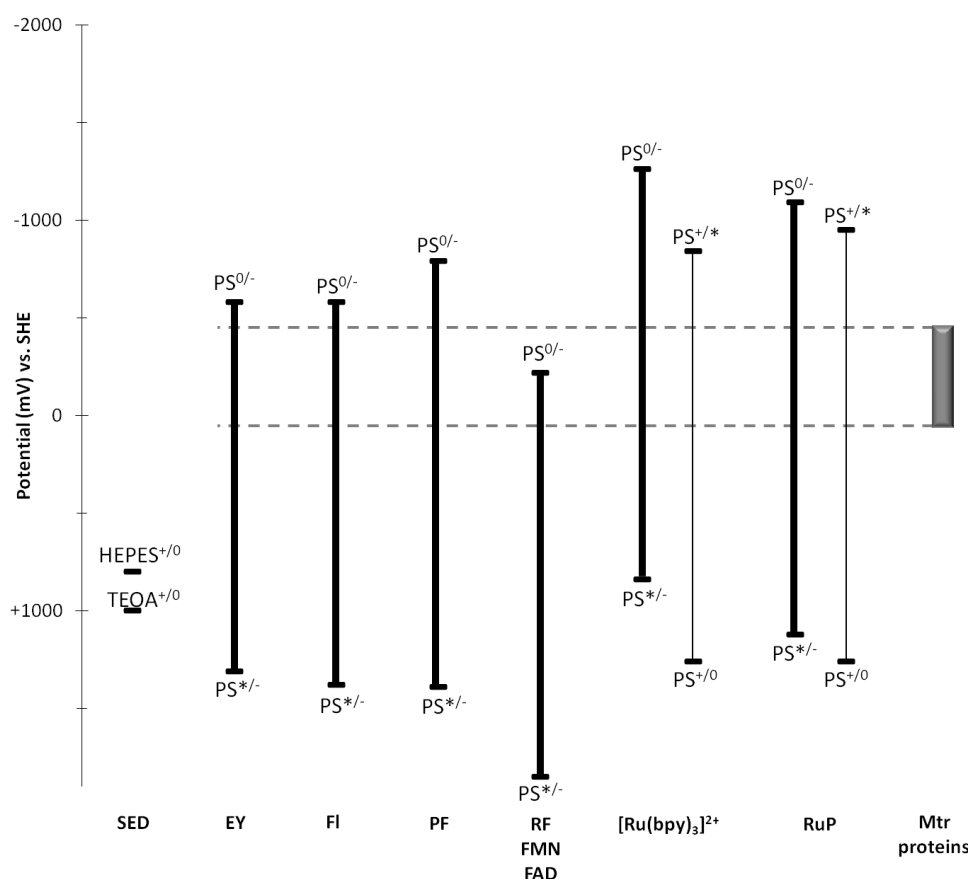


Figure 3.19 Overview of relevant (photo)reduction potentials for MtrC photoreduction.

(Photo)reduction potentials relevant to photoreduction of MtrC by eosin Y (EY), fluorescein (FI), proflavin (PF), RF, FMN, FAD, $[\text{Ru}(\text{bpy})_3]^{2+}$, and RuP at pH 7. Thick vertical lines relate to processes of reductive quenching, where $\text{PS}^{*/-}$ relates to the potential at which PS^* accepts a sacrificial electron from HEPES and/or TEOA to form PS^- and $\text{PS}^{0/-}$ relates to the potential at which PS^- reduces the electron acceptor, MtrC. Thin vertical lines relates to processes of oxidative quenching, where $\text{PS}^{+/0}$ relates to the potential at which PS^+ accepts a sacrificial electron from HEPES and/or TEOA to form PS^0 and $\text{PS}^{+/*}$ relates to the potential at which PS^* reduces MtrC. Only reductive quenching of eosin Y and fluorescein are included as photoreduction operates by this mechanism alone, described in Section 3.7. Potentials relevant to oxidation of HEPES and TEOA are indicated, together with the window spanned by the reduction potentials of MtrC, OmCA and MtrCAB. See text for details.

As previously described in Section 3.2.2.3, flavin photoreductions proceed via the reductive quenching of the relevant triplet photoexcited state, and are thus driven by the flavin two-electron reduction couple of -220 mV .^[90, 140, 141] As this midpoint reduction potential is located within the broad redox potential window of MtrC, the observed flavin photoreduction extent of $\sim 60 \%$ can be understood, Table 3.4. As described in Sections 3.2.2.1 and 3.2.2.2, irrespective of the photoreduction mechanism undertaken by eosin Y, fluorescein or proflavin, these processes are driven by (photo)redox couples with reductive potentials below -780 mV .^[9, 129] Consequently these photosensitisers possess the thermodynamic driving force to provide the full photoreduction of MtrC that is observed during irradiations, Table 3.4.

Photoreduction by $[\text{Ru}(\text{bpy})_3]^{2+}$ and RuP can occur via reductive and oxidative quenching mechanisms, as described in Section 3.2.1. Irrespective of the mechanistic route, photoreductions by these photosensitisers are driven by processes with reductive potentials below -840 mV .^[112, 118–120] These photoreduction potentials are sufficient to provide thermodynamic driving forces for MtrC photoreduction on a par to those of eosin Y, fluorescein and proflavin. Consequently it is striking that neither of the ruthenium complexes were able to achieve greater than 30 % photoreduction of MtrC despite being in large excess and being irradiated for much longer times in comparison to the other photosensitisers. A comparison of the timecourses of MtrC photoreductions provided by all photosensitisers has been made in Figure 3.20.

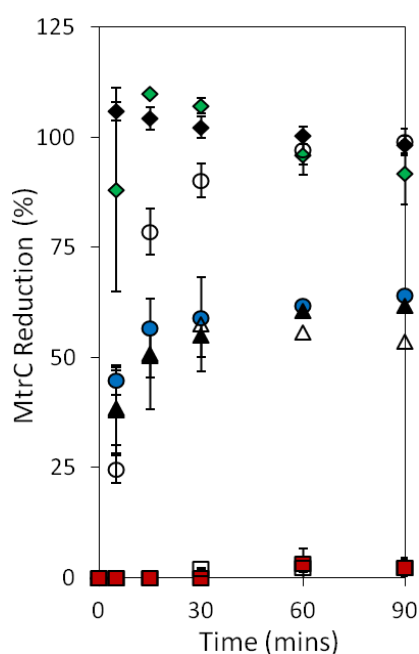


Figure 3.20. Timecourse of MtrC photoreduction as a function of photosensitiser identity.

Reduction of $0.5 \mu\text{M}$ MtrC over 90 mins irradiation at 0.4 kW m^{-2} with eosin Y (black diamonds), proflavin (green diamonds), fluorescein (open circles), FAD (blue circles), FMN (black triangles), or RF (open triangles) at MtrC:PS ratios of 1:20 ($10 \mu\text{M}$ PS), and with $[\text{Ru}(\text{bpy})_3]^{2+}$ (red squares) and RuP (open squares) both at MtrC:PS ratios greater than 1:200 (above $100 \mu\text{M}$ PS). Extent of reduction monitored via change in 552 nm absorbance for all except eosin Y (420 nm). Extent of reduction; and max and min observed values; represent the average of two independent experiments. Stirred, anaerobic samples in 50 mM HEPES, 2 mM CaCl_2 , 10 mM KCl, 50 mM TEOA, pH 7 at $20 \text{ }^\circ\text{C}$. Path length 1 cm.

The rate and success of any photoreduction is not only determined by thermodynamics, but also the competing rates of relevant electron transfer events and the relative stabilities of photosensitiser photoexcited, reduced and oxidised states, as described in Section 1.3.1.^[23, 121] Thus, the photoreduction of MtrC performed by the ruthenium complexes would be hindered if i) the lifetime of the triplet excited state was

very short, resulting in fast recombinations back to the ground state; ii) the rate of back electron transfer from successfully reduced MtrC to oxidised ruthenium complex was faster than that of the sacrificial electron donation of TEOA; or iii) the lifetime of the of the reduced or oxidised ruthenium complexes were relatively short lived. Despite this, it would be expected that 100 % MtrC photoreductions would be observed with the ruthenium complexes if irradiations were carried out for longer times, or at higher lamp powers. A detailed study into the kinetics associated with the mechanistic steps involved in these ruthenium photoreductions was beyond the scope of this study.

The timecourse profiles for flavin photoreductions of MtrC were similar, Figure 3.20. Rapid initial photoreductions in the first 5 mins irradiation was followed by slower approaches towards the maximum possible photoreduction. There is no evidence that the different ribityl chains interact with MtrC or have any impact on the photocatalytic cycles and kinetics behind the flavin photoreduction, which is not too surprising when it is the flavin moiety that is key to the (photo)electrochemistry.

Very rapid and complete photoreduction of MtrC was obtained within the first 5 mins of irradiations when eosin Y or proflavin was present, Figure 3.20. A slower photoreduction rate was observed with fluorescein, where full photoreduction of MtrC is obtained within 60 mins under these conditions. This is a striking contrast between the xanthenes, considering fluorescein possesses photoreduction potentials ($E_m = -1020$ and -980 mV) that are more favourable for photoreduction in comparison to those of eosin Y ($E_m = -820$ and -870 mV).^[9] It has been previously commented that fluorescein is less reactive than eosin Y due to the lack of halogen substituents which help to facilitate ISC and thus provide longer lived triplet excited states.^[23] This would result in faster, unproductive recombination of the triplet excited state being observed during irradiations when fluorescein was present in comparison to when eosin Y was present.

Results from photoreductions involving MtrC with the eight photosensitisers showed varying extents and rates could be achieved depending upon the identity of photosensitiser chosen. OmcA and MtrCAB photoreductions under equivalent conditions are discussed next. Comparisons between extents and rates of photoreduction observed for these *S. oneidensis* outer membrane cytochromes are made throughout.

3.6 Photoreduction of OmcA and MtrCAB and Comparison to MtrC

Visible-light-driven photoreductions of OmcA and MtrCAB were performed in an identical manner to those of MtrC, as described in Section 3.5. The only exceptions to this were the presence of Triton X-100 that was included to keep MtrCAB solubilised and, due to MtrCAB possessing twice the number of hemes of MtrC, solutions of MtrCAB were prepared with half the respective concentrations of OmcA and MtrC to give comparative heme concentrations. Upon irradiation of all samples the Soret peak red shifted and peaks appeared at 523 and 552 nm, indicative of ferrous heme formation. Thus, similarly to MtrC, all photosensitisers can provide visible-light-driven reductions of OmcA and MtrCAB under the chosen experimental conditions. Spectral analysis was as described for MtrC (Section 3.5) to take account of spectral contributions from photosensitisers. Table 3.5 summarises of the extents of OmcA and MtrCAB photoreduction achieved by the eight photosensitisers after 90 mins irradiation under comparable conditions.

	Extent of Heme Reduction (%)		
	MtrC	OmcA	MtrCAB
RF	60 ± 6	63 ± 5	62 ± 6
FMN^[a]	61 ± 3	59 ± 4	58 ± 4
FAD	62 ± 3	66 ± 8	61 ± 4
Fluorescein	100 ± 2	100 ± 2	100 ± 2
Proflavin	100 ± 2	100 ± 2	100 ± 2
Eosin Y	100 ± 2	100 ± 2	100 ± 2
[Ru(bpy)₃]²⁺[a]	N.D.	14 ± 6	N.D.
RuP^[a]	N.D.	N.D.	N.D.
No Photosensitiser	N.D.	N.D.	3 ± 2

Table 3.5. Extent of 5 μ M heme photoreduction achieved with photosensitisers at 90 mins irradiation.

Values represent the average of at least two independent experiments performed in anaerobic 50 mM HEPES, 2 mM CaCl₂, 10 mM KCl, 50 mM TEOA, pH 7 at 20 °C with 90 mins of irradiation at 0.4 kW m⁻². Triton X-100, ~ 0.06 % (v/v), was included for MtrCAB samples. N.D. denotes where no photoreduction is detected after this time. ^[a] Results are obtained from experiments performed in the presence of 10 μ M and 100 μ M photosensitiser, except for FMN and ruthenium complexes where values are only obtained from experiments performed in the presence of 10 μ M or 100 μ M photosensitiser, respectively. See text for details.

OmcA and MtrCAB photoreduction by FMN, FAD or RF showed that the maximum extent of photoreduction was ~ 60 %, shown in Appendix 5, 6 and 7 respectively. The extent of OmcA or MtrCAB photoreduction achieved by all flavins was independent to the heme:flavin ratio used. Photoreductions of either OmcA or MtrCAB with eosin Y, proflavin or fluorescein achieved essentially 100 % photoreduction

independent on whether photosensitiser was present in excessive or sub-stoichiometric amounts in comparison to protein, Appendix 8, 9 and 10 respectively.

Irradiations of OmcA and MtrCAB in the presence of either $[\text{Ru}(\text{bpy})_3]^{2+}$ or RuP, at heme:PS ratios greater than 1:20, saw slow and gradual formations of ferrous heme over the course of 5 hrs, Figure 3.21. After 5 hrs of irradiation $[\text{Ru}(\text{bpy})_3]^{2+}$ was able to achieve $31 \pm 4\%$ OmcA photoreduction and $15 \pm 1\%$ MtrCAB photoreduction, whereas RuP was able to photoreduce $9 \pm 1\%$ of OmcA and $25 \pm 9\%$ of MtrCAB. None of these photoreductions plateaued during the 5 hr irradiations or upon any further irradiation, and only complete heme reduction occurred upon addition of excess dithionite. It would be expected that 100% cytochrome photoreduction would be achieved with the ruthenium complexes if irradiations were carried out for longer times, or at higher lamp powers. In agreement with this proposal, irradiations of MtrCAB in presence of these ruthenium complexes at higher lamp powers of 2 kW m^{-2} achieved greater than 40% photoreduction within 90 mins, Figure 3.10.

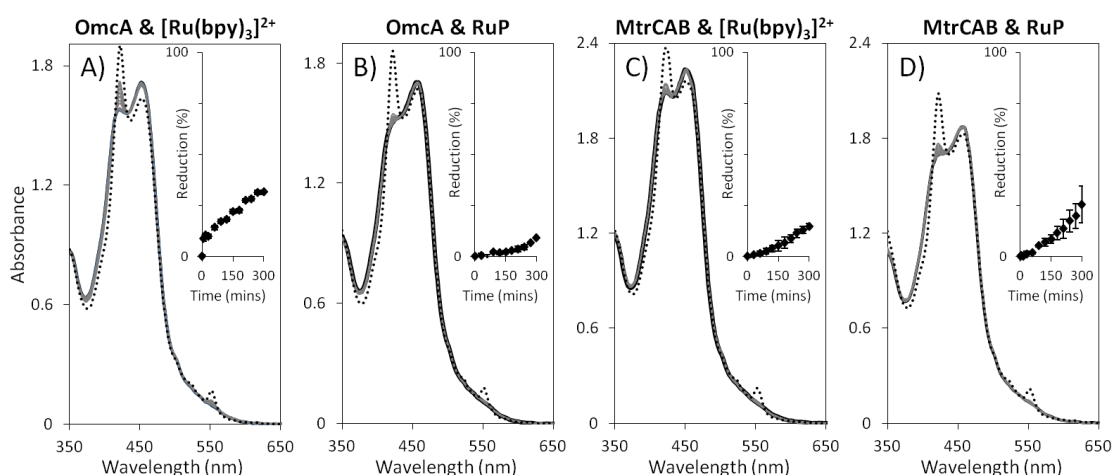


Figure 3.21. OmcA and MtrCAB photoreduction with ruthenium complexes at heme:PS ratios greater than 1:20.

A) $0.5 \mu\text{M}$ OmcA and $110 \mu\text{M}$ $[\text{Ru}(\text{bpy})_3]^{2+}$. B) $0.5 \mu\text{M}$ OmcA and $160 \mu\text{M}$ RuP. C) $0.25 \mu\text{M}$ MtrCAB and $150 \mu\text{M}$ $[\text{Ru}(\text{bpy})_3]^{2+}$. D) $0.25 \mu\text{M}$ MtrCAB and $180 \mu\text{M}$ RuP. As prepared samples (continuous black lines) were irradiated at 5, 15, 30 mins and every subsequent 30 mins for the remainder of 5 hrs at 0.4 kW m^{-2} (grey lines) prior to addition of excess of dithionite (dotted lines). Inserts show extent of heme reduction during irradiation, monitored via 552 nm absorbance. Extent of reduction; and max and min observed values; represent the average of two independent experiments. Stirred samples in anaerobic 50 mM HEPES, 2 mM CaCl_2 , 10 mM KCl, 50 mM TEOA, pH 7 at 20°C . $\sim 0.06\%$ Triton X-100 (v/v) was included for MtrCAB samples. Path length 1 cm.

OmcA and MtrCAB photoreductions occurred to similar extents as those of MtrC, Table 3.5. Protein film cyclic voltammetry and potentiometric titration experiments have shown that MtrCAB and OmcA both demonstrate similar envelopes of electrochemical

response to those of MtrC, where the hemes of these cytochromes are reversibly reduced and oxidised within +50 to -450 mV vs SHE at neutral pH.^[83, 154, 155] It is therefore not surprising that similar extents of photoreduction were observed, as the intrinsic thermodynamic driving forces behind the photoreductions does not drastically vary between these cytochromes.

A comparison of the timecourses of photoreduction by the organic photosensitisers is presented in Figure 3.22 for both OmcA (A) and MtrCAB (B). These comparisons highlight that flavin, eosin Y and proflavin at 10 μM can perform rapid complete OmcA and MtrCAB photoreductions of 5 μM heme. Fluorescein provided similar rapid complete MtrCAB photoreduction but OmcA photoreduction was slower, as similarly observed during MtrC photoreduction, Section 3.5.4 and Figure 3.20.

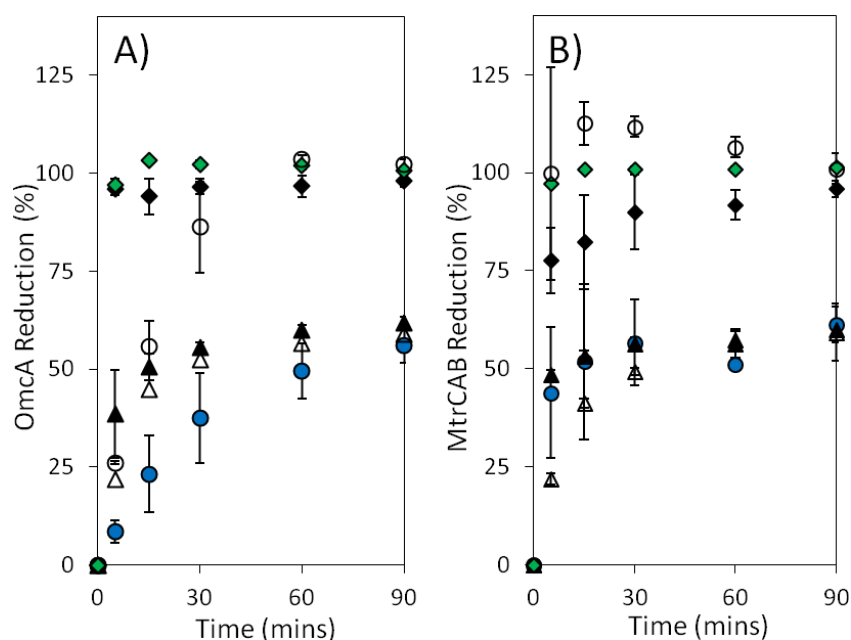


Figure 3.22. Timecourse of photoreduction for OmcA and MtrCAB as a function of photosensitiser identity.

Reduction of 0.5 μM OmcA (A) and 0.25 μM MtrCAB in $\sim 0.06\%$ (v/v) Triton X-100 (B) over 90 mins irradiation at 0.4 kW m^{-2} with eosin Y (black diamonds), proflavin (green diamonds), fluorescein (open circles), FAD (blue circles), FMN (black triangles), or RF (open triangles) at heme:PS ratios of 1:2 (10 μM PS). Extent of reduction monitored via change in 552 nm absorbance for all except eosin Y (420 nm). Extent of reduction; and max and min observed values; represent the average of two independent experiments. Stirred samples in anaerobic 50 mM HEPES, 2 mM CaCl_2 , 10 mM KCl, 50 mM TEOA, pH 7 at 20 $^\circ\text{C}$. Path length 1 cm.

The extents and rates of OmcA and MtrCAB photoreduction were dependent upon the identity of photosensitiser. Direct comparisons between the photoreduction rate for the three different cytochromes achieved by the same photosensitiser were performed but provided no definite insight into whether the cytochrome identity had an effect upon the

rate of photoreduction achieved. These comparisons were complicated by most photosensitisers being able to reach their maximum possible extent of cytochrome photoreduction before the first spectra was recorded when present in similar or excessive concentrations compared to that of the cytochrome. Transient absorbance spectroscopy measures changes in absorbance as a function of time after excitation by a flash of light. Rapid electron transfers in such systems have been studied by transient absorbance spectroscopy, and this technique might be able to reveal any effect cytochrome identity has upon the rate of photoreduction.^[121, 156] Comparisons between photoreductions performed here with the photosensitisers in catalytic amounts were also unreliable with respect to rate due to the lack of stirring under these conditions.

3.7 Identification of the Sacrificial Electron Donor(s) and Favourable Photoreduction Mechanisms

In addition to exploring and understanding the effects of photosensitiser and protein identity on photoreductions of *S. oneidensis* MR-1 outer membrane cytochromes it was of interest to identify the SED(s) operating in these experiments. As MtrCAB, MtrC and OmcA have very similar redox potential windows and photochemical behaviours, as shown in Section 3.6, it was decided to restrict these studies to just OmcA.

All photoreductions described above were performed in solutions of 50 mM TEOA, 50 mM HEPES, 2 mM CaCl₂, 10 mM KCl, pH 7 because TEOA is a well described SED and the remaining buffer components are those used in preparation of MV²⁺-containing MtrCAB (proteo)liposomes. Like TEOA, the buffer component HEPES contains tertiary amines that could be a sacrificial electron source. The potentials relevant to the tertiary amine oxidation of TEOA ($E_m = +1000$ mV) and HEPES ($E_m = +800$ mV) are very positive for reductants but they are effective in comparison to relevant potentials in the photosensitiser redox cycles, Figure 3.19 and Tables 3.1, 3.2 and 3.3.^[22, 23, 157]

To identify the contributions made by TEOA and HEPES, photoreductions of 0.5 μ M OmcA were performed in HEPES buffer lacking TEOA as well as in 50 mM phosphate, pH 7 with and without 50 mM TEOA present. Phosphate (Pi) is a buffer which is unable to act as a SED. Irradiations were carried out over 5 hrs following the addition of 10 μ M photosensitiser. No indication of OmcA reduction was observed in any of these four buffers during irradiation in the absence of photosensitisers, Appendix 11.

Figure 3.23 shows spectra gathered from OmcA photoreductions performed in the presence of eosin Y or fluorescein with different possible SED(s). Figure 3.24 shows a comparison of timecourses for these experiments. Eosin Y and fluorescein with TEOA, or HEPES, supported 100 % photoreduction of OmcA. However, no photoreduction or photodegradation was observed in Pi buffer during 5 hrs irradiation. Addition of TEOA with brief irradiation allowed complete photoreduction of OmcA to occur with both eosin Y and fluorescein. These observations suggest that eosin Y and fluorescein needs a SED present to perform cytochrome photoreductions. Thus, xanthene photoreductions must proceed via reductive quenching of PS* by the SED.

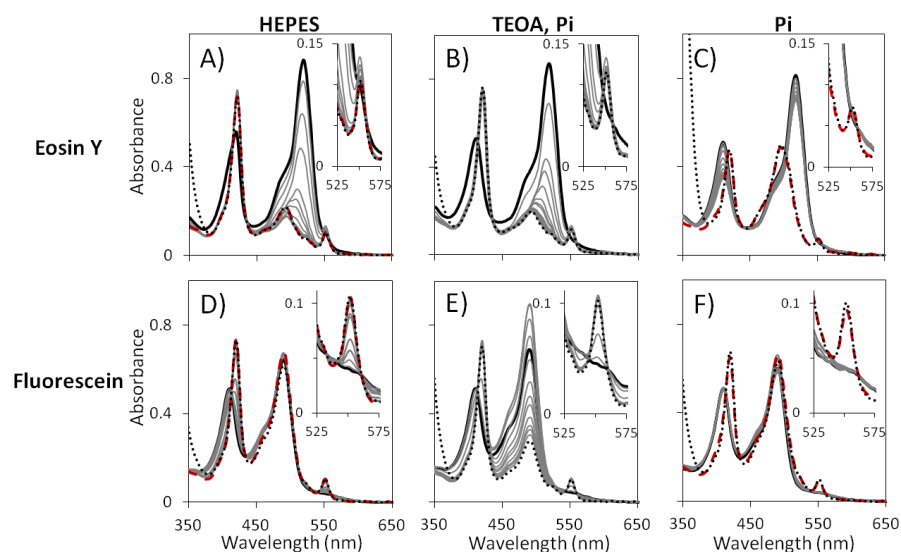


Figure 3.23. OmcA photoreduction, by eosin Y and fluorescein, in the presence and absence of the probable electron donors TEOA and HEPES.

0.5 μM OmcA with 10 μM of either eosin Y (A, B and C) or fluorescein (D, E and F), in 50 mM HEPES, 2 mM CaCl_2 , 10 mM KCl, pH 7 (A and D), 50 mM Pi, 50 mM TEOA, pH 7 (B and E) or 50 mM Pi, pH 7 (C and F). As prepared samples (continuous black lines) were irradiated for 5, 15, 30 mins and every subsequent 30 mins for the remainder of 5 hrs at 0.4 kW m^{-2} (grey lines) prior to addition of excess dithionite (dotted lines). For experiments lacking TEOA, prior to the addition of dithionite, excess TEOA was added before 15 mins irradiation at 0.4 kW m^{-2} was performed (red dashed lines). Inserts show magnified spectra between the wavelengths of 525 - 575 nm. Stirred samples in anaerobic buffers at 20°C . Path length 1 cm.

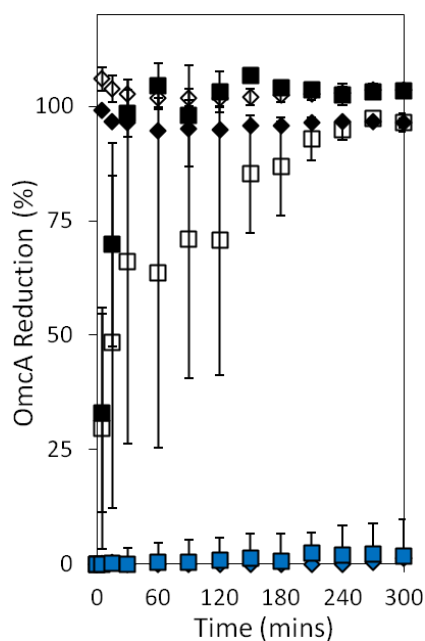


Figure 3.24. OmcA photoreduction by eosin Y or fluorescein requires a SED.

Extent of reduction of 0.5 μM OmcA by 10 μM of either eosin Y (diamonds) or fluorescein (squares) during irradiation at 0.4 kW m^{-2} over 5 hrs in 50 mM HEPES, 2 mM CaCl_2 , 10 mM KCl, pH 7 (open), 50 mM Pi, 50 mM TEOA, pH 7 (black) or 50 mM Pi, pH 7 (blue). Extent of reduction by eosin Y and fluorescein was monitored via change in 420 and 552 nm absorbances, respectively. Extent of reduction; and max and min observed values; represent the average of two independent experiments. Stirred samples in anaerobic buffers at 20 $^\circ\text{C}$. Path length 1 cm.

It is noteworthy that during irradiation with eosin Y in Pi buffer there was a decrease in the Soret peak which is indicative of cytochrome denaturing, Figure 3.23 C. This denaturing of OmcA was thought to be a result of the high energy of the long lived eosin Y triplet state which cannot be quenched in the absence of a SED. OmcA denaturing was not observed with fluorescein as the recombination of the triplet state is more favourable with this xanthene.^[23]

Omission of either TEOA or HEPES caused no impact on the extent of OmcA reduction achieved by eosin Y and fluorescein, with full heme reduction being observed within 5 hrs of irradiation. However, the rates of photosensitiser photodegradation and OmcA photoreduction by fluorescein were dependent on identity of the SED (TEOA > HEPES > NO SED).

Figure 3.25 and Appendix 12 show spectra gathered from OmcA photoreductions performed in the presence of proflavin or flavins with different possible SED(s). Figure 3.26 shows a comparison of timecourses for these experiments.

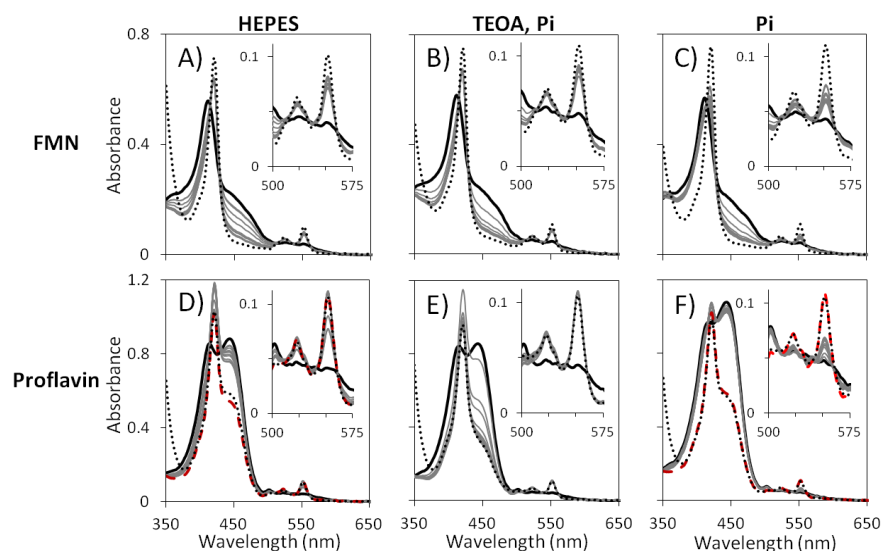


Figure 3.25. OmcA photoreduction, by FMN and proflavin, in the presence and absence of the probable electron donors TEOA and HEPES.

0.5 μM OmcA with 10 μM of either FMN (A, B and C) or proflavin (D, E and F), in 50 mM HEPES, 2 mM CaCl_2 , 10 mM KCl, pH 7 (A and D), 50 mM Pi, 50 mM TEOA, pH 7 (B and E) or 50 mM Pi, pH 7 (C and F). As prepared samples (continuous black lines) were irradiated for 5, 15 30 mins and every subsequent 30 mins for the remainder of 5 hrs at 0.4 kW m^{-2} (grey lines) prior to addition of excess dithionite (dotted lines). For proflavin experiments lacking TEOA, prior to the addition of dithionite, excess TEOA was added before 15 mins irradiation at 0.4 kW m^{-2} was performed (red dashed lines). Inserts show magnified spectra between the wavelengths of 500 - 575 nm. Stirred samples in anaerobic buffers at 20°C . Path length 1 cm.

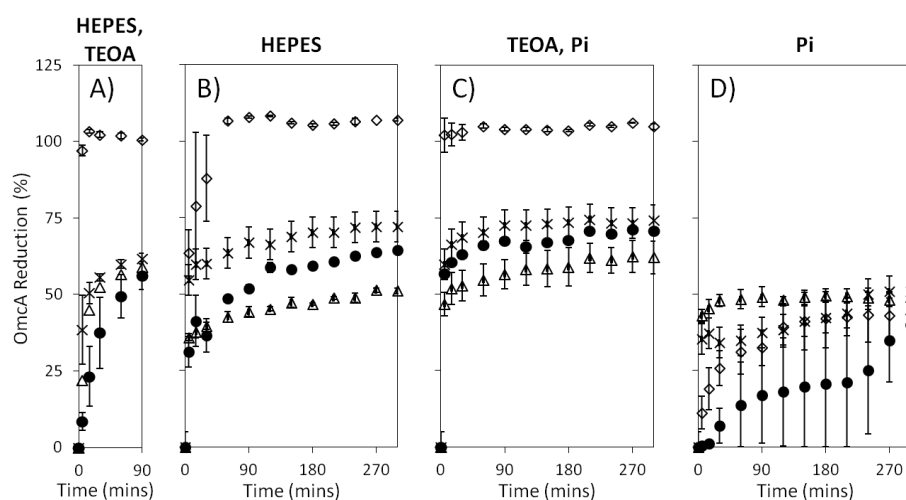


Figure 3.26. Complete OmcA photoreduction by flavin photosensitisers or proflavin depends upon the presence of electron donor.

Extent of reduction of 0.5 μM OmcA by 10 μM of either proflavin (diamonds), FAD (circles), FMN (crosses), or RF (triangles) during irradiation at 0.4 kW m^{-2} over 90 mins in 50 mM HEPES, 2 mM CaCl_2 , 10 mM KCl, 50 mM TEOA, pH 7 (A) or over 5 hrs in 50 mM HEPES, 2 mM CaCl_2 , 10 mM KCl, pH 7 (B), 50 mM Pi, 50 mM TEOA, pH 7 (C) or 50 mM Pi, pH 7 (D). Extent of reduction; and max and min observed values; represent the average of two independent experiments. Stirred samples in anaerobic buffers at 20°C . Path length 1 cm.

Omission of TEOA from the HEPES buffer caused minimal impact on the extent of OmcA reduction achieved by flavins and proflavin; however, photobleaching and photoreduction by proflavin occurred more slowly. Flavins and proflavin photoreductions of OmcA performed in 50 mM Pi, 50 mM TEOA, pH 7 obtained very similar results to those performed in 50 mM HEPES, 50 mM TEOA, 2 mM CaCl₂, 10 mM KCl, pH 7.

However, proflavin and flavins strikingly were only able to achieve ~ 40 % photoreduction of OmcA during 5 hrs irradiation when both TEOA and HEPES were absent. Flavin photoreduction of OmcA in the absence of a SED was expected as the ribityl side chain can reductively quench the corresponding PS* to form flavin hydroquinone, as described in Section 3.2.2.3.^[142, 144, 145] As the initial flavin concentrations were similar to the total heme concentration present, and as other competing photodegradations involving the ribityl group can occur, the hindered extent of OmcA photoreduction without a SED can be rationalised. Flavin photodegradation was confirmed upon completion of irradiations performed with RF and FAD via additional irradiation performed upon addition of TEOA which caused no heme photoreduction, Appendix 12. The rates of flavin self photoreduction and subsequent OmcA photoreduction varied with identity of flavin (RF > FMN > FAD), could be explained by the size of the ribityl side chains which are key to self photoreduction, Table 3.3. The bigger the ribityl chain the greater the protection around the intra-molecular SED site.

Addition of TEOA with brief irradiation allowed photobleaching and OmcA photoreduction by proflavin in Pi buffer, Figure 3.25 F. It is unclear how ~ 40 % OmcA reduction by proflavin was achieved in the absence of photosensitiser damage or SED. It is possible this photoreduction occurred via oxidative quenching and produces solvated electrons (Figure 3.4); however, it would then be assumed that 100 % photoreduction would be achievable as proflavin was in a similar concentration to the total heme present.

OmcA photoreductions by ruthenium complexes in the presence and absence of different electron donors are shown in Appendix 13. It was not possible to conclusively identify differences that would indicate preferential use of oxidative or reductive quenching pathways.

During this section the effect that the presence and identity of SED had upon OmcA photoreduction was explored. In addition to confirming that TEOA and HEPES can both act as electron donors during photoreductions, it was seen that cytochrome photoreductions were hindered or completely unsuccessful in the absence of SED(s). In the

absence of SED(s), the flavins and proflavin acted as both photosensitiser and SED, but xanthenes were unable to do this. These experiments also highlighted xanthene photoreductions must undergo via reductive quenching mechanisms. Photoreductions of OmcA performed in the presence of TEOA were faster than those performed in the presence of HEPES alone.

3.8 Discussion

Within this work, the rates of photoreduction by the organic photosensitisers were generally too fast under stirred, comparable conditions for any definitive conclusions to be made with respect to difference in rates caused by the cytochrome identity. A cytochrome-dependent difference in the rate of photoreduction was only clearly distinguished with fluorescein in the presence of TEOA, when heme and photosensitiser concentrations of 5 μM and 10 μM , respectively, were used. Under these conditions MtrCAB reduced more rapidly than MtrC, and the rate of MtrC reduction slightly exceeded that of OmcA (MtrCAB $\gg\gg$ MtrC $>$ OmcA). Under comparable conditions, photoreductions by $[\text{Ru}(\text{bpy})_3]^{2+}$ and RuP were strikingly much slower than those by the organic photosensitisers. This discussion tries to account for these differences in photoreduction rates, and predicts the locations of transient binding sites for photosensitisers, by considering the structures of the outer membrane cytochromes in detail. Additionally, methods to accelerate photoreductions by ruthenium complexes and the contributions that MtrC and OmcA flavocytochromes have within these photoreductions are discussed.

As discussed in Section 1.6.2, MtrC and OmcA are structural homologues composed of two split β -barrel domains and two heme domains which coordinate their ten hemes.^[87, 88] The hemes of MtrC and OmcA are highly solvent-exposed, Figure 3.27. Eight of the ten hemes in MtrC and OmcA are solvent-accessible. Only hemes 3 and 8 are completely buried inside the protein which makes them highly unlikely interaction sites for photosensitisers and other electron shuttles, Figure 3.27. The terminal hemes of the octaheme chain (hemes 10 and 5) are the most solvent-exposed and are thus proposed as the electron entrance and exit sites during EET.^[91] The terminal hemes of the tetraheme chain (hemes 2 and 7) are also highly solvent-exposed and have been proposed as potential flavin-binding sites due to their proximity to domains I and III which contain extended Greek key split-barrel structures, a common flavin-binding motif.^[91] Based upon

accessibility alone, it is predicted that photosensitisers would have more favourable interactions with these four terminal hemes than with the more buried hemes 1, 4, 6 and 9.

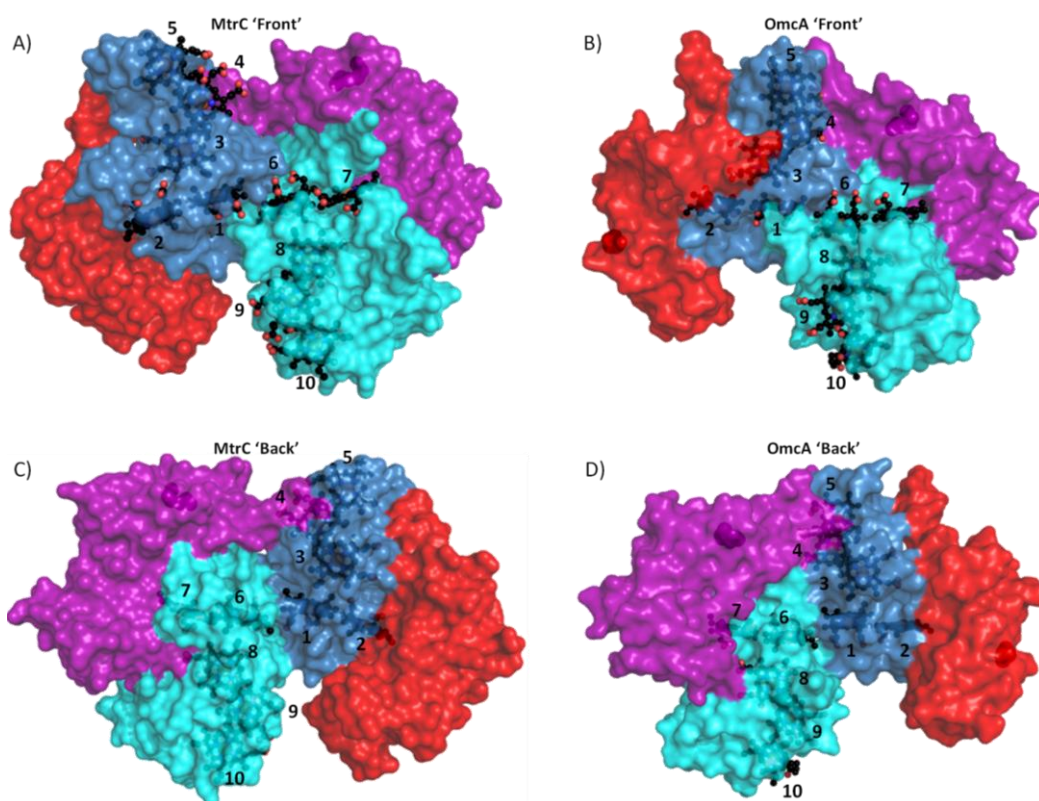


Figure 3.27. Comparison of the solvent-exposed hemes of MtrC and OmcA.

The structures of MtrC (A and C, PDB ID: 4LM8) and OmcA (B and D, 4LMH) represented with the surfaces of their four domains coloured red, blue, purple and cyan from the N termini to the C termini. Opposite surfaces to those shown in A and B are shown in C and D, respectively. Numbers denote the hemes, which are represented as spheres (C, black; O, red; N, blue, Fe, olive). Disulfide bond cysteines as spheres coloured for the corresponding domain.

The high level of heme-solvent exposure results in an overall electronegative charged surface, which is localised around the staggered heme cross of MtrC and OmcA, Figure 3.28. These electronegative densities are contributed to solvent-exposed, negatively charged propionate groups of hemes and the lack of positively charged residues located near the protein surface.^[91, 158] Positively charged regions in domains I and III, which surround the terminal hemes of the tetraheme chain (hemes 2 and 7), are thought to be present to decrease the observed charge on the surface that is induced by the solvent-exposed hemes.^[158] These positively charged regions could attract and favour electron exchange between negatively charged photosensitisers; such as flavins, eosin Y, fluorescein and the anionic proflavin radical. Negatively charged regions around hemes 5 and 10 would favour interactions between positively charged photosensitisers like the Ru(II) complexes.

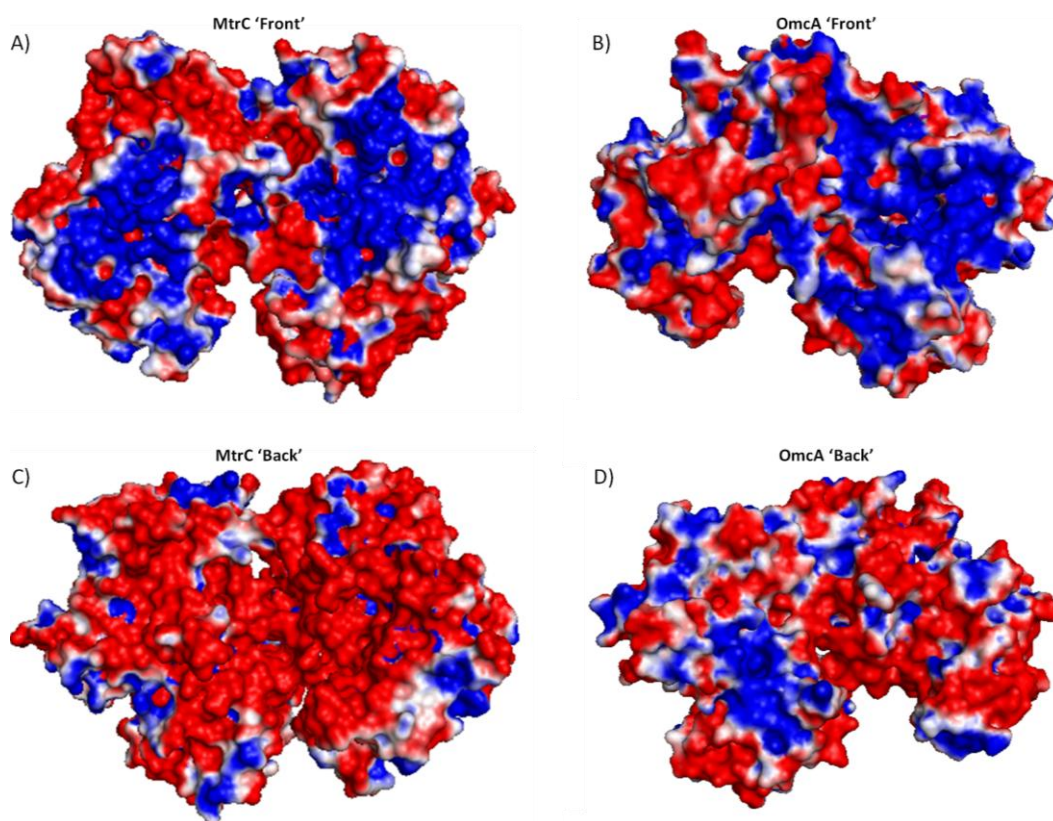


Figure 3.28. Comparison of the electrostatic surface potential of MtrC and OmcA.

The structures of MtrC (A and C, PDB ID: 4LM8) and OmcA (B and D, 4LMH) represented as electrostatic surface maps. Maps coloured using APBS with potentials scaled from -25 mV (red, negatively charged) to +25 mV (blue, positively charged). Opposite surfaces to those shown in A and B are shown in C and D, respectively.

Comparisons of solvent-exposed hemes, shown in Figure 3.27, reveal the hemes of OmcA are less accessible to solvent, and presumably photosensitisers, than those of MtrC. As OmcA is heavier than MtrC, and as the heme staggered cross is highly conserved, it would be expected that the presence of an extra 11 kDa of peptide would affect solvent accessibility to the hemes. This difference alone might explain why the photoreduction of OmcA by fluorescein was slower than that of MtrC. By having more limited heme-accessibility, transient interactions and successful electron transfers between photosensitisers and hemes would be less frequent. The lower level of heme-solvent exposure also alters the overall electronegative surface potential of OmcA by neutralising some of the negatively charged heme propionate groups, Figure 3.28.^[88] This could also have a substantial impact on the way that these proteins interact with photosensitisers.

As there is no structure currently available for MtrCAB, reasoning why cytochrome photoreduction by fluorescein was faster for MtrCAB in comparison to OmcA and MtrC is more difficult and more open to suggestion. MtrA, or the interface between MtrC and MtrA, could offer a preferable docking site for fluorescein, which brings fluorescein closer

to a heme than is possible when MtrC is alone. The fluorescein triplet excited state could be stabilised when in the presence of Triton X-100 which would lead to less unproductive recombinations of photoexcited electrons and more successful electron transfers to MtrCAB. Fluorescein could bind to Triton X-100 micelles and the resulting binding product could encourage interactions that are longer-lived and/or closer to hemes of MtrCAB. Photoreductions, similar to those described in this chapter, with soluble MtrA, Triton X-100-solubilised MtrAB, and MtrC or OmcA in the presence of Triton X-100 would help to distinguish these possible reasons for the faster photoreduction of MtrCAB observed by fluorescein.

For the other organic photosensitisers the rates of photoreduction were too fast under stirred, comparable conditions for any definitive conclusions to be made with respect to difference in rates caused by the cytochrome identity. To definitively prove whether cytochrome identity has any effect upon the rate of photoreduction a different method would be required to study these rapid electron transfers. Possible different techniques that could be used to study these rapid electron transfers and reveal if cytochrome identity has any effect upon the rate of photoreduction include transient absorbance spectroscopy, pump-probe spectroscopy, time-correlated single photon counting, and protein film (photo)electrochemistry.

Strikingly under comparable conditions, photoreductions by $[\text{Ru}(\text{bpy})_3]^{2+}$ and RuP were much slower than those by the organic photosensitisers. Since the thermodynamic drive generated by the quenching of the photoexcited states of the ruthenium complexes would be stronger than those seen with the organic photosensitisers, the effectiveness of the ruthenium complexes as photosensitisers relative to the organic dyes must be compromised by less favourable kinetics. This kinetic limitation could be a result of slow net electron exchange with cytochromes and SED(s) and/or rapid charge recombination of the photoexcited state and/or fast regeneration of the ruthenium complex by photoreduced cytochrome. As the triple state lifetimes of ruthenium complexes ($< 0.7 \mu\text{s}$) are much shorter than those of the organic photosensitisers (4 - 24 μs), it is most likely that rapid charge recombinations of the photoexcited ruthenium complexes is the underlying reason to the comparatively slow photoreductions by ruthenium complexes.^[126, 129, 143, 159, 160]

The addition of an electron relay is often used to accelerate the photoexcited electron transfer from ruthenium complexes to target electron acceptors.^[120, 121, 161] A previous study reported that direct transfer of photoexcited electrons was not observed

between a ruthenium photosensitiser and a hydrogenase in solution when in the presence of a SED alone.^[161] This was also true for when the photosensitiser and catalysts were covalently linked together. However, the addition of the redox mediator MV^{2+} allowed light-driven hydrogen production to successfully occur in both solution and covalently linked systems. MV^{2+} efficiently enhances the charge separation by quenching the photoexcited ruthenium complex and subsequently readily mediating the reducing equivalents to the hydrogenase. It is probable that the covalently linked ruthenium complex was not within adequate distance to transfer electrons to the catalytic site of the hydrogenase and therefore still required MV^{2+} to act as an electron mediator.

As previously mentioned in Section 3.2.1, rapid charge separation can be also achieved by covalently coupling ruthenium complexes to metal oxide semiconductor like TiO_2 . A previous study reported transfer of photoexcited electron from RuP to a molecular cobalt catalyst in the presence of a SED was negligible unless the dye and the catalyst were co-adsorbed on TiO_2 nanoparticles, which in turn allowed successful light-driven production of hydrogen.^[121] Co-adsorption of the photosensitiser and the catalyst on TiO_2 nanoparticles enhanced charge separation from photoexcited RuP through rapid injection of photoexcited electrons into the conduction band of TiO_2 which were then readily transferred to the catalyst.

As the conduction band of TiO_2 has a reductive potential of -700 mV at pH 7, RuP sensitised TiO_2 particles should possess the thermodynamic driving force to provide the complete photoreduction of outer membrane cytochromes.^[120, 121] Consequently it was attractive to establish whether MtrC or OmcA would adsorb on RuP: TiO_2 particles in an electroactive configuration which would allow more rapid cytochrome photoreduction in comparison to that achieved with RuP alone. Work performed by Dr Colin Lockwood at the University of East Anglia showed MtrC and OmcA could be successfully adsorbed on RuP sensitised TiO_2 particles in the presence of 150 mM the SED 2-(*N*-morpholino)ethanesulfonic acid at pH 6.^[162] The use of an integrating sphere spectrometer mitigated against the loss of incident light due to scattering by the particles which allowed the resolution of spectral features from the adsorbed oxidised cytochromes. Subsequent irradiations with a lamp power of 0.4 kW m^{-2} ($\lambda > 390 \text{ nm}$) resulted in clear and substantial cytochrome photoreductions within 10 mins. These experiments show the transfer of photoexcited electrons from ruthenium complexes to MtrC/OmcA can be greatly accelerated by their co-adsorption on TiO_2 particles.^[162]

Given flavins were used as photosensitisers during this study, alongside suggestions that MtrC and OmcA can undergo tight flavin binding to form flavocytochromes, it was of interest to characterise the response of such flavocytochromes when irradiated by visible-light.^[87, 90] The following experiment was performed by Dr Gaye White at the University of East Anglia.^[162] Flavocytochromes comprised of FMN tightly bound to MtrC were prepared as previously described by anaerobic incubation with glutathione and FMN followed by gel filtration to separate the flavocytochrome from free FMN.^[87] Electronic absorbance spectroscopy established that the hemes and FMN remained oxidised during this preparation, which was performed in the dark, and also during 90 mins irradiation.^[162] The fluorescence of FMN is partially quenched on binding to the glutathione reduced MtrC and is only recovered when FMN is released by oxidation of the flavocytochrome.^[87] This fluorescence quenching most likely occurs through Förster Resonance energy transfer from the photoexcited FMN to a close proximity heme, where the energy is subsequently dissipated as heat energy via molecular vibrations.

These observations suggest that bound FMN is unable to support photoreduction of the flavocytochrome because the photoexcited FMN is quenched more rapidly by energy transfer than by electron transfer. Therefore the photoreductions of outer membrane cytochromes by flavins as shown in this chapter is proposed to occur via electron transfer at a site other than that occupied by the flavin in the flavocytochrome. Molecular dynamics simulations of MtrC have suggested that the flavin binding site of the flavocytochromes is in the vicinity of heme 4 and is formed after a major conformational change which is caused by the cleavage of the disulphide bond.^[163]

3.9 Conclusions

At pH 7 with a lamp power of 0.4 kW m^{-2} ($\lambda > 390 \text{ nm}$) and a photosensitiser concentration of $10 \text{ }\mu\text{M}$, it was possible to perform quantitative comparison of the ability of the chosen photosensitisers to photoreduce outer membrane cytochromes of *S. oneidensis* MR-1, MtrC, OmcA and MtrCAB.^[162] In the presence of TEOA and/or HEPES as SED(s) the photosensitisers eosin Y, fluorescein and proflavin coupled reductive quenching of the respective photoexcited states to achieve complete reduction of the cytochromes. With TEOA and/or HEPES as SED(s) the flavin photosensitisers could only achieve ~ 60 % cytochrome photoreduction in accordance the lower thermodynamic driving force available for heme reduction by these photosensitisers. When reactions were

left for sufficiently long times, the maximum extent of cytochrome photoreduction achieved was independent on whether the concentration of organic photosensitiser was in excessive or catalytic amounts with respect to that of the protein.

Generally, the rates of photoreduction by the organic photosensitisers were too rapid under stirred, comparable conditions for any definitive conclusions to be made about the impact that the cytochrome identity had upon the rate of photoreduction. The rate of photoreduction by fluorescein was the only that was influenced by cytochrome identity (MtrCAB >>> MtrC > OmcA). The slower photoreduction of OmcA by fluorescein was attributed to the limited heme-accessibility due to the presence of an extra 15 % peptide than that within MtrC. Under identical conditions, photoreductions by $[\text{Ru}(\text{bpy})_3]^{2+}$ and RuP were strikingly much slower than those by the organic photosensitisers, and was only comparable when RuP and MtrC/OmcA was co-absorbed on TiO_2 particles.^[162]

Comparisons of the solvent-exposed hemes and the electrostatic surface potentials of MtrC and OmcA were able to suggest probable photosensitiser transient binding sites. As hemes 1, 3, 4, 6, 8 and 9 are significantly buried within the protein it was decided that these were unlikely interaction sites for photosensitisers. The terminal hemes of the staggered cross formation are highly solvent exposed and therefore provide ideal interaction sites for photosensitisers. The negatively charged regions around hemes 5 and 10 were suggested to favour interactions between positively charged ruthenium photosensitisers, whereas the positively charged regions around heme 2 and 7 would favour interactions with negatively charged, organic photosensitiser. When FMN was bound to MtrC as a flavocytochrome no photoreduction was observed, therefore photoreduction of outer membrane cytochromes by flavins must occur at a site other than that occupied by the flavin in the flavocytochrome.^[162]

Experimental conditions where photoreduction of outer membrane cytochromes occurred with eight selected photosensitisers were identified within this chapter. These conditions provide the basis for investigation of light-driven transmembrane electron transfer by MtrCAB. Proteoliposomes, unlike *S. oneidensis* MR-1 cells, provide a clean system in which only MtrCAB photoreduction and subsequent transmembrane electron transfers would be observed. The next chapter of this study describes the production of MV^{2+} -containing MtrCAB (proteo)liposomes which are initially used to explore interactions and reactions between the photosensitisers and (proteo)liposomes.

Chapter 4

Exploration of Interactions Between Photosensitisers and Methyl Viologen-Containing (Proteo)liposomes: MtrCAB Incorporation in Preformed Liposomes

4.1 Possible Interactions Between Photosensitisers and (Proteo)liposomes

To be able to study light-driven transmembrane electron transfers by MtrCAB two key components are required: i) a membrane-enclosed redox indicator which can monitor light-driven transmembrane electron transfers; and ii) a method that discriminates between electron transfer through MtrCAB and alternative electron transfer pathways.

MtrCAB proteoliposomes containing a cargo of MV^{2+} offer both of these required components. As previously discussed in Section 1.5.2, liposomes are spherical vesicles that have at least one lipid bilayer which encapsulates and isolates an internal aqueous volume. Proteoliposomes differ from liposomes by having one or more proteins inserted into the lipid bilayer. Insertion of MtrCAB into the lipid bilayer of liposomes has been shown to facilitate transmembrane electron transfers driven by chemical reductant/oxidants which are otherwise not possible, as discussed in Section 1.6.3. These MtrCAB proteoliposomes contained a redox indicator cargo of MV^{2+} .^[83, 92, 93] The redox reactions of MV, as shown in Figure 1.16, are ideal for studying transmembrane electron transfers via MtrCAB. The absorbance peak at 606 nm associated with blue MV^+ can be clearly monitored and distinguished from the essentially colourless MV^{2+} and MV^0 ; and both MV^{2+} and MV^+ are membrane-impermeable.^[83, 92–94]

Light-driven one-electron reduction of MV^{2+} has been previously demonstrated by eosin Y, fluorescein, proflavin, fluorescein, $[Ru(bpy)_3]^{2+}$ and RuP in the presence of SEDs, including TEOA.^[133, 164, 165] Light-driven reduction of MtrCAB in the presence of TEOA was demonstrated by these and other similar photosensitisers in Chapter 3. With these considerations in mind and as MtrCAB proteoliposomes containing MV^{2+} had been previously thoroughly characterised and developed, it was envisioned that these proteoliposomes could be adopted for the study of light-driven transmembrane electron transfers to MV^{2+} driven by photosensitisers in the presence of TEOA as a SED.^[83, 92, 93]

It can be envisioned that when MV^{2+} -containing proteoliposomes are irradiated in the presence of photosensitisers and TEOA, MtrCAB photoreduction would occur prior to MtrCAB facilitating transmembrane electron transfer to compartmentalised MV^{2+} which would then in turn be reduced, Figure 4.1 A. This ideal scenario for studying light-driven transmembrane electron transfer relies on photosensitisers: i) being externally located; ii) only interacting with external portions of MtrCAB; and iii) having no interaction with, or effect upon, the phospholipid bilayer that changes its permeability with respect to MV or photosensitisers. However, other possible scenarios can be envisioned which would also ultimately result in MV^{2+} photoreduction, Figure 4.1 B-F. These include photosensitisers: i) binding to, but not structurally affecting, the proteoliposome membrane within electron transfer distance of MtrCAB and/or MV^{2+} (Figure 4.1 B-C); ii) crossing the membrane to directly photoreduce MV^{2+} internally (Figure 4.1 D); iii) partially disrupting the membrane, either by binding to or crossing it, and allowing the release of cargo and subsequent direct photoreduction of MV^{2+} (Figure 4.1 E); or iv) causing complete lysis of the membrane and ultimately allowing direct photoreduction of MV^{2+} (Figure 4.1 F).

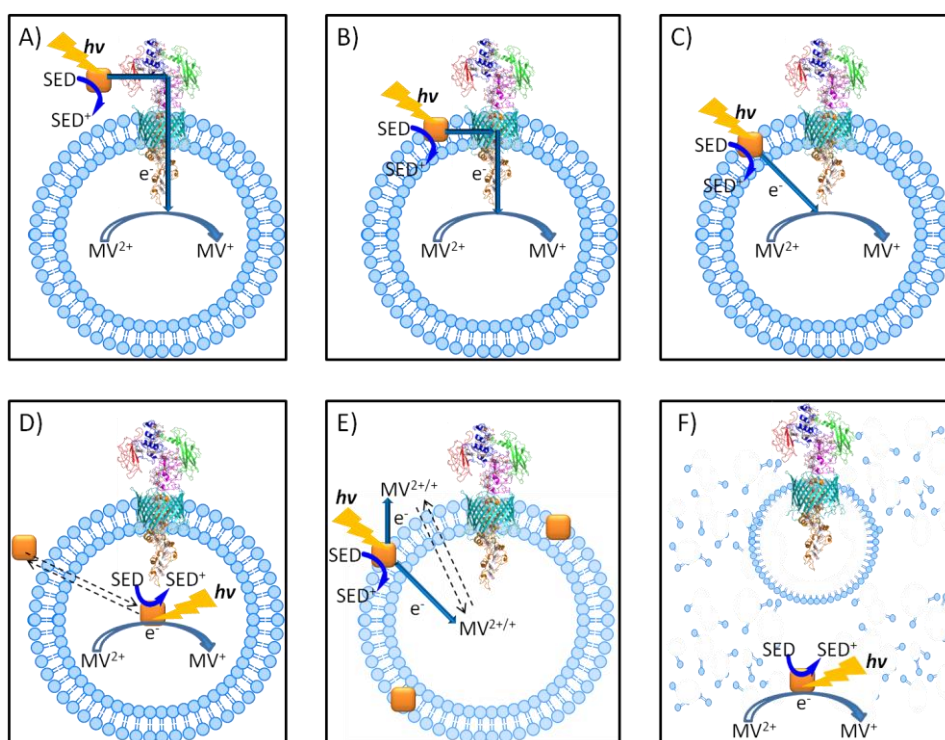


Figure 4.1. Possible interactions between MV^{2+} -containing MtrCAB proteoliposomes and photosensitisers which could result in MV^{2+} photoreduction.

These possible scenarios range from A) the most ideal scenario for studying light-driven transmembrane electron transfer where photosensitisers photoreduce MV^{2+} via MtrCAB, to F) the least ideal scenario where photosensitiser presence leads to complete proteoliposome lysis. See text for details. Possible interactions illustrated here could occur between proteoliposomes and any photosensitiser state (i.e. ground state or light-induced -photoexcited, -oxidised, or -reduced states) represented by orange squares.

Irradiation of photosensitisers and liposomes that do not contain MtrCAB would help to distinguish if any MV^{2+} photoreduction observed with proteoliposomes suspensions occurred via the MtrCAB complex (i.e. Figure 4.1 A-B) or via other mechanisms (i.e. Figure 4.1 C-F). Characterisation of (proteo)liposomes collected by centrifugation after incubations with photosensitisers would allow conclusions to be made with regard to whether photosensitisers bind to or cross liposome membranes (i.e. Figure 4.1.B-E) or whether they remain externally (i.e. Figure 4.1 A and F). As photosensitisers go through a series of different states during their photocatalytic cycles; i.e. ground, photoexcited, oxidised and reduced as shown in Figure 1.4; it is possible that one or more of these states could interact with or have an effect upon liposome membranes. Therefore characterisation of (proteo)liposomes after performing light and dark incubations with photosensitisers would provide insight into the effects, if any, that different photosensitiser states have upon the liposome membranes.

This chapter describes such experiments for the eight previously discussed photosensitisers. MtrCAB (proteo)liposomes without a redox indicator cargo were used for insight into the effects, if any, of photosensitisers on the liposome membranes without complications that could arise from the additional presence of MV, in Section 4.3. These observations were then further built upon using MV^{2+} -containing (proteo)liposomes, as described in Section 4.4. First the preparation and characterisation of MtrCAB (proteo)liposomes, with and without encapsulated MV^{2+} , is briefly described below.

4.2 Preparation and Characterisation of (Proteo)liposomes via MtrCAB Incorporation into Preformed Liposomes

The method used to incorporate MtrCAB into preformed liposomes is thoroughly described in Section 2.3.4. This method, which includes minor changes to the previously published method, was used to prepare (proteo)liposomes with and without MV^{2+} encapsulated for experiments that are discussed within this chapter.^[92, 93]

As the only deliberate modification to the (proteo)liposome protocol was the duration of Biobead incubation, which is a non-intrusive step, it was assumed the orientation, topology and incorporation heterogeneity of MtrCAB in proteoliposomes were identical to those previously reported.^[92, 93] During the course of this work it was discovered that MtrCAB incorporation and proteoliposome formation was highly dependent upon the concentration of Triton X-100 in the proteoliposome sample. This

varied from preparation to preparation due to concentration of Triton X-100 during the purification of the protein. During buffer exchange and protein concentration within a stirred Amicon pressure cell (30 kDa cutoff filter) Triton X-100 was also concentrated, due to having a large average micelle size of 80 kDa and a very slow monomer/micelle exchange rate. Therefore additions which ensured the same amount of MtrCAB resulted in different amounts of Triton X-100 to be included in proteoliposome preparations. The amount of Triton X-100 present within MtrCAB samples was assessed using the absorbance of Triton X-100, as described in Section 2.2.3, and was found to vary from 1 to 20 %. It was found that MtrCAB samples in ~ 2 % Triton X-100 provided optimal MtrCAB incorporation and proteoliposome formation and that larger amounts resulted in liposome lysis and smaller amounts hindered protein incorporation.

Physical characterisations of these (proteo)liposomes were performed after each individual preparation. DLS measurements showed the hydrodynamic radii of proteoliposomes and liposomes to be on par with those previously reported, 227 ± 126 nm and 95 ± 33 nm respectively, Figure 2.7.^[93] Bright-field microscopy was used to confirm the larger sizes and greater size diversity of proteoliposomes in comparison to liposomes, Figure 4.2.

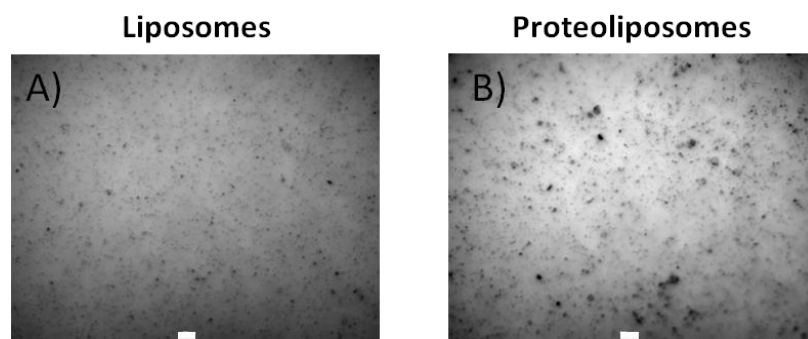


Figure 4.2. Bright-field images of (proteo)liposomes.

Bright-field microscopy images of 10 mg mL^{-1} lipid suspensions of liposomes (A) and proteoliposomes (B) prepared without MV^{2+} encapsulated. White scale bars represent 5000 nm.

Additional experiments demonstrated MtrCAB supported transmembrane electron transfer from the chemical reductant dithionite to MV^{2+} as previously reported, Section 1.6.3 and shown in Figure 1.17.^[83, 92, 93] Absorbance spectra of (proteo)liposomes show the apparent absorbance becomes greater towards shorter wavelengths, Figure 4.3 continuous black lines. This behaviour is typical of that caused by Rayleigh scattering. As (proteo)liposomes are smaller than the wavelengths of incoming light, this light is scattered instead of being detected by the spectrometer, which then interprets this as light absorbed

by the sample. The magnitude of absorbance due to this behaviour provides an indicator of (proteo)liposomes concentration in each sample.

It is noteworthy that the absorbance spectrum of proteoliposomes are identical to those of liposomes, with no heme spectral features being observed, compare Figure 4.3 continuous black lines to Figure 3.9 continuous black line of 0.45 μM MtrCAB. Assuming complete protein incorporation occurs during their preparation, it is expected that ~ 1 nM MtrCAB would be present within a 1 mg mL^{-1} lipid suspension of proteoliposomes and subsequent heme spectral contributions would be miniscule and masked by scattering contributions. Upon addition of a small excess of dithionite to anaerobic 1 mg mL^{-1} lipid suspensions of MV^{2+} -containing liposomes there were negligible changes to their electronic absorbance spectra over 10 mins, Figure 4.3 A dotted black line. However, a parallel addition of dithionite to proteoliposomes caused the appearance of a broad feature at 606 nm in accordance with MtrCAB allowing transmembrane electron transfer to perform the one-electron reduction of MV^{2+} to MV^+ , Figure 4.3 B dotted black line.

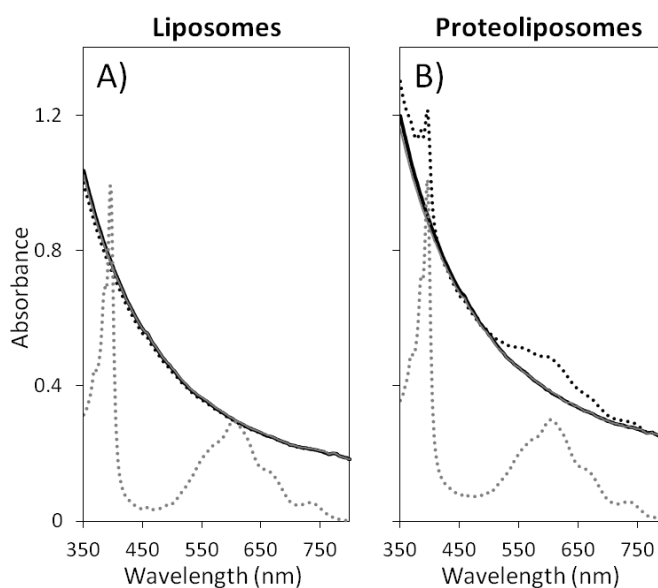


Figure 4.3. MtrCAB supports transmembrane electron transfer from chemical reductant to MV^{2+} encapsulated within liposomes.

1 mg mL^{-1} lipid suspensions of MV^{2+} -containing (proteo)liposomes prepared without incorporation of MtrCAB (A) or with MtrCAB (B). As prepared samples (continuous black lines) were irradiated for 5, 15, 30, 60 and 90 mins at 2 kW m^{-2} (continuous grey lines) prior to addition of excess dithionite and subsequent 10 mins incubation (dotted black lines). Addition of excess Triton X-100 to dithionite incubated samples (dotted grey lines) showed $\sim 22 \mu\text{M}$ MV^+ was present after being released from (proteo)liposomes. Stirred samples in anaerobic 50 mM HEPES, 2 mM CaCl_2 , 10 mM KCl, 50 mM TEOA, pH 7 at 20°C . Path length 1 cm.

Concentration of MV^{2+} reduced inside proteoliposomes was determined to be $\sim 9 \mu\text{M}$ using an extinction coefficient of $11.5 \text{ mM}^{-1} \text{ cm}^{-1}$ at 606 nm, which accounted for

light scattering caused by liposomes, Figure 4.3 B dotted black line.^[92] Solubilisation of (proteo)liposomes with Triton X-100, as evidenced by loss of scattering contributions to spectra, released encapsulated MV. This resulted in the appearance of a broad feature at 606 nm and a sharp peak at 410 nm confirming the release and subsequent reduction of all MV^{2+} , Figure 4.3 dotted grey lines. Utilising the extinction coefficient of $13.7 \text{ mM}^{-1} \text{ cm}^{-1}$ at 606 nm, the concentration of MV^{2+} after the release from (proteo)liposomes was determined to be $\sim 22 \text{ }\mu\text{M}$ in 1 mg mL^{-1} (proteo)liposome suspensions, Figure 4.3 dotted grey lines.^[93, 97] These calculations demonstrated that $\sim 41 \%$ of MV^{2+} was redox addressable in these proteoliposomes over the timecourse of this experiment which is comparable to that previously reported.^[93] Even though the extent of MV^{2+} reduction increases during dithionite incubation, it is not expected that all encapsulated MV^{2+} would be addressable in a proteoliposome suspension due to the uneven incorporation of MtrCAB across a sample with 0 to 200 MtrCAB molecules per liposome.^[93]

Similar timecourses and extents of MV^{2+} reduction were observed for (proteo)liposomes suspensions that had and had not been firstly irradiated for 90 mins using a lamp power of 2 kW m^{-2} , Figure 4.3. Irradiations within this chapter were performed prior to experiments which established an optimal lamp power, as discussed in Section 3.4.2. As a consequence light incubations were carried out using a lamp power of 2 kW m^{-2} and it is expected that the observations and conclusions drawn throughout would be valid at lower lamp powers.

4.3 Assessment of Photosensitiser Association with (Proteo)liposomes

Initial experiments with (proteo)liposomes with no MV^{2+} encapsulated and the eight chosen photosensitisers were performed to investigate whether photosensitisers affected or bound to the liposome membranes, Figure 4.1 B-F. To firstly assess whether photosensitisers associated with (proteo)liposomes, spectra of (proteo)liposome suspensions (1 mg mL^{-1} lipid) and photosensitisers were monitored during anaerobic incubations performed in darkness or under irradiation in the presence of excess TEOA. It would be expected that if bilayer stability was compromised during these incubations the scattering contributions of (proteo)liposome absorbance spectra would be affected, as seen upon addition of Triton X-100 which lyses (proteo)liposomes and causes their scattering contributions to be lost, Figure 4.3 dotted grey lines. Dark incubations of (proteo)liposomes in the absence of any photosensitisers resulted in negligible changes in

their spectra, Figure 4.4. The overlaying spectra therefore suggest these (proteo)liposomes are stable during these dark incubations, Figure 4.4 continuous lines. Negligible spectral changes were also observed during 2 kW m^{-2} irradiations of liposomes in the absence of any photosensitisers which suggests these liposomes are also stable during irradiation, Appendix 14.

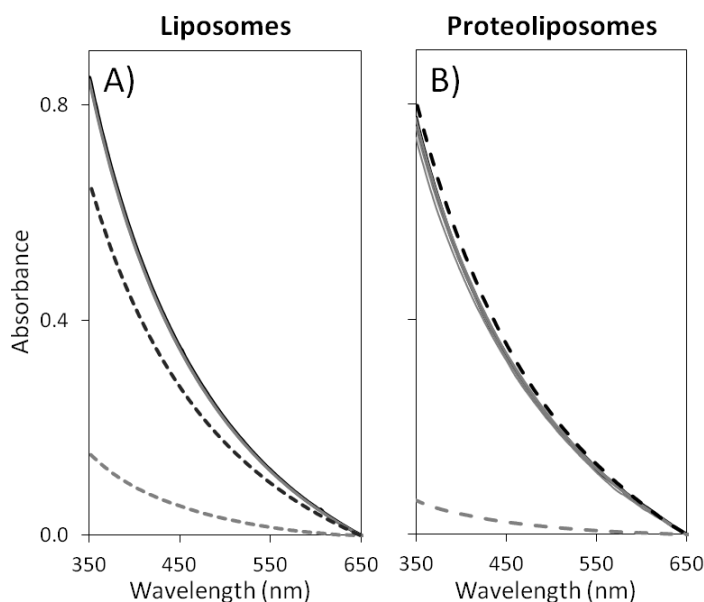


Figure 4.4. (Proteo)liposome absorbance spectra remain unaffected upon dark incubation in the absence of photosensitisers.

1 mg mL^{-1} lipid suspensions of (proteo)liposomes without MV^{2+} encapsulated (continuous black lines). Dark incubations of liposomes (A) and proteoliposomes (B) were performed for 5, 15, 30, 60 and 90 mins (continuous grey lines). Incubations were followed by ultracentrifugation to separate supernatants (dashed grey lines) from (proteo)liposome pellets that were resuspended in buffer (dashed black lines). Stirred samples in anaerobic 50 mM HEPES, 2 mM CaCl_2 , 10 mM KCl, 50 mM TEOA, pH 7 at 20°C . Path length 1 cm.

Absorbance spectra of supernatants and resuspended (proteo)liposome pellets that were collected by ultracentrifugation after these incubations confirmed ultracentrifugation was efficient at separating and allowing recovery of (proteo)liposomes from their external aqueous solutions, Figure 4.4 and Appendix 14 dashed lines. Consequently absorbance spectra of resuspended (proteo)liposome pellets and their external solutions collected via ultracentrifugation can be used to ascertain whether the photosensitisers remained in the external solutions or had associated with (proteo)liposomes.

Addition of $\sim 10 \mu\text{M}$ photosensitisers to suspensions of (proteo)liposomes (1 mg mL^{-1} lipid) produced spectra in which scattering contributions from (proteo)liposomes were overlaid with spectral features of photosensitisers. Small variations in photosensitiser concentrations and RF spectra seen in these data sets were due to inadequate checks for concentration and photosensitiser photodamage after individual

sample preparation at the early stages of this work. However, these variations do not affect the conclusions drawn from these experiments. No detectable spectral changes were observed during dark incubations of (proteo)liposomes in the presence of flavins, Figure 4.5 continuous grey lines. Similar incubations performed under irradiation also showed negligible changes in scattering contributions from liposomes but showed some decrease in the flavin spectral features, due to the production of fully reduced flavin species, Appendix 15 A-C continuous grey lines. Once these samples were ultracentrifuged the yellow flavin colour remained with the supernatants, as confirmed by their absorbance spectra, Figure 4.5 and Appendix 15 A-C dashed grey lines. Scattering contributions were only exhibited within the absorbance spectra of the resuspended (proteo)liposomes. These results indicate that the flavin photosensitisers do not disrupt or associate with (proteo)liposome membranes.

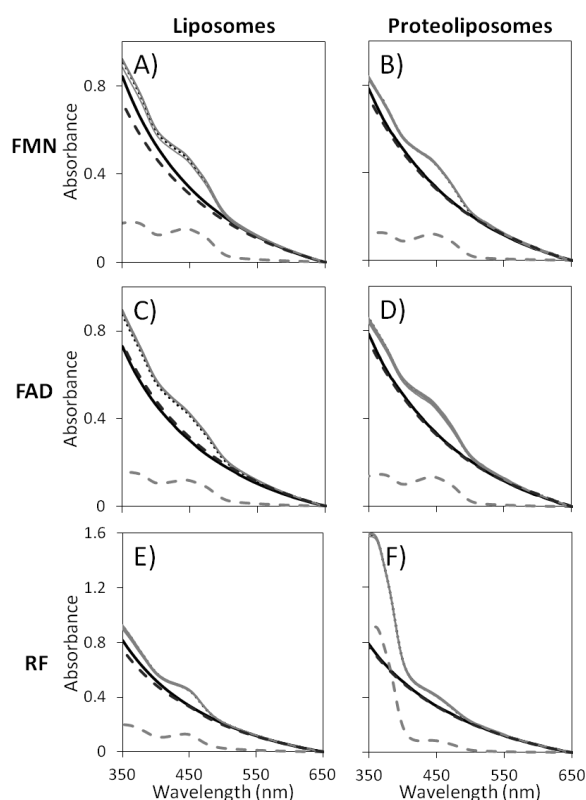


Figure 4.5. Dark incubations of flavins with (proteo)liposomes show no photosensitiser-membrane interactions.

Liposomes with 10 μM FMN (A), 4 μM FAD (C) or 9 μM RF (E). Proteoliposomes with 8 μM FMN (B), 11 μM FAD (D) or 6 μM RF (F). 1 mg mL^{-1} lipid suspensions of (proteo)liposomes without MV^{2+} encapsulated (continuous black lines). After photosensitiser additions (dotted lines), sample incubations in the dark for 5, 15, 30, 60 and 90 mins (continuous grey lines) were performed and subsequently were followed by ultracentrifugation to separate supernatants (dashed grey lines) from (proteo)liposome pellets that were resuspended in buffer (dashed black lines). Stirred samples in anaerobic 50 mM HEPES, 2 mM CaCl_2 , 10 mM KCl, 50 mM TEOA, pH 7 at 20 $^\circ\text{C}$. Path length 1 cm.

Strikingly different results were observed when similar dark incubations of (proteo)liposomes were performed in the presence of eosin Y, fluorescein or proflavin, Figure 4.6. There were negligible spectral changes when fluorescein or proflavin was incubated in the dark with (proteo)liposomes, Figure 4.6 C-F continuous grey lines. When eosin Y was incubated with (proteo)liposomes there were negligible changes to the scattering contributions of the absorbance spectra, but a red shift in the eosin Y absorbance maximum from 518 nm to 523 nm was observed, Figure 4.6 A-B continuous grey lines. It has been previously shown that the absorbance maxima of eosin Y shifts to higher wavelengths when it is in the presence of neutral and cationic detergent micelles or solvents with lower polarities.^[166–169] These perturbations in the absorbance spectra of eosin Y are due to hydrogen bonding with solvent, interactions with hydrophobic regions of neutral detergent micelles, or ionic interactions with cationic detergents.^[166–169]

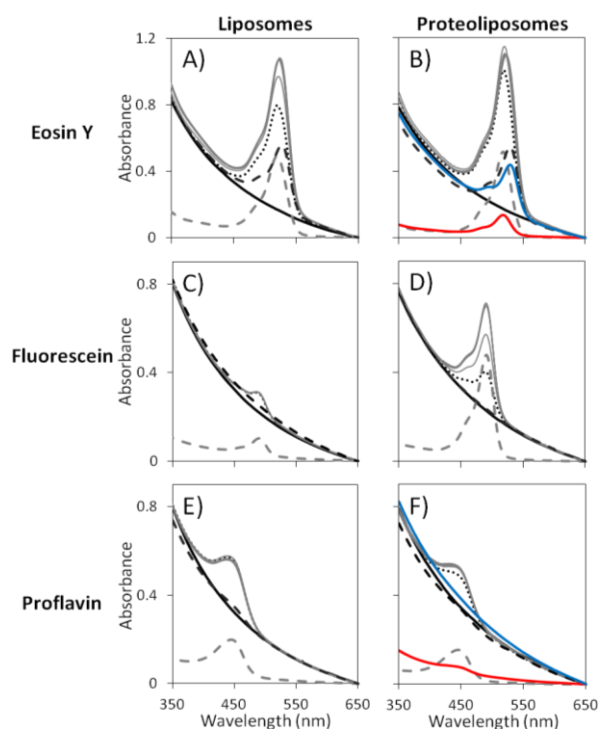


Figure 4.6. Dark Incubations of eosin Y, fluorescein and proflavin with (proteo)liposomes show photosensitiser-membrane interactions.

Liposomes with 8 μM eosin Y (A), 1 μM fluorescein (C) or 3 μM proflavin (E). Proteoliposomes with 10 μM eosin Y (B), 3 μM fluorescein (D) or 2 μM proflavin (F). 1 mg mL^{-1} lipid suspensions of (proteo)liposomes without MV^{2+} encapsulated (continuous black lines). After photosensitiser additions (dotted lines), sample incubations in the dark for 5, 15, 30, 60 and 90 mins (continuous grey lines) were performed and subsequently were followed by ultracentrifugation to separate supernatants (dashed grey lines) from (proteo)liposome pellets that were resuspended in buffer (dashed black lines). Resuspended proteoliposome suspensions from incubations with eosin Y and proflavin were ultracentrifuged a second time to again separate supernatants (red lines) from proteoliposome pellets that were resuspended in buffer (blue lines). Stirred samples in anaerobic 50 mM HEPES, 2 mM CaCl_2 , 10 mM KCl, 50 mM TEOA, pH 7 at 20 $^\circ\text{C}$. Path length 1 cm.

The absorbance spectra of the resuspended (proteo)liposome pellets and supernatants gathered after ultracentrifugation of these samples showed some eosin Y and proflavin associated with the lipid pellets, even if most remained in the supernatants, Figure 4.6 dashed lines. Additional ultracentrifugation and resuspension of these proteoliposomes were performed. This extra step proved that proflavin was only weakly associated with proteoliposomes as it was only located in the supernatant, whereas eosin Y was strongly associated and remained with lipid pellets, Figure 4.6 F and B respectively. The spectra of the resuspended (proteo)liposomes after incubations with fluorescein showed negligible fluorescein spectral features, indicating that it remained soluble within the supernatant.

The results from these three photosensitisers suggest that they do not disrupt liposome bilayers as there are negligible changes in scattering contributions of sample spectra during incubations. However; they do associate with these membranes in the binding strength order of eosin Y > proflavin > fluorescein. As these are charged photosensitisers (Table 3.2) and PC, which the (proteo)liposomes are made from, is a neutrally charged, zwitterionic phospholipid (Figure 1.8), it is thought that these photosensitisers could associate with hydrophobic regions of the bilayer. Such interactions would mimic interactions with the hydrophobic regions of neutral detergent micelles, which would be coupled with a similar red shift in the eosin Y absorbance maxima.^[166–168]

The ability of soluble organic compounds to partition from an aqueous phase into a more hydrophobic, organic phase can be quantified by partition coefficients. Partition coefficients are defined as the ratio of solute concentrations within two immiscible phases once at equilibrium, and can be obtained by mixing water containing a known solute concentration with appropriate volumes of octanol. Once equilibrium is reached the octanol can be separated and removed before the compound concentration remaining within the aqueous phase is calculated from spectroscopic measurements. Previous studies have compared partition coefficients of eosin Y and fluorescein under various experimental conditions at physiological pHs.^[170, 171] These studies showed the dianionic xanthene species that predominates at pH 7 is the most hydrophilic species, and the majority of eosin Y and fluorescein is found within aqueous phase with only some partition into cell membranes and organic matter.^[170, 171] It is thought xanthenes would be unable to cross a membrane (Figure 4.1 D) but would associate with the outer monolayer of a lipid membrane (Figure 4.1 B, C and E).^[172] This is due to their bulky tricyclic systems associating with the hydrophobic region of the bilayer but the anionic hydrophilic groups

remaining associated with the aqueous solution via hydrogen bonding. Proflavin is also an amphiphilic molecule with a bulky hydrophobic ring system and a cationic group, therefore it is likely to have a similar bilayer partitioning behaviour.

Extreme photobleaching of eosin Y, fluorescein and proflavin was observed during irradiations in the presence of liposomes which interfered with determining if these photosensitisers associated with liposomes under these conditions, Appendix 15 E-G. There were however no detectable changes in the liposome scattering during these incubations which suggests that upon irradiation these photosensitisers do not perturb the liposome bilayer, Appendix 14 E-G grey continuous lines.

Negligible spectral changes were observed when samples containing (proteo)liposomes and ruthenium complexes were left in the dark or irradiated, Figure 4.7 and Appendix 15 D and H grey continuous lines. Once these samples were ultracentrifuged, the spectral features associated with the ruthenium complexes remained with the supernatant, and the spectra of the resuspended (proteo)liposomes only exhibited scattering associated with lipid vesicles, Figure 4.7 and Appendix 15 D and H dashed lines. These results show the ruthenium complexes do not disrupt or associate with the (proteo)liposome membrane.

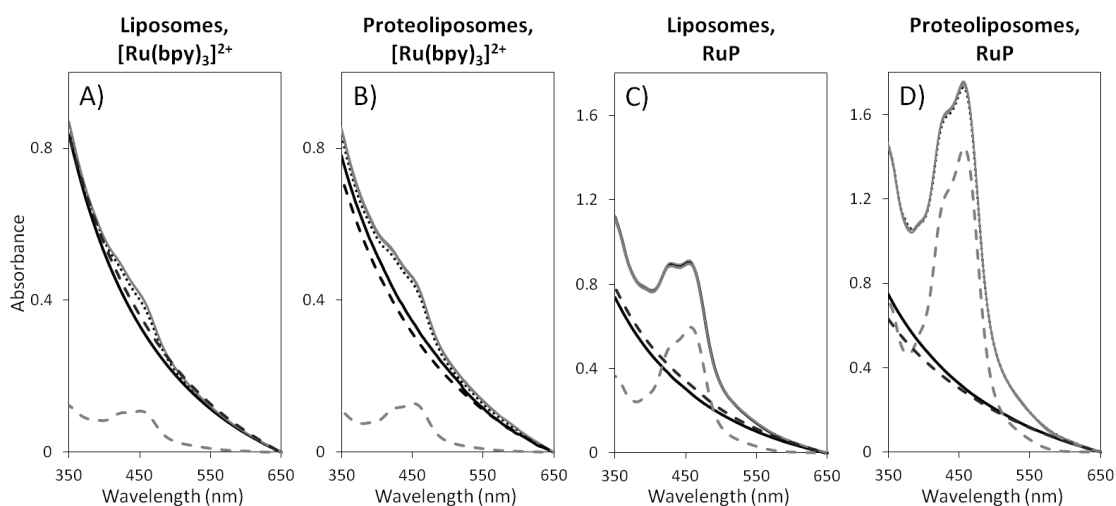


Figure 4.7. Dark incubations of ruthenium complexes with (proteo)liposomes show no photosensitiser-membrane interactions.

Liposomes with 5 μM $[\text{Ru}(\text{bpy})_3]^{2+}$ (A) or 6 μM RuP (C). Proteoliposomes with 7 μM $[\text{Ru}(\text{bpy})_3]^{2+}$ (B) or 139 μM RuP (D). 1 mg mL^{-1} lipid suspensions of (proteo)liposomes without MV^{2+} encapsulated (continuous black lines). After photosensitiser additions (dotted lines), sample incubations in the dark for 5, 15, 30, 60 and 90 mins (continuous grey lines) were performed and subsequently were followed by ultracentrifugation to separate supernatants (dashed grey lines) from (proteo)liposome pellets that were resuspended in buffer (dashed black lines). Stirred samples in anaerobic 50 mM HEPES, 2 mM CaCl_2 , 10 mM KCl, 50 mM TEOA, pH 7 at 20 $^\circ\text{C}$. Path length 1 cm.

These experiments indicated that (proteo)liposomes did not burst during irradiations or dark incubations with any of the studied photosensitisers. This was supported by DLS measurements that showed there were minimal variations in the average hydrodynamic radii of liposomes after dark incubations with or without photosensitisers, Table 4.1. Thus there is no evidence for the scenario of Figure 4.1 F for any of the studied photosensitisers. Ultracentrifugations proved that flavins and ruthenium complexes did not associate with (proteo)liposomes. However, eosin Y, proflavin and possibly fluorescein did associate with (proteo)liposomes, probably by partitioning into the hydrophobic region of the lipid bilayer, as illustrated schematically in Figure 4.1 B, C and E.

	Liposome Average Hydrodynamic Radius (nm)
RF	66 ± 13
FMN	73 ± 24
FAD	72 ± 24
Fluorescein	69 ± 16
Proflavin	67 ± 16
Eosin Y	69 ± 15
[Ru(bpy)₃]²⁺	72 ± 25
RuP	69 ± 23
No Photosensitiser	68 ± 23

Table 4.1. Liposome radii are unaffected by the presence of photosensitisers.

Average hydrodynamic radii gathered from DLS measurements of liposomes without encapsulated MV²⁺ after dark 90 mins incubation with or without photosensitisers.

The experiments described above provided information upon the photosensitisers' location and the subsequent liposome membrane stability. However, no information was obtained on whether: i) exchange occurred between the external and internal aqueous environments, Figure 4.1 E; or ii) if photosensitisers that associated with the membrane were within electron transfer distance of MtrCAB and/or the internal aqueous volume, Figure 4.1 B-C. It was decided to perform similar irradiations using liposomes containing MV²⁺ to ascertain whether the photosensitiser presence caused undesirable interactions with internally encapsulated MV²⁺. The reasoning behind this and results from the corresponding experiments are discussed below.

4.4 Methyl Viologen as a Probe of Liposome Permeability

As MV is a membrane-impermeable redox indicator, encapsulated MV²⁺ can be used as a probe of liposome permeability in the presence of external chemicals. Ideally if MV²⁺ is only located internally and the liposome bilayer is impermeable to photoexcited electrons

and photosensitisers then no photoreduction of encapsulated MV^{2+} should be detected with external photosensitisers and TEOA. Eosin Y, fluorescein, proflavin, $[Ru(bpy)_3]^{2+}$ and RuP all have photoreduction couples that are sufficiently negative to photoreduce MV^{2+} to MV^+ .^[9, 112, 118–120, 129] Experiments have previously demonstrated that these photosensitisers can perform light-driven, one-electron reductions of MV^{2+} , when in the presence of SEDs.^[133, 164, 165] For FMN, FAD and RF we are not aware there is an experimental precedent of MV^{2+} photoreduction. The flavin photoreduction potential ($E_m \approx -220$ mV) is thermodynamically unfavourable to carry out photoreduction of MV^{2+} ($E_m = -450$ mV); however, thermodynamic considerations using the Nernst equation suggest there is a possibility that flavins could carry out partial MV^{2+} photoreduction.^[90, 94, 140, 141]

The Nernst equation (Equation 4.1) relates the equilibrium potential, E , to the standard midpoint potential of a reduction couple, E_m , and the concentrations of the oxidised and reduced species, [Ox] and [Red] respectively; where R is the gas constant, T is the temperature, n is the number of electrons involved in the reduction and F is the Faraday constant. By rearranging the Nernst equation it is possible to predict the percentage of reduction that would be achieved when at any applied potential.

$$E = E_m + (RT/nF)\ln([Ox]/[Red]) \quad (4.1)$$

Constant irradiation of flavins causes the percentage of the reduced species present to become essentially 100 %, which then makes the actual acting photoreduction potential more reducing than that of the midpoint potential of -220 mV.^[90, 140, 141] The Nernst equation plot for the two-electron reduction of flavins shows that under this scenario the effective flavin photoreduction potential could be approximately -360 mV, Figure 4.8 dotted line. The Nernst equation plot for the one-electron reduction of MV^{2+} shows that when this potential is applied approximately 22 % photoreduction of MV^{2+} would be achieved, Figure 4.8 continuous lines. It can therefore be concluded that all flavins have the potential to carry out partial photoreduction of MV^{2+} .

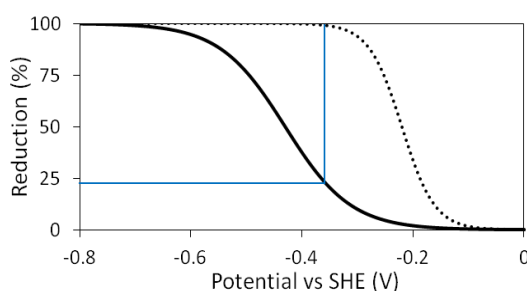


Figure 4.8. Comparison of Nernst equations of one-electron reduction of MV^{2+} (continuous line, $E_m = -440$ mV) and two-electron reduction of flavin (dotted line, $E_m \approx -220$ mV).

Within the following sections, the propensity of MV^{2+} for photoreduction by chosen photosensitisers under the experimental conditions described above is discussed prior to subsequent comparison to the behaviours seen when liposomes containing MV^{2+} were irradiated in the presence of these photosensitisers. To finalise, MV^{2+} leakage from liposomes during incubations in the presence or absence of photosensitisers is discussed.

4.4.1 Propensity of Methyl Viologen for Light-Driven Reduction

To assess the speed and extent of MV^{2+} photoreduction by photosensitisers selected for this study, irradiations of anaerobic solutions of 50 μM MV^{2+} were carried out in the presence of 50 mM TEOA and ~ 10 μM photosensitiser over 90 mins. Spectra obtained after additions of one of the eight photosensitisers were typical of MV^{2+} . Subsequent addition of the chemical reductant sodium dithionite ($E_m \approx -500$ mV) causes the appearance of peaks at 410 and 606 nm in accordance with the one-electron reduction of MV^{2+} to MV^+ , Figure 4.3 B dotted grey line.^[95] By following changes in intensity at 606 nm the photoreduction of MV^{2+} can be monitored. MV^+ present can be determined using the extinction coefficient of 13.7 $mM^{-1} cm^{-1}$ at 606 nm, and subsequently the extent of photoreduction can be calculated with reference to the total 50 μM of MV present. Irradiations of MV^{2+} by all photosensitisers under the conditions described above are presented within the following subsections.

4.4.1.1 Ruthenium Complexes

Irradiations of 50 μM MV^{2+} in the presence of ~ 10 μM ruthenium complexes resulted in the gradual increase of maxima at 410 and 606 nm which correlated to the photoreduction of MV^{2+} , Figure 4.9. Both ruthenium complexes possess photoreduction couples below -840 mV which should be able to achieve full photoreduction of MV^{2+} , Table 3.3.^[112, 118–120] However, as previously stated in Section 3.9, it is not uncommon for systems with favourable thermodynamics to be hindered by the relative kinetics associated with electron transfers and non-productive, competitive processes involving recombinations and futile redox cycles. Faster MV^{2+} photoreduction to greater maximum extents were observed during irradiations when MV^{2+} was present in 500 μM excess of 10 μM ruthenium complexes, Figure 4.9 inserts. This confirms that the kinetic limitation seen during slow MV^{2+} photoreductions by ruthenium complexes was most likely due to rapid charge recombinations of the photoexcited ruthenium complex.

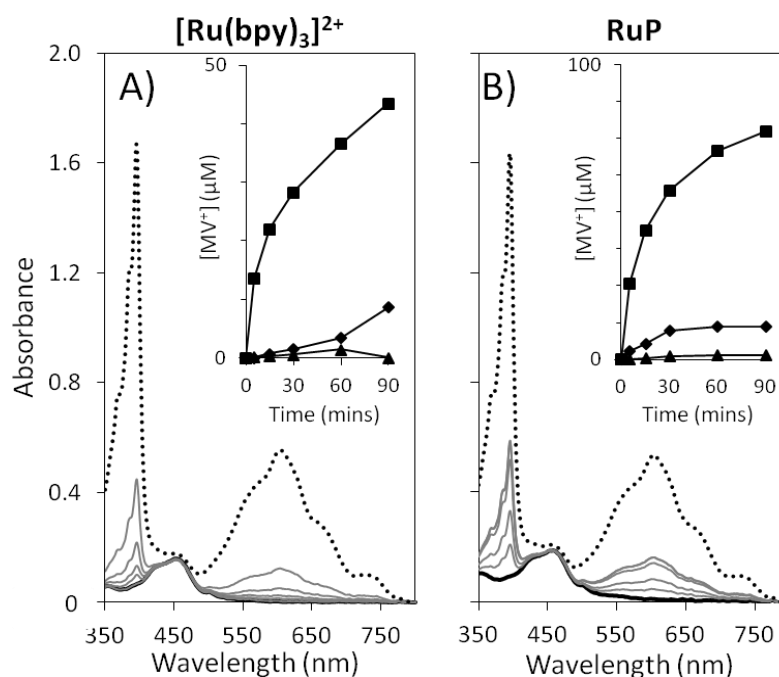


Figure 4.9. MV²⁺ photoreduction by ruthenium complexes.

50 μM MV²⁺ with either 11 μM [Ru(bpy)₃]²⁺ (A) or 18 μM RuP (B). As prepared samples (continuous black lines) were irradiated or 5, 15, 30, 60 and 90 mins at 2 kW m⁻² (continuous grey lines) prior to addition of excess of dithionite (dotted lines). Inserts show amount of MV²⁺ reduced to MV⁺, calculated using MV⁺ extinction coefficient of 13.7 mM⁻¹ cm⁻¹ at 606 nm, for MV²⁺:PS ratios of 50:1 (squares, 500 μM MV²⁺), 5:1 (diamonds, 50 μM MV²⁺) and 0.5:1 (triangles, 5 μM MV²⁺) with ~ 10 μM ruthenium complex. Stirred samples in anaerobic 50 mM HEPES, 2 mM CaCl₂, 10 mM KCl, 50 mM TEOA, pH 7 at 20 °C. Path length 1 cm.

4.4.1.2 Flavins

Figure 4.10 shows spectra obtained during irradiations of 50 μM MV²⁺ in the presence of 10 μM flavins. The spectral features of oxidised flavin decreased during irradiations indicating that fully reduced flavin was formed; however, only with RF was any MV²⁺ reduction observed. Inspection of these spectral changes confirmed that absorbance changes at 606 nm were dominated by contributions from the MV²⁺ photoreduction with no influence from flavin spectral changes. The maximum extent of MV²⁺ photoreduction achieved by RF was calculated to be ~ 20 %, whereas the extent of MV²⁺ photoreduction did not exceed 2 % for either FMN or FAD, Figure 4.10 inserts. This extent of MV²⁺ photoreduction achieved by RF confirms thermodynamic predictions that flavins do have the potential to carry out partial MV²⁺ photoreductions during irradiations, as described in Section 4.4.

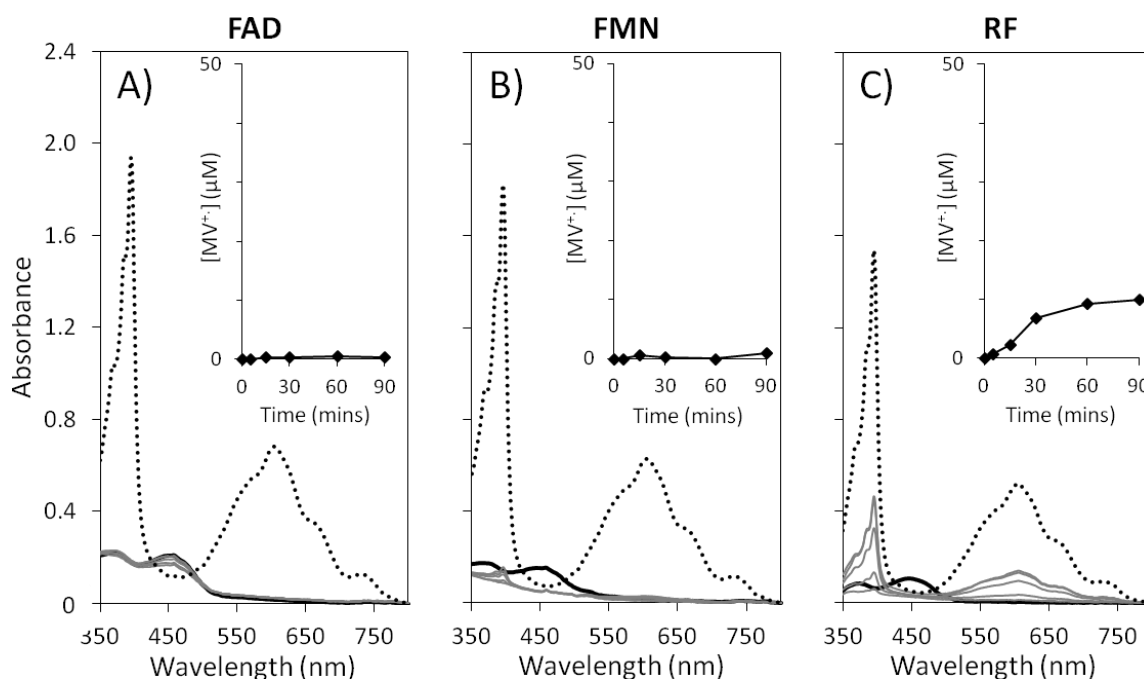


Figure 4.10. MV^{2+} photoreduction by flavin photosensitisers.

50 μM MV^{2+} with $\sim 10 \mu M$ of either FAD (A), FMN (B) or RF (C). As prepared samples (continuous black lines) were irradiated for 5, 15, 30, 60 and 90 mins at 2 kW m^{-2} (continuous grey lines) prior to addition of excess dithionite (dotted lines). Inserts show amount of MV^{2+} reduced to MV^+ , calculated using MV^+ extinction coefficient of $13.7 \text{ mM}^{-1} \text{ cm}^{-1}$ at 606 nm. Stirred samples in anaerobic 50 mM HEPES, 2 mM CaCl_2 , 10 mM KCl, 50 mM TEOA, pH 7 at 20°C . Path length 1 cm.

More detailed inspection of spectra obtained during irradiation of FMN and MV^{2+} showed the gradual appearance of the 410 nm peak associated with formation of MV^+ , which was absent during irradiation of FAD with MV^{2+} , Figure 4.10 B and A respectively. The rates of flavin photoreduction and subsequent MV^{2+} photoreduction that varied with flavin identity ($\text{RF} > \text{FMN} > \text{FAD}$) could possibly be explained by the size of the ribityl side chains, with the bigger the ribityl chain hindering photoreduction of MV^{2+} . It is thought however that all flavins would be able to reach $\sim 20\%$ MV^{2+} photoreduction if irradiated for longer time periods.

4.4.1.3 Eosin Y, Fluorescein and Proflavin

Figure 4.11 shows spectra obtained during irradiations of 50 μM MV^{2+} in the presence of 10 μM of eosin Y, fluorescein or proflavin. Irradiations of MV^{2+} with eosin Y or proflavin resulted in the increase of peaks with maxima at 410 and 606 nm which correlated to the complete photoreduction of 50 μM MV^{2+} within 30 mins, Figure 4.11 A and C. During the remaining 60 mins of irradiation the absorbance at 606 nm did however decrease and then completely disappear, indicative of the loss of MV^+ , Figure 4.11 inserts. Similar results

were observed during irradiations of MV^{2+} in the presence of excess fluorescein; however, when MV^{2+} was present in excess only partial MV^{2+} photoreduction was observed without the subsequent loss of MV^+ , Figure 4.11.B.

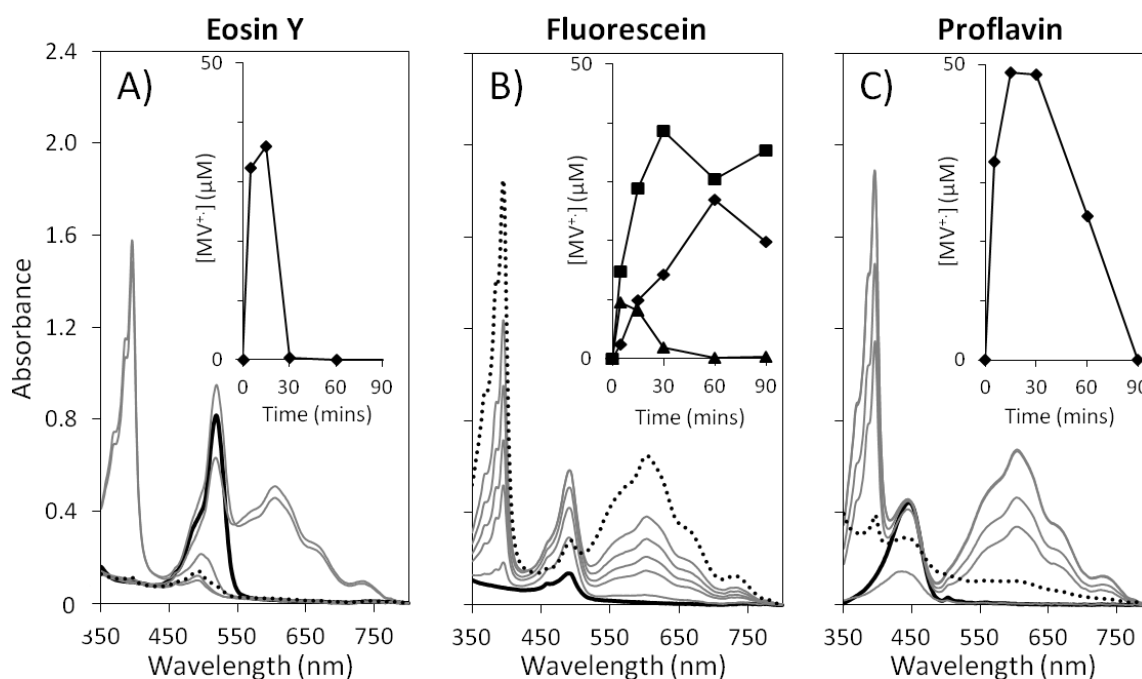


Figure 4.11. MV^{2+} photoreduction by eosin Y, fluorescein and proflavin.

50 μM MV^{2+} with either 10 μM eosin Y (A), 2 μM fluorescein (B) or 6 μM proflavin (C). As prepared samples (continuous black lines) were irradiated for 5, 15, 30, 60 and 90 mins at 2 $kW\ m^{-2}$ (continuous grey lines) prior to addition of excess dithionite (dotted black lines). Inserts show amount of MV^{2+} reduced to MV^+ , calculated using MV^+ extinction coefficient of 13.7 $mM^{-1}\ cm^{-1}$ at 606 nm, for MV^{2+} :PS ratios of 50:1 (squares, 500 μM MV^{2+}), 5:1 (diamonds, 50 μM MV^{2+}) and 0.5:1 (triangles, 5 μM MV^{2+}) with $\sim 10\ \mu M$ photosensitiser. Stirred samples in anaerobic 50 mM HEPES, 2 mM $CaCl_2$, 10 mM KCl, 50 mM TEOA, pH 7 at 20 $^{\circ}C$. Path length 1 cm.

Addition of dithionite to each of these photosensitiser- MV solutions following irradiation did not result in the appearance of 606 nm peak that is associated with MV^+ , Figure 4.11 dotted black lines. As a consequence it was considered that formation and subsequent disappearance of MV^+ during these irradiations could be due to the complete reduction of MV^{2+} to form the essentially colourless MV^0 species. Complete photoreduction of MV^{2+} during these irradiations was thermodynamically possible as eosin Y, fluorescein and proflavin all possess photoreduction potentials similar to or more negative than that of the MV^+/MV^0 redox couple ($E_m = -900\ mV$), Table 3.2.^[9, 94, 129] To assess redox properties of these photosensitiser- MV solutions before and after irradiation they were characterised by cyclic voltammetry.

Cyclic voltammograms were separately obtained in ambient light for 200 μM of MV^{2+} , eosin Y, fluorescein, or proflavin to provide information on reduction and oxidation

of their ground states. The cyclic voltammogram obtained for MV^{2+} had two reversible redox pairs with mid-point potentials of -430 and -740 mV, which are similar to those reported previously for the MV^{2+}/MV^+ and MV^+/MV^0 redox couples respectively, Figure 4.12 A.^[94] The cyclic voltammograms obtained for eosin Y and fluorescein were very similar to each other with both possessing an asymmetric negative peak associated with the semi-reversible one-electron reduction of these xanthenes, Figure 4.12 B and D. The cyclic voltammogram obtained for proflavin showed widely separated peaks for reduction (negative peak) and oxidation (positive peak) due to the one-electron, one proton transfer between the PFH^+ and $PF^{\cdot-}$ species, Figure 4.12 F.

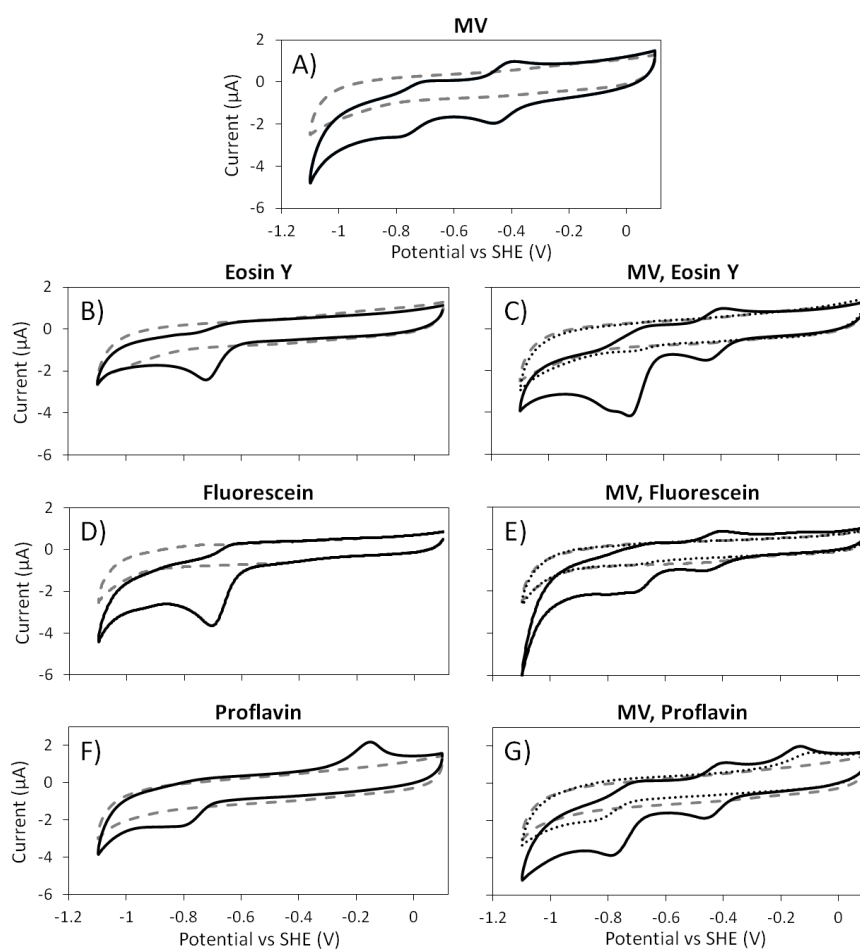


Figure 4.12. Irradiation of MV^{2+} in presence of eosin Y, fluorescein or proflavin, affects their electrochemistry.

Cyclic voltammograms of MV^{2+} (A); eosin Y (B); MV^{2+} and eosin Y (C); fluorescein (D); MV^{2+} and fluorescein (E); proflavin (F); and MV^{2+} and proflavin (G). All species present at 200 μ M. Baselines (dashed lines) were recorded prior to as prepared sample cyclic voltammograms (continuous black lines). Similar solutions of MV^{2+} with photosensitizer were prepared for irradiation at 2 kW m^{-2} until blue colour of MV^+ was obtained and subsequently lost, Appendix 16. Cyclic voltammograms of these irradiated samples were then recorded (dotted black lines). Anaerobic samples in 50 mM HEPES, 2 mM CaCl_2 , 10 mM KCl, 50 mM TEOA, pH 7. Recorded at 20 mV s^{-1} , 20 $^\circ\text{C}$.

Cyclic voltammograms of 200 μM MV^{2+} in the presence of 200 μM photosensitisers were obtained before and after irradiations similar to those described above, Figure 4.12. Cyclic voltammograms of MV^{2+} with either eosin Y, fluorescein or proflavin prior to irradiation were essentially combinations of the individual cyclic voltammogram features of MV^{2+} and the corresponding photosensitiser, Figure 4.12 C, E and G continuous lines. Formation and subsequent disappearance of MV^+ in the solutions was monitored via the 606 nm absorbance peak and irradiations were only stopped once this peak had completely disappeared, Appendix 16. The cyclic voltammograms of these solutions after irradiation were strikingly different to those obtained prior to irradiation, with photosensitiser redox peaks being severely diminished and peaks associated with the MV redox couples having completely disappeared, Figure 4.12 C, E and G dotted lines.

These results show that these photosensitisers and MV are both being consumed during these irradiations and must react to form colourless, redox-inactive molecules. As the blue colour of the MV^+ species was observed during these irradiations, MV^+ must be formed prior to the formation of these redox-inactive molecules. The MV and photosensitiser species which actually react to form this redox-inactive molecule, and the mechanism by which this happens, is unknown and was beyond the scope of this work.

4.4.2 Irradiation of Liposomes Containing Methyl Viologen

To assess if photoreduction of MV^{2+} encapsulated with liposomes was possible without MtrCAB acting as an electron conduit, irradiations of 1 mg mL⁻¹ lipid suspensions of liposomes containing $\sim 20 \mu\text{M}$ MV^{2+} were carried out in the presence of 50 mM TEOA and $\sim 10 \mu\text{M}$ photosensitiser over 90 mins. Spectra obtained after additions of one of the eight photosensitisers were typical to that of liposomes containing MV^{2+} . Subsequent additions of the chemical reductant sodium dithionite ($E_m \approx -500$ mV) and Triton X-100 caused the appearance of peaks at 410 and 606 nm in accordance with the one-electron reduction of MV^{2+} to MV^+ , Figure 4.3 B dotted grey line.^[95] The concentration of MV^+ present was determined after liposome solubilisation using the extinction coefficient of 13.7 mM⁻¹ cm⁻¹ at 606 nm. By following changes in intensity at 606 nm the photoreduction of MV^{2+} can be monitored. The MV^+ present during irradiation, prior to liposome solubilisation, was determined using the extinction coefficient of 11.5 mM⁻¹ cm⁻¹ at 606 nm, and subsequently the extent of photoreduction can be calculated with reference to

this and the total concentration of MV^+ present after liposome solubilisation. Irradiations of liposomes containing MV^{2+} by all photosensitisers under the conditions described above are presented within the following subsections.

To ensure the liposome membrane was stable and encapsulated MV^{2+} was not released into the external solution during irradiation, an addition of dithionite to a liposome suspension was made after 90 mins irradiation, Figure 4.3 A. Spectra recorded after irradiation and dithionite addition showed minimal changes in accordance with membrane stability, Figure 4.3 A grey lines and dotted black line respectively.

4.4.2.1 Ruthenium Complexes

Irradiations of liposomes containing MV^{2+} in the presence of Ru(II) dyes resulted in no detectable spectral changes which related to MV^{2+} photoreduction or loss of liposome membrane stability, Figure 4.13. Bearing in mind Ru(II) dyes were able to photoreduce MV^{2+} in solution under identical conditions, these results imply that ruthenium complexes do not disrupt liposome membranes to carryout photoreduction of MV^{2+} in liposomes.

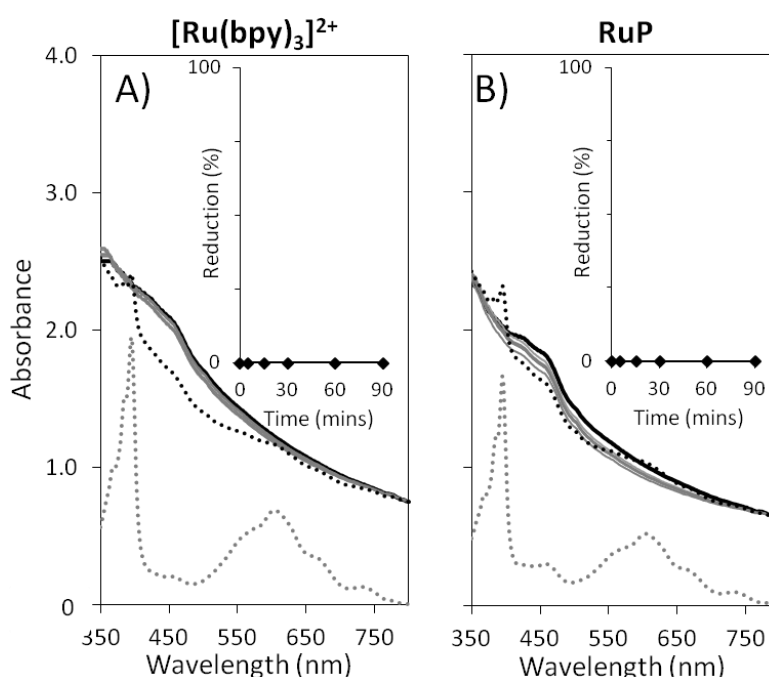


Figure 4.13. No photoreduction of MV^{2+} within liposomes by Ru(II) complexes.

1 mg mL⁻¹ lipid suspensions of MV^{2+} -containing liposomes with either 14 μ M $[Ru(bpy)_3]^{2+}$ (A) or 29 μ M RuP (B). As prepared samples (continuous black lines) were irradiated or 5, 15, 30, 60 and 90 mins at 2 kW m⁻² (continuous grey lines) prior to addition of excess dithionite (dotted black lines). Addition of excess Triton X-100 to dithionite incubated samples (dotted grey lines) showed \sim 22 μ M MV^+ was present after being released from liposomes. Inserts show extent of MV^{2+} reduction during irradiation, monitored via 606 nm absorbance. See text for calculation details. Stirred samples in anaerobic 50 mM HEPES, 2 mM CaCl₂, 10 mM KCl, 50 mM TEOA, pH 7 at 20 °C. Path length 1 cm.

4.4.2.2 Flavins

Figure 4.14 shows spectra obtained during irradiations of MV^{2+} -containing liposomes in the presence of $\sim 10 \mu\text{M}$ flavins. The spectral features of oxidised flavin decreased during irradiations indicating that fully reduced flavin was formed; however, there were no detectable spectral changes which related to MV^{2+} photoreduction or loss of liposome membrane stability, Figure 4.14. Bearing in mind that RF was able to carry out partial photoreduction of MV^{2+} , it is noteworthy that loss of liposome stability and photoreduction of MV^{2+} was not observed during irradiations of MV^{2+} -containing liposomes in the presence of RF. This implies that RF does not disrupt the liposome bilayer to allow the photoreduction of internally compartmentalised MV^{2+} within liposomes. From these experiments we can conclude that FMN and FAD do not disrupt the liposome membrane; however, as no significant photoreduction of MV^{2+} was observed in solution it can only be assumed that these behave like RF and cannot photoreduce liposome encapsulated MV^{2+} .

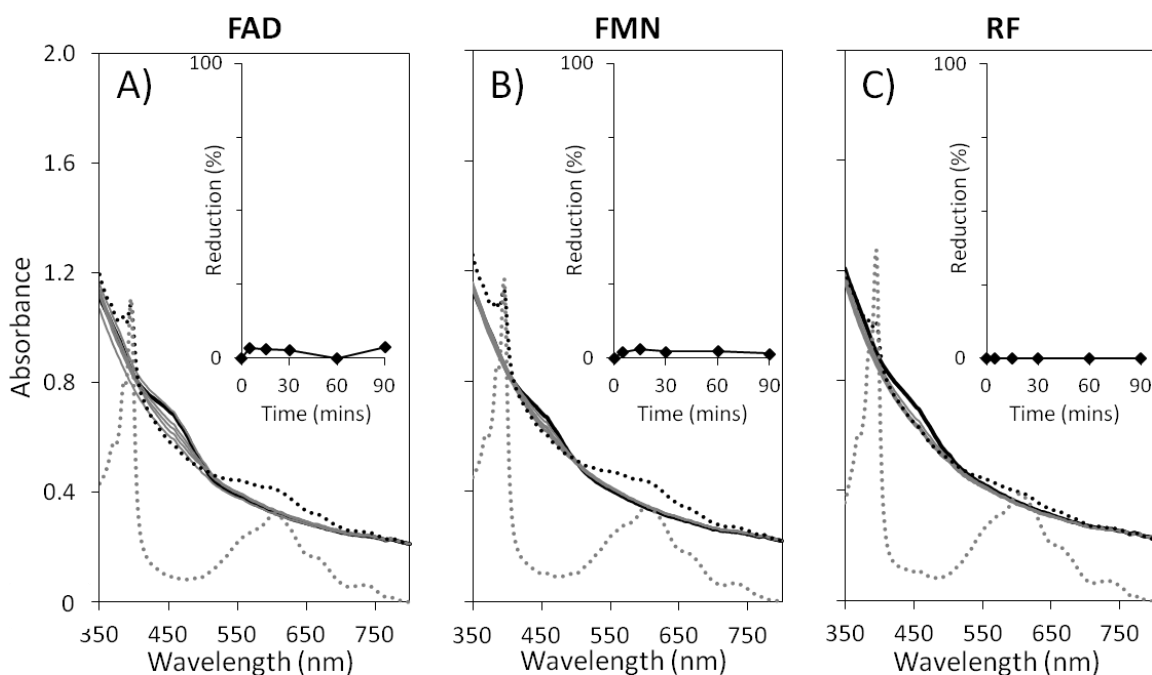


Figure 4.14. No photoreduction of MV^{2+} within liposomes by flavin photosensitisers.

1 mg mL^{-1} lipid suspensions of MV^{2+} -containing liposomes with $\sim 10 \mu\text{M}$ of either FAD (A), FMN (B) or RF (C). As prepared samples (continuous black lines) were irradiated for 5, 15, 30, 60 and 90 mins at 2 kW m^{-2} (continuous grey lines) prior to addition of excess dithionite (dotted black lines). Addition of excess Triton X-100 to dithionite incubated samples (dotted grey lines) showed $\sim 22 \mu\text{M}$ MV^+ was present after being released from liposomes. Inserts show extent of MV^{2+} reduction during irradiation, monitored via 606 nm absorbance. See text for calculation details. Stirred samples in anaerobic 50 mM HEPES, 2 mM CaCl_2 , 10 mM KCl, 50 mM TEOA, pH 7 at 20°C . Path length 1 cm.

4.4.2.3 Eosin Y, Fluorescein and Proflavin

Irradiations of MV^{2+} -containing liposomes in the presence of eosin Y, fluorescein or proflavin resulted in the photoreduction of encapsulated MV^{2+} prior to the subsequent disappearance of MV^+ , Figure 4.15. These disappearances of MV^+ is presumably associated with the formation of the colourless redox indicative molecules like those seen when solutions of MV^{2+} in the presence of eosin Y, fluorescein and proflavin were irradiated, as described in Section 4.4.1.3.

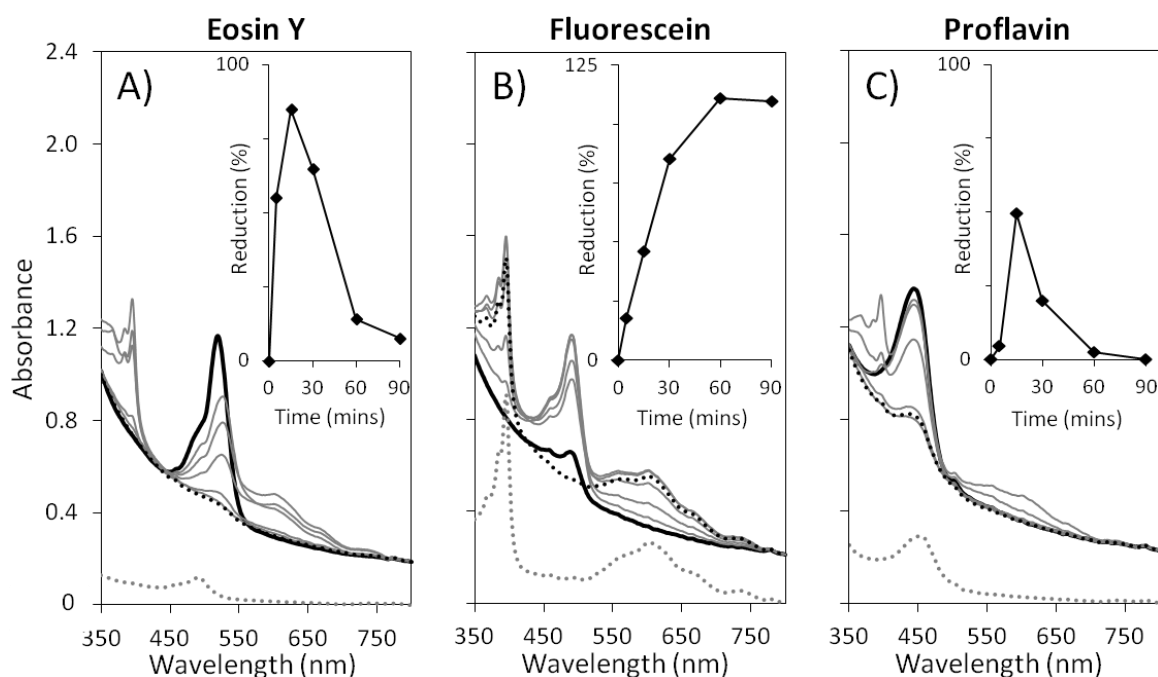


Figure 4.15. Photoreduction of MV^{2+} and subsequent photosensitiser-MV complex formation observed during irradiations of liposomes with eosin Y, fluorescein and proflavin.

1 mg mL⁻¹ lipid suspensions of MV^{2+} -containing liposomes with either 9 μ M eosin Y (A), 2 μ M fluorescein (B) or 8 μ M proflavin (C). As prepared samples (continuous black lines) were irradiated for 5, 15, 30, 60 and 90 mins at 2 kW m⁻² (continuous grey lines) prior to addition of excess dithionite (dotted black lines). Addition of excess Triton X-100 to dithionite incubated samples (dotted grey lines) showed ~22 μ M MV^+ was present after being released from (proteo)liposomes. Inserts show extent of MV^{2+} reduction during irradiation, monitored via 606 nm absorbance. See text for calculation details. Stirred samples in anaerobic 50 mM HEPES, 2 mM CaCl₂, 10 mM KCl, 50 mM TEOA, pH 7 at 20 °C. Path length 1 cm.

Taken together the results indicate that eosin Y, fluorescein and proflavin are able to photoreduce MV^{2+} encapsulated within liposomes without the need of MtrCAB being present. These photosensitisers can bind to but not cross liposome membranes, therefore the possible mechanisms which would allow the complete photoreduction of compartmentalised MV^{2+} include: i) photosensitisers being within electron transfer distance to photoreduce compartmentalised MV^{2+} (Figure 4.1 C); ii) photosensitisers

causing partial disruption of liposome membrane to allow the release of and subsequent direct photoreduction of MV^{2+} (Figure 4.1 E); or iii) a new theory where any minuscule amount of MV^{2+} remaining within the external solution after liposome preparation reacts with these photosensitisers to form a membrane-impermeable species which assists in reducing internal MV^{2+} . This new theory comes from the possibility that non-encapsulated MV^{2+} could form the membrane-impermeable MV^0 or redox-inactive MV-photosensitiser complexes that are probably membrane-impermeable themselves. These experiments do show that liposomes containing MV^{2+} do not burst during irradiations with eosin Y, fluorescein or proflavin, which rules out a mechanism like that envisioned in Figure 4.1 F.

4.4.3 Assessment of Methyl Viologen Leakage from Liposomes in Presence of Photosensitisers

In light of the results presented above it was of interest to obtain an independent assessment of the location of MV^{2+} following incubations of MV^{2+} -containing liposomes with photosensitisers. It was expected that this would confirm MV^{2+} was confined to the interior of liposomes when in the presence of externally located flavins and ruthenium complexes. For eosin Y, proflavin and fluorescein, confinement of MV^{2+} within liposomes would indicate photosensitiser incorporation into the liposome bilayer allows internalised reduction of MV^{2+} , as envisioned in Figure 4.1 C. However, the presence of MV^{2+} in the external solution would indicate change in permeability of the liposome bilayer to MV such that photoreduction may occur outside the liposome, as envisioned in Figure 4.1 E.

Experiments in which dark and light incubations of liposomes containing MV^{2+} in the absence or presence of photosensitisers were performed to assess whether the presence of the photosensitisers resulted in the leakage or exchange of compartmentalised MV with external solutions, Figure 4.1 E. Anaerobic incubations of MV^{2+} -containing liposomes suspensions (1 mg mL^{-1} lipid) were carried out in the presence of excess TEOA and $\sim 10 \text{ }\mu\text{M}$ photosensitiser over 30 mins either in darkness or under 2 kW m^{-2} irradiation. This time duration was chosen to avoid the light-driven formation of MV-photosensitiser complexes. After incubations were complete, samples were centrifuged to separate solutions from pelleted liposomes which were subsequently resuspended in an identical buffer volume. Additions of an excess of dithionite were added to both of these fractions to reduce any non-encapsulated MV^{2+} before complete reduction of all MV^{2+} was achieved via additions of excess anaerobic Triton X-100. Before photosensitiser additions the

absorbance scattering spectra were typical of those of liposomes containing fully oxidised MV^{2+} , and dithionite additions gave absorbance peaks associated with MV^+ .

Detailed inspection of spectra obtained following dark incubations of liposomes in the presence or absence of photosensitisers typically showed some non-encapsulated MV^{2+} in both the supernatants and resuspended liposome pellets of all samples, Figures 4.16 and 4.17. This detectable level of non-encapsulated MV^{2+} was most likely to be induced by the centrifugation of these samples. The total amounts of MV^{2+} observed in these samples after the additions of Triton X-100 were independent to the photosensitiser present.

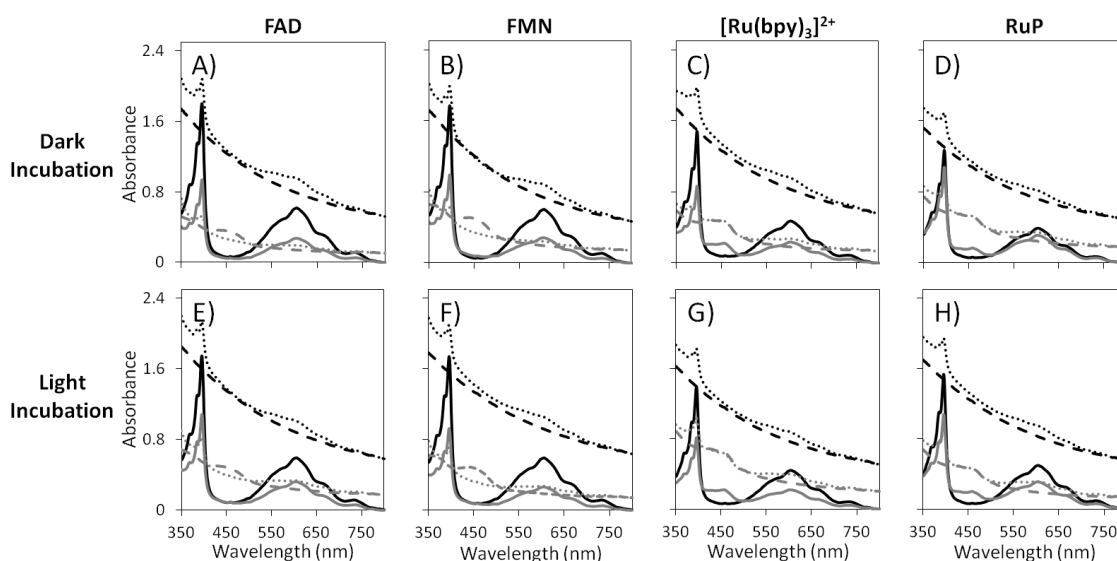


Figure 4.16. MV^{2+} leakage from liposomes after dark or light incubation, in presence of flavins or ruthenium complexes.

1 mg mL^{-1} lipid suspensions of MV^{2+} -containing liposomes in the presence of $\sim 10 \mu\text{M}$ of FAD (A and E), FMN (B and F), $[\text{Ru}(\text{bpy})_3]^{2+}$ (C and G) or RuP (D and H). As prepared samples were incubated for 30 mins under either dark (A, B, C and D) or light conditions (E, F, G and H). Irradiations were performed at 2 kW m^{-2} . Incubations were followed by centrifugation to separate supernatants (dashed grey lines) from liposome pellets that were resuspended in buffer (dashed black lines). Additions of excess dithionite to supernatants (dotted grey lines) and resuspended liposome pellets (black dotted lines) were followed by addition of excess Triton X-100 to dithionite incubated samples (continuous grey and black lines respectively). Samples in anaerobic 50 mM HEPES, 2 mM CaCl_2 , 10 mM KCl, 50 mM TEOA, pH 7 at $20 \text{ }^\circ\text{C}$. Path length 1 cm.

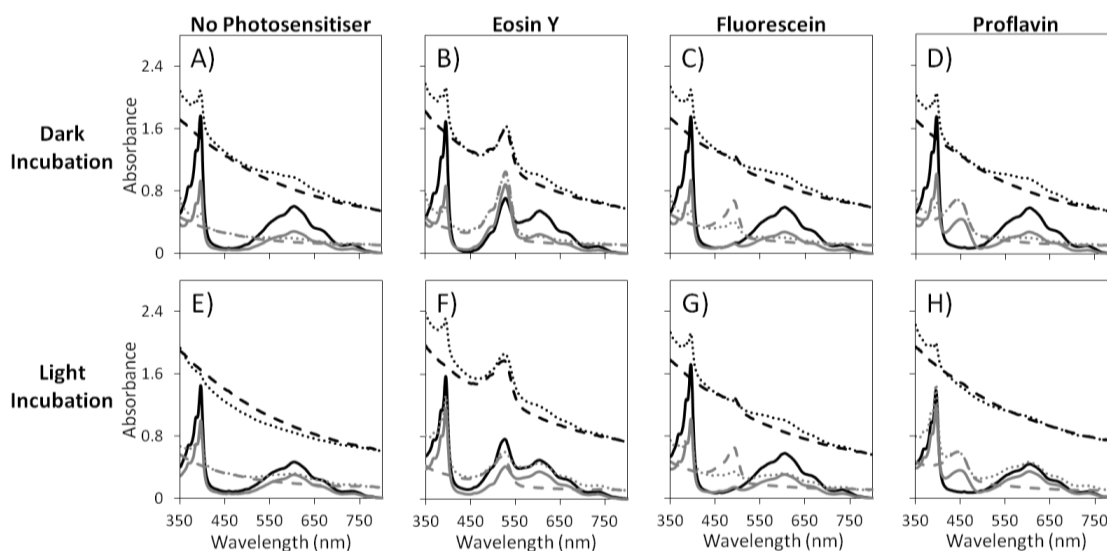


Figure 4.17. MV²⁺ leakage from liposomes after dark or light incubation, in presence of xanthene or proflavin, or their absence.

1 mg mL⁻¹ lipid suspensions of MV²⁺-containing liposomes in the absence of photosensitiser (A and E) or in the presence of ~ 10 μM of eosin Y (B and F), fluorescein (C and G) or proflavin (D and H). As prepared samples were incubated for 30 mins under either dark (A, B, C and D) or light conditions (E, F, G and H). Irradiations were performed at 2 kW m⁻². Incubations were followed by centrifugation to separate supernatants (dashed grey lines) from liposome pellets that were resuspended in buffer (dashed black lines). Additions of excess dithionite to supernatants (dotted grey lines) and resuspended liposome pellets (dotted black lines) were followed by additions of excess Triton X-100 to dithionite incubated samples (continuous grey and black lines respectively). Samples in anaerobic 50 mM HEPES, 2 mM CaCl₂, 10 mM KCl, 50 mM TEOA, pH 7 at 20 °C. Path length 1 cm.

Similar amounts of non-encapsulated MV²⁺ and total MV²⁺ associated with the liposomes and the supernatants were detected when MV²⁺-containing liposomes were irradiated in absence of a photosensitiser or in the presence of a flavin or a ruthenium complex, Figure 4.16 E-H and Figure 4.17 E. A striking difference was seen when MV²⁺-containing liposomes were irradiated in the presence of eosin Y, fluorescein or proflavin, Figure 4.17 F-H. In these experiments greater levels of MV²⁺ were observed in their respective supernatants.

The percentages of the total dithionite accessible MV²⁺ seen within these mixtures mirror these observations, Figure 4.18. These experiments generally saw 32 ± 6 % of the total MV²⁺ within these liposome suspensions was non-encapsulated after sample centrifugation. Dramatically increased percentages of non-encapsulated MV²⁺ were however observed when MV²⁺-containing liposomes were irradiated in the presence of eosin Y, fluorescein or proflavin, with 65 %, 45 % and 50 % of MV²⁺ being dithionite accessible respectively.

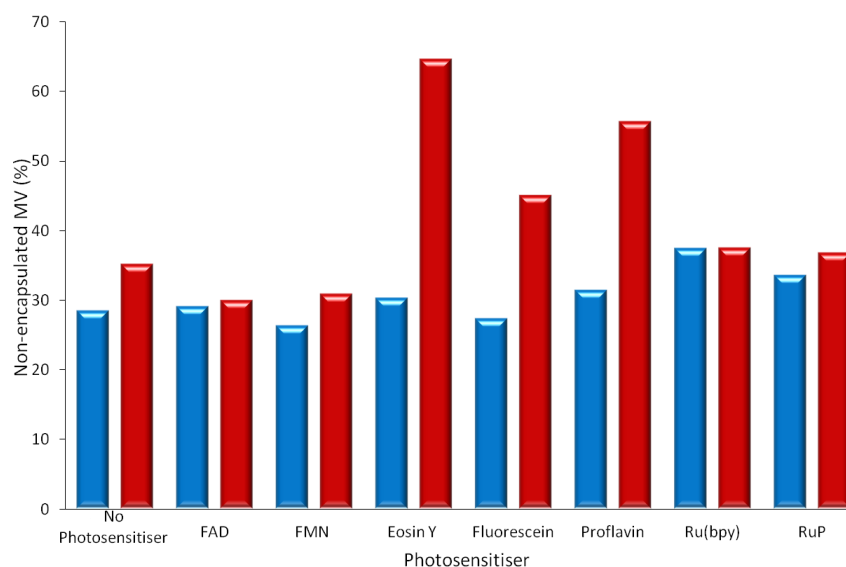


Figure 4.18. Summary of MV^{2+} leakage from liposomes after dark (blue) or light (red) incubations performed in the absence or presence of photosensitisers.

This comparison is representative of experiments shown in Figures 4.16 and 4.17. Percentage of non-encapsulated MV^{2+} was calculated via comparing concentrations of MV^+ present after addition of excess dithionite to supernatants and resuspended liposomes (Figures 4.16 and 4.17, dotted lines) to the total concentration of MV^+ present after addition of Triton X-100 to supernatants and resuspended liposomes (Figures 4.16 and 4.17, continuous lines).

Concentrations of MV^+ in aqueous solutions and within liposomes suspensions were calculated using extinction coefficients of 13.7 and $11.5 \text{ mM}^{-1} \text{ cm}^{-1}$, respectively, at 606 nm . Stirred samples in anaerobic 50 mM HEPES , 2 mM CaCl_2 , 10 mM KCl , 50 mM TEOA , $\text{pH } 7$ at $20 \text{ }^\circ\text{C}$.

These results show that upon irradiation eosin Y, fluorescein and proflavin lead to the leakage of compartmentalised MV^{2+} from liposomes, as presented in Figure 4.1 E. The extent of MV^{2+} that is released into the external solution by these photosensitisers goes in the order of eosin Y > proflavin > fluorescein; however, the mechanism by which these photosensitisers allow this exchange between the internal and external solutions is unknown. These results do however show that upon irradiation flavin and ruthenium complexes do not lead to the leakage of compartmentalised MV^{2+} encapsulated within liposomes, unlike in Figure 4.1.E. The relatively high percentage of non-encapsulated MV^{2+} detected after sample centrifugation during these experiments does not detract from the main conclusions drawn here.

4.5 Discussion

During the course of this work there were a number of complications which hindered obtaining repeatable results. This discussion describes these complications, their possible origins and the attempts to overcome them.

During this work it was discovered that the concentration of Triton X-100 present during proteoliposome preparation had a major impact on MtrCAB incorporation and proteoliposome formation, Section 4.2. It was found that the presence of too much Triton X-100 resulted in liposome lysis and too little would hinder protein incorporation. To control this variation the percentage of Triton X-100 in MtrCAB samples was assessed and adjusted accordingly to ~ 2 % prior to proteoliposome preparations.

It was also discovered that complete removal of non-encapsulated MV^{2+} was not always achieved and the amount of non-encapsulated MV^{2+} varied between proteoliposomes and liposomes originating from the same preparation. A variety of different methods was tried to ensure complete removal of non-encapsulated MV^{2+} after (proteo)liposomes preparation, including: extra ultracentrifugations; incubations with Biobeads to remove hydrophobic MV^{2+} ; separations via columns; and incubations with chelex beads to remove charged MV^{2+} . All of these methods however resulted in some non-encapsulated MV^{2+} remaining or in the lysis of (proteo)liposomes and subsequent increase in non-encapsulated MV^{2+} . MV^{2+} has been previously reported to bind to the surface of lipid vesicles, including those made of PC.^[173, 174] This binding was suggested to be driven by hydrophobic interactions between the viologen alkyl chains and the hydrophobic region of the lipid membrane.^[174] It is therefore entirely possible that complete removal of external MV^{2+} from (proteo)liposomes suspensions would be impossible. The presence of any non-encapsulated MV^{2+} could account for formation of redox-inactive molecules and complete reduction of compartmentalised MV^{2+} within liposomes during irradiations in the presence of eosin Y, fluorescein and proflavin.

4.6 Conclusions

Within this chapter a number of conclusions have been made about interactions between photosensitisers and (proteo)liposomes with and without encapsulated MV^{2+} , as summarised in Table 4.2. (Proteo)liposomes are not burst during irradiation or dark incubations with any of the photosensitisers present, Figure 4.1.F. Flavins and ruthenium

complexes do not associate with or perturb liposome membranes to cause leakage of MV²⁺ from the liposome interior. Even though partial photoreduction of MV²⁺ in aqueous solution can occur via irradiations with flavins or ruthenium complexes, no photoreductions of MV²⁺ within liposomes were observed under the same conditions. As flavin and ruthenium complexes are also able to perform photoreduction of MtrCAB in detergent suspensions we can conclude these should be ideal photosensitisers to study light-driven transmembrane electron transfers via MtrCAB to redox indicator cargos within proteoliposomes as desired, Figure 4.1.A.

	MtrCAB Electron Transfer <u>Fig. 4.1 A</u>	Membrane- Bound PS but MtrCAB Electron Transfer <u>Fig. 4.1 B</u>	Membrane- Bound PS and Direct Electron Transfer <u>Fig. 4.1 C</u>	PS Crossing Liposome Membrane <u>Fig. 4.1 D</u>	Permeability of Liposome Membrane to MV <u>Fig 4.1 E</u>	Liposome Lysis <u>Fig 4.1 F</u>
Flavins	Yes	No	No	No	No	No
Fluorescein	Yes	Yes	Yes	No	Yes	No
Proflavin	Yes	Yes	Yes	No	Yes	No
Eosin Y	Yes	Yes	Yes	No	Yes	No
Ru(II) Dyes	Yes	No	No	No	No	No
Dithionite	Yes	No	No	No	No	No

Table 4.2. Summary of possible interaction mechanisms between MV²⁺-containing MtrCAB proteoliposomes and photosensitisers which result in MV²⁺ photoreduction.

Conclusions drawn from this chapter where **Yes** indicates a possible interaction mechanism and No indicates an interaction mechanism that was not detected.

Eosin Y, proflavin and fluorescein were shown to associate with phospholipid membranes probably via partitioning within the hydrophobic region of the outer lipid monolayer. It has been shown that these photosensitisers can perform photoreductions of MV²⁺ to form MV⁺ prior to subsequent undesirable photoreductions and/or photoreactions which form colourless redox-inactive MV-photosensitiser complexes. Upon irradiation these photosensitisers initiated unwanted mechanisms for electrons to access encapsulated MV²⁺ within liposomes without MtrCAB being present, like those suggested in Figure 4.1 C and E. It could however be possible that redox-inactive molecules formed between these photosensitisers and MV are membrane-impermeable and lead to leakage and complete reduction of MV encapsulated within liposomes. It is therefore possible that eosin Y, proflavin and fluorescein may be able to perform light-driven transmembrane electron transfer via MtrCAB if a redox indicator lacking such complications was encapsulated with proteoliposomes, Figure 4.1 A and B.

In view of these findings it was decided to explore other (proteo)liposome preparation methods which may more controllably allow: i) the amount of MtrCAB added

to be independent of the concentration of the detergent used to assist proteoliposome formation; ii) the encapsulation of redox indicators which do not associate with lipid bilayers, as found with MV^{2+} ; or iii) the encapsulation of redox indicators which form undesirable membrane-impermeable products, as found with MV^{2+} . The next chapter discusses the development of a (proteo)liposome preparation to address point i). This method was found to allow greater MtrCAB incorporation within proteoliposome bilayers, such that the heme spectra of MtrCAB can be used as a redox indicator as described in Chapter 3. The next chapter also explores interactions and photoreductions observed between the eight photosensitisers and these (proteo)liposomes. Chapter 6 then describes results of experiments that aimed to identify redox indicators that could replace MV^{2+} in proteoliposomes studies.

Chapter 5

Photoreduction of MtrCAB in Liposome Bilayers: Proteoliposomes Formed by Simultaneous Protein Incorporation and Liposome Assembly

5.1 Overview of Strategies for Proteoliposome Formation

Despite the extensive use and diverse applications of proteoliposomes, the mechanisms of their formation and protein insertion are poorly understood and there is no one reconstitution method that works equally as well for all membrane proteins.^[66] Nevertheless, protein reconstitution methods used can be grouped into three categories: i) organic solvent-mediated reconstitutions via reverse-phase evaporation or rehydration of lipid-protein films, which is uncommon due to protein denaturing; ii) mechanical-mediated reconstitutions via sonication, french pressing or freeze-thawing of preformed vesicles; or iii) detergent-mediated reconstitutions of detergent-protein micelles by direct incorporation, or excess detergent removal via dialysis, dilution or adsorption to polystyrene beads.^[66] Each reconstitution method comes with its own pros and cons, but these also vary depending upon the identity and amount of the protein needing to be reconstituted, the composition of the membrane, the liposome size and relative membrane curvature, and the materials being encapsulated within proteoliposomes.^[66]

The previous chapter described the formation of MtrCAB proteoliposomes in which MtrCAB was incorporated into preformed liposomes via a combination of mechanical- and detergent-mediated reconstitution methods.^[83, 92, 93] It was likely that the mechanical freeze-thaw steps within this method were key to MtrCAB incorporation, but variation in the MtrCAB:Triton X-100 ratio in samples from different purifications affected the reproducibility of protein insertion. It also proved difficult to reliably remove MV²⁺ from the exterior of (proteo)liposomes prepared by this method. With the aim of avoiding these variations, and specifically to allow greater levels of MtrCAB to be incorporated, it was decided to develop a proteoliposome preparation which relied upon only one of the reconstitution strategies.

As previously stated, each method of protein reconstitution has its own pros and cons.^[66] Organic solvent-mediated reconstitution of MtrCAB was not explored due to the possibility of protein denaturing upon exposure to organic solvents. Mechanical-mediated reconstitutions were not explored either due to the irreproducibility, protein inactivation

and aggregation which can be introduced via sonication, french pressing or freeze-thawing within these preparations.^[66] It was instead decided to focus upon a detergent-mediated reconstitution as this is the most straightforward, successful, reproducible, and frequently used strategy for proteoliposome preparation.^[66, 175] During such reconstitutions, detergent-protein micelles are mixed with either detergent-treated liposomes or detergent-lipid micelles before removal of detergent molecules to allow progressive incorporation of protein in the lipid bilayers. Prior to explaining how detergent-mediated reconstitutions work, some basic information on detergents is required.

5.1.1 Detergents and Detergent-Mediated (Proteo)liposome Formation

Detergents are amphiphilic molecules which are more water-soluble than lipids and thus are extremely effective in membrane solubilisation. Detergent molecules self-assemble into a roughly spherical arrangement where their hydrophobic carbon tails are sequestered and their hydrophilic head groups are exposed to aqueous solution. These detergent micelles spontaneously form at a defined detergent concentration, known as the critical micellar concentration (CMC).^[176] When detergent concentrations are below the CMC all the detergent molecules are present as monomers. As the concentration increases beyond the CMC, the monomer concentration remains constant while the micelle concentration increases.^[176] As micelle formation is dynamic there is constant interchange between detergent present as monomers and in micelles. Detergent micelles are classified by their size which can be described either by the average number of molecules per micelle, known as the aggregation number, or by the average micelle weight.

The mechanisms of detergent solubilisation of liposomes, subsequent liposome reformation upon detergent removal, and the understanding of detergent-lipid interactions are well described.^[66, 175] There is a three stage profile to liposome solubilisation, where three scenarios can be envisioned for constant lipid concentration with detergent concentrations going from zero/low to high, Figure 5.1.^[66] At low detergent concentrations, detergent monomers partition into the bilayer whilst not disrupting them, Figure 5.1 I. The membrane partitioning ability of detergents depends upon how the detergent interacts with the phospholipids. As the detergent concentration increases towards the CMC, the monomer concentration and the amount of detergent located in the bilayer increases until the bilayer becomes detergent-saturated. At detergent concentrations higher than the CMC, the liposome bilayers are disrupted and the released lipids form

micelles containing both lipid and detergent, Figure 5.1 II. This transition between liposomes and lipid-detergent micelles is dynamic and there is a detergent concentration range in which both species coexist. When detergent concentrations are even greater lipids are completely solubilised within detergent-lipid micelles, Figure 5.1 III.

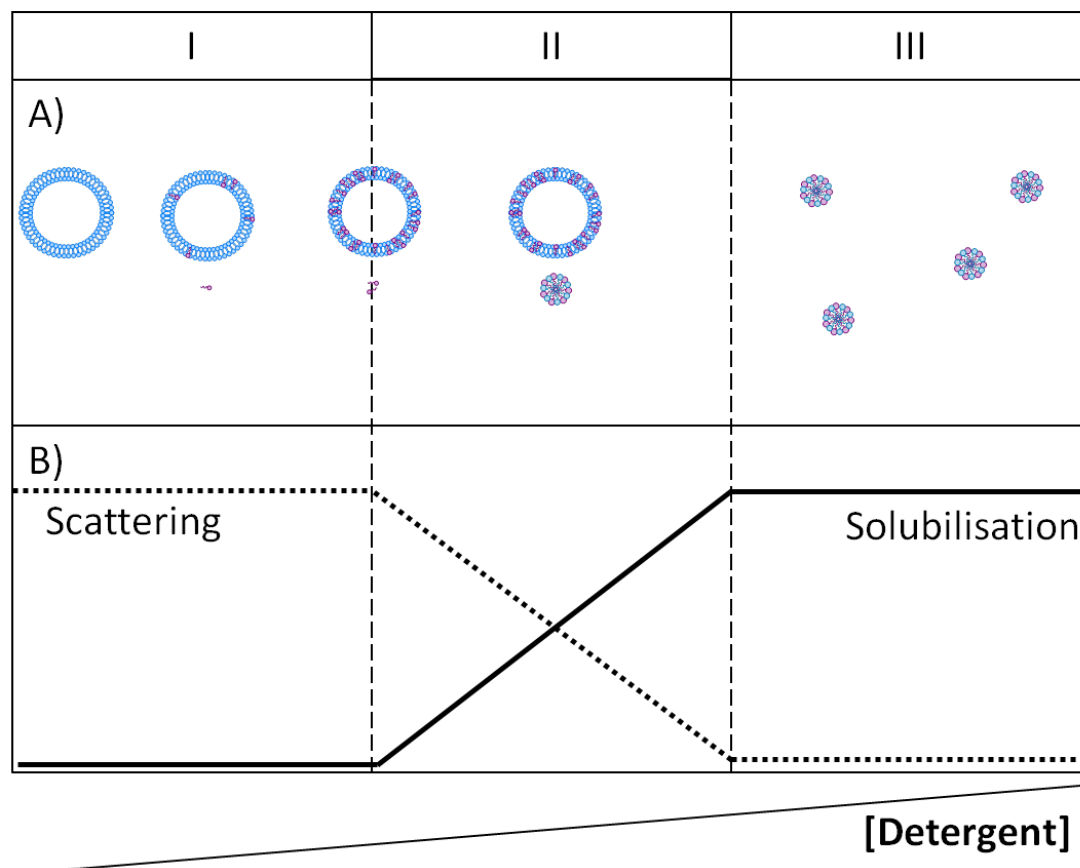


Figure 5.1. Idealised three-stage profile of the solubilisation of liposomes by increasing detergent concentrations.

A) Cartoon of liposome solubilisation. B) Changes in scattering contribution (dotted line) observed at different stages of liposome solubilisation (continuous line). The regions labelled I, II and III correspond respectively to ranges of detergents where liposomes only, liposomes and micelles or micelles only are present. Purple structures represent detergent molecules.

The precise conditions that induce transitions between the three situations described above depend upon the size of liposomes and the nature of the lipids and detergents. Progression through stages I, II and III as detergent is added to a liposome suspension can be followed by using electronic absorbance spectroscopy to monitor light scattering due to the presence of liposomes, Figure 5.1 B.^[66, 175] Initially, in the simplest case, the intensity of the light scattered due to liposomes remains essentially unchanged as detergent molecules partition into the membrane, Figure 5.1 I. In practice detergents partitioning into the membrane can also cause the size of liposomes, and scattered light, to increase during this stage. As detergent concentration increases, liposomes are progressively solubilised

and the light scattering decreases (Figure 5.1 II), until complete solubilisation occurs and the scattering contribution is completely lost, Figure 5.1 III.

The concept for liposome formation from lipid-detergent micelles, via decreasing the detergent concentration, is based upon the reverse of liposome solubilisation and involves similar intermediates, Figure 5.1.^[66, 175] When the detergent concentration within a lipid-detergent micelle solution (Figure 5.1 III) is decreased towards and below the CMC a liposome bilayer should assemble in a sequence of events that is opposite to those seen during liposome solubilisation, i.e. going from III to II, Figure 5.1. If a membrane protein is present within a protein-detergent micelle during this process it will be simultaneously incorporated into the assembled bilayer. Insertion of membrane proteins can occur also when detergent concentration is decreased within a mixture of detergent-saturated liposomes (Figure 5.1 I/II) and protein-detergent micelles. This can occur as there is dynamic transition between detergent-saturated liposomes and protein-detergent micelles which results in proteoliposomes.

There are various detergent removal methods which are chosen based upon the detergent properties and the desired rate of removal.^[66] Biobeads are effective at removing most detergents but can also absorb other hydrophobic molecules like proteins. Dialysis is slow but effective in removing detergents with high CMCs and small sizes. Gel filtration is relatively slow but effective at separating detergent micelles and lipid-protein-detergent micelles with large size differences. Another procedure for obtaining proteoliposomes from lipid-protein-detergent micelles consists of rapidly diluting the reconstitution mixture so detergent concentration falls below the CMC. This results in the loss of detergent micelles, and protein and lipid monomers to quickly form proteoliposomes which can be collected via ultracentrifugation.

Proteoliposome formation via rapid dilution of lipid-protein-detergent micelles is a well-controlled process and the procedure can be optimised for greater protein incorporation or more homogenous protein orientation as desired.^[66, 175] Rapid dilutions can either be performed on mixtures containing: i) lipid-protein-detergent micelles where liposomes are completely solubilised; ii) detergent-saturated liposomes and detergent-protein micelles; or iii) a mixture of the latter two.^[66, 175] It is thought the extent of liposome solubilisation impacts the amount and orientation of the protein incorporated after rapid dilution.^[66] Rapid dilution of a mixture of detergent-liposomes (i.e. Figure 5.1 I) and detergent-protein micelles results in homogenous, unidirectional protein orientation

but lower levels of protein incorporation.^[66] Rapid dilution of fully solubilised protein-lipid mixtures (i.e. Figure 5.1 III) however results in random protein orientation but maximum possible protein incorporation.^[66]

It was therefore decided to try to prepare MtrCAB proteoliposomes via rapid dilution of MtrCAB-detergent and lipid-detergent micelles as this method should allow greater MtrCAB incorporation within liposome bilayers. This method was also tried as it provides more control over the amount of detergent present and which should help reproducibility across different (proteo)liposome preparations. It also decided that MtrCAB, purified in Triton X-100, should be buffer exchanged into a different detergent with a smaller micelle size. *N,N*-dimethyl-*n*-dodecylamine *N*-oxide (LDAO) was selected as this detergent has a low CMC, which is similar to that of Triton X-100, but a significantly smaller micelle size, Table 5.1. It was decided to use *n*-octylglucoside (OG) as the detergent to solubilise liposomes because of the high CMC it possesses, Table 5.1. The preparation and characterisation of such (proteo)liposomes from rapid dilution of MtrCAB-detergent and lipid-detergent micelles is described next. Sections of this work were performed in collaboration with Dr Ee Taek Hwang and Dr Lars Jeuken at the University of Leeds.

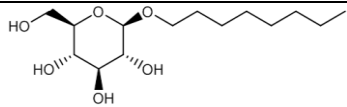
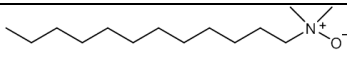
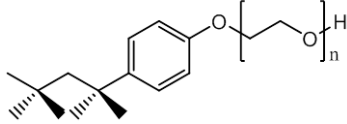
Detergent	Structure	Monomer RMM (g mol ⁻¹)	CMC (mM)	Average Micelle Size (g mol ⁻¹)	Aggregation Number
OG (<i>n</i> -octylglucoside)		292.4	20-25	25,000	84
LDAO (<i>N,N</i> -dimethyl- <i>n</i> -dodecylamine <i>N</i> -oxide)		229.4	1-2	17,000	76
Triton X-100 (<i>n</i> = 9-10)		~ 625	0.2	80,000	100-155

Table 5.1. Properties of detergents used in this study.

5.2 Preparation and Characterisation of MtrCAB Proteoliposomes from Rapid Dilution of Lipid-Detergent and Lipid-Detergent Micelles

The protocol for the preparation of (proteo)liposomes from rapid dilution of lipid-detergent micelles, with or without MtrCAB-detergent micelles present, is generalised in Figure 5.2. DLS was used to monitor the average hydrodynamic radii of lipid vesicles made during the formation of (proteo)liposomes. Proposals for the nature of the lipid vesicle structures have been made by comparison of radii reported here with observations from literature, as outlined in Section 1.5.2.2.^[63, 66]

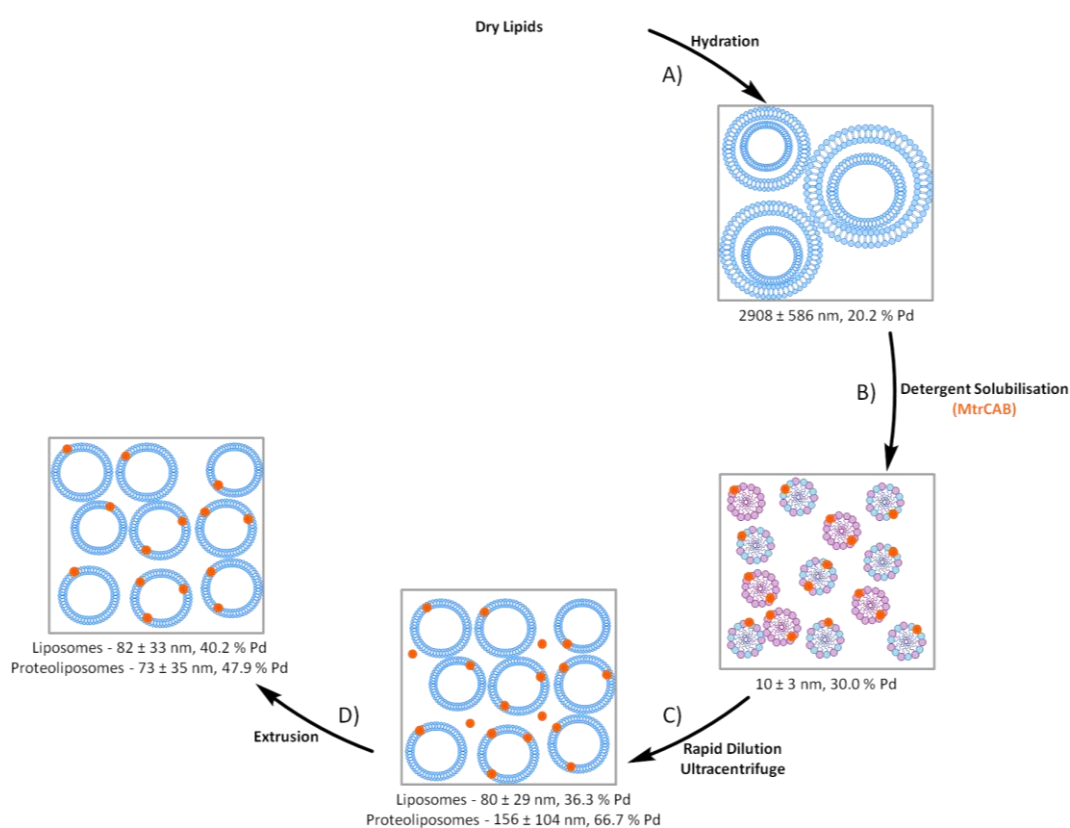


Figure 5.2. Summary of the preparation of (proteo)liposomes from rapid dilution of lipid-detergent micelles, with or without MtrCAB-detergent micelles, with average hydrodynamic radii after key steps.

Average hydrodynamic radii and polydispersity (Pd) determined from DLS measurements. Data are representative of that from several preparations of (proteo)liposomes. Orange circles represent MtrCAB. Purple structures represent detergent molecules. Structures of MLVs and LUVs indicated are deduced from literature of similar systems, as described in Section 1.5.2.2.

Suspensions of 10.3 mg mL^{-1} chicken egg PC (details in Table 1.1) were prepared via vortexing in 50 mM HEPES, 2 mM CaCl_2 , pH 7, Figure 5.2 A. To these highly polydisperse MLVs, with an average radius of 2900 ± 600 nm, 282 μL of 250 mM OG in 50 mM HEPES, 2 mM CaCl_2 , pH 7 was added to give final lipid and OG concentrations of

8 mg mL⁻¹ and 55 mM respectively. This addition caused the cloudy liposome suspension to completely solubilise, resulting in a clear solution of lipid-detergent micelles with a small hydrodynamic radius of ~ 10 nm, Figure 5.2 B. The OG concentration that was required to completely solubilise the liposome suspensions in this step was determined in separate experiments where sequential addition of OG were made to similar liposome suspensions whilst electronic absorbance spectroscopy was used to monitor their absorbance at 540 nm, Figure 5.3.A.

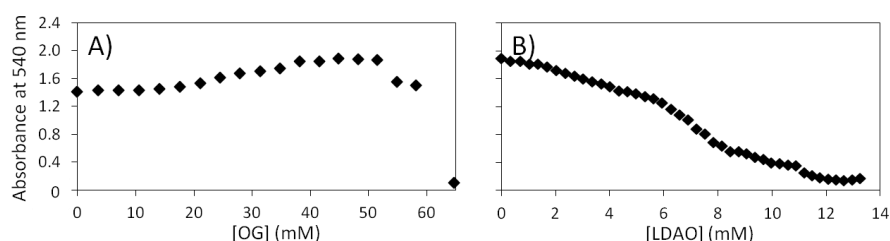


Figure 5.3. Solubilisation of liposomes upon sequential addition of OG or LDAO.

Liposomes suspensions (4 mg mL⁻¹ lipid) prepared by hydrating powdered PC in 50 mM HEPES, 2 mM CaCl₂, 10 mM KCl, 50 mM TEOA, pH 7. Additions of OG (A) or LDAO (B) were made to samples. Extent of liposome solubilisation was monitored via 540 nm. Liposomes were fully solubilised once an absorbance of essentially 0 was obtained.

After 20 mins equilibration time, 32 μ L of 4 μ M MtrCAB in 5 mM LDAO, 20 mM HEPES, pH 7 was added to give a MtrCAB concentration of ~ 130 nM, which corresponds to ~ 0.3 % (w/w) protein to lipid. This addition resulted in a LDAO concentration of 160 μ M which is below that of the CMC of LDAO (Table 5.1), such that the LDAO concentration has no further influence upon proteoliposome formation in subsequent steps, Figure 5.3 B. When making liposomes no equivalent addition of LDAO was made.

The mixed micellar solution, containing a mixture of lipid-detergent micelles with or without MtrCAB-detergent micelles present, were subsequently subjected to ~ 10 fold dilutions, Figure 5.2 C. This dilution caused the OG concentration to decrease below the OG CMC, Table 5.1 and Figure 5.3 A, to ~ 5.2 mM which results in spontaneous (proteo)liposomes formation. As the lipids are completely solubilised and then rapidly diluted it is predicted that MtrCAB will probably orientate with 50 % of MtrCAB with MtrC being associated with the exterior solution and 50 % having the opposite orientation.

After 15 mins the sample was subjected to ultracentrifugation at 195000 g, 4 $^{\circ}$ C for 1 hr 40 mins to recover any (proteo)liposomes that had formed during rapid dilution, Figure 5.2 C. It was notable that the pink proteoliposome pellet was found on top of a darker red pellet, Figure 5.4 A. Resulting (proteo)liposome pellets were resuspended in

50 mM HEPES, 2 mM CaCl₂, 10 mM KCl, 50 mM TEOA, pH 7 to give liposome and proteoliposome suspensions. It was notable that the proteoliposome suspension contained a red precipitate which was thought to be unincorporated MtrCAB which was not soluble in the absence of detergent. DLS showed the hydrodynamic radii of liposomes and proteoliposomes suspensions to be 80 ± 29 and 155 ± 104 nm respectively, where size differences was presumably due to the presence of precipitated MtrCAB in proteoliposomes suspensions. These suspensions were extruded by 11 passes through polycarbonate membranes with a defined pore size of 0.2 μ m to generate LUVs with a more uniform radius around 80 nm, Figure 5.2 D. After extrusion, the normally-white polycarbonate membrane and resulting proteoliposome suspension showed evidence of the removal of the previously mentioned red precipitate from proteoliposome suspensions, Figure 5.4 B. The removal of the precipitate was confirmed by the similar radii obtained for liposome and proteoliposome suspensions after extrusion, 82 ± 33 and 73 ± 35 nm respectively. The presence of unincorporated precipitated MtrCAB suggests that this proteoliposome preparation achieves the highest possible incorporation of MtrCAB within PC liposome membranes in 50 mM HEPES, 2 mM CaCl₂, 10 mM KCl, 50 mM TEOA, pH 7 to completely saturate the membrane with MtrCAB.

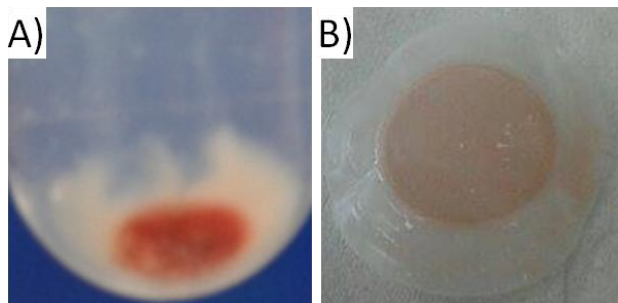


Figure 5.4. Evidence of MtrCAB saturation of liposome bilayers being achieved during preparation of proteoliposomes from rapid dilution of MtrCAB-detergent and lipid-detergent micelles.

Pellets formed from ultracentrifugation of 50 mg lipid after rapid dilution in the presence of MtrCAB (A). Extrusion membrane dyed with excess MtrCAB (B). See text for details.

In addition to using DLS, physical characteristics of these (proteo)liposomes were obtained from UV-vis spectroscopy, SDS-PAGE analysis, and bright-field microscopy. Figure 5.5 shows the spectra of 1 mg mL⁻¹ lipid suspensions of these (proteo)liposomes. Comparisons of the absorbance at 400 nm shows 1 mg mL⁻¹ lipid suspensions of these (proteo)liposomes ($Abs_{400nm} = 0.07$) exhibit at least a 8-fold smaller light scattering contribution than those of 1 mg mL⁻¹ lipid suspensions of (proteo)liposomes prepared by the previous method ($Abs_{400nm} = 0.54$ to 0.72), Figures 4.3 and 4.4. This 8-fold decrease in

light scattering is due to the smaller radii of (proteo)liposomes prepared by the rapid dilution method in comparison to the larger radii of those prepared by the original reported method.

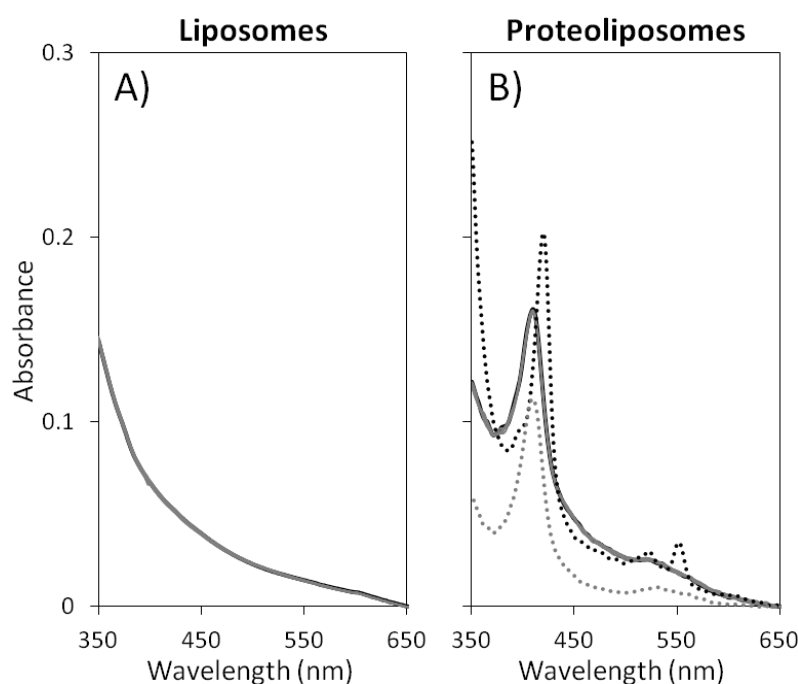


Figure 5.5. Proteoliposome absorbance spectra show a detectable presence of MtrCAB in liposome bilayers.

1 mg mL⁻¹ lipid suspensions of (proteo)liposomes prepared via rapid dilution method with either no protein (A) or with MtrCAB (B). As prepared samples (continuous black lines) were irradiated for 5, 15, 30, 60 and 90 mins at 0.4 kW m⁻² (continuous grey lines) prior to addition of excess dithionite to proteoliposomes (dotted black line). Addition of excess Triton X-100 to reduced proteoliposomes and subsequent air oxidation (dotted grey line) showed approximately 60 nM MtrCAB was present. Stirred samples in anaerobic 50 mM HEPES, 2 mM CaCl₂, 10 mM KCl, 50 mM TEOA, pH 7 at 20 °C. Path length 1 cm.

The absorbance spectrum of proteoliposomes exhibits an intense absorption in the Soret region with a maximum at 410 nm and a broad lower-intensity feature in the α/β -region between 500 and 600 nm, Figure 5.5 B continuous black line. These spectral features are associated with the detectable presence of heme within these proteoliposomes whereas no such features were seen with proteoliposomes prepared via the original method (Figures 4.3.B and 4.4.B continuous black lines). This comparison reveals that MtrCAB incorporation achieved by this new method was greater than that achieved in the original reported method.^[83, 92, 93] Addition of dithionite to proteoliposomes caused the Soret band to intensify and shift to 420 nm and the appearance of sharp peaks at 523 and 552 nm, which are spectral changes that are typically seen upon full heme reduction, Figure 5.5 B dotted black line. Solubilisation of proteoliposomes with Triton X-100 isolated the heme spectrum by removal of the liposome scattering contribution and, by using the extinction

coefficient of oxidised MtrCAB, the total MtrCAB concentration was determined to be ~ 60 nM for a 1 mg mL⁻¹ lipid suspension.

Assuming proteoliposomes are unilamellar with a cross sectional length of ~ 5 nm and the lipid density is 1 g cm⁻³, the average radii in nm, r , can be used to calculate the volume (Equation 5.1) and mass of lipid bilayer of a single vesicle.

$$\text{Bilayer volume} = \left(\frac{4}{3}\pi r^3\right) - \left(\frac{4}{3}\pi(r-5)^3\right) \quad (5.1)$$

This mass can then be used to calculate the number of proteoliposomes present within a 1 mg mL⁻¹ lipid suspension. By assuming a uniform distribution of MtrCAB, the number of MtrCAB molecules per proteoliposome can be predicted with knowledge of the numbers of proteoliposomes and MtrCAB molecules present. If it is assumed all MtrCAB was incorporated in the original published method, it would be predicted that there would only be 1-2 MtrCAB molecules per lipid vesicle. In contrast, it is predicted that proteoliposomes prepared via rapid dilution method would have 12 MtrCAB molecules per lipid vesicle, and subsequently there is ~ 10-fold increase in MtrCAB incorporation.

SDS-PAGE analysis was used to resolve and visualise proteins within proteoliposomes prepared by this new method, Figure 5.6. As a comparison, purified MtrCAB was included on the gel as a measure of the expected protein composition, Figure 5.6. This analysis revealed that both samples possessed two protein bands that stained for heme-dependent peroxidase activity which were MtrC (~ 75 kDa) and MtrA (~ 32 kDa), and an additional band running slightly higher than MtrC at ~ 80 kDa was visualised on gels stained with Coomassie blue. This was confirmed to be MtrB via western blotting using MtrB-specific antibodies. The relative intensities of the protein bands seen for proteoliposomes are similar to those of the purified MtrCAB, which suggests that MtrCAB is inserted into membranes as the intact complex.

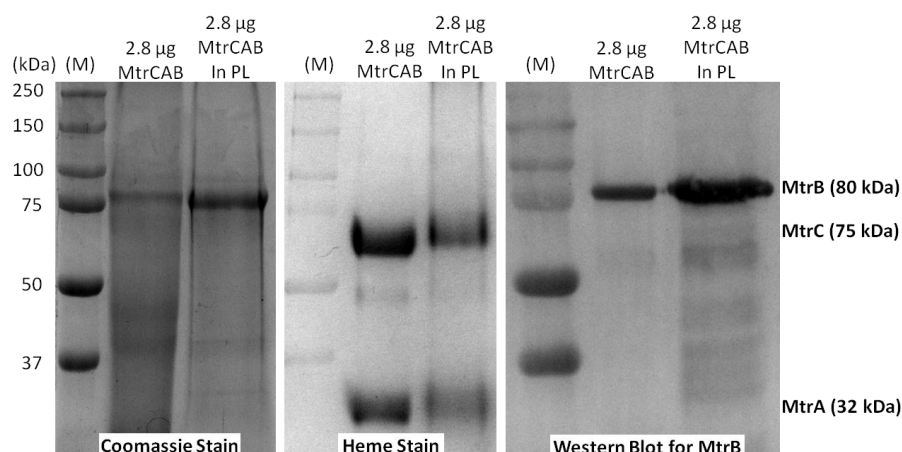


Figure 5.6. SDS-PAGE analysis of MtrCAB in aqueous solution and within proteoliposomes. Three replica samples were resolved using 12.5 % (w/v) SDS-PAGE and were subsequently visualised by Coomassie staining, heme staining or via western blotting using MtrB-specific antibodies. Lane 1, molecular weight markers of 250, 150, 100, 75, 50, and 37 kDa (M); lane 2, MtrCAB in LDAO; lane 3, MtrCAB proteoliposomes. MtrCAB proteoliposomes were prepared for SDS-PAGE analysis via ice-cold ethanol precipitation, prior to centrifugation collecting the precipitated protein which was separated from ethanol and air dried.

Microscopy techniques were used to confirm sizes, polydispersity and structures of (proteo)liposomes prepared via this new method. Bright-field microscopy was unable to visualise these (proteo)liposomes due to their smaller sizes and size diversity, which generally confirms these (proteo)liposomes to be smaller and more homogenous in comparison to (proteo)liposomes prepared by the original method, Figure 4.2.

5.3 Possible Interactions Between Photosensitisers and (Proteo)liposomes with Greater MtrCAB Incorporation

Both proteoliposomes and liposomes prepared by rapid dilution of lipid-detergent with/without MtrCAB-detergent micelles were shown to have homogenous sizes around 80 nm, and proteoliposomes prepared by this method were able to incorporate greater amounts of MtrCAB, most likely, up until the point of membrane saturation. Consequently absorbance spectra of these proteoliposomes contain spectral features that are typical of the hemes of MtrCAB. Addition of dithionite caused these spectral features to transform in agreement with all the hemes being redox addressable by the externally located reductant.

Light-driven reduction of MtrCAB in detergent suspensions in presence of TEOA by the eight chosen photosensitisers was demonstrated in Chapter 3. These MtrCAB photoreductions likely occurred via random collisions between photosensitisers and multiple points on the surfaces of the MtrCAB complex that lie in proximity to the hemes.

Productive, i.e. electrons transfer competent, collisions between photosensitisers and MtrCAB located within liposome membranes could however be more limited due to the photosensitiser location. Photoreduction of MtrCAB within liposome membranes can be envisioned to occur by a number of different scenarios, which are similar to those summarised in Figure 4.1 A-B, D and F. It is key to remember that even though the possible scenarios of photosensitiser-proteoliposome interactions and the components of proteoliposomes are independent of the proteoliposome preparation method used, it is possible that the greater extent of MtrCAB incorporation seen via the rapid dilution method could result in membrane permeability to photosensitisers to be different to those seen in Chapter 4. This could, therefore, mean that the interaction mechanisms between proteoliposomes, with greater MtrCAB incorporated, and photosensitisers are different to those summarised in Table 4.2. Therefore characterisation of liposomes collected by ultracentrifugation after dark incubations with photosensitisers, similar to those performed in Section 4.3, were performed to allow conclusions to be made with regard to whether photosensitisers interact with liposomes prepared via this new method. The following section describes such experiments for the eight previously discussed photosensitisers. The results of this work are extended in Section 5.5 to assess whether photoreduction of MtrCAB within membranes could be achieved upon irradiation in the presence of any of these photosensitisers and TEOA.

5.4 Assessment of Photosensitiser Association with Liposomes

Experiments with liposomes, prepared via rapid dilution of lipid-detergent micelles, and the eight chosen photosensitisers, similar to those performed in Section 4.3, were performed to investigate whether photosensitisers affected membrane stability or bound to the liposome membranes, Figure 4.1 B and F. Unlike in experiments performed in Section 4.3, photosensitiser additions were made so their absorbance maxima were above an absorbance reading of 1 to ensure conclusions on photosensitiser associations were not influenced by different extinction coefficients, Figure 5.7 continuous black lines. To assess whether photosensitisers associates with or lyse liposomes, spectra of liposomes and photosensitisers were monitored during dark incubations. It would be expected that if bilayer stability was compromised the scattering contributions of the liposome spectra would be affected, as seen upon addition of Triton X-100 which lyses liposomes and causes scattering contributions to be lost, Figure 4.3 dotted grey lines. To ascertain whether the photosensitisers remained in the external solutions or had associated with liposome

membranes, ultracentrifugations were performed after incubations to separate liposomes from their external solutions. Electronic absorbance spectroscopy was then used to identify whether photosensitisers were located in the external solutions or with the liposome pellet.

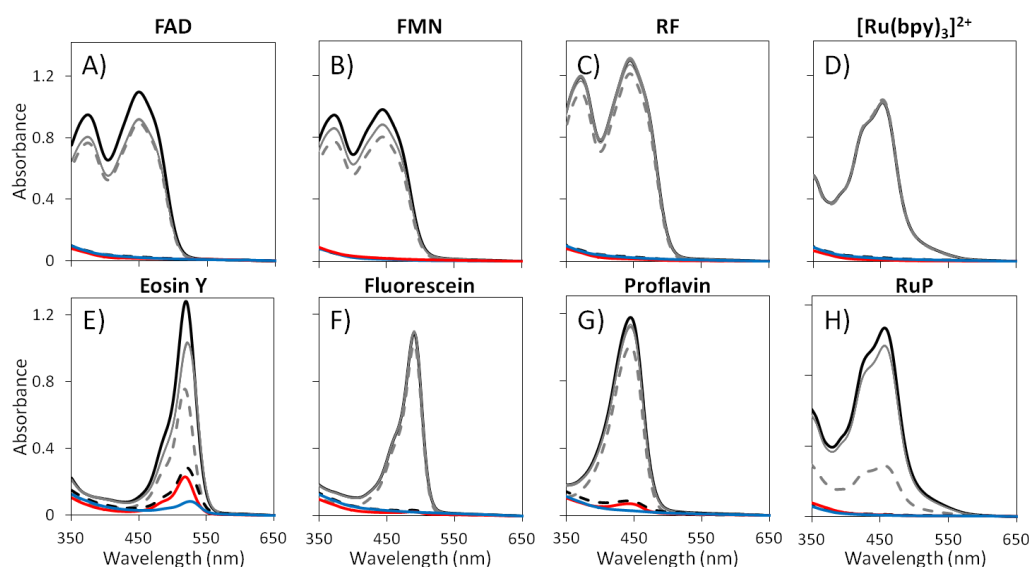


Figure 5.7. Photosensitisers' interactions with liposomes are independent to the liposome preparation used.

1 mg mL⁻¹ lipid suspensions of liposomes, prepared via rapid dilution method, with either 94 μM FAD (A), 75 μM FMN (B), 100 μM RF (C), 68 μM [Ru(bpy)₃]²⁺ (D), 16 μM eosin Y (E), 16 μM fluorescein (F), 15 μM proflavin (G) or 101 μM RuP (F). As prepared samples (continuous black lines) were incubated in the dark for 5, 15, 30, 60 and 90 mins (continuous grey lines) prior to being ultracentrifuged to separate supernatants (dashed grey lines) from liposome pellets that were resuspended in buffer (dashed black lines). Resuspended liposomes were ultracentrifuged a second time to again separate supernatants (red lines) from liposome suspensions that were resuspended in buffer (blue lines). Stirred samples in anaerobic 50 mM HEPES, 2 mM CaCl₂, 10 mM KCl, 50 mM TEOA, pH 7 at 20 °C. Path length 1 cm.

The results from photosensitiser incubations with liposomes prepared via the new method were identical to results previously seen with (proteo)liposomes prepared via the previous method, Section 4.3. Therefore photosensitisers' interactions with PC bilayers are independent to the (proteo)liposome preparation used.

5.5 Visible-Light-Driven Reduction of Proteoliposome Incorporated MtrCAB and Comparison with that for MtrCAB in Detergent Suspensions

To assess if photoreduction of MtrCAB within liposome bilayers was possible, irradiations of 1 mg mL⁻¹ lipid suspensions of proteoliposomes, prepared via rapid dilution of lipid-detergent and MtrCAB-detergent micelles, were performed in the presence of 50 mM TEOA and ~ 10 μM photosensitiser for 90 mins. A lamp power of 0.4 kW m⁻² was used to avoid photosensitiser photobleaching. As approximately 60 nM MtrCAB is present

within a 1 mg mL^{-1} lipid suspension of proteoliposomes, these irradiations were performed using heme:PS ratio of $\sim 1:10$ ($\sim 1 \text{ }\mu\text{M}$ heme: $\sim 10 \text{ }\mu\text{M}$ PS). These irradiations of proteoliposomes were performed in an identical manner to those of MtrCAB in aqueous solution, as described in Section 3.6. The only exception to this was Triton X-100 was not required as MtrCAB here was located within membranes.

Spectra obtained after additions of one of the eight photosensitisers were typical of proteoliposomes containing fully oxidised MtrCAB, Figure 5.8 and 5.9 black continuous lines. Irradiation of proteoliposomes in the absence of photosensitisers provided no indication of heme reduction, Figure 5.5 B grey lines. Subsequent addition of the chemical reductant sodium dithionite caused the Soret band to intensify and shift to 420 nm, and the appearance of sharp peaks at 523 and 552 nm in accordance with complete reduction to form ferrous hemes, Figure 5.5 B dotted black line. By assuming that each heme of MtrCAB equally contributes to the total absorbance change and by following changes in intensity at 552 nm or 420 nm, the extent of photoreduction can be determined with reference to relevant absorbance of oxidised and dithionite-reduced samples.

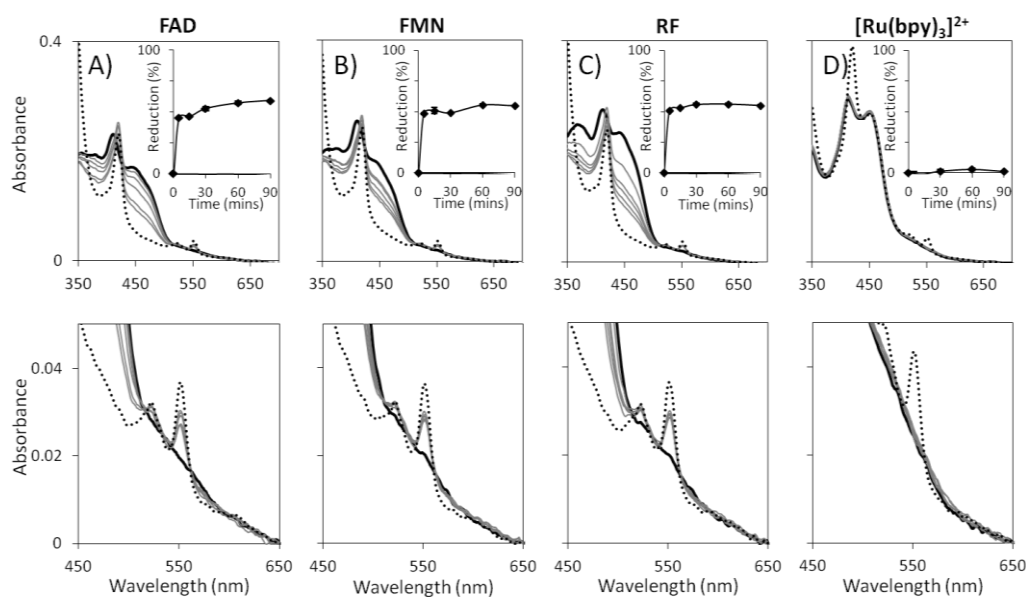


Figure 5.8. Flavin photoreduction of MtrCAB within proteoliposomes.

1 mg mL^{-1} lipid suspensions of proteoliposomes, prepared via rapid dilution method, with either $11 \text{ }\mu\text{M}$ FAD (A), $10 \text{ }\mu\text{M}$ FMN (B), $14 \text{ }\mu\text{M}$ RF (C) or $16 \text{ }\mu\text{M}$ $[\text{Ru}(\text{bpy})_3]^{2+}$ (D). Bottom panels are respective spectra of those above, focused on the heme α/β -region. As prepared samples (continuous black lines) were irradiated for 5, 15, 30, 60 and 90 mins at 0.4 kW m^{-2} (continuous grey lines) prior to addition of excess dithionite (dotted lines). Inserts show extent of MtrCAB reduction during irradiation, monitored via 552 nm absorbance. Extent of reduction; and max and min observed values; represent the average of two independent, stirred experiments performed in anaerobic 50 mM HEPES, 2 mM CaCl_2 , 10 mM KCl, 50 mM TEOA, pH 7 at $20 \text{ }^\circ\text{C}$. Path length 1 cm.

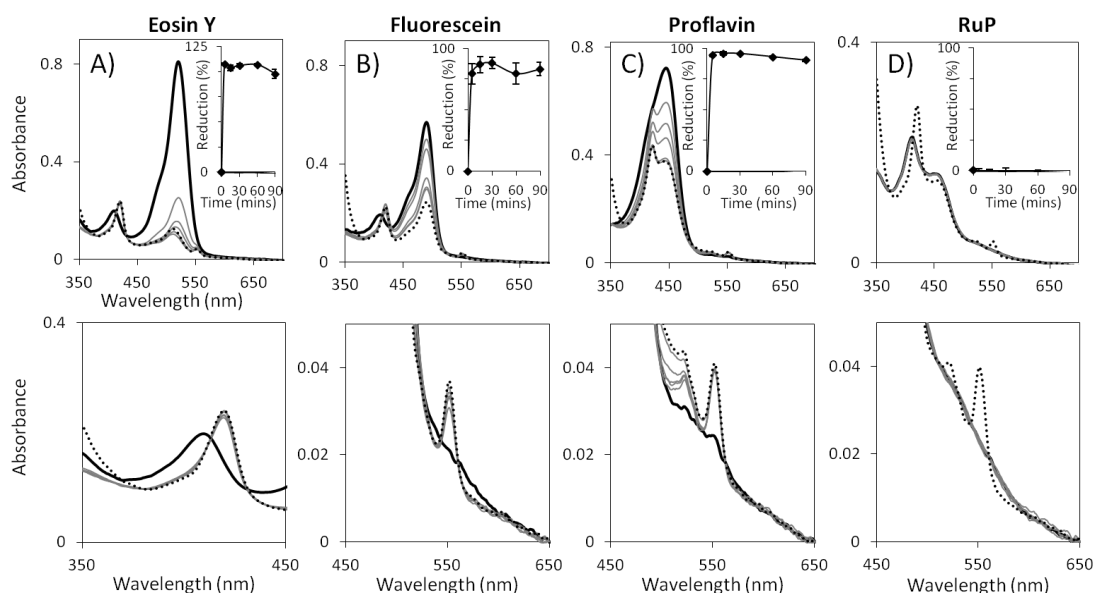


Figure 5.9. Xanthene and proflavin photoreduction of MtrCAB within proteoliposomes.

1 mg mL⁻¹ lipid suspensions of proteoliposomes, prepared via rapid dilution method, with either 10 μM eosin Y (A), 8 μM fluorescein (B), 9 μM proflavin (C) or 11 μM RuP (D). Bottom panels are respective spectra of those above, focused on the heme α/β-region for all except eosin Y (Soret peak). As prepared samples (continuous black lines) were irradiated for 5, 15, 30, 60 and 90 mins at 0.4 kW m⁻² (continuous grey lines) prior to addition of excess dithionite (dotted lines). Inserts show extent of MtrCAB reduction during irradiation, monitored via 552 nm absorbance for all except eosin Y (420 nm). Extent of reduction; and max and min observed values; represent the average of two independent, stirred experiments performed in anaerobic 50 mM HEPES, 2 mM CaCl₂, 10 mM KCl, 50 mM TEOA, pH 7 at 20 °C. Path length 1 cm.

Irradiations of these proteoliposome suspensions in the presence of organic photosensitisers resulted in the appearance of peaks with maxima at 523 and 552 nm, as well as a Soret shift to higher wavelengths, indicative of heme photoreduction, Figure 5.8 A-C and 5.9 A-C grey lines. These photosensitisers were able to achieve extents of MtrCAB photoreduction that were similar to those achieved when MtrCAB was in aqueous solution; with flavins achieving rapid partial MtrCAB photoreduction to ~ 55 %; and xanthenes and proflavin achieving rapid full heme reductions.

Due to the ability of eosin Y, proflavin and fluorescein to associate with (prote)liposome membranes, it was of interest to confirm whether it was possible for these membrane-associated photosensitisers to photoreduce MtrCAB within lipid bilayers. Consequently proteoliposome samples with eosin Y, fluorescein and proflavin associated to the lipid bilayer were prepared by incubating liposome suspensions (1 mg mL⁻¹ lipid) with ~ 10 μM of the respective photosensitiser in the dark in the presence of excess TEOA for 90 mins, Figure 5.10 A-C continuous lines. To ensure only membrane-associated photosensitisers remained in these samples, they were subsequently ultracentrifuged to

pellet and separate proteoliposomes from their external solutions before being resuspended in an identical buffer volume. The absorbance spectra of resuspended proteoliposome pellets showed 2 μM eosin Y and less than 0.6 μM of proflavin and fluorescein had associated with the proteoliposome membranes, Figure 5.10 A-C dashed black lines. To assess if photoreduction of MtrCAB within liposome bilayers was possible, these samples were irradiated in an identical manner as described above, Figure 5.10 D-F.

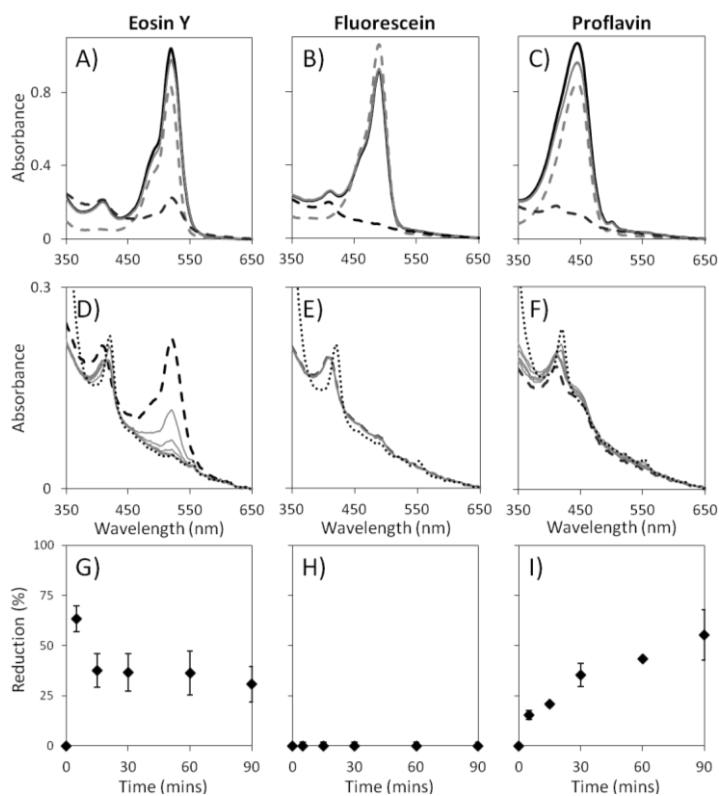


Figure 5.10. Preparation and subsequent irradiation of MtrCAB proteoliposomes with eosin Y, fluorescein or proflavin associated to the lipid bilayers.

A-C) 1 mg mL⁻¹ lipid suspensions of proteoliposomes, prepared via rapid dilution method, with 13 μM of either eosin Y (A), fluorescein (B) or proflavin (C). As prepared samples (continuous black lines) were incubated in the dark for 5, 15, 30, 60 and 90 mins (continuous grey lines) prior to being ultracentrifuged to separate supernatants (dashed grey lines) from proteoliposome pellets that were resuspended in buffer (dashed black lines).

D-F) Resuspended proteoliposomes (dashed black lines) were irradiated for 5, 15, 30, 60 and 90 mins at 0.4 kW m⁻² (continuous grey lines) prior to addition of excess dithionite (dotted lines). G-I) Extent of MtrCAB reduction during irradiation, monitored via 552 nm absorbance for all except eosin Y (420 nm). Extent of reduction; and max and min observed values; represent the average of two independent, stirred experiments performed in anaerobic 50 mM HEPES, 2 mM CaCl₂, 10 mM KCl, 50 mM TEOA, pH 7 at 20 °C. Path length 1 cm.

Inspection of experiments performed with eosin Y bound to the proteoliposome membrane showed that after 5 mins irradiation, MtrCAB within the membrane had become ~ 65 % photoreduced, Figure 5.10 D and G. During the remaining 90 mins irradiation both the percentage of reduced heme and Soret peak decreased in accordance with heme

reoxidation, Figure 5.10 D and G. Closer inspection of the eosin Y spectral peak showed photobleaching occurred during irradiation. This photosensitiser photodamage is not surprising as only 2 μM eosin Y was present within these experiments. With proflavin associated to the proteoliposome membrane slow and gradual MtrCAB photoreduction during irradiation which reached $\sim 55\%$ reduced after 90 mins. Irradiation of fluorescein that was associated to the proteoliposome membrane provided no detectable heme reduction within 90 mins. This was probably due to the low concentration of fluorescein that was associated to the membrane. Taken together these results indicate that even though MtrCAB photoreduction can be initiated by these membrane-bound photosensitisers, the photoreduction they can achieve is limited due to the small amounts of photosensitiser that is associated with the membrane. Therefore the rapid, complete photoreduction of MtrCAB proteoliposomes seen with eosin Y, fluorescein and proflavin must be contributed to random collisions between photosensitisers in the external aqueous solution and the external portions of MtrCAB, Figure 4.1 A.

Irradiations of these proteoliposomes in the presence of either ruthenium complex were not able to achieve any detectable heme photoreduction within 90 mins of irradiation, Figure 5.8 D and 5.9 D. It was expected that photoreduction of MtrCAB in proteoliposomes would be achieved with the ruthenium complexes if irradiations were carried out at higher lamp powers; however, similar experiments performed at a higher lamp power of 2 kW m^{-2} were also unable to detect any photoreduction of MtrCAB within 90 mins, Appendix 17. It is most likely that rapid charge recombination within the photoexcited ruthenium complexes dominate in these experiments and that rapid charge separation must be imposed if MtrCAB photoreduction is to occur at a measurable rate.

In light of this, it was attractive to establish whether MtrCAB within proteoliposomes would adsorb on RuP:TiO₂ particles to allow photoreduction of MtrCAB as the transfer of photoexcited electrons from RuP to MtrC/OmcA was greatly accelerated by co-adsorption of these proteins on TiO₂ particles, Section 3.9. Work was performed alongside Dr Colin Lockwood, University of East Anglia, to prove if MtrCAB could be photoreduced by RuP sensitised TiO₂ particles in the presence of 150 mM of the SED 2-(*N*-morpholino)ethanesulfonic acid at pH 6. Heme spectral features were recorded with an integrating sphere spectrometer which mitigated against the loss of incident light due to light scattering by the TiO₂ particles in addition to the proteoliposomes. Subsequent irradiations with a lamp power of 0.4 kW m^{-2} ($\lambda > 390 \text{ nm}$) resulted in cytochrome photoreductions over 60 mins, Figure 5.11. These experiments show the transfer of

photoexcited electrons from ruthenium complexes to MtrCAB within lipid bilayers were more effective and rapid when ruthenium complexes were adsorbed on TiO₂ particles. The mechanism of transfer of photoexcited electrons between RuP and MtrCAB, whether it is through collisional encounters with RuP:TiO₂ particles or via direct transfer from RuP:TiO₂ particles being adsorbed on MtrCAB of proteoliposomes, still remains to be established. To distinguish these possibilities, experiments could be performed where proteoliposome suspensions are irradiated in the presence of RuP:TiO₂ particles which are completely saturated with RuP and would then be unable to co-adsorb MtrCAB. In this case photoreduction of MtrCAB proteoliposomes would have to rely upon random collisions between RuP:TiO₂ particles in solution.

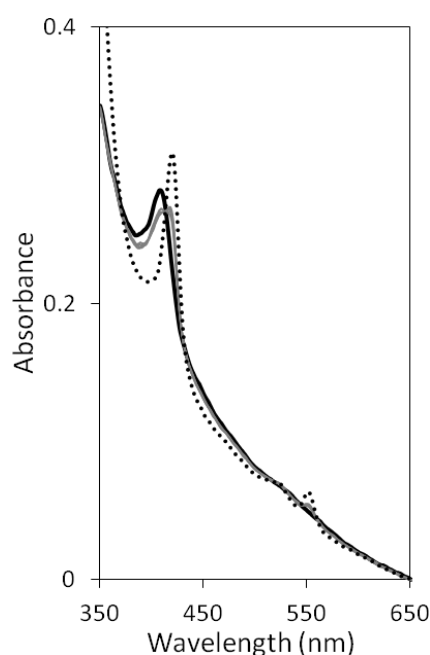


Figure 5.11. Photoreduction of MtrCAB within proteoliposomes by irradiation with RuP-sensitised TiO₂ particles.

1 mg mL⁻¹ lipid suspension of proteoliposomes, prepared via rapid dilution method, with 0.05 mg of RuP:TiO₂. As prepared samples (continuous black line) were irradiated for 5, 15, 30 and 60 mins at 0.4 kW m⁻² (continuous grey lines) prior to addition of excess dithionite (dotted black line). Stirred samples in anaerobic 150 mM 2-(*N*-morpholino)ethanesulfonic acid, pH 6 at 20 °C. Path length 1 cm.

As the extent of MtrCAB photoreduction was independent of whether MtrCAB was located in membranes or within detergent micelles it is likely the mechanisms, thermodynamics and kinetics behind these photoreductions are all identical regardless of location of MtrCAB. This highlights that irrespective of the probable 50:50 orientation of MtrCAB within the proteoliposome bilayers that all the hemes must be redox accessible irrespective of orientation, and therefore the orientation should not have an effect upon light-driven transmembrane electron transfers to internal redox indicators.

5.6 Conclusions

Within this chapter a new method of MtrCAB (proteo)liposome preparation has been described that incorporates greater levels of MtrCAB than previously reported.^[83, 92, 93] This allowed the heme spectra to be used to monitor photoreduction of MtrCAB, and it was established that these (proteo)liposomes do not burst during irradiation or dark incubations with any of the photosensitisers used in this work, as presented in Figure 4.1 F.

Flavins and ruthenium complexes do not associate with liposome membranes. As flavins were also able to photoreduce MtrCAB within proteoliposomes, we can confirm that flavins have all the desirable qualities required of photosensitisers to study light-driven transmembrane electron transfer via MtrCAB to redox indicator cargos within proteoliposomes, as idealised in Figure 4.1 A. Ruthenium complexes may also be ideal photosensitisers to study such electron transfer; however, photoreductions of MtrCAB within lipid bilayers by these photosensitisers did not occur under the experimental conditions used within this study, Figures 5.8 D and 5.9 D. Ruthenium complexes are therefore not investigated any further or discussed within Chapter 6.

Eosin Y, proflavin and fluorescein were shown to associate with phospholipid membranes. This association probably occurs via semi-partitioning within the hydrophobic region of the outer lipid monolayer and not via crossing the membrane to be located in the aqueous interior of liposome (i.e. Figure 4.1 D). Upon irradiation these photosensitisers initiated photoreduction of MtrCAB within the bilayers of liposomes, which was majorly driven by photosensitisers in the external aqueous solution instead of membrane-associated photosensitisers. Therefore it is possible that these photosensitisers may be able to imitate light-driven transmembrane electron transfer via MtrCAB to redox indicator cargos within proteoliposomes, scenarios of Figure 4.1 A and B.

Extents of MtrCAB photoreduction observed within liposome membranes were very similar to those obtained for MtrCAB in detergent suspensions. The new MtrCAB proteoliposome preparation has therefore shown that electrons can be passed from the external facing heme to the internal facing heme of MtrCAB within lipid bilayers. The next requirement for the study of light-driven transmembrane electron transfer via MtrCAB in these new proteoliposomes is the selection of a suitable redox indicator. Such a redox indicator encapsulated within these new proteoliposomes will be able to establish conclusively that photoexcited electrons can be passed through MtrCAB to the internal

aqueous compartment. The next chapter of this study describes the characterisation of redox indicators that could replace MV^{2+} in proteoliposomes and the demonstration of light-driven MtrCAB supported transmembrane electron transfer to one of these redox indicators, namely reactive red 120.

Chapter 6

Encapsulation of Redox Indicators within (Proteo)liposomes to Demonstrate Visible-Light-Driven Transmembrane Electron Transfer

6.1 Properties Ideal for Redox Indicators within (Proteo)liposomes

The previous chapter described a new method of MtrCAB (proteo)liposome preparation that incorporated greater levels of MtrCAB than previously reported, which allowed the heme spectra to be used to monitor photoreduction of MtrCAB within the lipid bilayer of proteoliposomes.^[83, 92, 93] However; these (proteo)liposomes were unable to provide information regarding light-driven transmembrane electron transfer supported by MtrCAB due to the lack of an internally encapsulated redox indicator. Properties that are required from such a redox indicator which can monitor light-driven transmembrane electron transfer include: i) membrane-impermeable oxidised and reduced states which do not disrupt liposome membranes; ii) a reduction potential that is more positive than those of the hemes in MtrCAB; iii) high encapsulation; iv) appropriate change in extinction coefficient with redox state to allow colour change to be monitored during irradiation; and v) no undesirable reactions with photosensitisers.

Given enough time, virtually any molecule will diffuse across a lipid bilayer via its concentration gradient. The rate at which a molecule diffuses across a lipid bilayer does depend on the size of the molecule, but mostly depends on its relative hydrophobicity. Hydrophobic molecules readily partition into a lipid bilayer and from there can rapidly diffuse across a lipid bilayer. In contrast, lipid bilayers are highly impermeable to charged hydrophilic molecules due to their charge and high degree of hydration which prevents the molecules from entering the hydrophobic region of the bilayer. In finding an alternative to MV^{2+} as a redox indicator that could be internalised and studied alongside MtrCAB it was decided to focus upon redox molecules with numerous charged groups for their ability to be encapsulated in MtrCAB (proteo)liposomes. This chapter initially describes characterisation of a range of such redox indicators and the subsequent screening for their ability to be encapsulated in (proteo)liposomes, which would then be used to study visible-light-driven transmembrane electron transfer by MtrCAB. This section of work was performed alongside Dr Ee Taek Hwang at the University of Leeds.

6.2 Characterisation of Redox Indicators Chosen for Encapsulation within (Proteo)liposomes

Five water-soluble redox indicators, containing multiple charged groups, were investigated to explore the possibility of their encapsulation within (proteo)liposomes to study visible-light-driven transmembrane electron transfer supported by MtrCAB. The structures, redox reactions, and spectral and electrochemical properties of these redox indicators are discussed in the next sections and are summarised in Table 6.1. Where no or limited information has been previously reported, assessment of the electrochemical and spectral properties was carried out. To assess electrochemical properties, solutions containing 200 μM redox indicator were characterised by cyclic voltammetry. To assess spectral properties, electronic absorbance spectra were obtained for 50 μM redox indicator as prepared, after reduction with the chemical reductant dithionite and after being subsequently air-oxidised.

Redox Indicators	Structure	λ_{max} (nm)	ϵ ($\text{mM}^{-1} \text{cm}^{-1}$)	E_{m} (V)	$E_{\text{p}}^{\text{red}}$ (V)
Resazurin		608 ^[177]	~ 39.0 ^[177]	0.07 ^[178] -0.09 ^[178]	N/A
Indigotetrasulfonic Acid		591	24.1	-0.01	N/A
Amaranth		520	24.7	N/A	-0.35
RB5 (Reactive black 5)		595	23.1	N/A	-0.13 -0.35 -0.57
RR120 (Reactive red 120)		511	32.0	N/A	-0.47 -0.58

Table 6.1. Structural, spectroscopic and electrochemical properties of resazurin, indigotetrasulfonic acid, amaranth, RB5 and RR120 at pH 7.

λ_{max} and ϵ for indigotetrasulfonic acid, amaranth, RB5 and RR120 were determined from UV-visible spectra of 100, 50, 25, 10 and 5 μM dye using the Beer-Lambert law. Within this concentration range absorbance was proportional to dye concentration. E_{m} and $E_{\text{p}}^{\text{red}}$ for indigotetrasulfonic acid, amaranth, RB5 and RR120 were determined from cyclic voltammetry of 200 μM dye, shown in Figures 6.3 and 6.5. All potentials are reported versus SHE. Samples in 50 mM HEPES, 2 mM CaCl_2 10 mM KCl, pH 7.

6.2.1 Resazurin

Resazurin is a phenoxazin-3-one dye with a cyclic nitrone functional group which is widely used in measuring cell viability, metabolic activity and microbial activity in sediments.^[178] Reduction of resazurin in aqueous solution occurs in two two-electron processes, as shown in Figure 6.1.^[178] The species and the details of electron transfer mechanisms are pH-dependent.^[178] At neutral pH, the anionic form of resazurin predominates and undergoes an irreversible two-electron reduction, with a reduction potential of 70 mV, to form of anionic resorufin, Figure 6.1.^[178] A reversible two-electron, three-proton process, with a reduction potential of -90 mV, then leads to the formation of hydroresorufin, Figure 6.1.^[178] Photoreduction of resazurin to resorufin has been previously reported with TiO₂.^[177, 179]

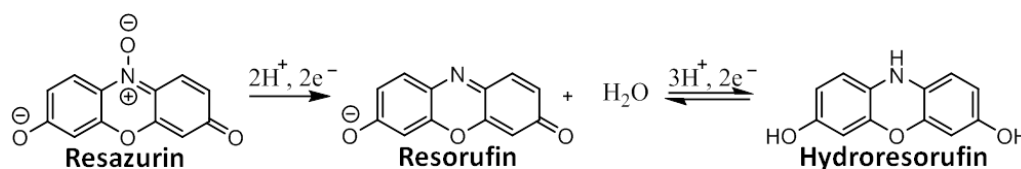


Figure 6.1. Resazurin redox reactions at pH 7.^[178]

The electronic absorption spectrum of resazurin in aqueous solution exhibits a peak with an absorbance maximum at 608 nm with a molar extinction coefficient of $\sim 39.0 \text{ mM}^{-1} \text{ cm}^{-1}$, which is characteristic of π - π^* transitions originating from the tricyclic ring system, as shown in Table 6.1.^[177, 179] Reduction of resazurin to resorufin provides colour changes from purple to pink caused by the absorbance band shift to 580 nm, and further reduction results in the loss of spectral contribution due to formation of colourless hydroresorufin.^[177, 179]

6.2.2 Indigotetrasulfonic Acid

Indigotetrasulfonic acid is a redox indicator with a tetraanionic form at pH 7, Table 6.1. Indigotetrasulfonic acid contains a quinone moiety which is thought to give this molecule its redox properties, Table 6.1 and Figure 6.2. Quinones, like flavins, are able to participate in both one- and two-electron transfers and are therefore able to exist as either an oxidised quinone, an one-electron reduced semiquinone radical or a two-electron reduced hydroquinone, as shown in Figure 6.2.

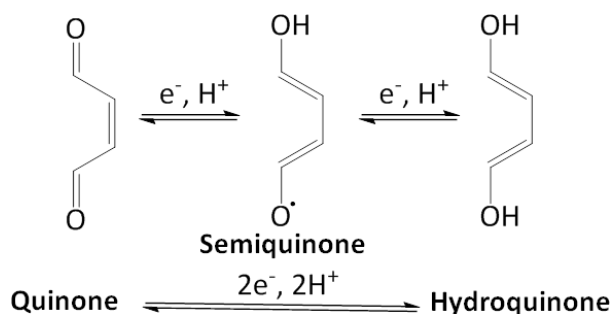


Figure 6.2. Indigotetrasulfonic acid redox reactions are based on those of quinones at pH 7.

The electronic absorption spectrum of indigotetrasulfonic acid possesses one peak with an absorbance maximum at 591 nm, Figure 6.3 A continuous line. This peak has a molar extinction coefficient of $24.1 \text{ mM}^{-1} \text{ cm}^{-1}$ due to π - π^* transitions originating from its large conjugate ring system. Addition of excess dithionite caused this band to disappear whilst a new broad peak appeared at 390 nm, Figure 6.3 A dotted lines. Subsequent air oxidation of this sample saw the gradual reappearance of the peak at 591 nm and disappearance of the peak at 390 nm, Figure 6.3 A dashed line, suggesting that air oxidation of dithionite-reduced indigotetrasulfonic acid is slow.

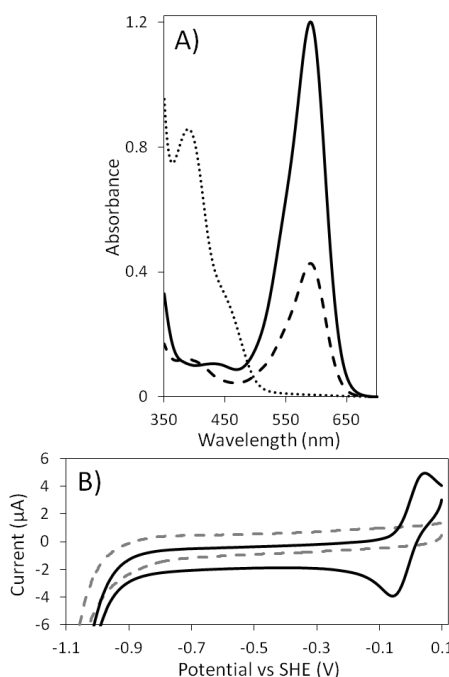


Figure 6.3. Spectroscopic and electrochemical characterisation of indigotetrasulfonic acid.

A) Electronic absorbance spectra of $50 \mu\text{M}$ indigotetrasulfonic acid (continuous line) prior to addition of excess dithionite (dotted line). Stirred sample was then air oxidised (dashed line). Path length 1 cm. B) Cyclic voltammogram of $200 \mu\text{M}$ indigotetrasulfonic acid, recorded at 20 mV s^{-1} , $20 \text{ }^\circ\text{C}$. Baseline (dashed line) was recorded prior to cyclic voltammogram of indigotetrasulfonic acid was recorded (continuous line). Sample in anaerobic 50 mM HEPES, 2 mM CaCl_2 , 10 mM KCl , pH 7.

The cyclic voltammogram obtained for indigotetrasulfonic acid had a single pair of peaks corresponding to reversible oxidation and reduction occurring at a mid-point potential of -10 mV, Figure 6.3 B. As addition of excess dithionite ($E_m \approx -500$ mV) causes the complete reduction of indigotetrasulfonic acid from its quinone form to its hydroquinone form, this reversible peak is most likely due to a two-electron reduction process.^[95] The peak separation of this reversible peak is larger than expected due to kinetic complications, slow interfacial electron transfer or proton couple electron transfer, Figure 6.3 B.

6.2.3 Azo Dyes

Azo dyes are compounds which contain a single or multiple azo groups ($-N=N-$), Table 6.1 and Figure 6.4. Aryl azo compounds are generally, water-soluble anionic compounds which have vivid colours due to $\pi-\pi^*$ transitions originating from their conjugated ring systems. These properties make aryl azo compounds ideal for use as dyes in textile industries where anionic groups, such as sulphonate groups, are capable of forming covalent bonds with amino groups present within the textiles.^[180] The irreversible reduction of azo groups to amines involves the transfer of four electrons and occurs in two two-electron reductions, as shown in Figure 6.4.

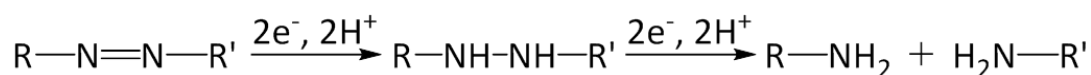


Figure 6.4. Reduction reactions of azo groups.

R and R' represents different organic side chains.

Amaranth, reactive black 5 (RB5) and reactive red 120 (RR120) are commonly used azo dyes with tri-, tetra- and hexa-anionic forms respectively at pH 7, Table 6.1. The structures, spectral and electrochemical properties of amaranth, RB5 and RR120 are summarised in Table 6.1 and Figure 6.5. These three chosen azo dyes were investigated to explore the possibility of their encapsulation within MtrCAB (proteo)liposomes due to their relatively large structures, multiple anionic charged groups, and because their reductions produces anionic amines which should be membrane-impermeable. Amaranth contains one azo group, and RB5 and RR120 both contain two azo groups, Table 6.1. The electronic absorption spectra of amaranth, RB5 and RR120 in aqueous solution all possess one predominately broad peak with an absorbance maximum at 520, 595 and 511 nm, respectively. Addition of excess dithionite caused these peaks to disappear due to the reduction of the azo groups of these molecules and the cleavage their large conjugated ring

systems, Figure 6.5 dotted lines. Subsequent air exposure of these dithionite incubated samples produced no further spectral changes, Figure 6.5 dashed black lines. These observations confirm reductions of these azo dyes are irreversible and that they produce essentially colourless amines.

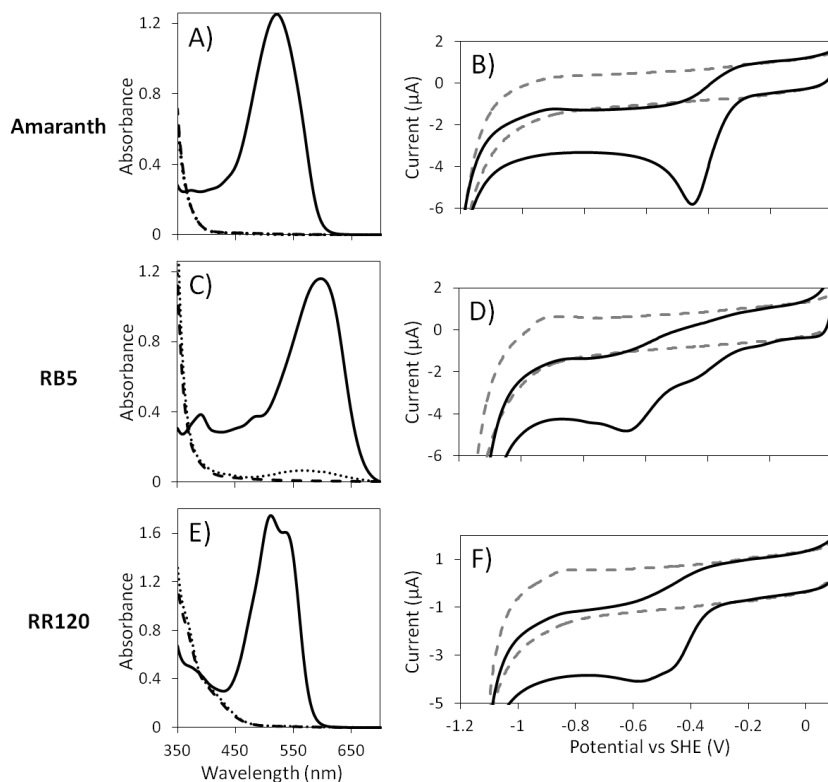


Figure 6.5. Spectroscopic and electrochemical characterisation of amaranth, RB5 and RR120.

Electronic absorbance spectra of 50 μM of either amaranth (A), RB5 (C) or RR120 (E). As prepared samples (continuous lines) were reduced by addition of excess dithionite (dotted lines). Stirred samples were then air exposed (dashed lines). Path length 1 cm. Cyclic voltammograms of 200 μM of either amaranth (B), RB5 (D) or RR120 (F), recorded at 20 mV s^{-1} , 20 $^{\circ}\text{C}$. Baselines (dashed lines) were recorded prior to cyclic voltammograms of the azo dyes were recorded (continuous lines). Samples in anaerobic 50 mM HEPES, 2 mM CaCl_2 , 10 mM KCl, pH 7.

The cyclic voltammogram obtained for amaranth had a single reductive peak with a potential of -350 mV, which is attributed to the irreversible reduction of the azo group to amines in a single step, Figure 6.5 B. The cyclic voltammogram obtained for RB5 had three reductive peaks with potentials of -130, -350 and -570 mV, which are similar to those reported previously for the irreversible reduction of the two azo groups within this molecule, Figure 6.5 D.^[180] The cyclic voltammogram obtained for RR120 had two reductive peaks with potentials of -470 and -580 mV, which are associated with the irreversible reduction of the two azo groups of RR120, Figure 6.5 F. The lack of oxidative contribution to these cyclic voltammograms is consistent with irreversible reduction of azo groups in each case.

6.3 Redox Indicator Encapsulation within (Proteo)liposomes

Initial experiments involving the five redox indicators described above were performed to assess the ability of these molecules to be encapsulated within MtrCAB (proteo)liposomes prepared by the rapid dilution of lipid-detergent micelles with/without MtrCAB-detergent micelles, as described in Chapter 5. To allow the encapsulation of these redox indicators to (proteo)liposomes, 10 mM of redox indicator was added to the detergent solubilised lipid suspension after 20 mins incubation with 55 mM OG, Figure 5.2 B. To recover any (proteo)liposomes that had formed during rapid dilution, samples were subjected to ultracentrifugation and were then resuspended in buffer to give liposome and proteoliposome suspensions which were subsequently extruded by 11 passes through polycarbonate membranes with a defined pore size of 0.2 μm , as described in Section 5.2. If any of these redox indicators significantly compromised the bilayer stability and consequently the formation of (proteo)liposomes it would be expected that ultracentrifugation would be unable to recover any (proteo)liposomes. These preparations and subsequent experiments were performed in a buffer of 20 mM MOPS, 30 mM Na_2SO_4 , pH 7.4, which is a buffer that is optimised for cyclic voltammetry of MtrC adsorbed on self-assembled monolayers-modified gold electrodes.^[181] It is expected that observations and conclusions drawn throughout this section would be valid in a buffer of 50 mM HEPES, 2 mM CaCl_2 , 10 mM KCl, pH 7 that has been used throughout this thesis.

Characterisations of the (proteo)liposome samples that potentially contained the redox indicators introduced above were performed by UV-vis spectroscopy. Parallel dithionite additions to these MtrCAB proteoliposomes and liposomes were used to assess: i) whether these redox indicators had been successfully encapsulated within liposomes in high amounts; ii) whether these redox indicators had associated with the lipid membrane, as previously seen for MV^{2+} ; and iii) if MtrCAB supported transmembrane electron transfer to the encapsulated redox indicator. By assuming the extinction coefficients of the redox indicators (Table 6.1) were unaffected by their location within liposomes, estimations of the concentrations of redox indicator present within (proteo)liposome suspensions were made. If it is assumed no transmembrane electron transfer occurred with the liposomes, any spectral changes observed upon dithionite addition to these samples would be due to the reduction of non-encapsulated/membrane-associated redox indicator. The results from such experiments are discussed below.

6.3.1 Redox Indicator Encapsulation within (Proteo)liposomes Prepared from Phosphatidylcholine

Ultracentrifugations performed after the rapid dilution of lipid-detergent micelles with/without MtrCAB-detergent micelles in the presence of 10 mM of either resazurin, RB5 or RR120 were unable to recover any (proteo)liposome pellets, which suggests these redox indicators interfere with (proteo)liposome formation. Ultracentrifugations performed after the rapid dilution of lipid-detergent micelles with/without MtrCAB-detergent micelles in the presence of 10 mM of either indigotetrasulfonic acid or amaranth recovered blue and red coloured (proteo)liposome pellets, respectively. Figure 6.6 shows the spectra of 1 mg mL^{-1} lipid suspensions of these (proteo)liposomes after completion of their respective preparations. Table 6.2 summarises of the encapsulated and total (encapsulated and non-encapsulated) concentrations of indigotetrasulfonic acid and amaranth present within these (proteo)liposomes suspensions.

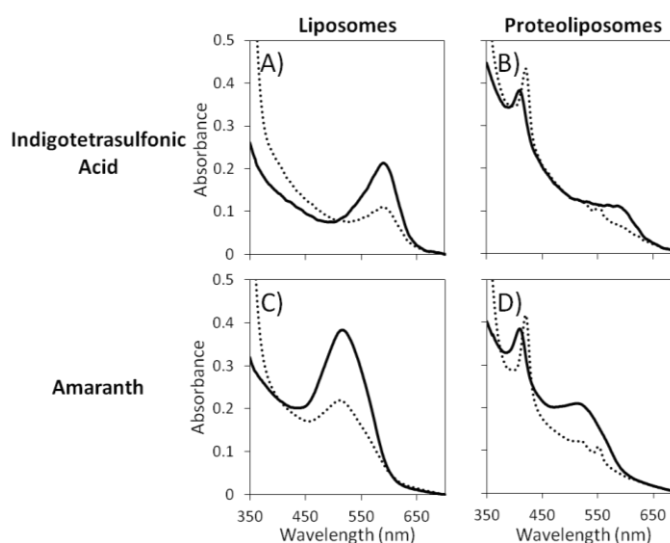


Figure 6.6. Encapsulation of indigotetrasulfonic acid and amaranth within (proteo)liposomes prepared from phosphatidylcholine.

1 mg mL^{-1} lipid suspensions of liposomes (A and C) and proteoliposomes (B and D) prepared via rapid dilution method using PC lipid in the presence of 10 mM of either indigotetrasulfonic acid (A and B) or amaranth (C and D). As prepared samples (continuous lines) prior to addition of excess dithionite and subsequent 1 min incubation (dotted lines). Stirred samples in anaerobic 20 mM MOPS, 30 mM Na_2SO_4 , pH 7.4 at 20 °C. Path length 1 cm.

		Total Concentration (μM)	Encapsulated Concentration (μM)
Indigotetrasulfonic acid	Liposomes	9	4.5
	Proteoliposomes	2	1
Amaranth	Liposomes	15	5
	Proteoliposomes	3	1

Table 6.2. Total and encapsulated concentrations of indigotetrasulfonic acid and amaranth within 1 mg mL⁻¹ lipid suspensions of (proteo)liposomes prepared from phosphatidylcholine.

The absorbance spectrum of liposomes containing indigotetrasulfonic acid showed a peak with an absorbance maxima at 591 nm which corresponds to ~ 9 μM indigotetrasulfonic acid being present within the 1 mg mL⁻¹ liposome suspension, Figure 6.6 A continuous line. Addition of dithionite caused the intensity of this peak to decrease due the reduction of non-encapsulated indigotetrasulfonic acid and showed only ~ 4.5 μM indigotetrasulfonic acid was encapsulated within liposomes, Figure 6.6 A dotted line. The absorbance spectrum of proteoliposomes containing indigotetrasulfonic acid exhibits an intense absorption in the Soret region with a maximum at 410 nm that is associated with the heme present; however, the α/β-region was obscured by spectral contributions from ~ 2 μM indigotetrasulfonic acid present within the 1 mg mL⁻¹ proteoliposome suspension, Figure 6.6 B continuous line. Addition of dithionite to these proteoliposomes caused spectral changes which are associated with the complete reduction of MtrCAB and indigotetrasulfonic acid, Figure 6.6 B dotted line.

The absorbance spectrum of liposomes containing amaranth showed a broad peak with an absorbance maxima at 520 nm which corresponds to ~ 15 μM amaranth being present within the 1 mg mL⁻¹ liposome suspension, Figure 6.6 C continuous line. Addition of dithionite caused the intensity of this peak to decrease and revealed that ~ 5 μM amaranth was encapsulated within liposomes, Figure 6.6 C dotted line. The absorbance spectrum of proteoliposomes containing amaranth exhibits an intense absorption in the Soret region with a maximum at 410 nm that is associated with heme being present; however, the α/β-region was obscured by the 520 nm peak associated with ~ 3 μM amaranth present within the proteoliposome suspension, Figure 6.6 D continuous line. Addition of dithionite to these proteoliposomes resulted in spectral changes which are associated with the complete reduction of MtrCAB and amaranth, Figure 6.6 D dotted line.

These experiments indicated that both indigotetrasulfonic acid and amaranth could both be successfully encapsulated within MtrCAB (proteo)liposomes prepared via the rapid dilution method. Addition of dithionite to these liposomes suspensions revealed that

50 % of indigotetrasulfonic acid and 66 % of amaranth was dithionite accessible and was therefore non-encapsulated. This revealed only $\sim 5 \mu\text{M}$ of these redox indicators was encapsulated within their respective 1 mg mL^{-1} liposome suspensions. As MtrCAB should support dithionite induced transmembrane electron transfer, redox indicators within MtrCAB proteoliposome suspensions should be completely dithionite accessible. This makes distinguishing the concentrations of encapsulated and non-encapsulated redox indicators present within proteoliposome suspensions via dithionite additions impossible. However, by assuming similar percentages of non-encapsulated redox indicator are present in samples of liposomes and proteoliposomes prepared in parallel, it was estimated that only $\sim 1 \mu\text{M}$ of indigotetrasulfonic acid and of amaranth was encapsulated within their respective proteoliposome suspensions. The difference between the concentration of encapsulated redox indicator found within liposomes and proteoliposomes is not surprising as these would have approximately the same size but the internal aqueous volume within proteoliposomes would be smaller due to portions of MtrCAB extending into this aqueous volume. The low encapsulation of indigotetrasulfonic acid and amaranth within proteoliposomes and the high percentages of non-encapsulation are not ideal for monitoring spectral changes due to light-induced transmembrane electron transfers.

The encapsulation of the five chosen redox indicators within (proteo)liposomes prepared via rapid dilution was mostly unsuccessful, with the presence of resazurin, RB5 and RR120 hindering (proteo)liposome formation. The exact mechanism by which these redox indicators interfered with (proteo)liposome formation was beyond the scope of this study; however, it is possible that ionic interactions occur between the anionic groups of these redox indicators (Table 6.1) and the positively charged group found within the lipid PC, Figure 1.8. Consequently it was decided to trial encapsulation of these redox indicators within MtrCAB (proteo)liposomes prepared with a different lipid composition which would provide an overall negative charge to limit these possible interactions. As described previously in Section 1.5.2.1 and Figure 1.9, *E. coli* total lipid extract contains the anionic phospholipid PG which provides the membranes of *E. coli* microbes an overall negative charge. Therefore the ability of the chosen redox indicators to be encapsulated within (proteo)liposomes composed from *E. coli* lipids and prepared by the rapid dilution of lipid-detergent micelles with/without MtrCAB-detergent micelles was assessed. Other than the lipid identity the preparation method protocol, as described in Section 5.2, and the experiments to carry out these assessments were identical to those previously described in this section. The results from such experiments are discussed below.

6.3.2 Redox Indicator Encapsulation within (Proteo)liposomes Prepared from *E. coli* Total Lipid Extract

Ultracentrifugations performed after the rapid dilution of *E. coli* lipid-detergent micelles with/without MtrCAB-detergent micelles in the presence of 10 mM RB5 were unable to recover significant (proteo)liposome pellets, suggesting that RB5 interferes with this (proteo)liposome formation. Ultracentrifugations performed after the rapid dilution of *E. coli* lipid-detergent micelles with/without MtrCAB-detergent micelles in the presence of 10 mM indigotetrasulfonic acid or resazurin recovered blue (proteo)liposome pellets, while those in the presence of 10 mM amaranth or RR120 recovered red pellets. Figure 6.7 shows the spectra of 1 mg mL⁻¹ lipid suspensions of (proteo)liposomes containing either indigotetrasulfonic acid, resazurin or amaranth after completion of their preparations. Table 6.3 summarises of the encapsulated and total concentrations of indigotetrasulfonic acid, resazurin and amaranth present within these (proteo)liposomes suspensions.

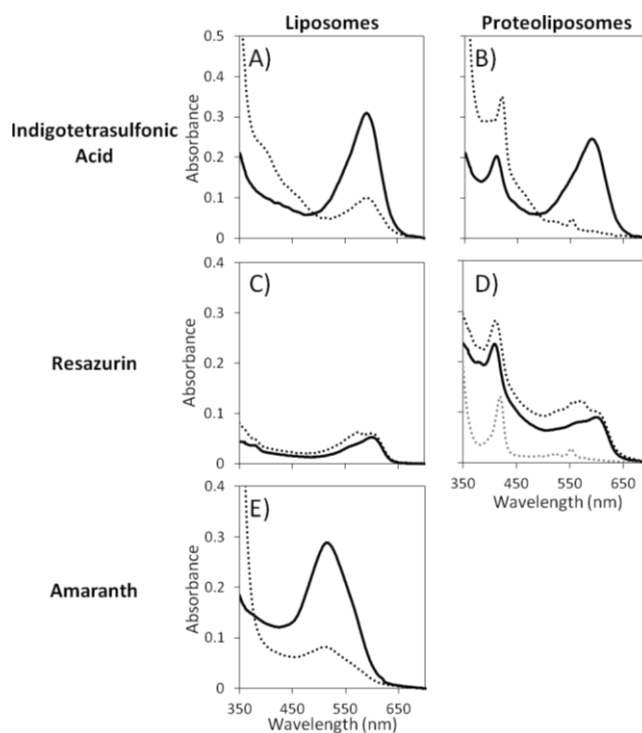


Figure 6.7. Encapsulation of indigotetrasulfonic acid, resazurin and amaranth within (proteo)liposomes prepared from *E. coli* total lipid extract.

1 mg mL⁻¹ lipid suspensions of liposomes (A, C and E) and proteoliposomes (B and D) prepared via rapid dilution of *E. coli* lipid-detergent micelles with/without MtrCAB-detergent micelles in the presence of 10 mM of either indigotetrasulfonic acid (A and B), resazurin (C and D), or amaranth (E). As prepared samples (continuous lines) prior to addition of excess dithionite and subsequent 1 min incubation (dotted black lines). Addition of excess Triton X-100 to dithionite incubated proteoliposomes thought to contain resazurin (dotted grey lines). Stirred samples in anaerobic 20 mM MOPS, 30 mM Na₂SO₄, pH 7.4 at 20 °C. Path length 1 cm.

		Total Concentration (μM)	Encapsulated Concentration (μM)
Indigotetrasulfonic acid	Liposomes	13	4
	Proteoliposomes	9	3
Resazurin	Liposomes	1-2	N/A
	Proteoliposomes	1-2	N/A
Amaranth	Liposomes	12	N/A
RR120	Liposomes	16	10
	Proteoliposomes	25	16

Table 6.3. Total and encapsulated concentrations of indigotetrasulfonic acid, resazurin, amaranth and RR120 within 1 mg mL⁻¹ lipid suspensions of (proteo)liposomes prepared from *E. coli* total lipid extract.

The absorbance spectra of liposomes containing indigotetrasulfonic acid showed ~ 13 μM indigotetrasulfonic acid was present within the 1 mg mL⁻¹ liposome suspension, Figure 6.7 A continuous line. Addition of dithionite caused the intensity of this peak to decrease due the reduction of non-encapsulated indigotetrasulfonic acid. This showed that only ~ 30 % of the indigotetrasulfonic acid (~ 4 μM) was encapsulated within liposomes, Figure 6.7 A dotted line. The absorbance spectrum of proteoliposomes containing indigotetrasulfonic acid exhibits an intense absorption in the Soret region with a maximum at 410 nm typical of oxidised MtrCAB, Figure 6.7 B continuous line. This confirms MtrCAB incorporation in proteoliposomes prepared via rapid dilution of MtrCAB-detergent and lipid-detergent micelles is independent of the lipid identity. The α/β-region was obscured by spectral contributions from indigotetrasulfonic acid, Figure 6.7 B continuous line. The absorbance at 591 nm corresponded to ~ 9 μM indigotetrasulfonic acid being present within the 1 mg mL⁻¹ proteoliposome suspension, and subsequent addition of dithionite to these proteoliposomes caused spectral changes which are associated with the complete reduction of MtrCAB and indigotetrasulfonic acid, Figure 6.7 B dotted black line. Assuming a similar percentage of non-encapsulated indigotetrasulfonic acid is present in these liposomes and proteoliposomes that were prepared in parallel, it would be estimated that only ~ 3 μM of this indigotetrasulfonic acid was encapsulated within this proteoliposome suspensions. The high percentage of non-encapsulation within these proteoliposomes would make distinguishing reductions of external indigotetrasulfonic acid from those of internal indigotetrasulfonic acid difficult, and therefore these were not suitable for studying light-induced transmembrane electron transfers.

The absorbance spectra of (proteo)liposomes containing resazurin exhibits a low intensity, broad peak at ~ 600 nm, which corresponds to 1-2 μM resazurin being present

within these 1 mg mL⁻¹ (proteo)liposomes suspensions, Figure 6.7 C and D continuous lines. Parallel additions of dithionite to these suspensions caused this absorbance peak to shift to 580 nm in accordance with the reduction of resazurin to resorufin, Figure 6.7 C and D dotted black lines. Complete reduction of resazurin to hydroresorufin was only observed upon the solubilisation of proteoliposomes with Triton X-100, as evidenced by the loss of scattering contributions to the spectra, Figure 6.7 D dotted grey lines. It is likely that complete reduction of resazurin within proteoliposomes is not observed due to the build up of charge differences across the membrane, as previously reported with MtrCAB proteoliposomes containing MV²⁺.^[93] Due to this complication, and low encapsulation seen, it was decided that resazurin (proteo)liposomes should not be used to study light-driven transmembrane electron transfers.

The absorbance spectrum of liposomes containing amaranth showed a broad peak with an absorbance maxima at 520 nm which corresponds to ~ 12 µM amaranth being present within the 1 mg mL⁻¹ liposome suspension, Figure 6.7 E continuous line. Addition of dithionite caused the intensity of both this peak and the scattering contribution from liposomes to decrease, Figure 6.7 E dotted black line. As addition of dithionite to other similarly prepared liposomes does not result in any loss of scattering contribution, this later observation suggests reduction of amaranth compromises the stability of the *E. coli* lipid bilayer. This thus makes amaranth an unsuitable redox indicator for encapsulation within (proteo)liposomes composed of *E. coli* lipids.

Figure 6.8 shows the spectra of 1 mg mL⁻¹ lipid suspensions of (proteo)liposomes containing RR120 after completion of their preparations. The absorbance spectrum of liposomes containing RR120 showed a high intensity, broad peak with an absorbance maxima at 511 nm which corresponds to approximately 16 µM RR120 being present within the 1 mg mL⁻¹ liposome suspension, Figure 6.8 A continuous line. Addition of dithionite caused the intensity of this peak to decrease due the reduction of non-encapsulated RR120 and revealed that more than 60 % of this RR120 (~ 10 µM) was encapsulated within liposomes, Figure 6.8 A dotted line. No further loss in this absorbance was observed over longer time periods. The absorbance spectrum of proteoliposomes containing RR120 exhibits an absorption in the Soret region with a maximum at 410 nm that is typical of oxidised MtrCAB, Figure 6.8 B continuous line. The α/β-region was dominated by spectral contributions from the approximate 25 µM RR120 that was present within the 1 mg mL⁻¹ proteoliposome suspension, Figure 6.8 B continuous line. Addition of dithionite to these proteoliposomes caused spectral changes which are associated with

the complete reduction of MtrCAB and, significantly, also of RR120, Figure 6.8 B dotted line. Assuming a similar percentage of non-encapsulated RR120 for the liposomes and proteoliposomes that were prepared in parallel, it was estimated that approximately 16 μM RR120 was encapsulated within this proteoliposome suspensions.

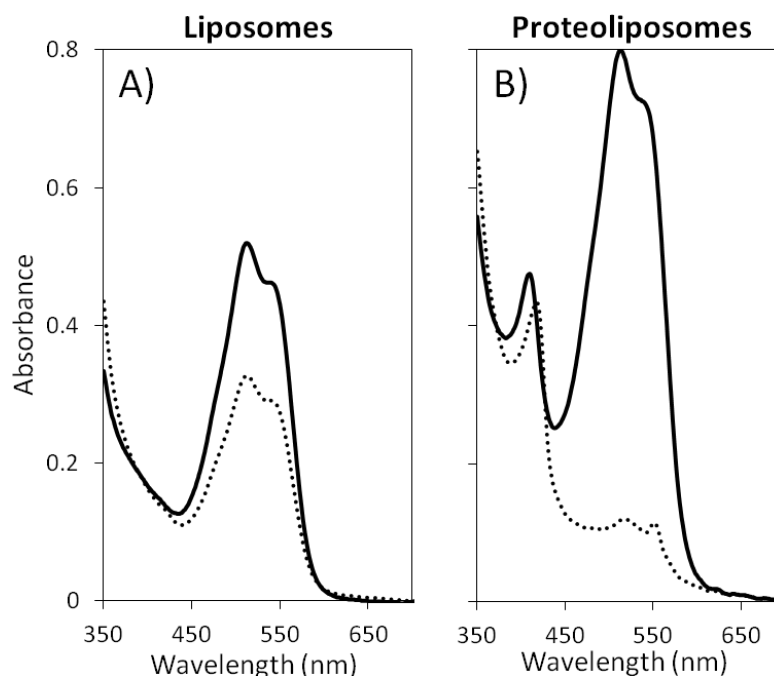


Figure 6.8. Encapsulation of RR120 in (proteo)liposomes comprised of *E. coli* lipids.

1 mg mL^{-1} lipid suspensions of liposomes (A) and proteoliposomes (B) prepared via rapid dilution of *E. coli* lipid-detergent micelles with/without MtrCAB-detergent micelles in the presence of 10 mM RR120. As prepared samples (continuous lines) prior to addition of excess dithionite and subsequent 1 min incubation (dotted lines). Stirred samples in anaerobic 20 mM MOPS, 30 mM Na_2SO_4 , pH 7.4 at 20 $^\circ\text{C}$. Path length 1 cm.

The colour changes that occurred after parallel dithionite additions to the proteoliposomes and liposomes containing RR120 was clearly followed by eye, Figure 6.9, and demonstrates that MtrCAB acts as a nanowire, allowing transmembrane electron transfer to RR120. These results show that RR120-containing (proteo)liposomes, prepared by the rapid dilution of *E. coli* lipid-detergent micelles with/without MtrCAB-detergent micelles, have potential for being used to study of light-driven transmembrane electron transfer via MtrCAB. The characterisation of (proteo)liposomes containing RR120 is described next.

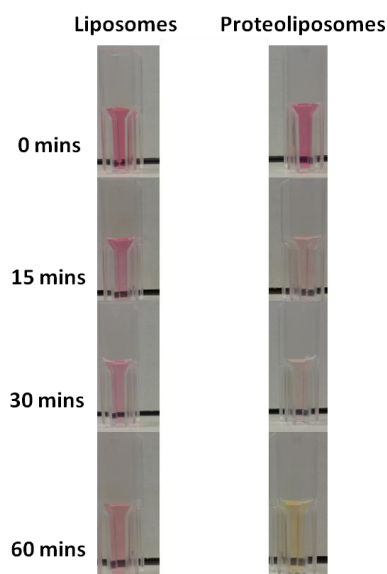


Figure 6.9. RR120 reduction within (proteo)liposomes prepared from *E. coli* lipids.

1 mg mL⁻¹ lipid suspensions of liposomes (A) and proteoliposomes (B) prepared via rapid dilution method of *E. coli* lipid-detergent micelles with/without MtrCAB-detergent micelles in the presence of 10 mM RR120. As prepared samples prior to addition of excess dithionite (0 mins) and after 15, 30 and 60 mins as noted. Samples in anaerobic 20 mM MOPS, 30 mM Na₂SO₄, pH 7.4 at 20 °C.

6.4 Preparation and Characterisation of RR120-Containing (Proteo)liposomes

Prepared from *E. coli* Total Lipid Extract

The protocol for preparation of (proteo)liposomes containing RR120 from rapid dilution of *E. coli* lipid-detergent micelles with/without MtrCAB-detergent micelles is outlined in Figure 6.10. The details of this protocol are outlined in Section 5.2 with the differences being that *E. coli* total lipid extract was used instead of PC, Figure 6.10 A, and the addition of 10 mM RR120 to the completely solubilised lipid suspension after 20 mins incubation with 55 mM OG, Figure 6.10 B. It should be noted that these preparations and subsequent experiments were performed in a buffer of 50 mM HEPES, 2 mM CaCl₂, 10 mM KCl, pH 7. At the end of their preparations, (proteo)liposome suspensions were incubated for 1 hour with Biobeads (0.1 g per 1 mg of lipid in 5 mg mL⁻¹ lipid suspension) to remove non-capsulated hydrophobic RR120. Even with these modifications to the (proteo)liposome protocol, it was assumed the orientation, topology and incorporation heterogeneity of MtrCAB in proteoliposomes are identical to those described in Chapter 5.

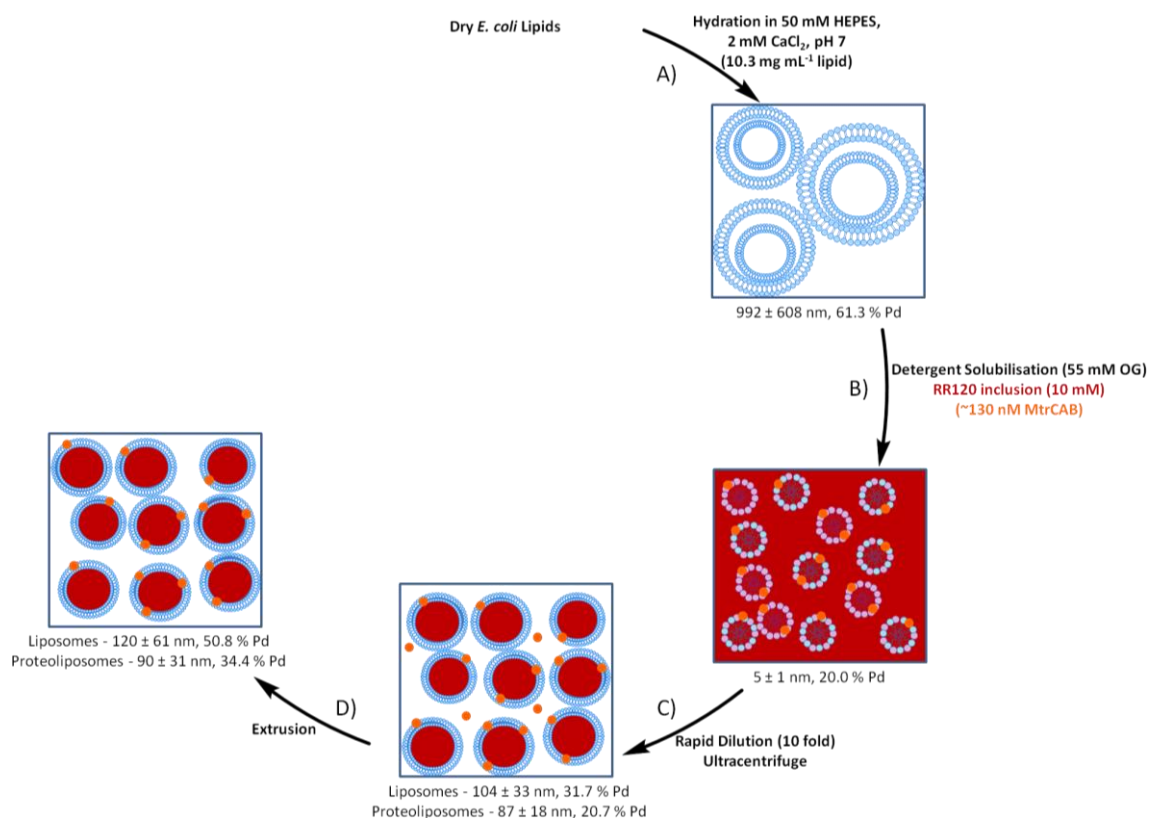


Figure 6.10. Summary of the preparation of (proteo)liposomes containing RR120 from rapid dilution of *E. coli* lipid-detergent micelles with/without MtrCAB-detergent micelles, with average hydrodynamic radii after key steps.

Average hydrodynamic radii and polydispersity (Pd) determined from DLS measurements. Data are representative of that from several preparations of (proteo)liposomes. Orange circles represent MtrCAB. Purple structures represent detergent molecules. Structures of MLVs and LUVs indicated are deduced from literature of similar systems, as described in Section 1.5.2.2.

DLS measurements showed the hydrodynamic radii of RR120-containing proteoliposomes and liposomes to be 90 ± 31 and 120 ± 61 nm, respectively. Cryo-TEM, performed by Miss Anna Stikane and Dr Rebecca Thompson at the University of Leeds, was used to obtain information on the structure and classification of these (proteo)liposome vesicles, Figure 6.11. Cryo-TEM images were able to distinguish the leaflets of lipid bilayers, and confirmed that these (proteo)liposomes containing RR120 had radii below 100 nm and proteoliposomes were more homogeneous in size than those prepared via the incorporation of MtrCAB into preformed liposomes, Section 4.2. These images also showed the (proteo)liposome suspensions consisted mostly of large unilamellar vesicles, Figure 6.11.

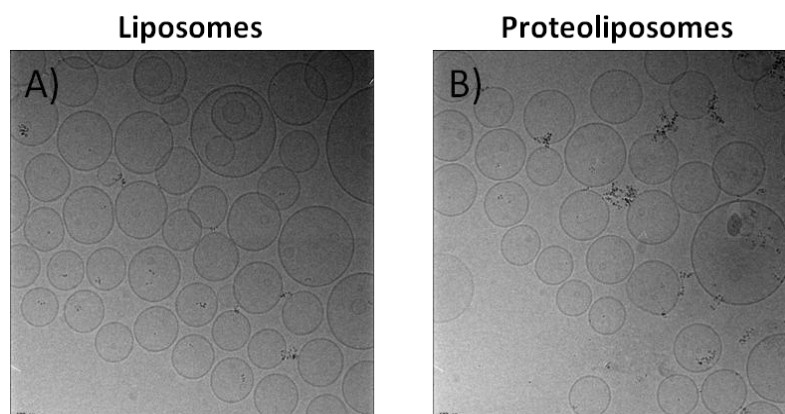


Figure 6.11. Cryo-TEM images of (proteo)liposomes containing RR120.
Cryo-TEM images of liposomes (A) and proteoliposomes (B) prepared via rapid dilution method. Black scale bars represent 100 nm. Images courtesy of Miss Anna Stikane.

Figure 6.12 shows the spectra of 1 mg mL^{-1} lipid suspensions of (proteo)liposomes containing RR120 in a buffer of 50 mM HEPES, 2 mM CaCl_2 , 10 mM KCl, pH 7 exhibits a broad peak with an absorbance maximum at 511 nm due to the RR120. The absorbance spectrum of the proteoliposome sample also exhibits a Soret band with a maximum at 410 nm which is typical of oxidised MtrCAB, Figure 6.12 B continuous line. By using the extinction coefficient of RR120 (Table 6.1), the RR120 concentration within these proteoliposome and liposome samples was determined to be 6 and $9 \mu\text{M}$, respectively.

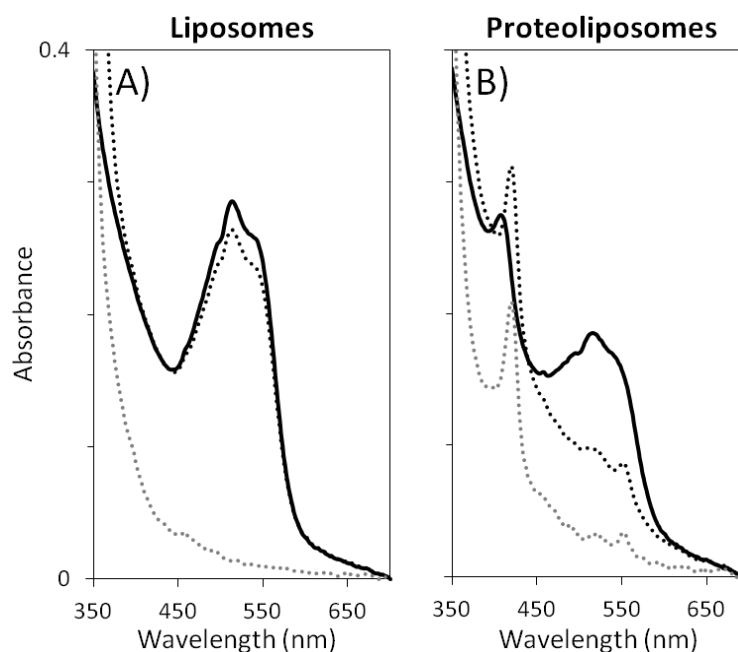


Figure 6.12. Absorbance spectra of (proteo)liposomes containing RR120.
 1 mg mL^{-1} lipid suspensions of liposomes (A) and proteoliposomes (B) prepared via rapid dilution of *E. coli* lipid-detergent micelles with/without MtrCAB-detergent micelles in the presence of 10 mM RR120. As prepared samples (continuous lines) prior to additions of excess dithionite and subsequent 1 min incubation (dotted black lines) and of excess Triton X-100 (dotted grey line). Stirred samples in anaerobic 50 mM HEPES, 2 mM CaCl_2 , 10 mM KCl, pH 7 at 20°C . Path length 1 cm.

Parallel dithionite additions made to RR120-containing MtrCAB proteoliposomes and liposomes clearly demonstrated transmembrane electron transfer from dithionite to RR120 is dependent on the presence of MtrCAB, Figure 6.12. Addition of dithionite to liposomes caused the intensity of the peak at 511 nm to slightly decrease, Figure 6.12 A dotted black line, due the reduction of $\sim 0.5 \mu\text{M}$ RR120 that is not encapsulated within the liposomes. Complete dithionite-reduction of RR120 was only observed after solubilisation of liposomes with Triton X-100, Figure 6.12 A dotted grey lines. By contrast to the lack of spectral change induced by addition of dithionite to the intact RR120 liposomes, addition of dithionite to proteoliposomes caused the Soret band to intensify and shift to 420 nm, the complete disappearance of the broad peak at 511 nm, and the appearance of sharp peaks at 523 and 552 nm, Figure 6.12 B dotted black line. These spectral changes are associated with the complete reduction of both MtrCAB and RR120. Solubilisation of proteoliposomes with Triton X-100 isolated the reduced heme spectrum by removal of the liposome scattering contribution, Figure 6.12 C dotted grey line. By using the extinction coefficient of MtrCAB, the total MtrCAB concentration was determined to be $\sim 60 \text{ nM}$ for a 1 mg mL^{-1} lipid suspension. By using Equation 5.1 and calculating the number of proteoliposomes present within a 1 mg mL^{-1} lipid suspension, it is predicted that these proteoliposomes would have an average of 13 MtrCAB per lipid vesicle.

This experiment is essentially the same as previously shown in Figure 6.8, with the major difference being the buffer that was used in preparations and experiments; with 50 mM HEPES, 2 mM CaCl_2 , 10 mM KCl, pH 7 being used here instead of 20 mM MOPS, 30 mM Na_2SO_4 , pH 7.4. It is possible that the smaller amounts of RR120 that is encapsulated in these (proteo)liposome samples in comparison to previous samples (Figure 6.8) is due to these differences in buffer and electrolyte, but this may also just be due to preparation to preparation variability. It is notable that significantly less reduction of RR120 in liposome suspensions was observed upon addition of dithionite ($\sim 8 \%$) than previously seen in Figure 6.8 ($\sim 37 \%$). This indicates that the incubation of liposome samples with Biobeads was effective at removing non-encapsulated RR120, which would presumably also be true for proteoliposome samples. With consideration that very little RR120 is located outside liposomes, and presumably outside proteoliposomes, these (proteo)liposomes offer a good alternative to MV^{2+} as an internalised redox indicator. The complete removal of MV^{2+} from liposomes was presumed to be impossible due to hydrophobic interactions between the viologen alkyl chains and hydrophobic portion of the lipid membrane.^[174] Due to the presence of the multiple anionic groups of RR120

(Table 6.1), such hydrophobic interactions and inability to completely remove non-encapsulated RR120 are not expected.

In agreement with this hypothesis we are not aware of any previous reports which demonstrate RR120 binding to the surface of lipid membranes. It was still of interest to us to determine whether RR120 could bind to lipid membranes composed of *E. coli* lipids and whether complete removal of non-encapsulated RR120 was possible. Consequently liposomes without encapsulated RR120 were prepared in an identical manner to those described above before 24 μM RR120 was added to a 1 mg mL^{-1} lipid suspension of these liposomes and subsequently incubated in the dark, in the presence of TEOA for 90 mins, Figure 6.13 continuous lines. Minimal spectral changes were observed during incubations of liposomes with external RR120, Figure 6.13 continuous grey lines, confirming RR120 does not affect the stability of liposome membranes composed of *E. coli* lipids. After 90 min incubation was complete, ultracentrifugation pelleted the liposomes which were separated from the supernatant before being resuspended in an identical buffer volume. After ultracentrifugation, the spectral features associated with RR120 were completely located within the supernatant, and the spectra of the resuspended liposomes only exhibited scattering contributions associated with liposomes, Figure 6.13 dashed lines. Thus the external RR120 remained externally located and did not associate with liposome membranes composed of *E. coli* lipids, therefore it is entirely possible that complete removal of external RR120 from (proteo)liposomes could be achieved.

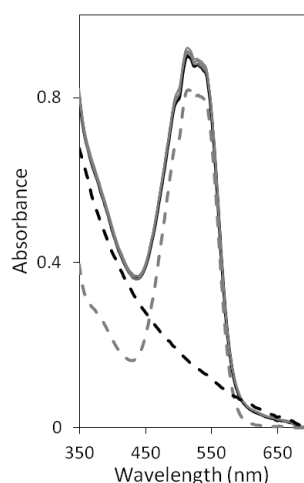


Figure 6.13. RR120 interactions with liposomes comprised of *E. coli* lipids.

1 mg mL^{-1} lipid suspension of liposomes, prepared via rapid dilution of *E. coli* lipid-detergent micelles, with 24 μM RR120 (continuous black line) was incubated in the dark for 5, 15, 30, 60 and 90 mins (continuous grey lines) prior to being ultracentrifuged to separate supernatants (dashed grey line) from liposome pellets that were resuspended in buffer (dashed black line). Stirred sample in anaerobic 50 mM HEPES, 2 mM CaCl_2 , 10 mM KCl, 50 mM TEOA, pH 7 at 20 $^\circ\text{C}$. Path length 1 cm.

6.5 Possible Interactions Between Photosensitisers and RR120-Containing (Proteo)liposomes Prepared from *E. coli* Total Lipid Extract

Light-driven reduction of MtrCAB within liposome membranes composed of PC in presence of TEOA by FMN, FAD, RF, eosin Y, fluorescein and proflavin was described in Chapter 5. Eosin Y, fluorescein and proflavin were shown to associate with PC membranes but their photoreductions of MtrCAB proteoliposomes were mainly due to random collisions between photosensitisers in the external solution and the external surface of the MtrCAB complex in proximity to the hemes.

Photoreduction of MtrCAB within liposome membranes and subsequent transmembrane electron transfer to internal encapsulated RR120 can be envisioned to be induced by these photosensitisers. However, a number of different scenarios which result in the photoreduction of RR120 within proteoliposomes can be envisioned, which are similar to those summarised in Figure 4.1. It is possible that by changing the membrane lipid composition from PC to *E. coli* total lipid extract and by encapsulating RR120 within (proteo)liposomes, the interactions between photosensitisers and (proteo)liposomes could be different to those seen in Chapter 5. Therefore characterisation of liposomes containing RR120 collected by ultracentrifugation after dark incubations with photosensitisers, similar to those performed in Section 5.4, were performed to allow conclusions to be made with regard to whether photosensitisers interact with these liposomes. The following section describes such experiments for the flavins, xanthenes and proflavin photosensitisers. These observations were then further built upon using RR120-containing (proteo)liposomes, as described in Section 6.8.

6.6 Assessment of Photosensitiser Association with Liposomes

Experiments with liposomes containing RR120, prepared via rapid dilution of *E. coli* lipid-detergent micelles, and the six chosen photosensitisers were performed to investigate whether photosensitisers affected membrane stability or bound to the liposome membranes, Figure 4.1 B, C and F. To assess whether photosensitisers associate with or lyse liposomes containing RR120, incubations of liposomes in the presence of photosensitisers were performed in an identical manner to those described in Section 5.4, as shown in Figure 6.14.

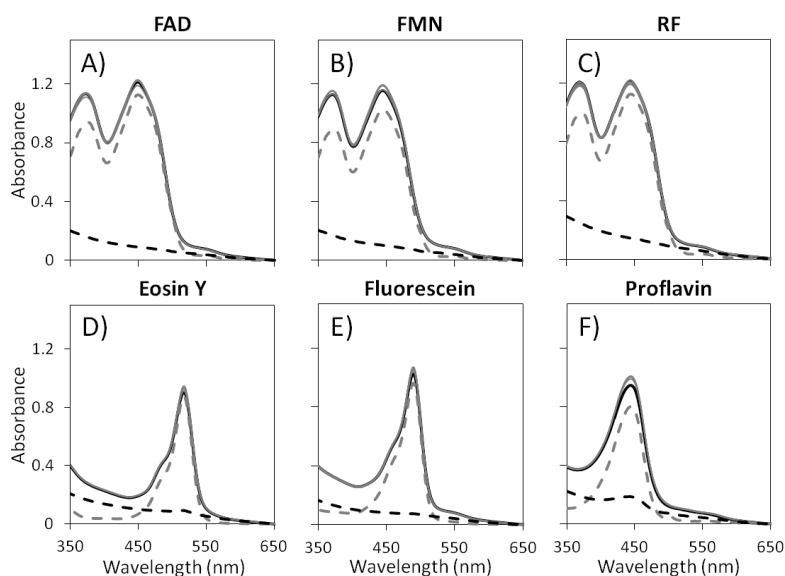


Figure 6.14. Photosensitiser interactions with RR120-containing liposomes.

1 mg mL⁻¹ lipid suspensions of liposomes containing RR120, prepared via rapid dilution of *E. coli* lipid-detergent micelles, with either 94 μM FAD (A), 81 μM FMN (B), 84 μM RF (C), 10 μM eosin Y (D), 14 μM fluorescein (E) or 11 μM proflavin (F). As prepared samples (continuous black lines) were incubated in the dark for 5, 15, 30, 60 and 90 mins (continuous grey lines) prior to being ultracentrifuged to separate supernatants (dashed grey lines) from liposome pellets that were resuspended in buffer (dashed black lines). Stirred samples in anaerobic 50 mM HEPES, 2 mM CaCl₂, 10 mM KCl, 50 mM TEOA, pH 7 at 20 °C. Path length 1 cm.

Minimal spectral changes were observed during incubations of liposomes with photosensitisers, Figure 6.14 continuous grey lines. This indicates the liposome membranes composed of *E. coli* lipids were stable and did not burst in the presence of any of the photosensitisers; therefore there is no evidence for the scenario of Figure 4.1 F for any of the studied photosensitisers. After incubations were complete, ultracentrifugation pelleted the liposomes which were subsequently resuspended in an identical buffer volume.

Once liposomes containing RR120 incubated with flavins had been pelleted by ultracentrifugation, the spectral features associated with flavins were completely located within the supernatant, and the spectra of the resuspended liposomes only exhibited spectral features associated with liposomes containing RR120, Figure 6.14 A-C dashed lines. Thus flavins remained externally located and did not associate with liposomes containing RR120. The absorbance spectra of resuspended RR120-containing liposome pellets gathered after ultracentrifugation of liposomes that had been incubated with xanthenes or proflavin showed less than 0.1 μM or 1 μM of these respective photosensitisers associated within these liposome membranes, Figure 6.14 D-F dashed black lines. Within previous chapters it has been proposed that these photosensitisers associate with the outer membrane of PC lipid membranes with the conjugated rings

associating with the hydrophobic region and the charged hydrophilic groups associating with the external solution. It is likely that eosin Y and fluorescein associate with the outer membrane of these *E. coli* lipid membranes in a similar manner; however, the presence of negatively charged PG lipids causes their association to be less than that is seen with PC lipid membranes. There is an increase in the amount of proflavin associated with membranes composed of *E. coli* lipids in comparison to those composed of PC lipid which is probably due to the additional presence of ionic binding between negatively charged PG lipid and this cationic photosensitiser.

6.7 RR120 as a Probe of Liposome Permeability

As RR120 is membrane-impermeable, encapsulated RR120 can be used as a probe of liposome permeability in the presence of external chemicals. Ideally if RR120 is only located internally and the liposome bilayer is impermeable to photoexcited electrons and photosensitisers then no photoreduction of encapsulated RR120 should be detected with external photosensitisers and TEOA. It is also possible that membrane-associated eosin Y, fluorescein and proflavin could also be within electron transfer distance of internal RR120, as presented in Figure 4.1 C.

We are not aware of any previous reports which demonstrate the photoreduction of RR120. Eosin Y, fluorescein and proflavin all have photoreduction potentials below -780 mV (Table 3.2) which are sufficiently negative to carry out complete photoreduction of RR120 (Table 6.1). The flavin photoreduction potential ($E_m \approx -220$ mV) is more positive than the peak potentials in cyclic voltammogram for reduction of RR120 ($E_p^{\text{red}} = -470$ and -580 mV). Under constant irradiation, the percentage of reduced flavin becomes essentially 100 % such that the effective flavin photoreduction potential would be ~ -360 mV, Figure 4.8 dotted line. The cyclic voltammogram obtained for RR120 reports reductive currents starting at potential of -300 mV, Figure 6.5 F. It can therefore be concluded that flavins have the potential to carry out photoreduction of RR120.

Within the following sections, the propensity of RR120 for photoreduction by flavins, xanthenes and proflavin is discussed prior to subsequent comparison to the behaviours seen when liposomes containing RR120 were irradiated in the presence of these photosensitisers.

6.7.1 Propensity of RR120 for Light-Driven Reduction

To assess the speed and extent of RR120 photoreduction by organic photosensitisers used in this study, irradiations of anaerobic solutions of 10 μM RR120 were carried out in the presence of 50 mM TEOA and 10 μM photosensitiser. A lamp power of 0.4 kW m^{-2} was used to avoid photosensitiser photobleaching. Irradiation of RR120 in the absence of photosensitisers provided no indication of azo reduction, Figure 6.15 grey lines. Spectra obtained after additions of one of the six organic photosensitisers were essentially combinations of the spectral features of 10 μM of both RR120 and the corresponding photosensitiser. Subsequent addition of dithionite resulted in disappearance of the broad peaks at 511 nm in accordance with the reduction of RR120, Figure 6.15 dotted line. By following changes in intensity at 511 nm, or 550 nm, the photoreduction of RR120 can be monitored and the extent of photoreduction can be determined with reference to absorbance of oxidised and dithionite-reduced samples. Irradiations of RR120 by all organic photosensitisers under the conditions described above are presented within the following subsections.

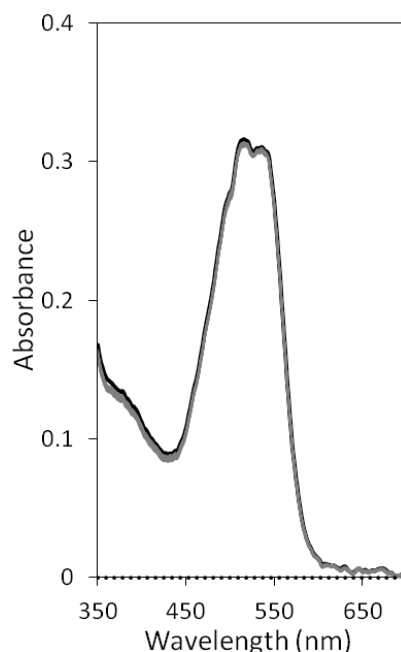


Figure 6.15. Irradiation of RR120 with no photosensitisers.

10 μM RR120 (continuous black line) was irradiated for 1, 2, 3, 4, 5, 15, 30, 60 and 90 mins at 0.4 kW m^{-2} (grey lines) prior to addition of dithionite (dotted line). Stirred sample in anaerobic 50 mM HEPES, 2 mM CaCl_2 , 10 mM KCl, 50 mM TEOA, pH 7 at 20°C . Path length 1 cm.

6.7.1.1 Eosin Y, Fluorescein and Proflavin

Figure 6.16 shows spectra obtained during irradiations of 10 μM RR120 in the presence of 10 μM of eosin Y, fluorescein or proflavin. The spectral features of proflavin did not significantly overlap with the absorbance peak of RR120; however, eosin Y possesses an absorbance peak at 520 nm which significantly overlap with this absorbance peak, Figure 6.16 A and C. Therefore the extents of RR120 reduction by eosin Y could not be monitored by following the absorbance at a single wavelength. Fluorescein possesses an absorbance peak at 490 nm which significantly overlap with the 510 nm region of a RR120 spectrum but has less spectral impact on the 550 nm region, Figure 6.16 B, therefore RR120 photoreduction by fluorescein had to be followed by the absorbance at 550 nm. Irradiations of RR120 with eosin Y, fluorescein or proflavin resulted in the decrease of the broad peak with maxima at 511 nm to leave spectral features of the corresponding photosensitiser, Figure 6.16. This correlated with the complete photoreduction of 10 μM RR120 which occurred within 30 mins for eosin Y and proflavin and 90 mins for fluorescein, Figure 6.16.

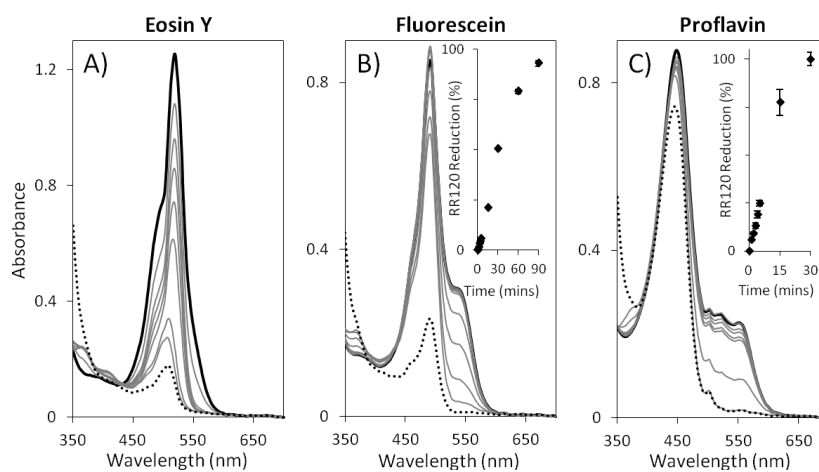


Figure 6.16. RR120 photoreduction by eosin Y, fluorescein and proflavin.

10 μM RR120 with 10 μM of either eosin Y (A), fluorescein (B) or proflavin (C). As prepared samples (continuous black lines) were irradiated for 1, 2, 3, 4, 5, 15, and 30 mins; and 60 and 90 mins for fluorescein; at 0.4 kW m^{-2} (grey lines) prior to addition of excess dithionite (dotted lines). Inserts show extent of RR120 reduction during irradiation, monitored via 511 nm or 550 nm absorbance for proflavin and fluorescein, respectively. Extent of reduction; and max and min observed values; represent the average of two independent, stirred experiments performed in anaerobic 50 mM HEPES, 2 mM CaCl_2 , 10 mM KCl, 50 mM TEOA, pH 7 at 20 $^\circ\text{C}$. Path length 1 cm.

6.7.1.2 Flavins

Figure 6.17 shows spectra obtained during irradiations of 10 μM RR120 in the presence of 10 μM flavins. The spectral features of oxidised flavin and RR120 both decreased during

irradiations indicating that fully reduced flavin was formed and subsequently RR120 photoreduction occurred, Figure 6.17. Inspection of these spectral changes confirmed that absorbance changes at 511 nm were dominated by contributions from RR120 photoreduction with no influence from flavin spectral changes. Complete photoreduction of RR120 by RF occurred within 60 mins; however, FMN and FAD were only able to achieve 90 % and 60 % RR120 photoreduction within the same time, Figure 6.17 inserts. The rate of RR120 photoreduction observed here varied with flavin identity (RF > FMN > FAD). The complete RR120 photoreduction achieved by RF confirms thermodynamic predictions that flavins can carry out complete RR120 photoreductions during irradiations, as described in Section 6.7.

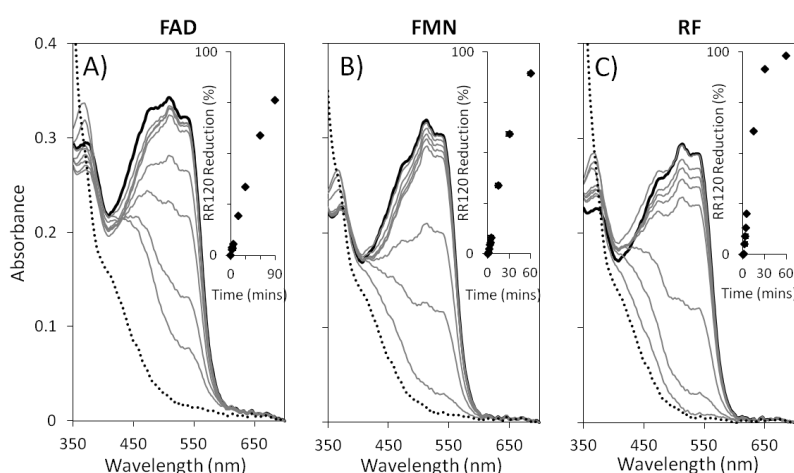


Figure 6.17. RR120 photoreduction by flavin photosensitisers.

10 μM RR120 with 10 μM of either FAD (A), FMN (B) or RF (C). As prepared samples (continuous black lines) were irradiated for 1, 2, 3, 4, 5, 15, 30 and 60 mins; and 90 mins for FAD; at 0.4 kW m^{-2} (grey lines) prior to addition of excess dithionite (dotted lines). Inserts show extent of RR120 reduction during irradiation, monitored via 511 nm absorbance. Extent of reduction; and max and min observed values; represent the average of two independent, stirred experiments performed in anaerobic 50 mM HEPES, 2 mM CaCl_2 , 10 mM KCl, 50 mM TEOA, pH 7 at 20 $^\circ\text{C}$. Path length 1 cm.

6.7.2 Irradiation of Liposomes Containing RR120

To assess if photoreduction of RR120 encapsulated within liposomes was possible without MtrCAB acting as an electron conduit, irradiations of 1 mg mL^{-1} lipid suspensions of liposomes containing $\sim 5 \mu\text{M}$ RR120 were carried out in the presence of 50 mM TEOA and 10 μM photosensitiser, using a lamp power of 0.4 kW m^{-2} . Spectra recorded after irradiation and dithionite addition showed minimal changes in accordance with membrane stability. Subsequent additions of Triton X-100 caused the disappearance of the broad peaks at 511 nm in accordance with the reduction of RR120, Figure 6.12 A dotted lines.

By following changes in intensity at 511 nm, or 550 nm, the photoreduction of RR120 within liposomes can be monitored and the extent of photoreduction can be determined with reference to absorbance of oxidised and dithionite-reduced samples. Irradiations of liposomes containing RR120 by all organic photosensitisers under the conditions described above are presented next.

6.7.2.1 Eosin Y, Fluorescein and Proflavin

Irradiations of RR120-containing liposomes in the presence of eosin Y, fluorescein or proflavin resulted in the decrease of the broad peak with maxima at 511 nm to leave the scattering contribution of the liposomes and the spectral features of the corresponding photosensitiser, Figure 6.18. This correlated with the complete photoreduction of RR120 within liposome suspensions which occurred within 30 mins for eosin Y and proflavin and 60 mins for fluorescein, Figure 6.18.

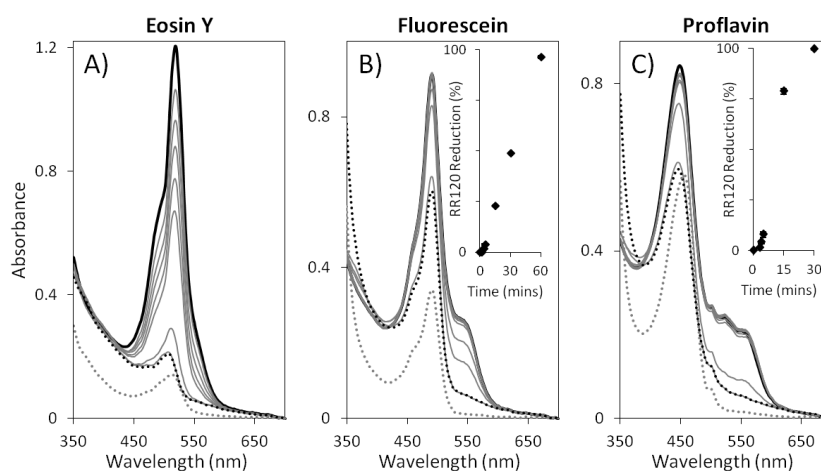


Figure 6.18. Irradiations of liposomes containing RR120 in the presence of eosin Y, fluorescein and proflavin.

1 mg mL⁻¹ lipid suspensions of RR120-containing liposomes with 10 μM of either eosin Y (A), fluorescein (B) or proflavin (C). As prepared samples (continuous black lines) were irradiated for 1, 2, 3, 4, 5, 15, and 30 mins; and 60 mins for fluorescein; at 0.4 kW m⁻² (continuous grey lines) prior to additions of excess dithionite and subsequent 1 min incubation (dotted black lines) and of excess Triton X-100 (dotted grey lines). Inserts show extent of RR120 reduction during irradiation, monitored via 511 nm or 550 nm absorbance for proflavin and fluorescein, respectively. Extent of reduction; and max and min observed values; represent the average of two independent, stirred experiments performed in anaerobic 50 mM HEPES, 2 mM CaCl₂, 10 mM KCl, 50 mM TEOA, pH 7 at 20 °C. Path length 1 cm.

These results demonstrate that eosin Y, proflavin and fluorescein are able to carry out the complete photoreduction of RR120 encapsulated within liposomes without the need of MtrCAB being present to act as a transmembrane electron conduit. These photosensitisers have been shown to partition into the hydrophobic region of the outer lipid

monolayer of membranes and not cross them. As loss of liposome stability was not observed during these irradiations, it is most likely that photoreductions of RR120 within liposomes by eosin Y, fluorescein and proflavin occurs via membrane-associated photosensitisers being within electron transfer distance to internal RR120, Figure 4.1 C. Therefore these photosensitisers are not ideal for studying light-driven transmembrane electron transfer via MtrCAB.

6.7.2.2 Flavins

Figure 6.19 shows spectra obtained during irradiations of RR120-containing liposomes in the presence of 10 μM flavins. The spectral features of oxidised flavin decreased during irradiations indicating that fully reduced flavin was formed, Figure 6.19. The spectral features of RR120 also decreased during these irradiations in accordance with flavins being able to partially photoreduce RR120 within the liposome suspensions Figure 6.19.

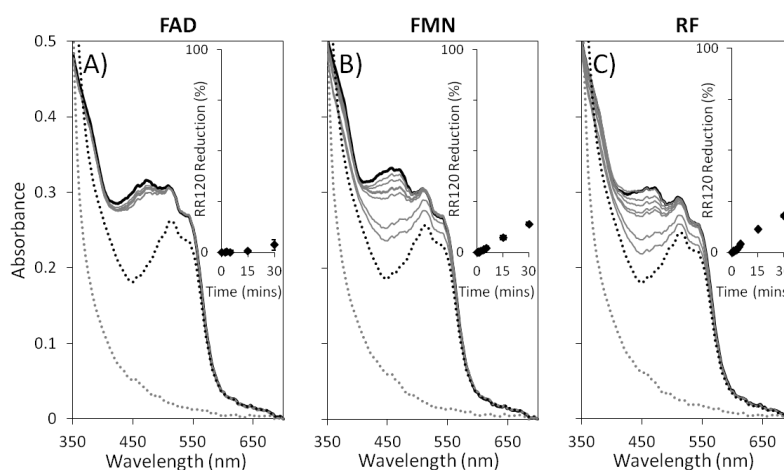


Figure 6.19. Irradiations of liposomes containing RR120 in the presence of flavins.

1 mg mL^{-1} lipid suspensions of RR120-containing liposomes with 10 μM of either FAD (A), FMN (B) or RF (C). As prepared samples (continuous black lines) were irradiated for 1, 2, 3, 4, 5, 15, and 30 mins at 0.4 kW m^{-2} (continuous grey lines) prior to additions of excess dithionite and subsequent 1 min incubation (dotted black lines) and of excess Triton X-100 (dotted grey lines). Inserts show extent of RR120 reduction during irradiated, monitored via 511 nm absorbance. Extent of reduction; and max and min observed values; represent the average of two independent, stirred experiments performed in anaerobic 50 mM HEPES, 2 mM CaCl_2 , 10 mM KCl, 50 mM TEOA, pH 7 at 20 $^{\circ}\text{C}$. Path length 1 cm.

Within 30 mins FAD, FMN and RF were only able to achieve $\sim 4\%$, 14% and 18% photoreduction of the $\sim 5 \mu\text{M}$ RR120 contained in these liposome suspensions, Figure 6.19 inserts. Much greater extents of RR120 photoreduction were observed under similar conditions with 10 μM RR120 in aqueous solution, Figure 6.17 inserts. Additions of dithionite caused further reduction of RR120, but complete reduction was only observed

upon the addition of Triton X-100, Figure 6.19 dotted lines. With these considerations in mind, and as there was no loss of liposome stability observed during these irradiations, it is likely that the RR120 photoreduction observed in these experiments was due to the reduction of non-encapsulated RR120 in the liposome suspensions only.

Due to the slow and steady rates of photoreduction observed during these timecourses, linear trendlines could be used to determine and compare the initial rates of RR120 photoreduction by flavins within aqueous solution and liposome suspensions. The initial photoreduction rates of RR120 in aqueous solution that was achieved by RF, FMN and FAD were determined to be 4.0, 2.0 and 0.9 % min⁻¹, respectively. The initial photoreduction rates of RR120 in liposome suspensions achieved by RF and FMN were similar to those observed in aqueous solution, 3.1 and 2.1 % min⁻¹ respectively. This similarity supports the theory that only non-encapsulated RR120 was photoreduced within liposomes suspensions, as it would be expected that initial rate would be hindered if external flavins had to pass photoexcited electrons to internally encapsulated RR120.

From these experiments we can conclude that RF, FMN and FAD do not disrupt the liposome membrane to allow the photoreduction of internally compartmentalised RR120 within liposomes. As flavins are able to photoreduce RR120 in aqueous solution and MtrCAB within the membrane of proteoliposomes, flavins alongside MtrCAB proteoliposomes containing RR120 have all the desirable qualities required to study light-driven transmembrane electron transfer via MtrCAB, as idealised in Figure 4.1 A. The results from experiments performed to assess whether chosen flavins could perform the photoreduction of proteoliposomes containing RR120 via MtrCAB are discussed next.

6.8 Flavin-Dependent Photoreduction of RR120 inside MtrCAB Proteoliposomes by Transmembrane Electron Transfer

To assess if photoreduction of MtrCAB, within liposome bilayers composed of *E. coli* lipids, and internally compartmentalised RR120 by flavins was possible, irradiations of 1 mg mL⁻¹ lipid suspensions of proteoliposomes containing RR120 were performed in the presence of 50 mM TEOA and ~ 10 µM flavin using a lamp power of 0.4 kW m⁻².

Spectra obtained after additions of one of the three flavins were essentially combinations of the spectral features of oxidised MtrCAB proteoliposomes containing RR120 and 10 µM of the corresponding flavin, Figure 6.20 continuous black lines.

Irradiations of suspensions of these proteoliposomes containing RR120 in the presence of flavins caused: i) the spectral features of oxidised flavin to decrease indicating that fully reduced flavin was formed; ii) the Soret peak of oxidised MtrCAB to shift to a higher wavelength of 419 nm, which is indicative of partial photoreduction of the hemes of MtrCAB; iii) the spectral features from RR120 to decrease due to photoreduction of RR120 within the proteoliposome suspensions; and iv) the appearance of peaks with maxima at 523 and 552 nm due to heme photoreduction. Inspection of these spectral changes confirmed that absorbance changes at 511 nm were dominated by contributions from RR120 photoreduction with no or negligible influence from flavin or MtrCAB spectral changes, respectively. By following changes in intensity at 511 nm the photoreduction of RR120 within proteoliposomes can be monitored and the extent of photoreduction can be determined with reference to absorbance at 511 nm of oxidised and dithionite-reduced samples. Due to the overlapping spectral features of RR120 and flavins the changes in intensity at 552 nm or 420 nm cannot be used to determine the extent of MtrCAB photoreduction achieved during these irradiations.

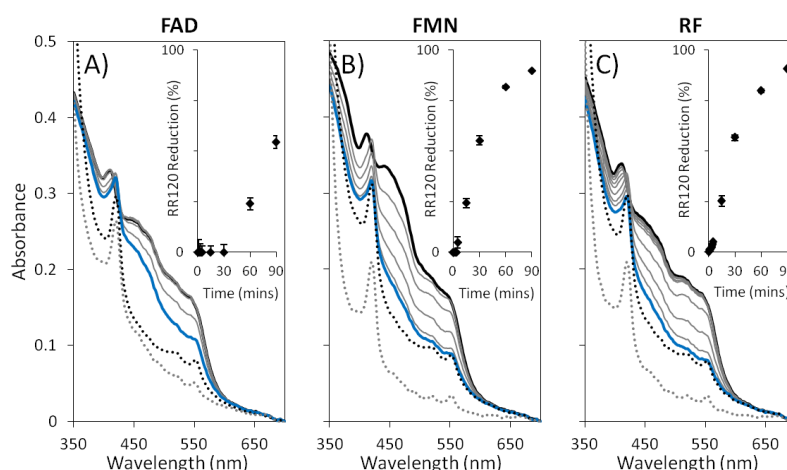


Figure 6.20. Irradiations of MtrCAB proteoliposomes containing RR120 in the presence of flavin photosensitisers.

1 mg mL⁻¹ lipid suspensions of RR120-containing proteoliposomes with 10 μM of either FAD (A), FMN (B) or RF (C). As prepared samples (continuous black lines) were irradiated for 1, 2, 3, 4, 5, 15, 30, 60 (continuous grey lines) and 90 mins at 0.4 kW m⁻² (blue lines) prior to additions of excess dithionite and subsequent 1 min incubation (dotted black lines) and of excess Triton X-100 (dotted grey lines). Inserts show extent of RR120 reduction during irradiation, monitored via 511 nm absorbance. Extent of reduction; and max and min observed values; represent the average of two independent, stirred experiments performed in anaerobic 50 mM HEPES, 2 mM CaCl₂, 10 mM KCl, 50 mM TEOA, pH 7 at 20 °C. Path length 1 cm.

Within 90 mins irradiations, near complete photoreduction of RR120 within suspensions of proteoliposomes containing RR120 was observed by RF and FMN, 91 %

and 90 % respectively, Figure 6.20 inserts. Similar irradiations performed with FAD were only able to achieve 55 % RR120 photoreduction within the same time, Figure 6.20 inserts. The initial rates of RR120 photoreduction that was achieved by RF, FMN and FAD were determined to be 1.9, 2.0 and 0.9 % min⁻¹, respectively. These observations confirm the complete photoreduction of RR120 within MtrCAB proteoliposomes can be induced by irradiation in the presence of flavin photosensitisers. Considering that similar irradiations of RR120 liposomes, i.e., without MtrCAB present were unable to achieve significant photoreduction of RR120 (Figure 6.19), the photoreduction of RR120 within proteoliposomes must occur via transmembrane electron transfer facilitated by the MtrCAB complex.

6.9 Discussion

The following discussion considers the initial rates of RR120 photoreduction that was achieved by RF, FMN and FAD in aqueous solution and (proteo)liposome suspensions and tries to account for their differences. Prior to this, the discussion describes the attempts to completely remove non-encapsulated RR120 from (proteo)liposome suspensions and the impact this has on the conclusions of this work.

The complete removal of non-encapsulated RR120 was not always achieved and the amount of non-encapsulated RR120 varied between different preparations of (proteo)liposomes. A variety of different methods was tried to ensure complete removal of non-encapsulated RR120 after preparation of (proteo)liposomes, including: extra ultracentrifugations; separations via columns; and incubations of different time durations with Biobeads to remove hydrophobic RR120. All of these methods resulted in some non-encapsulated RR120 remaining or in the lysis of (proteo)liposomes and subsequent increased levels of non-encapsulated RR120. Currently the most successful method of removing non-encapsulated RR120 from (proteo)liposome suspensions has been found to be 1 hour incubation with Biobeads (0.1 g per 1 mg of lipid in 5 mg mL⁻¹ lipid suspension).

It has been shown that RR120 does not bind to these liposome membranes, therefore it is entirely possible that the complete removal of external RR120 from (proteo)liposomes suspensions could be achieved. It is hoped that future work may reveal an optimised method for removing non-encapsulated RR120 after the preparation of (proteo)liposomes containing RR120; however, the presence of some non-encapsulated RR120 does not detract from the main conclusions drawn from this work.

The initial rates of RR120 photoreduction achieved by RF, FMN and FAD within this work, as summarised in Table 6.4, varied with flavin identity. Within aqueous solution, the rates of RR120 photoreduction varied with flavin identity, as shown in Table 6.4 to be RF > FMN > FAD. This difference in rates could possibly be explained by the size of the ribityl side chains, with the bigger the ribityl chain hindering photoreduction of RR120. This pattern and effect that flavin identity has upon RR120 photoreduction has been previously observed in MV²⁺ photoreduction (Section 4.4.1.2) and in OmcA photoreduction (Section 3.7). This pattern caused by flavin identity was also observed for the initial photoreduction rate of RR120 within liposome suspension, which is thought to be observed due to the present of non-encapsulated RR120 within liposome suspensions.

	Initial Rate of RR120 Photoreduction (% min ⁻¹)		
	Aqueous Solution	Liposome Suspension	Proteoliposome Suspension
RF	4.0	3.1	1.9
FMN	2.0	2.1	2.0
FAD	0.9	N.D.	0.9

Table 6.4. Initial rate of RR120 photoreduction achieved by flavins.

Values gained from linear trendlines from the average of at least two independent experiments performed in anaerobic 50 mM HEPES, 2 mM CaCl₂, 10 mM KCl, 50 mM TEOA, pH 7 at 20 °C, with irradiation at 0.4 kW m⁻² in the presence of 10 μM of either FAD, FMN or RF. N.D. denotes where no initial photoreduction is detected. See text for details.

The initial photoreduction rates of RR120 within proteoliposomes achieved by FMN and FAD were nearly identical to those observed when RR120 was in aqueous solution, as shown in Table 6.4. As the complete photoreduction of RR120 within proteoliposomes would have to be facilitated by transfer membrane electron transfer along the MtrCAB complex, the initial rate of RR120 photoreduction could be limited either by MtrCAB transmembrane electron transfer or by electron transfer between the flavins and MtrCAB. As the initial rates of RR120 photoreduction achieved by FMN and FAD were independent of the location of RR120, i.e. in aqueous solution or encapsulated within proteoliposomes, it is likely that these initial rates are limited by electron transfer between the photoreduced flavins and MtrCAB. In contrast the initial rates of photoreduction of RR120 within proteoliposomes initiated by RF and FMN are similar to each other (~ 2.0 % min⁻¹) but half the rate achieved with RF when RR120 was in aqueous solution (4.0 % min⁻¹). This suggests that the initial rates of RR120 photoreduction within proteoliposome suspensions by RF was limited by the rate of transmembrane electron transfer along MtrCAB.

Even though the extent of MtrCAB photoreduction achieved during these irradiations could not be monitored due to the spectral overlaps from the spectral features of RR120 and flavins the absorbance maxima of the Soret peak could be followed. Addition of dithionite causes the absorbance maximum of the Soret peak to shift to 420 nm in accordance with complete reduction of the hemes of MtrCAB, Figure 6.12 B dotted line.^[95] During these irradiations the absorbance maxima of the Soret only reached 419 nm which highlights that MtrCAB was not completely photoreduced by flavins. This partial photoreduction of MtrCAB is due to the photoreduction potential of flavins being located in the middle of the MtrCAB heme potential window. This is the likely reason why photoreduction of RR120 proteoliposomes by RF and FMN is limited by the rate of transmembrane electron transfer along MtrCAB. It is possible that using different photosensitisers with more negative photoreduction potentials would allow a thermodynamically downhill reduction cascade that would improve the rate of RR120 photoreduction with proteoliposomes suspension.

6.10 Conclusions

Within this chapter a range of redox indicators were characterised and screened for their ability to be encapsulated in MtrCAB (proteo)liposomes. The encapsulation of these redox indicators in (proteo)liposomes composed of PC lipids was mostly unsuccessful, with either (proteo)liposome formation being hindered or low encapsulation being observed. The encapsulation of these redox indicators in (proteo)liposomes composed of *E. coli* lipids was more successful due to the presence of anionic phospholipid PG that provides an overall negative charge to the proteoliposome membrane which repels the negatively charged redox indicators. (Proteo)liposomes containing RR120 showed high encapsulations and low percentages of non encapsulated RR120. Parallel dithionite additions made to RR120-containing MtrCAB proteoliposomes and liposomes demonstrated MtrCAB acts as a nanowire by facilitating transmembrane electron transfer to allow the complete reduction of encapsulated RR120 in proteoliposomes. The heme spectra and the broad absorbance peak with an absorbance maxima at 511 nm spectra associated with these proteoliposomes can be used to monitor the photoreduction of MtrCAB and RR120, respectively.

It was established that these (proteo)liposomes containing RR120 do not burst during irradiation or dark incubations with any of the organic photosensitisers used in this

work, as presented in Figure 4.1 F. Eosin Y, proflavin and fluorescein were shown to associate with liposome membranes composed of *E. coli* lipids. This association probably occurs via semi-partitioning within the hydrophobic region of the outer lipid monolayer (i.e. Figure 4.1 B-C) and not via crossing the membrane to be located in the aqueous interior of liposome (i.e. Figure 4.1 D). Upon irradiation these photosensitisers initiated complete photoreduction of RR120 encapsulated within liposomes without the need of MtrCAB being present to act as a transmembrane electron wire. As loss of liposome stability was not observed, it is most likely that photoreductions of RR120 within liposomes occurred by these membrane-associating photosensitisers being within electron transfer distance to compartmentalised RR120, Figure 4.1 C. Eosin Y, fluorescein and proflavin were therefore not investigated any further as they were unsuitable for studying light-driven transmembrane electron transfers via MtrCAB.

FMN, FAD and RF were shown to not associate with liposomes membrane composed of *E. coli* lipids. Upon irradiation these flavin photosensitisers initiated slow steady photoreduction of 10 μ M RR120 in aqueous solution until completion. Irradiation with flavins initiated partial photoreduction of RR120 in suspensions of liposomes which was associated with the reduction of non-encapsulated RR120 that was present in the external solution. Irradiations of MtrCAB proteoliposomes containing RR120 in the presence of flavins resulted in the partial photoreduction of MtrCAB and the complete photoreduction of RR120, both non-encapsulated and encapsulated. All this evidence combined demonstrates that the photoreduction of RR120 within proteoliposomes must occur via transmembrane electron transfer facilitated by the MtrCAB complex, and thus that MtrCAB in proteoliposome bilayers has the ability to transfer photoexcited electrons to internalised redox molecules.

Within aqueous solution, the rates of RR120 photoreduction varied with flavin identity (RF > FMN > FAD). The initial rates of RR120 photoreduction achieved by FMN and FAD were independent of the location of RR120, i.e. in aqueous solution or encapsulated within proteoliposomes, therefore it was thought that these initial rates were limited by electron transfer between the photoreduced flavins and MtrCAB. In contrast the initial rate of RR120 photoreduction by RF was hindered by ~ 50% when RR120 was located within proteoliposomes instead of aqueous solution. This suggested that the initial rates of RR120 photoreduction within proteoliposome suspensions by RF was limited by the rate of transmembrane electron transfer along MtrCAB.

The next chapter of this work discusses the future possibilities for different chemical reactions to be contained within MtrCAB proteoliposomes and other possibilities for MtrCAB proteoliposomes to be used to help determine the structure of membrane-bound MtrCAB and understand nanowires of *S. oneidensis*. This discussion also includes how the photosensitisers used within this work have initiated reactions within cultures of *S. oneidensis* when they were irradiated.

Chapter 7

Summary and Future Perspectives

Incorporation of the transmembrane spanning porin:cytochrome complex, MtrCAB, in non-conductive membranes of liposomes was previously shown to allow transmembrane electron transfer from an external chemical reductant to an internalised electron acceptor, MV^{2+} , that would otherwise not be observed.^[83, 92, 93] In this study the possibility of extending this property of MtrCAB to allow transfer of photoexcited electrons from external photosensitisers to internalised redox indicators was explored. It is envisaged that this advance would pave the way to using MtrCAB proteoliposomes with appropriate cargos as nanoreaction compartments where light-driven chemistry would be catalysed.

The research in this study used a stepwise approach to explore this potential by identifying if MtrCAB could accept photoexcited electrons from externally located photosensitisers and transfer these across a liposome bilayer to drive internal reductive transformations. Eight soluble photosensitisers, i.e. FAD, FMN, RF, eosin Y, fluorescein, proflavin, $[Ru(bpy)_3]^{2+}$ and RuP, were assessed for their ability to photoreduce *S. oneidensis* outer membrane cytochromes and MtrCAB proteoliposomes, in the presence of TEOA as the SED. The previously reported method used for preparing MtrCAB proteoliposomes containing MV^{2+} proved unsuitable to investigate light-induced, transmembrane electron transfer due to irreproducibility of MtrCAB incorporation and inability to completely remove MV^{2+} bound to their exterior surface.^[83, 92, 93] Therefore a new method of preparing proteoliposomes was developed which allowed greater MtrCAB incorporation within proteoliposome bilayers, such that MtrCAB could be used as an independent redox indicator in addition to internally compartmentalised redox indicators.

Ruthenium complexes did not associate with the membranes of (proteo)liposomes; however, no photoreduction of MtrCAB within proteoliposomes was observed under experimental conditions used within this study due to the rapid charge recombination of their photoexcited states. By contrast eosin Y, fluorescein and proflavin photoreduced MtrCAB completely but partitioned within lipid bilayers such that they transferred of photoexcited electrons to compartmentalised redox molecules in the absence of MtrCAB. The flavin photosensitisers, FMN, FAD and RF, showed the desired properties of not associating with (proteo)liposome membranes and being able to photoreduce MtrCAB such that electrons were transferred through the protein complex to the internalised redox indicator RR120. This demonstrates that, in conjunction with appropriate photosensitisers

and SEDs, MtrCAB in proteoliposome bilayers will transfer photoexcited electrons to internalised redox molecules.

Future work could use MtrCAB proteoliposomes with internalised RR120 to assess the ability of other photosensitisers to drive the desired transmembrane electron transfer. Such photosensitisers may offer more negative photoreduction potentials than those of flavins which may increase the rate of photoreduction. One photosensitiser of particular interest is the RuP:TiO₂ nanoparticle system which has been shown to photoreduce extracellular cytochromes of *S. oneidensis* (Chapter 3) and is not expected to associate with lipid membranes. Other SEDs could also be screened for their ability to improve the rates of photosensitiser regeneration and subsequently MtrCAB (proteo)liposome photoreduction.

This work has demonstrated that different soluble redox indicators can be compartmentalised within MtrCAB proteoliposomes. Additionally, Dr Matt Lawes of the University of East Anglia previously demonstrated that a soluble electron transfer protein, cytochrome *c*, could be compartmentalised within MtrCAB proteoliposomes and could receive electrons from externally located dithionite.^[182] It can therefore be envisioned that MtrCAB proteoliposomes could be developed to contain other interesting soluble enzymes which would be able to harness light to drive reductive transformations within their internal volumes. Enzymatic transformations which could be compartmentalised within MtrCAB proteoliposomes include: i) reduction of protons to hydrogen by hydrogenases; ii) reduction of carbon dioxide to formate by formate dehydrogenases; and iii) reduction of nitrous oxide to N₂ by nitrous oxide reductases. These selected transformations are of interest to artificial photosynthetic systems due to their ability to produce high energy fuels and/or remove potent greenhouse gases via the utilisation of solar energy alone.^[7, 15, 20, 183] In addition to enzyme transformations, it can be envisioned that other reductive transformations can be compartmentalised and performed within MtrCAB proteoliposomes; such as the formation of hydrogen by platinum nanoparticles or molecular mimics of hydrogenases and the formation of gold nanoparticles by the reduction of internalised gold (III). The later transformation are attractive due to the ability to controllably form gold nanoparticles with a desired size and a narrow size distribution arising from the growth restriction within the nanocompartment.^[184]

In addition to exploring the different photosensitisers, SEDs and internalised reductive transformations that are available, the identity of the transmembrane electron

protein or the compartment wall could also be individually varied to form other light-driven nanocompartment systems similar to MtrCAB proteoliposomes but with different properties of interest. The incorporation of active PSI complex within the membranes of liposomes is attractive as it would facilitate the photoreduction of internalised chemicals without the need of an additional external photosensitiser.^[185] This system would also allow the direct study of the light-driven mechanisms of electron transfer by PSI, without the complication of the presence of other chemicals and proteins that are found in the host cell. Within this work it has been shown that the membrane composition of MtrCAB (proteo)liposomes can be modified to allow greater encapsulation of internalised redox indicators and limit undesired interactions with external photosensitisers. The incorporation of MtrCAB within the polymer membranes of polymersomes may offer vesicles which are more chemically robust and versatile in comparison to those of proteoliposomes.

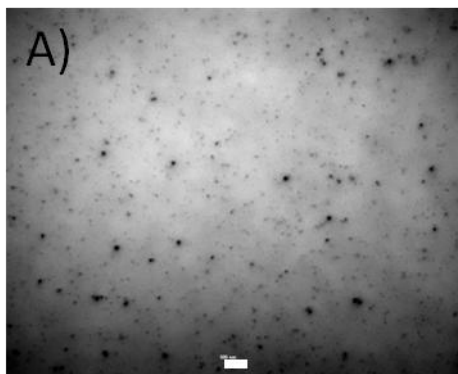
The photoreductions of *S. oneidensis* outer membrane cytochromes and the study of photosensitiser interactions with PC lipid membranes demonstrated within this thesis provide a framework to inform the development strategies to achieve catalytic transformations within *S. oneidensis*. This would remove the need for proteoliposome preparation and protein purification of both MtrCAB and any compartmentalised enzymes. The growth of *S. oneidensis* cultures are inexpensive, comparatively easy, and scalable in comparison to MtrCAB proteoliposome preparations; and offer the additional benefits of cell-secretion of flavin photosensitisers and enzyme self-repair and regeneration if the microbes have the energy available to do so.^[33] Additionally, the diverse metabolic pathways of *S. oneidensis* offer numerous possible reductive transformations which could synthesise high energy and/or high value chemicals of hydrogen, formate, lactate and succinate.^[186, 187] Electrosynthesis of succinate by *S. oneidensis* is driven by electron transfer from MtrCAB to periplasmic fumarate reductases via CymA and the quinone pool of the inner membrane, $E_m(\text{fumarate/succinate}) \approx 30 \text{ mV}$ at pH 7.^[188] The light-driven synthesis of succinate; and formate or hydrogen by periplasmic formate dehydrogenases or hydrogenases, respectively; can be envisioned to occur in a similar manner. The light-driven production of these products and additional productions could be enhanced and induced through genetic engineering of natural metabolic pathways of *S. oneidensis*. Experiments that explore the possibilities of employing the photosensitisers described here for artificial photosynthesis of these products, and others, by *S. oneidensis* are ongoing in our laboratories.

The proteoliposomes with greater amounts of MtrCAB incorporated within the membranes that were developed within this work provides new opportunities to help determine the structure of MtrCAB within lipid membranes. Even though considerable success has been made in solving the crystal structures of the extracellular outer membrane cytochromes of *S. oneidensis*, the crystal structure of the membrane-associated MtrCAB complex is still unknown.^[87, 88, 91, 189] Crystallographic structures of membrane proteins are difficult to obtain due to their hydrophobic nature and the need for detergent to be present during crystallisation.^[190] Cryo-TEM can also be used to rapidly and reliably solve the structures of proteins at near-atomic resolutions.^[191–193] In addition to the structures of soluble protein, cryo-TEM methods have been able to obtain images of membrane proteins in their lipid environments.^[192, 193] Single-particle reconstructions of membrane proteins can be obtained from hundreds of side view images of the proteins in spherical liposomes.^[192, 193] The spherical shape of liposomes allows the lipid membrane contribution to each image to be computationally removed and also aids in the determination of the orientation of each protein with respect to the centre of the liposome.^[193] 3D structures of the membrane protein can then be determined using image processing in combination with the orientations of the proteins.^[192, 193] Given the higher density of MtrCAB within proteoliposomes developed as a result of this work, MtrCAB proteoliposomes could allow successful cryo-TEM imaging of MtrCAB within lipid membranes and which could subsequently allow a structure of MtrCAB to be obtained.

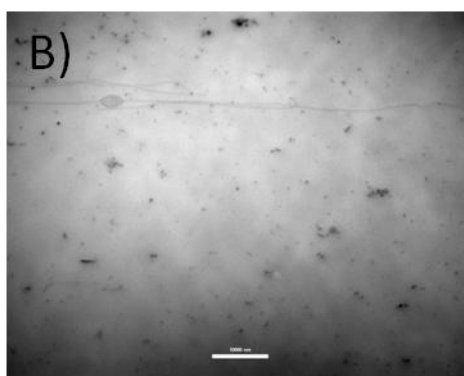
Beyond the immediate motivation for this work, the work presented in this thesis has the capacity to benefit studies of structural and functional properties of MtrCAB. MtrCAB proteoliposomes can also be used to help understand nanowires of *S. oneidensis*. Recently it was discovered by the group of Prof. Moh El-Naggar at the University of Southern California that the extracellular nanowires of *S. oneidensis* were up to 10 nm extensions of the periplasm and outer membrane, and that MtrCAB was located within these outer membrane extensions.^[76, 80, 81] Unpublished work in collaboration with this group has been able to demonstrate that spherical MtrCAB (proteo)liposomes can be manipulated using sheer force to form nanowire like structures which can span up to 100 μm , Figure 7.1. The sheer force that is required to achieve such tubular like structures is achieved by applying a laminar pump flow to samples of (proteo)liposomes that were placed on ethanol cleaned, 43 mm \times 50 mm, No. 1 coverslips 30 mins prior to imaging. Being able to prepare such tubular MtrCAB (proteo)liposome structures allows the

properties nanowires, such as their conductance, to be investigated without the hindrance of other chemicals that are required from the *in vivo* growth of nanowires.

Proteoliposomes



Nanowire like Structures



Nanowire like Structures

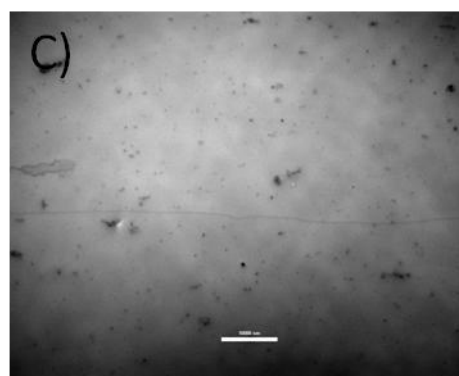


Figure 7.1. Bright-field images of proteoliposomes before and after the application of sheer force which allows nanowire like structures to be formed.

A) Bright-field microscopy image of 10 mg mL^{-1} lipid suspension of proteoliposomes, where the white scale bar represents 5000 nm. B and C) Bright-field microscopy images of as prepared sample after the application of sheer force, achieved by running a laminar pump flow across the sample, which allowed the formation of tubular liposomes. White scale bars represent 10000 nm.

References

1. Lewis, N. S. and Nocera, D. G. (2006) Powering the Planet: Chemical Challenges in Solar Energy Utilization. *Proc. Natl. Acad. Sci.* **103**, 15729–15735
2. Hoffert, M. I., Caldeira, K., Jain, A. K., Haites, E. F., Harvey, L. D. D., Potter, S. D., Schlesinger, M. E., Schneider, S. H., Watts, R. G., Wigley, T. M. L. and Wuebbles, D. J. (1998) Energy Implications of Future Stabilization of Atmospheric CO₂ Content. *Nature* **395**, 881–884
3. Nakićenović, N. (2000) Special Report on Emissions Scenarios. Cambridge: Cambridge University Press.
4. Lewis, N. S. and Crabtree, G. (2005) Basic Research Needs for Solar Energy Utilization. Washington DC: US Department of Energy, Office of Basic Energy Science.
5. Reece, S. Y., Hamel, J. A., Sung, K., Jarvi, T. D., Esswein, A. J., Pijpers, J. J. H. and Nocera, D. G. (2011) Wireless Solar Water Splitting Using Silicon-Based Semiconductors and Earth-Abundant Catalysts. *Science* **334**, 645–648
6. White, J. L., Herb, J. T., Kaczur, J. J., Majsztrik, P. W. and Bocarsly, A. B. (2014) Photons to Formate: Efficient Electrochemical Solar Energy Conversion via Reduction of Carbon Dioxide. *J. CO₂ Util.* **7**, 1–5
7. Benson, E. E., Kubiak, C. P., Sathrum, A. J. and Smieja, J. M. (2009) Electrocatalytic and Homogeneous Approaches to Conversion of CO₂ to Liquid Fuels. *Chem. Soc. Rev.* **38**, 89–99
8. Frischmann, P. D., Mahata, K. and Würthner, F. (2013) Powering the Future of Molecular Artificial Photosynthesis with Light-Harvesting Metallosupramolecular Dye Assemblies. *Chem. Soc. Rev.* **42**, 1847–1870
9. Lazarides, T., McCormick, T., Du, P., Luo, G., Lindley, B. and Eisenberg, R. (2009) Making Hydrogen from Water Using a Homogeneous System Without Noble Metals. *J. Am. Chem. Soc.* **131**, 9192–9194
10. DeRosa, M. C. and Crutchley, R. J. (2002) Photosensitized Singlet Oxygen and its Applications. *Coord. Chem. Rev.* **233-234**, 351–371

11. Carmo, M., Fritz, D. L., Mergel, J. and Stolten, D. (2013) A Comprehensive Review on PEM Water Electrolysis. *Int. J. Hydrogen Energy* **38**, 4901–4934
12. Vignais, P. M., Billoud, B. and Meyer, J. (2001) Classification and Phylogeny of Hydrogenases. *FEMS Microbiol. Rev.* **25**, 455–501
13. Shima, S. and Thauer, R. K. (2007) A Third Type of Hydrogenase Catalyzing H₂ Activation. *Chem. Rec.* **7**, 37–46
14. Vincent, K. A., Parkin, A. and Armstrong, F. A. (2007) Investigating and Exploiting the Electrocatalytic Properties of Hydrogenases. *Chem. Rev.* **107**, 4366–4413
15. Barber, J. and Tran, P. D. (2013) From Natural to Artificial Photosynthesis. *J. R. Soc. Interface* **10**, 1–18
16. King, P. W. (2013) Designing Interfaces of Hydrogenase-Nanomaterial Hybrids for Efficient Solar Conversion. *Biochim. Biophys. Acta* **1827**, 949–957
17. Tard, C. and Pickett, C. J. (2009) Structural and Functional Analogues of the Active Sites of the [Fe]-, [NiFe]-, and [FeFe]-Hydrogenases. *Chem Rev* **109**, 2245–2274
18. Esswein, A. J., Veige, A. S. and Nocera, D. G. (2005) A Photocycle for Hydrogen Production from Two-Electron Mixed-Valence Complexes. *J. Am. Chem. Soc.* **127**, 16641–16651
19. Artero, V., Chavarot-Kerlidou, M. and Fontecave, M. (2011) Splitting Water with Cobalt. *Angew. Chemie Int. Ed.* **50**, 7238–7266
20. Shi, J., Jiang, Y., Jiang, Z., Wang, X., Wang, X., Zhang, S., Han, P. and Yang, C. (2015) Enzymatic Conversion of Carbon Dioxide. *Chem. Soc. Rev.* **44**, 5981–6000
21. Pellegrin, Y. and Odobel, F. (2017) Sacrificial Electron Donor Reagents for Solar Fuel Production. *Comptes Rendus Chim.* **20**, 283–295
22. Kasuga, K., Miyasaka, H. and Handa, M. (1995) Photoreduction of Methylviologen Catalysed by Tri- or Tetra-Sulphophthalocyaninatozinc(II) in Aqueous Solutions. *Polyhedron* **14**, 1675–1679
23. Eckenhoff, W. T. and Eisenberg, R. (2012) Molecular Systems for Light Driven Hydrogen Production. *Dalt. Trans.* **41**, 13004–13021

24. Reithmeier, R., Bruckmeier, C. and Rieger, B. (2012) Conversion of CO₂ via Visible Light Promoted Homogeneous Redox Catalysis. *Catalysts* **2**, 544–571
25. Chan, S.-F., Chou, M., Creutz, C., Matsubara, T. and Sutin, N. (1981) Mechanism of the Formation of Dihydrogen from the Photoinduced Reactions of Poly(pyridine)ruthenium(II) and Poly(pyridine)rhodium(III) Complexes. *J. Am. Chem. Soc.* **103**, 369–379
26. Nocera, D. G. (2012) The Artificial Leaf. *Acc. Chem. Res.* **45**, 767–776
27. Van Noorden, R. (2012) ‘Artificial Leaf’ Faces Economic Hurdle. *Nature News* doi: 10.1038/nature.2012.10703 [Accessed 18th April 2017]
28. Liu, C., Colón, B., Ziesack, M., Silver, P. A. and Nocera, D. G. (2016) Water Splitting-Biosynthetic System with CO₂ Reduction Efficiencies Exceeding Photosynthesis. *Science* **352**, 1210–1213
29. Park, J. H., Lee, S. H., Cha, G. S., Choi, D. S., Nam, D. H., Lee, J. H., Lee, J.-K., Yun, C.-H., Jeong, K. J. and Park, C. B. (2015) Cofactor-Free Light-Driven Whole-Cell Cytochrome P450 Catalysis. *Angew. Chem. Int. Ed. Engl.* **54**, 969–973
30. Sakimoto, K. K., Wong, A. B. and Yang, P. (2016) Self-Photosensitization of Nonphotosynthetic Bacteria for Solar-to-Chemical Production. *Science* **351**, 74–77
31. Howes, L. (2013) Artificial Leaf in the Shade but Still Growing. *Chemistry World* [online] url: <https://www.chemistryworld.com/news/artificial-leaf-in-the-shade-but-still-growing/6417.article> [Accessed 18th April 2017].
32. Torella, J. P., Gagliardi, C. J., Chen, J. S., Bediako, D. K., Colón, B., Way, J. C., Silver, P. A. and Nocera, D. G. (2015) Efficient Solar-to-Fuels Production from a Hybrid Microbial-Water-Splitting Catalyst System. *Proc. Natl. Acad. Sci.* **112**, 2337–2342
33. Lovley, D. R. and Nevin, K. P. (2011) A Shift in the Current: New Applications and Concepts for Microbe-Electrode Electron Exchange. *Curr. Opin. Biotechnol.* **22**, 441–448
34. Lee, S. H., Kwon, Y.-C., Kim, D.-M. and Park, C. B. (2013) Cytochrome P450-Catalyzed O-Dealkylation Coupled With Photochemical NADPH Regeneration. *Biotechnol. Bioeng* **110**, 383–390

35. Mandal, D., Bolander, M. E., Mukhopadhyay, D., Sarkar, G. and Mukherjee, P. (2006) The use of Microorganisms for the Formation of Metal Nanoparticles and Their Application. *Appl. Microbiol. Biotechnol.* **69**, 485–492
36. Holmes, J. D., Farrar, J. A., Richardson, D. J., Russell, D. A. and Sodeaul, J. R. (1997) Bacterial Cadmium Sulfide Semiconductor Particles: An Assessment of their Photoactivity by EPR Spectroscopy. *Photochemistry* **65**, 811–817
37. Holmes, J. D., Richardson, D. J., Saed, S., Evans-Gowing, R., Russell, D. A. and Sodeau, J. R. (1997) Cadmium-Specific Formation of Metal Sulfide ‘Q-Particles’ by *Klebsiella pneumoniae*. *Microbiology* **143**, 2521–2530
38. Cunningham, D. P. and Lundie, L. L. (1993) Precipitation of Cadmium by *Clostridium thermoaceticum*. *Appl. Environ. Microbiol.* **59**, 7–14
39. Sweeney, R. Y., Mao, C., Gao, X., Burt, J. L., Belcher, A. M., Georgiou, G. and Iverson, B. L. (2004) Bacterial Biosynthesis of Cadmium Sulfide Nanocrystals. *Chem. Biol.* **11**, 1553–1559
40. Urban, P. L. (2014) Compartmentalised Chemistry: From Studies on the Origin of Life to Engineered Biochemical Systems. *New J. Chem.* **38**, 5135–5141
41. Peters, R. J. R. W., Louzao, I. and van Hest, J. C. M. (2012) From Polymeric Nanoreactors to Artificial Organelles. *Chem. Sci.* **3**, 335–342
42. Schoonen, L. and van Hest, J. C. M. (2016) Compartmentalization Approaches in Soft Matter Science: From Nanoreactor Development to Organelle Mimics. *Adv. Mater.* **28**, 1109–1128
43. Roodbeen, R. and van Hest, J. C. M. (2009) Synthetic Cells and Organelles: Compartmentalization Strategies. *BioEssays* **31**, 1299–1308
44. Papagianni, M. (2012) Recent Advances in Engineering the Central Carbon Metabolism of Industrially Important Bacteria. *Microb. Cell Fact.* **11**, 1–13
45. Pitts, K. E., Dobbin, P. S., Reyes-Ramirez, F., Thomson, A. J., Richardson, D. J. and Seward, H. E. (2003) Characterization of the *Shewanella oneidensis* MR-1 Decaheme Cytochrome MtrA: Expression in *Escherichia coli* Confers the Ability to Reduce Soluble Fe(III) Chelates. *J. Biol. Chem.* **278**, 27758–27765

46. Jensen, H. M., Albers, A. E., Malley, K. R., Londer, Y. Y., Cohen, B. E., Helms, B. A., Weigele, P., Groves, J. T. and Ajo-Franklin, C. M. (2010) Engineering of a Synthetic Electron Conduit in Living Cells. *Proc. Natl. Acad. Sci.* **107**, 19213–19218
47. Beveridge, T. J. (1999) Structures of Gram-Negative Cell Walls and Their Derived Membrane Vesicles. *J. Bacteriol.* **181**, 4725–4733
48. Kim, J.-Y., Doody, A. M., Chen, D. J., Cremona, G. H., Shuler, M. L., Putnam, D. and DeLisa, M. P. (2008) Engineered Bacterial Outer Membrane Vesicles with Enhanced Functionality. *J. Mol. Biol.* **380**, 51–66
49. Park, M., Sun, Q., Liu, F., DeLisa, M. P. and Chen, W. (2014) Positional Assembly of Enzymes on Bacterial Outer Membrane Vesicles for Cascade Reactions. *PLoS One* **9**, 1–6
50. Maity, B., Fujita, K. and Ueno, T. (2015) Use of the Confined Spaces of Apo-Ferritin and Virus Capsids as Nanoreactors for Catalytic Reactions. *Curr. Opin. Chem. Biol.* **25**, 88–97
51. De la Escosura, A., Nolte, R. J. M. and Cornelissen, J. J. L. M. (2009) Viruses and Protein Cages as Nanocontainers and Nanoreactors. *J. Mater. Chem.* **19**, 2274–2278
52. Uchida, M., Kosuge, H., Terashima, M., Willits, D. A., Liepold, O., Young, M. J., McConnell, M. V and Douglas, T. (2011) Protein Cage Nanoparticles Bearing the LyP-1 Peptide for Enhanced Imaging of Macrophage-Rich Vascular Lesions. *ACS Nano* **5**, 2493–2502
53. Fischlechner, M. and Donath, E. (2007) Viruses as Building Blocks for Materials and Devices. *Angew. Chemie Int. Ed.* **46**, 3184–3193
54. Comellas-Aragonès, M., Engelkamp, H., Claessen, V. I., Sommerdijk, N. A. J. M., Rowan, A. E., Christianen, P. C. M., Maan, J. C., Verduin, B. J. M., Cornelissen, J. J. L. M. and Nolte, R. J. M. (2007) A Virus-Based Single-Enzyme Nanoreactor. *Nat. Nanotechnol.* **2**, 635–639
55. Peters, R. J. R. W., Marguet, M., Marais, S., Fraaije, M. W., van Hest, J. C. M. and Lecommandoux, S. (2014) Cascade Reactions in Multicompartmentalized Polymersomes. *Angew. Chemie Int. Ed.* **53**, 146–150

56. Discher, D. E. and Eisenberg, A. (2002) Polymer Vesicles. *Science* **297**, 967–974
57. van Dongen, S. F. M., Nallani, M., Cornelissen, J. J. L. M., Nolte, R. J. M. and van Hest, J. C. M. (2009) A Three-Enzyme Cascade Reaction Through Positional Assembly of Enzymes in a Polymersome Nanoreactor. *Chem. Eur. J.* **15**, 1107–1114
58. Nallani, M., Benito, S., Onaca, O., Graff, A., Lindemann, M., Winterhalter, M., Meier, W. and Schwaneberg, U. (2006) A Nanocompartment System (Synthosome) Designed for Biotechnological Applications. *J. Biotechnol.* **123**, 50–59
59. Choi, H. and Montemagno, C. D. (2005) Artificial Organelle: ATP Synthesis from Cellular Mimetic Polymersomes. *Nano Lett.* **5**, 2538–2542
60. Vriezema, D. M., Hoogboom, J., Velonia, K., Takazawa, K., Christianen, P. C. M., Maan, J. C., Rowan, A. E. and Nolte, R. J. M. (2003) Vesicles and Polymerized Vesicles from Thiophene-Containing Rod-Coil Block Copolymers. *Angew. Chemie Int. Ed.* **42**, 772–776
61. Nardin, C., Thoeni, S., Widmer, J., Winterhalter, M. and Meier, W. (2000) Nanoreactors Based on (Polymerized) ABA-Triblock Copolymer Vesicles. *Chem. Commun.* 1433–1434
62. Sessa, G. and Weissmann, G. (1970) Incorporation of Lysozyme into Liposomes: A Model for Structure-Linked Latency. *J. Biol. Chem.* **245**, 3295–3301
63. van Swaay, D. and deMello, A. (2013) Microfluidic Methods for Forming Liposomes. *Lab Chip* **13**, 752–767
64. van Hoogevest, P. and Wendel, A. (2014) The use of Natural and Synthetic Phospholipids as Pharmaceutical Excipients. *Eur. J. Lipid Sci. Technol.* **116**, 1088–1107
65. Walde, P., Cosentino, K., Engel, H. and Stano, P. (2010) Giant Vesicles: Preparations and Applications. *ChemBioChem* **11**, 848–865
66. Rigaud, J.-L., Pitard, B. and Levy, D. (1995) Reconstitution of Membrane Proteins into Liposomes: Application to Energy-Transducing Membrane Proteins. *Biochim. Biophys. Acta* **1231**, 223–246
67. Robinson, J. N. and Cole-Hamilton, D. J. (1991) Electron Transfer Across Vesicle Bilayers. *Chem. Soc. Rev.* **20**, 49–94

68. Kurihara, K. and Fendler, J. H. (1983) Electron-Transfer Catalysis by Surfactant Vesicle Stabilized Colloidal Platinum. *J. Am. Chem. Soc.* **105**, 6152–6153
69. White, G. F., Edwards, M. J., Gomez-Perez, L., Richardson, D. J., Butt, J. N. and Clarke, T. A. (2016) Mechanisms of Bacterial Extracellular Electron Exchange. *Adv. Microb. Physiol.* **68**, 87–138
70. Leys, D. and Scrutton, N. S. (2004) Electrical Circuitry in Biology: Emerging Principles from Protein Structure. *Curr. Opin. Struct. Biol.* **14**, 642–647
71. Shi, L., Rosso, K. M., Clarke, T. A., Richardson, D. J., Zachara, J. M. and Fredrickson, J. K. (2012) Molecular Underpinnings of Fe(III) Oxide Reduction by *Shewanella oneidensis* MR-1. *Front. Microbiol.* **3**, 1–10
72. Myers, C. R. and Nealson, K. H. (1988) Bacterial Manganese Reduction and Growth with Manganese Oxide as the Sole Electron Acceptor. *Science* **240**, 1319-1321
73. Lovley, D. R., Phillips, E. J. P. and Lonergan, D. J. (1989) Hydrogen and Formate Oxidation Coupled to Dissimilatory Reduction of Iron or Manganese by *Alteromonas putrefaciens*. *Appl. Environ. Microbiol.* **55**, 700–706
74. Shi, L., Squier, T. C., Zachara, J. M. and Fredrickson, J. K. (2007) Respiration of Metal (Hydr)oxides by *Shewanella* and *Geobacter*: A key Role for Multihaem *c*-type Cytochromes. *Mol. Microbiol.* **65**, 12–20
75. Ross, D. E., Ruebush, S. S., Brantley, S. L., Hartshorne, R. S., Clarke, T. A., Richardson, D. J. and Tien, M. (2007) Characterization of Protein-Protein Interactions Involved in Iron Reduction by *Shewanella oneidensis* MR-1. *Appl. Environ. Microbiol.* **73**, 5797–5808
76. Richardson, D. J., Butt, J. N., Fredrickson, J. K., Zachara, J. M., Shi, L., Edwards, M. J., White, G., Baiden, N., Gates, A. J., Marritt, S. J. and Clarke, T. A. (2012) The ‘Porin-Cytochrome’ Model for Microbe-to-Mineral Electron Transfer. *Mol. Microbiol.* **85**, 201–212
77. Breuer, M., Rosso, K. M., Blumberger, J. and Butt, J. N. (2015) Multi-Haem Cytochromes in *Shewanella oneidensis* MR-1: Structures, Functions and Opportunities. *J. R. Soc. Interface* **12**, 1–27

78. von Canstein, H., Ogawa, J., Shimizu, S. and Lloyd, J. R. (2008) Secretion of Flavins by *Shewanella* Species and Their Role in Extracellular Electron Transfer. *Appl. Environ. Microbiol.* **74**, 615–623
79. Brutinel, E. D. and Gralnick, J. A. (2012) Shuttling Happens: Soluble Flavin Mediators of Extracellular Electron Transfer in *Shewanella*. *Appl. Microbiol. Biotechnol.* **93**, 41–48
80. Pirbadian, S., Barchinger, S. E., Leung, K. M., Byun, H. S., Jangir, Y., Bouhenni, R. A., Reed, S. B., Romine, M. F., Saffarini, D. A., Shi, L., Gorby, Y. A., Golbeck, J. H. and El-Naggar, M. Y. (2014) *Shewanella oneidensis* MR-1 Nanowires are Outer Membrane and Periplasmic Extensions of the Extracellular Electron Transport Components. *Proc. Natl. Acad. Sci.* **111**, 12883–12888
81. El-Naggar, M. Y., Wanger, G., Leung, K. M., Yuzvinsky, T. D., Southam, G., Yang, J., Lau, W. M., Nealson, K. H. and Gorby, Y. A. (2010) Electrical Transport Along Bacterial Nanowires from *Shewanella oneidensis* MR-1. *Proc. Natl. Acad. Sci.* **107**, 18127–18131
82. Richardson, D. J., Butt, J. N. and Clarke, T. A. (2013) Controlling Electron Transfer at the Microbe-Mineral Interface. *Proc. Natl. Acad. Sci.* **110**, 7537–7538
83. Hartshorne, R. S., Reardon, C. L., Ross, D., Nuester, J., Clarke, T. A., Gates, A. J., Mills, P. C., Fredrickson, J. K., Zachara, J. M., Shi, L., Beliaev, A. S., Marshall, M. J., Tien, M., Brantley, S., Butt, J. N. and Richardson, D. J. (2009) Characterization of an Electron Conduit Between Bacteria and the Extracellular Environment. *Proc. Natl. Acad. Sci.* **106**, 22169–22174
84. Clarke, T. A., Holley, T., Hartshorne, R. S., Fredrickson, J. K., Zachara, J. M., Shi, L. and Richardson, D. J. (2008) The Role of Multihaem Cytochromes in the Respiration of Nitrite in *Escherichia coli* and Fe(III) in *Shewanella oneidensis*. *Biochem. Soc. Trans.* **36**, 1005–1010
85. Firer-Sherwood, M. A., Ando, N., Drennan, C. L. and Elliott, S. J. (2011) Solution-Based Structural Analysis of the Decaheme Cytochrome, MtrA, by Small-Angle X-ray Scattering and Analytical Ultracentrifugation. *J. Phys. Chem. B* **115**, 11208–11214

86. Schulz, G. E. (2002) The Structure of Bacterial Outer Membrane Proteins. *Biochim. Biophys. Acta* **1565**, 308–317
87. Edwards, M. J., White, G. F., Norman, M., Tome-Fernandez, A., Ainsworth, E., Shi, L., Fredrickson, J. K., Zachara, J. M., Butt, J. N., Richardson, D. J. and Clarke, T. A. (2015) Redox Linked Flavin Sites in Extracellular Decaheme Proteins Involved in Microbe-Mineral Electron Transfer. *Sci. Rep.* **5**, 1–11
88. Edwards, M. J., Baiden, N. A., Johs, A., Tomanicek, S. J., Liang, L., Shi, L., Fredrickson, J. K., Zachara, J. M., Gates, A. J., Butt, J. N., Richardson, D. J. and Clarke, T. A. (2014) The X-ray Crystal Structure of *Shewanella oneidensis* OmcA Reveals new Insight at the Microbe-Mineral Interface. *FEBS Lett.* **588**, 1886–1890
89. Coursolle, D. and Gralnick, J. A. (2010) Modularity of the Mtr Respiratory Pathway of *Shewanella oneidensis* Strain MR-1. *Mol. Microbiol.* **77**, 995–1008
90. Okamoto, A., Hashimoto, K., Nealon, K. H. and Nakamura, R. (2013) Rate Enhancement of Bacterial Extracellular Electron Transport Involves Bound Flavin Semiquinones. *Proc. Natl. Acad. Sci.* **110**, 7856–7861
91. Clarke, T. A., Edwards, M. J., Gates, A. J., Hall, A., White, G. F., Bradley, J., Reardon, C. L., Shi, L., Beliaev, A. S., Marshall, M. J., Wang, Z., Watmough, N. J., Fredrickson, J. K., Zachara, J. M., Butt, J. N. and Richardson, D. J. (2011) Structure of a Bacterial Cell Surface Decaheme Electron Conduit. *Proc. Natl. Acad. Sci.* **108**, 9384–9389
92. White, G. F., Shi, Z., Shi, L., Wang, Z., Dohnalkova, A. C., Marshall, M. J., Fredrickson, J. K., Zachara, J. M., Butt, J. N., Richardson, D. J. and Clarke, T. A. (2013) Rapid Electron Exchange Between Surface-Exposed Bacterial Cytochromes and Fe(III) Minerals. *Proc. Natl. Acad. Sci.* **110**, 6346–6351
93. White, G. F., Shi, Z., Shi, L., Dohnalkova, A. C., Fredrickson, J. K., Zachara, J. M., Butt, J. N., Richardson, D. J. and Clarke, T. A. (2012) Development of a Proteoliposome Model to Probe Transmembrane Electron-Transfer Reactions. *Biochem. Soc. Trans.* **40**, 1257–1260
94. Bird, C. L. and Kuhn, A. T. (1981) Electrochemistry of the Viologens. *Chem. Soc. Rev.* **10**, 49–82

95. Mayhew, S. G. (1978) The Redox Potential of Dithionite and SO_2^- From Equilibrium Reactions with Flavodoxins, Methyl Viologen and Hydrogen Plus Hydrogenase. *Eur. J. Biochem.* **85**, 535–547
96. Gillaizeau-Gauthier, I., Odobel, F., Alebbi, M., Argazzi, R., Costa, E., Bignozzi, C. A., Qu, P. and Meyer, G. J. (2001) Phosphonate-Based Bipyridine Dyes for Stable Photovoltaic Devices. *Inorg. Chem.* **40**, 6073–6079
97. Watanabe, T. and Honda, K. (1982) Measurement of the Extinction Coefficient of the Methyl Viologen Cation Radical and the Efficiency of its Formation by Semiconductor Photocatalysts. *J. Phys. Chem.* **86**, 2617–2619
98. Laemmli, U. K. (1970) Cleavage of Structural Proteins During the Assembly of the Head of Bacteriophage T4. *Nature* **227**, 680–685
99. Goodhew, C. F., Brown, K. R. and Pettigrew, G. W. (1986) Haem Staining in Gels, a Useful Tool in the Study of Bacterial *c*-type Cytochromes. *Biochim. Biophys. Acta* **852**, 288–294
100. Berglund, G. I., Carlsson, G. H., Smith, A. T., Szöke, H., Henriksen, A. and Hajdu, J. (2002) The Catalytic Pathway of Horseradish Peroxidase at High Resolution. *Nature* **417**, 463–468
101. Guo, Y., Ma, Q., Cao, F., Zhao, Q. and Ji, X. (2015) Colorimetric Detection of Hypochlorite in tap Water Based on the Oxidation of 3,3',5,5'-Tetramethyl Benzidine. *Anal. Methods* **7**, 4055–4058
102. Marshall, M. J., Beliaev, A. S., Dohnalkova, A. C., Kennedy, D. W., Shi, L., Wang, Z., Boyanov, M. I., Lai, B., Kemner, K. M., McLean, J. S., Reed, S. B., Culley, D. E., Bailey, V. L., Simonson, C. J., Saffarini, D. A., Romine, M. F., Zachara, J. M. and Fredrickson, J. K. (2006) *c*-Type Cytochrome-Dependent Formation of U(IV) Nanoparticles by *Shewanella oneidensis*. *PLoS Biol.* **4**, 1324-1333
103. Heath, G. R., Li, M., Polignano, I. L., Richens, J. L., Catucci, G., O'Shea, P., Sadeghi, S. J., Gilardi, G., Butt, J. N. and Jeuken, L. J. C. (2016) Layer-by-Layer Assembly of Supported Lipid Bilayer Poly-L-Lysine Multilayers. *Biomacromolecules* **17**, 324–335

104. Nichols, J. W. and Deamer, D. W. (1980) Net Proton-Hydroxyl Permeability of Large Unilamellar Liposomes Measured by an Acid-Base Titration Technique. *Proc. Natl. Acad. Sci.* **77**, 2038–2042
105. Tran, P. D., Wong, L. H., Barber, J. and Loo, J. S. C. (2012) Recent Advances in Hybrid Photocatalysts for Solar Fuel Production. *Energy Environ. Sci.* **5**, 5902–5918
106. Woolerton, T. W., Sheard, S., Chaudhary, Y. S. and Armstrong, F. A. (2012) Enzymes and Bio-Inspired Electrocatalysts in Solar Devices. *Energy Environ. Sci.* **5**, 7470–7490
107. Bachmeier, A. and Armstrong, F. (2015) Solar-Driven Proton and Carbon Dioxide Reduction to Fuels - Lessons from Metalloenzymes. *Curr. Opin. Chem. Biol.* **25**, 141–151
108. Hutton, G. A. M., Reuillard, B., Martindale, B. C. M., Caputo, C. A., Lockwood, C. W. J., Butt, J. N. and Reisner, E. (2016) Carbon Dots as Versatile Photosensitizers for Solar-Driven Catalysis with Redox Enzymes. *J. Am. Chem. Soc.* **138**, 16722–16730
109. Hernandez, M. E. and Newman, D. K. (2001) Extracellular Electron Transfer. *Cell. Mol. Life Sci.* **58**, 1562–1571
110. Watanabe, K., Manefield, M., Lee, M. and Kouzuma, A. (2009) Electron Shuttles in Biotechnology. *Curr. Opin. Biotechnol.* **20**, 633–641
111. Lidan, L., Yong, X., Yicheng, W., Bilian, C. and Feng, Z. (2014) Electron Transfer Mediators in Microbial Electrochemical Systems. *Prog. Chem.* **26**, 1859–1866
112. Park, H., Bae, E., Lee, J.-J., Park, J. and Choi, W. (2006) Effect of the Anchoring Group in Ru-Bipyridyl Sensitizers on the Photoelectrochemical Behavior of Dye-Sensitized TiO₂ Electrodes: Carboxylate Versus Phosphonate Linkages. *J. Phys. Chem. B* **110**, 8740–8749
113. Ardo, S. and Meyer, G. J. (2009) Photodriven Heterogeneous Charge Transfer with Transition-Metal Compounds Anchored to TiO₂ Semiconductor Surfaces. *Chem. Soc. Rev.* **38**, 115–164

114. Reisner, E., Powell, D. J., Cavazza, C., Fontecilla-Camps, J. C. and Armstrong, F. A. (2009) Visible Light-Driven H₂ Production by Hydrogenases Attached to Dye-Sensitized TiO₂ Nanoparticles. *J. Am. Chem. Soc.* **131**, 18457-18466
115. Balzani, V., Bergamini, G., Marchioni, F. and Ceroni, P. (2006) Ru(II)-Bipyridine Complexes in Supramolecular Systems, Devices and Machines. *Coord. Chem. Rev.* **250**, 1254–1266
116. Juris, A., Balzani, V., Barigelletti, F., Campagna, S., Belser, P. and von Zelewsky, A. (1988) Ru(II) Polypyridine Complexes: Photophysics, Photochemistry, Electrochemistry, and Chemiluminescence. *Coord. Chem. Rev.* **84**, 85–277
117. Reisner, E., Fontecilla-Camps, J. C. and Armstrong, F. A. (2009) Catalytic Electrochemistry of a [NiFeSe]-Hydrogenase on TiO₂ and Demonstration of its Suitability for Visible-Light Driven H₂ Production. *Chem. Commun.* 550–552
118. Bock, C. R., Connor, J. A., Gutierrez, A. R., Meyer, T. J., Whitten, D. G., Sullivan, B. P. and Nagle, J. K. (1979) Estimation of Excited-State Redox Potentials by Electron-Transfer Quenching. Application of Electron-Transfer Theory to Excited-State Redox Processes. *J. Am. Chem. Soc.* **101**, 4815–4824
119. Willkomm, J., Muresan, N. M. and Reisner, E. (2015) Enhancing H₂ Evolution Performance of an Immobilised Cobalt Catalyst by Rational Ligand Design. *Chem. Sci.* **6**, 2727–2736
120. Gross, M. A., Reynal, A., Durrant, J. R. and Reisner, E. (2014) Versatile Photocatalytic Systems for H₂ Generation in Water Based on an Efficient DuBois-Type Nickel Catalyst. *J. Am. Chem. Soc.* **136**, 356–366
121. Lakadamyali, F., Reynal, A., Kato, M., Durrant, J. R. and Reisner, E. (2012) Electron Transfer in Dye-Sensitised Semiconductors Modified with Molecular Cobalt Catalysts: Photoreduction of Aqueous Protons. *Chemistry* **18**, 15464–15475
122. Lakadamyali, F., Kato, M. and Reisner, E. (2012) Colloidal Metal Oxide Particles Loaded with Synthetic Catalysts for Solar H₂ Production. *Faraday Discuss.* **155**, 191–205

123. Abe, R., Hara, K., Sayama, K., Domen, K. and Arakawa, H. (2000) Steady Hydrogen Evolution from Water on Eosin Y-Fixed TiO₂ Photocatalyst Using a Silane-Coupling Reagent Under Visible Light Irradiation. *J. Photochem. Photobiol. A Chem.* **137**, 63–69
124. Batistela, V. R., Pellosi, D. S., de Souza, F. D., da Costa, W. F., de Oliveira Santin, S. M., de Souza, V. R., Caetano, W., de Oliveira, H. P. M., Scarminio, I. S. and Hioka, N. (2011) pKa Determinations of Xanthene Derivates in Aqueous Solutions by Multivariate Analysis Applied to UV–Vis Spectrophotometric Data. *Spectrochim. Acta Part A Mol. Biomol. Spectrosc.* **79**, 889–897
125. Suvarna, K. S., Layton, C. and Bancroft, J. D. (2013) Bancroft's Theory and Practice of Histological Techniques. 7th Ed. Philadelphia: Elsevier Health Sciences. 173
126. Hari, D. P. and König, B. (2014) Synthetic Applications of Eosin Y in Photoredox Catalysis. *Chem. Commun.* **50**, 6688–6699
127. Mau, A. W.-H., Johansen, O. and Sasse, W. H. F. (1985) Xanthene Dyes as Sensitizers for the Photoreduction of Water. *Photochem. Photobiol.* **41**, 503–509
128. Ghosh, T., Slanina, T. and König, B. (2015) Visible Light Photocatalytic Reduction of Aldehydes by Rh(III)–H: A Detailed Mechanistic Study. *Chem. Sci.* **6**, 2027–2034
129. Pileni, M.-P. and Grätzel, M. (1980) Light-Induced Redox Reactions of Proflavin in Aqueous and Micellar Solution. *J. Phys. Chem.* **84**, 2402–2406
130. De, S., Das, S. and Girigoswami, A. (2005) Environmental Effects on the Aggregation of Some Xanthene Dyes Used in Lasers. *Spectrochim. Acta Part A Mol. Biomol. Spectrosc.* **61**, 1821–1833
131. Armstrong, R. W. and Panzer, N. M. (1972) A Comparison of the Interaction of an Acridine Dye and a Triphenylmethane Dye with Deoxyribonucleic Acid. *J. Am. Chem. Soc.* **94**, 7650–7653
132. Kalyanasundaram, K. and Grätzel, M. (1979) Proflavine-Sensitized Photoproduction of H₂ from Water with Electron-Donors and a Colloidal Redox Catalyst. *Chem. Commun.* 1137–1138

133. Kalyanasundaram, K. and Dung, D. (1980) Role of Proflavin as a Photosensitizer for the Light-Induced Hydrogen Evolution from Water. *J. Phys. Chem.* **84**, 2551-2556
134. Mataga, N., Kaifu, Y. and Koizumi, M. (1956) On the Base Strength of Some Nitrogen Heterocycles in the Excited State. *Bull. Chem. Soc. Jpn.* **29**, 373-379
135. Haugen, G. R. and Melhuish, W. H. (1964) Association and Self-Quenching of Proflavine in Water. *Trans. Farad. Soc.* **60**, 386-394
136. Heelis, P. F. (1982) The Photophysical and Photochemical Properties of Flavins (Isoalloxazines). *Chem. Soc. Rev.* **11**, 15-39
137. Tan, S. L. J., Kan, J. M. and Webster, R. D. (2013) Differences in Proton-Coupled Electron-Transfer Reactions of Flavin Mononucleotide (FMN) and Flavin Adenine Dinucleotide (FAD) Between Buffered and Unbuffered Aqueous Solutions. *J. Phys. Chem. B.* **117**, 13755-13766
138. Silva, E. and Edwards, A. M. (2006) *Flavins: Photochemistry and Photobiology*. Cambridge: The Royal Society of Chemistry.
139. Mayhew, S. G. (1971) Studies on Flavin Binding in Flavodoxins. *Biochim. Biophys. Acta* **235**, 289-302
140. Lowe, H. J. and Clark, W. M. (1956) Studies on Oxidation-Reduction: XXIV. Oxidation-Reduction Potentials of Flavin Adenine Dinucleotide. *J. Biol. Chem.* **221**, 983-992
141. Sober, H. (1968) *CRC Handbook of Biochemistry: Selected Data for Molecular Biology*. Florida: The Chemical Rubber Publishing Co.
142. Radda, G. K. and Calvin, M. (1964) Chemical and Photochemical Reductions of Flavin Nucleotides and Analogs. *Biochemistry* **3**, 384-393
143. Song, S.-H., Dick, B. and Penzkofer, A. (2007) Photo-Induced Reduction of Flavin Mononucleotide in Aqueous Solutions. *Chem. Phys.* **332**, 55-65
144. Moore, W. M., Spence, J. T., Raymond, F. A. and Colson, S. D. (1963) The Photochemistry of Riboflavin. I. The Hydrogen Transfer Process in the Anaerobic Photobleaching of Flavins. *J. Am. Chem. Soc.* **85**, 3367-3372

145. Holmström, B. and Oster, G. (1961) Riboflavin as an Electron Donor in Photochemical Reactions. *J. Am. Chem. Soc.* **83**, 1867–1871
146. Schuman Jorns, M., Schöllnhammer, G. and Hemmerich, P. (1975) Intramolecular Addition of the Riboflavin Side Chain. Anion-Catalyzed Neutral Photochemistry. *Eur. J. Biochem.* **57**, 35–48
147. Cairns, W. L. and Metzler, D. E. (1971) Photochemical Degradation of Flavins. VI. A New Photoproduct and its Use in Studying the Photolytic Mechanism. *J. Am. Chem. Soc.* **93**, 2772–2777
148. Smith, E. C. and Metzler, D. E. (1963) The Photochemical Degradation of Riboflavin. *J. Am. Chem. Soc.* **85**, 3285–3288
149. Ahmad, I., Fasihullah, Q. and Vaid, F. H. M. (2006) Photolysis of Formylmethylflavin in Aqueous and Organic Solvents. *Photochem. Photobiol. Sci.* **5**, 680–685
150. Ahmad, I., Fasihullah, Q. and Vaid, F. H. M. (2006) Effect of Light Intensity and Wavelengths on Photodegradation Reactions of Riboflavin in Aqueous Solution. *J. Photochem. Photobiol. B Biol.* **82**, 21–27
151. Pettigrew, G. W. and Moore, G. R. (1987) *Cytochromes c Biological Aspects*. Germany: Springer-Verlag Berlin Heidelberg
152. Moore, G. R. and Pettigrew, G. W. (1990) *Cytochrome c: Evolutionary, Structural and Physicochemical Aspects*. Germany: Springer-Verlag Berlin Heidelberg
153. Hartshorne, R. S., Jepson, B. N., Clarke, T. A., Field, S. J., Fredrickson, J., Zachara, J., Shi, L., Butt, J. N. and Richardson, D. J. (2007) Characterization of *Shewanella oneidensis* MtrC: A Cell-Surface Decaheme Cytochrome Involved in Respiratory Electron Transport to Extracellular Electron Acceptors. *J. Biol. Inorg. Chem.* **12**, 1083–1094
154. Firer-Sherwood, M., Pulcu, G. S. and Elliott, S. J. (2008) Electrochemical Interrogations of the Mtr Cytochromes from *Shewanella*: Opening a Potential Window. *J. Biol. Inorg. Chem.* **13**, 849–854

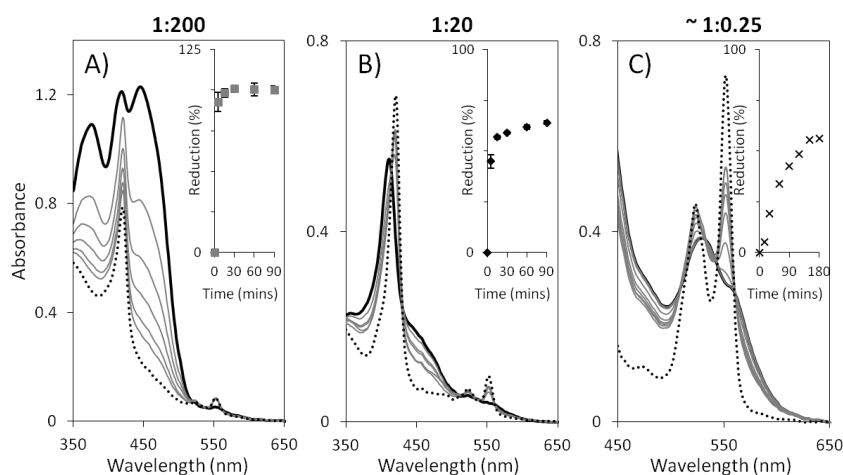
155. Field, S. J., Dobbin, P. S., Cheesman, M. R., Watmough, N. J., Thomson, A. J. and Richardson, D. J. (2000) Purification and Magneto-Optical Spectroscopic Characterization of Cytoplasmic Membrane and Outer Membrane Multiheme *c*-Type Cytochromes from *Shewanella frigidimarina* NCIMB400. *J. Biol. Chem.* **275**, 8515–8522
156. Reynal, A., Pastor, E., Gross, M. A., Selim, S., Reisner, E. and Durrant, J. (2015) Unravelling the pH-Dependence of a Molecular Photocatalytic System for Hydrogen Production. *Chem. Sci.* **6**, 4855–4859
157. Grady, J. K., Chasteen, N. D. and Harris, D. C. (1988) Radicals from ‘Good’s’ Buffers. *Anal. Biochem.* **173**, 111–115
158. Edwards, M. J., Fredrickson, J. K., Zachara, J. M., Richardson, D. J. and Clarke, T. A. (2012) Analysis of Structural MtrC Models Based on Homology with the Crystal Structure of MtrF. *Biochem. Soc. Trans.* **40**, 1181–1185
159. Song, A., Zhang, J., Zhang, M., Shen, T. and Tang, J. (2000) Spectral Properties and Structure of Fluorescein and its Alkyl Derivatives in Micelles. *Colloids Surfaces A Physicochem. Eng. Asp.* **167**, 253–262
160. Chatak, U. R., Sanyal, B. and Ghosh, S. (1976) Laser Flash Spectroscopy of Tris(2,2'-bipyridine)ruthenium(II) in Solution. *J. Am. Chem. Soc.* **98**, 3722–3724
161. Zadvornyy, O. A., Lucon, J. E., Gerlach, R., Zorin, N. A., Douglas, T., Elgren, T. E. and Peters, J. W. (2012) Photo-Induced H₂ Production by [NiFe]-Hydrogenase from *T. roseopersicina* Covalently Linked to a Ru(II) Photosensitizer. *J. Inorg. Biochem.* **106**, 151–155
162. Ainsworth, E. V, Lockwood, C. W. J., White, G. F., Hwang, E. T., Sakai, T., Gross, M. A., Richardson, D. J., Clarke, T. A., Jeuken, L. J. C., Reisner, E. and Butt, J. N. (2016) Photoreduction of *Shewanella oneidensis* Extracellular Cytochromes by Organic Chromophores and Dye-Sensitized TiO₂. *ChemBioChem* **17**, 2324–2333
163. Breuer, M., Rosso, K. M. and Blumberger, J. (2015) Flavin Binding to the Deca-heme Cytochrome MtrC: Insights from Computational Molecular Simulation. *Biophys. J.* **109**, 2614–2624

164. Islam, S., Konishi, T., Fujitsuka, M., Ito, O., Nakamura, Y. and Usui, Y. (2000) Photosensitized Reduction of Methyl Viologen Using Eosin-Y in Presence of a Sacrificial Electron Donor in Water-Alcohol Mixture. *Photochem. Photobiol.* **71**, 675–680
165. Gurunathan, K., Maruthamuthu, P. and Sastri, M. V. C. (1997) Photocatalytic Hydrogen Production by Dye-Sensitised Pt/SnO and Pt/SnO₂/RuO₂ in Aqueous Methyl Viologen Solution. *Int. J. Hydrogen Energy* **22**, 57–62
166. Bhowmik, B. B. and Ganguly, P. (2005) Photophysics of Xanthene Dyes in Surfactant Solution. *Spectrochim. Acta Part A* **61**, 1997–2003
167. Bhowmik, B. B. and Ganguly, P. (2005) Photophysical Studies of Some Dyes in Aqueous Solution of Triton X-100. *Spectrochim. Acta Part A* **62**, 808–813
168. Kong, L., Liu, Z., Hu, X. and Liu, S. (2010) Absorption, Fluorescence and Resonance Rayleigh Scattering Spectra of Hydrophobic Hydrogen Bonding of Eosin Y/Triton X-100 Nanoparticles and Their Analytical Applications. *Sci. China Chem.* **53**, 2363–2372
169. Chakraborty, M. and Panda, A. K. (2011) Spectral Behaviour of Eosin Y in Different Solvents and Aqueous Surfactant Media. *Spectrochim. Acta Part A* **81**, 458–465
170. Oba, Y. and Poulson, S. R. (2012) Octanol-Water Partition Coefficients (K_{ow}) vs. pH for Fluorescent Dye Tracers (Fluorescein, Eosin Y), and Implications for Hydrologic Tracer Tests. *Geochem. J.* **46**, 517–520
171. Valzeno, D. P. and Pooler, J. P. (1982) Cell Membrane Photomodification: Relative Effectiveness of Halogenated Fluoresceins for Photohemolysis. *Photochem. Photobiol.* **35**, 343–350
172. Kato, H., Komagoe, K., Nakanishi, Y., Inoue, T. and Katsu, T. (2012) Xanthene Dyes Induce Membrane Permeabilization of Bacteria and Erythrocytes by Photoinactivation. *Photochem. Photobiol.* **88**, 423–431
173. Charalambous, K., Miller, D., Curnow, P. and Booth, P. J. (2008) Lipid Bilayer Composition Influences Small Multidrug Transporters. *BMC Biochem.* **9**, 1–12

174. Kuhn, E. R. and Hurst, J. K. (1993) Mechanisms of Vectorial Transmembrane Reduction of Viologens Across Phosphatidylcholine Bilayer Membranes. *J. Phys. Chem.* **97**, 1712–1721
175. Geertsma, E. R., Mahmood, N. N. A. B., Schuurman-Wolters, G. K. and Poolman, B. (2008) Membrane Reconstitution of ABC Transporters and Assays of Translocator Function. *Nat. Protoc.* **3**, 256–266
176. Helenius, A. R. I. and Simons, K. A. I. (1975) Solubilization of Membranes by Detergents. *Biochim. Biophys. Acta* **415**, 29–79
177. Mills, A., Cusick, A. and Hepburn, J. (2009) The Kinetics of Semiconductor Photocatalysis in Activity-Indicator Films. *J. Adv. Oxid. Technol.* **12**, 152–157
178. Khazalpour, S. and Nematollahi, D. (2014) Electrochemical Study of Alamar Blue (Resazurin) in Aqueous Solutions and Room-Temperature Ionic Liquid 1-Butyl-3-Methylimidazolium Tetrafluoroborate at a Glassy Carbon Electrode. *RSC Adv.* **4**, 8431–8438
179. Ponja, S., Sathasivam, S., Chadwick, N., Kafizas, A., Bawaked, S. M., Obaid, A. Y., Al-Thabaiti, S., Basahel, S. N., Parkin, I. P. and Carmalt, C. J. (2013) Aerosol Assisted Chemical Vapour Deposition of Hydrophobic TiO₂-SnO₂ Composite Film with Novel Microstructure and Enhanced Photocatalytic Activity. *J. Mater. Chem. A* **1**, 6271–6278
180. Kariyajjanavar, P., Narayana, J., Nayaka, Y. A. and Umanaik, M. (2010) Electrochemical Degradation and Cyclic Voltammetric Studies of Textile Reactive Azo Dye Cibacron Navy WB. *Port. Electrochim. Acta* **28**, 265–277
181. Hwang, E. T., Sheikh, K., Orchard, K. L., Hojo, D., Radu, V., Lee, C.-Y., Ainsworth, E., Lockwood, C., Gross, M. A., Adschiri, T., Reisner, E., Butt, J. N. and Jeuken, L. J. C. (2015) A Decaheme Cytochrome as a Molecular Electron Conduit in Dye-Sensitized Photoanodes. *Adv. Funct. Mater.* **25**, 2308–2315
182. Lawes, M. (2015). Structural and Spectroscopic Studies on the Porin-Cytochrome Complex from *Shewanella oneidensis* MR-1. University of East Anglia
183. Zumft, W. G. and Kroneck, P. M. H. (2007) Respiratory Transformation of Nitrous Oxide (N₂O) to Dinitrogen by Bacteria and Archaea. *Adv. Microb. Physiol.* **52**, 107-227

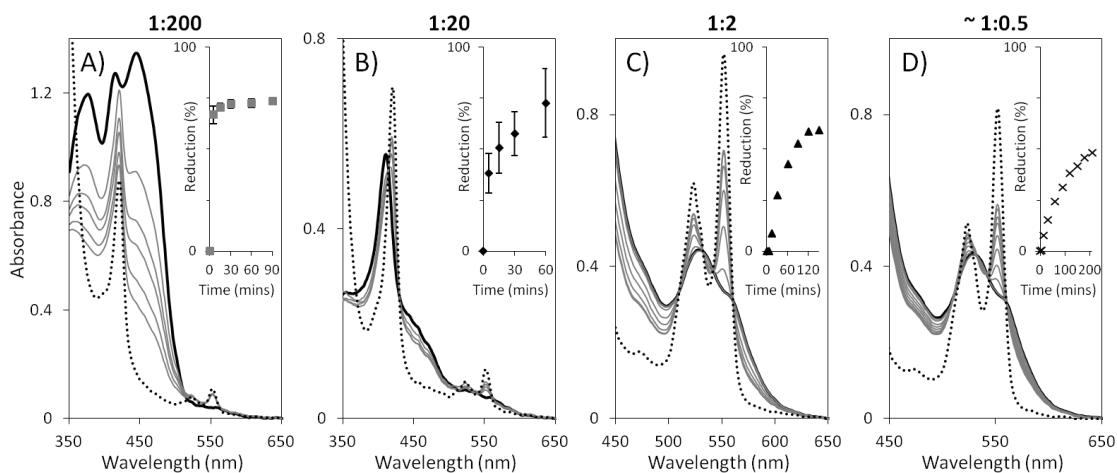
184. Fan, R., Chew, S. W., Cheong, V. V. and Orner, B. P. (2010) Fabrication of Gold Nanoparticles Inside Unmodified Horse Spleen Apoferritin. *Small* **6**, 1483–1487
185. Kubota, H., Sakurai, I., Katayama, K., Mizusawa, N. and Ohashi, S. (2010) Purification and Characterization of Photosystem I Complex from *Synechocystis* sp. PCC 6803 by Expressing Histidine-Tagged Subunits. *Biochim. Biophys. Acta* **1797**, 98–105
186. Kracke, F., Vassilev, I. and Krömer, J. O. (2015) Microbial Electron Transport and Energy Conservation - The Foundation for Optimizing Bioelectrochemical Systems. *Front. Microbiol.* **6**, 1–18
187. Meshulam-Simon, G., Behrens, S., Choo, A. D. and Spormann, A. M. (2007) Hydrogen Metabolism in *Shewanella oneidensis* MR-1. *Appl. Environ. Microbiol.* **73**, 1153–1165
188. Ross, D. E., Flynn, J. M., Baron, D. B., Gralnick, J. A. and Bond, D. R. (2011) Towards Electrosynthesis in *Shewanella*: Energetics of Reversing the Mtr Pathway for Reductive Metabolism. *PLoS One* **6**, 1–9
189. Edwards, M. J., Hall, A., Shi, L., Fredrickson, J. K., Zachara, J. M., Butt, J. N., Richardson, D. J. and Clarke, T. A. (2012) The Crystal Structure of the Extracellular 11-Heme Cytochrome UndA Reveals a Conserved 10-Heme Motif and Defined Binding Site for Soluble Iron Chelates. *Structure* **20**, 1275–1284
190. Carpenter, E. P., Beis, K., Cameron, A. D. and Iwata, S. (2008) Overcoming the Challenges of Membrane Protein Crystallography. *Curr. Opin. Struct. Biol.* **18**, 581–586
191. Wang, R. Y.-R., Kudryashev, M., Li, X., Egelman, E. H., Basler, M., Cheng, Y., Baker, D. and Dimaio, F. (2015) De novo Protein Structure Determination from Near-Atomic Resolution Cryo-EM Maps. *Nat. Methods* **12**, 335–338
192. Tilley, S. J., Orlova, E. V, Gilbert, R. J. C., Andrew, P. W. and Saibil, H. R. (2005) Structural Basis of Pore Formation by the Bacterial Toxin Pneumolysin. *Cell* **121**, 247–256
193. Wang, L. and Sigworth, F. J. (2010) Liposomes on a Streptavidin Crystal: A System to Study Membrane Proteins by Cryo-EM. *Methods Enzymol.* **481**, 147–164

Appendix



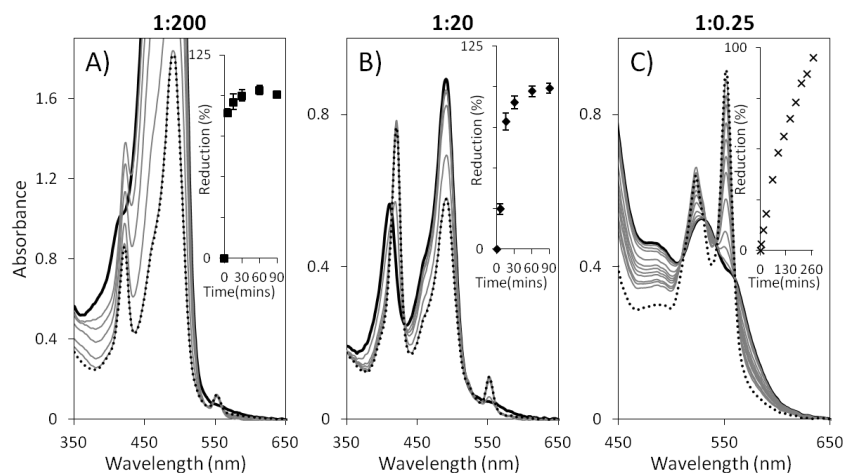
Appendix 1. MtrC photoreduction with FAD at MtrC:FAD ratios of 1:200 (A), 1:20 (B) and ~1:0.25 (C).

A) 0.5 μM MtrC and 100 μM FAD. B) 0.5 μM MtrC and 10 μM FAD. C) 39 μM MtrC and 9 μM FAD, unstirred in a 1 mm cuvette (Soret region absorbance above detection limit). As prepared samples (continuous black lines) were irradiated for 5, 15, 30, 60 and 90 mins or longer at 0.4 kW m^{-2} (grey lines) prior to addition of excess of dithionite (dotted lines). Inserts show extent of MtrC reduction during irradiation, monitored via 552 nm absorbance. For experiments containing 0.5 μM MtrC, extent of reduction; and max and min observed values; represent average of two independent experiments. Grey symbols show biased extents of reductions - see text for details. Stirred samples in anaerobic 50 mM HEPES, 2 mM CaCl_2 , 10 mM KCl, 50 mM TEOA, pH 7 at 20 $^{\circ}\text{C}$.



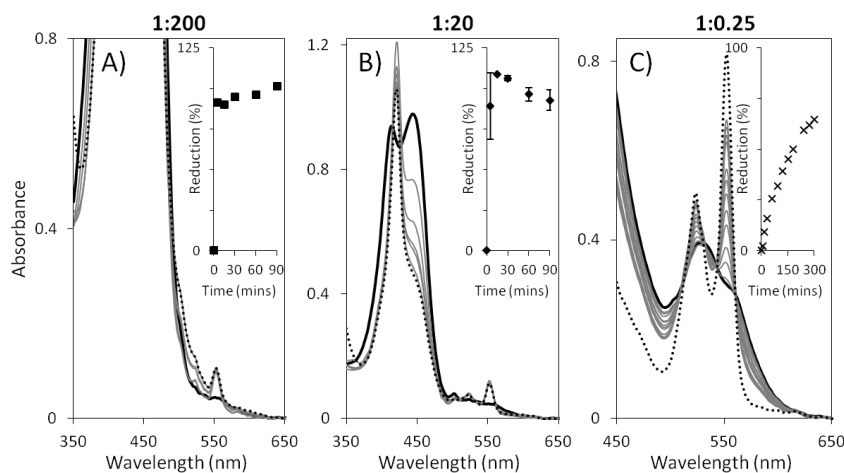
Appendix 2. MtrC photoreduction with RF at MtrC:RF ratios of 1:200 (A), 1:20 (B), 1:2 (C) and ~1:0.5 (D).

A) 0.5 μM MtrC and 100 μM RF. B) 0.5 μM MtrC and 10 μM RF. C) 5 μM MtrC and 10 μM RF. D) 43 μM MtrC and 20 μM RF, unstirred in a 1 mm cuvette (Soret region absorbance above detection limit). As prepared samples (continuous black lines) were irradiated for 5, 15, 30, 60 and 90 mins or longer at 0.4 kW m^{-2} (grey lines) prior to addition of excess of dithionite (dotted lines). Inserts show extent of MtrC reduction during irradiation, monitored via 552 nm absorbance. For experiments containing 0.5 μM MtrC, extent of reduction; and max and min observed values; represent the average of two independent experiments. Grey symbols show biased extents of reductions - see text for details. Stirred samples in anaerobic 50 mM HEPES, 2 mM CaCl_2 , 10 mM KCl, 50 mM TEOA, pH 7 at 20 $^{\circ}\text{C}$.



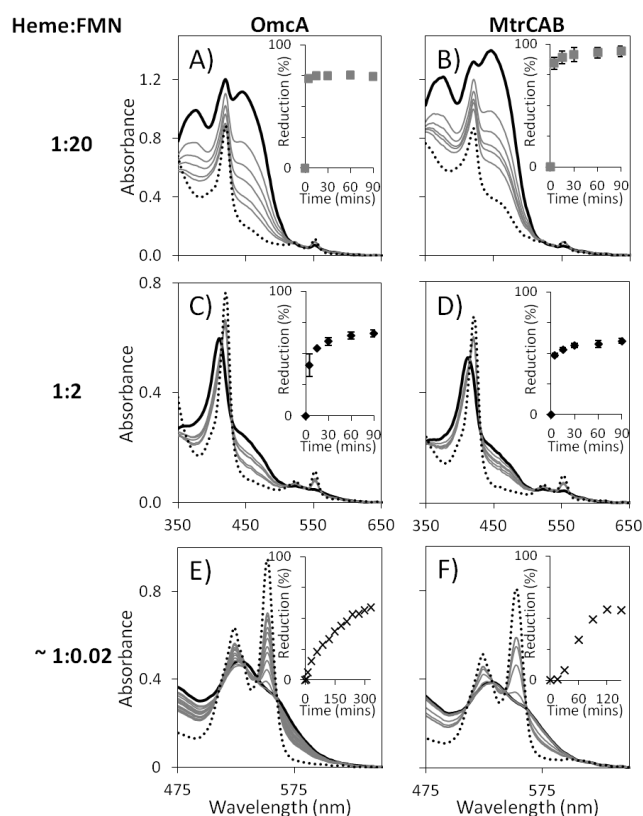
Appendix 3. MtrC photoreduction with fluorescein at MtrC:fluorescein ratios of 1:200 (A), 1:20 (B) and 1:0.25 (C).

A) 0.5 μM MtrC and 100 μM fluorescein. B) 0.5 μM MtrC and 10 μM fluorescein. C) 55 μM MtrC and 17 μM fluorescein, unstirred within a 1 mm cuvette (Soret region absorbance above detection limit). As prepared samples (continuous black lines) were irradiated for 5, 15, 30, 60 and 90 mins or longer at 0.4 kW m^{-2} (grey lines) prior to addition of excess of dithionite (dotted lines). Inserts show extent of MtrC reduction during irradiation, monitored via 552 nm absorbance. For experiments containing 0.5 μM MtrC, extent of reduction; and max and min observed values; represent the average of two independent experiments. Stirred samples in anaerobic 50 mM HEPES, 2 mM CaCl_2 , 10 mM KCl, 50 mM TEOA, pH 7 at 20°C .



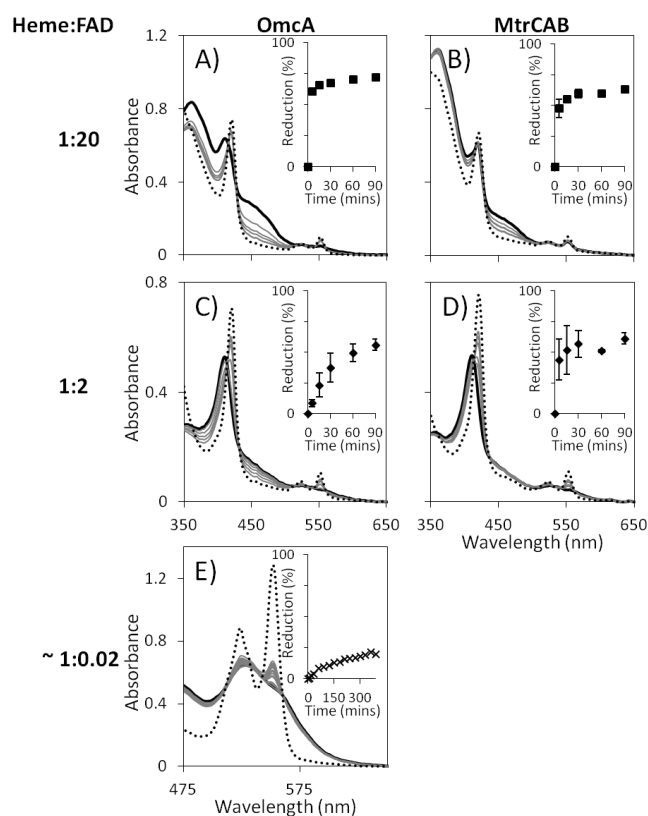
Appendix 4. MtrC photoreduction with proflavin at MtrC:proflavin ratios of 1:200 (A), 1:20 (B) and 1:0.25 (C).

A) 0.5 μM MtrC and 100 μM proflavin. B) 0.5 μM MtrC and 10 μM proflavin. C) 40 μM MtrC and 10 μM proflavin, unstirred within a 1 mm cuvette (Soret region absorbance above detection limit). As prepared samples (continuous black lines) were irradiated for 5, 15, 30, 60 and 90 mins or longer at 0.4 kW m^{-2} (grey lines) prior to addition of excess of dithionite (dotted lines). Inserts show extent of MtrC reduction during irradiation, monitored via 552 nm absorbance. For experiments containing 0.5 μM MtrC, extent of reduction; and max and min observed values; represent the average of two independent experiments. Stirred samples in 50 mM HEPES, 2 mM CaCl_2 , 10 mM KCl, 50 mM TEOA, pH 7 at 20°C .



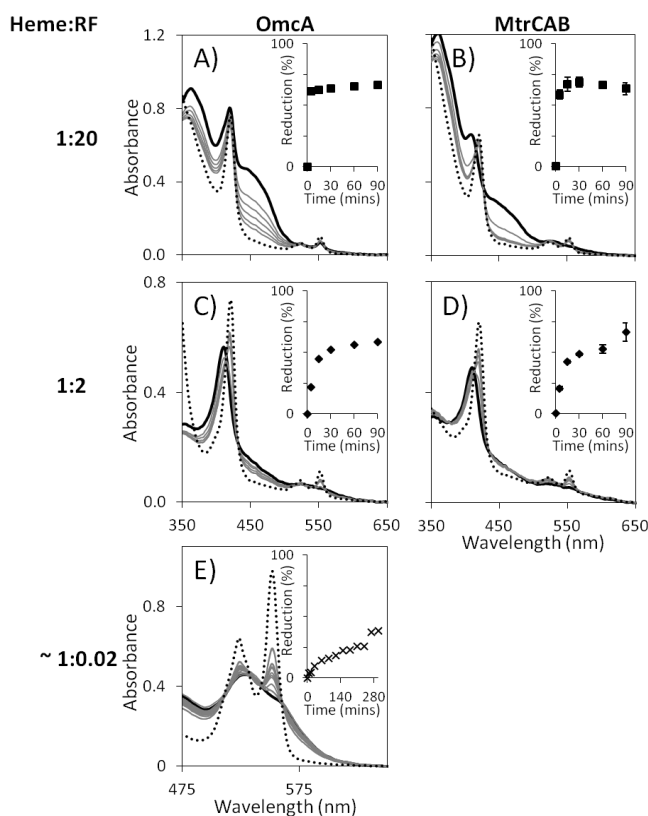
Appendix 5. OmcA and MtrCAB photoreduction with different heme:FMN ratios.

A) 0.5 μM OmcA and 100 μM FMN. B) 0.25 μM MtrCAB and 100 μM FMN. C) 0.5 μM OmcA and 10 μM FMN. D) 0.25 μM MtrCAB and 10 μM FMN. E) 42 μM OmcA and 28 μM FMN, unstirred in a 1 mm cuvette (Soret region absorbance above detection limit). F) 13 μM MtrCAB and 13 μM FMN, unstirred in a 1 mm cuvette (Soret region absorbance above detection limit). As prepared samples (continuous black lines) were irradiated at 0.4 kW m^{-2} for 90 mins or longer (grey lines) prior to addition of excess dithionite (dotted lines). Inserts show extent of heme reduction during irradiation, monitored via 552 nm absorbance. For experiments containing 5 μM heme, extent of reduction; and max and min values; represent the average of two independent experiments. Grey symbols show biased extents of reductions - see text for details. Stirred samples in anaerobic 50 mM HEPES, 2 mM CaCl_2 , 10 mM KCl, 50 mM TEOA, pH 7 at 20 $^\circ\text{C}$. \sim 0.06 % Triton X-100 (v/v) was included for MtrCAB samples.



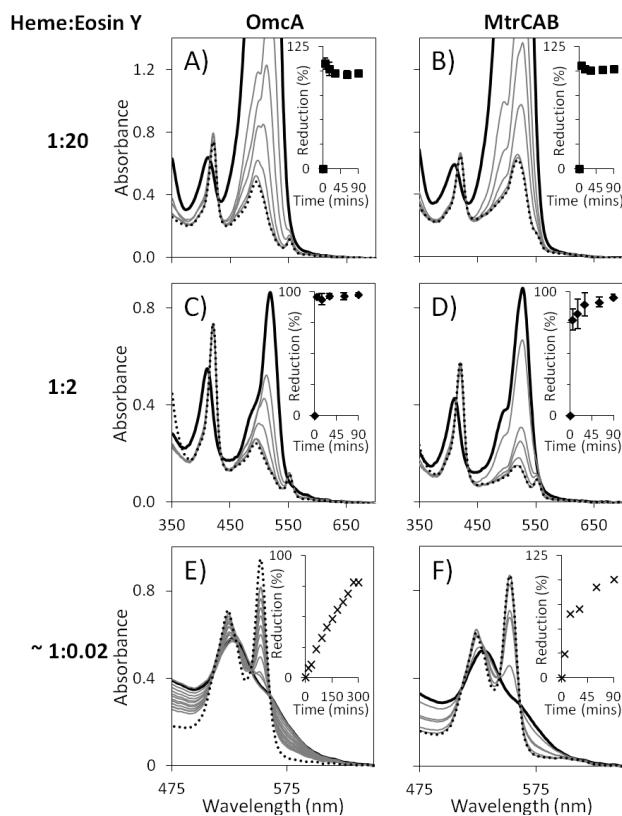
Appendix 6. OmcA and MtrCAB photoreduction with different heme:FAD ratios.

A) 0.5 μM OmcA and 100 μM FAD. B) 0.25 μM MtrCAB and 100 μM FAD. C) 0.5 μM OmcA and 10 μM FAD. D) 0.25 μM MtrCAB and 10 μM FAD. E) 62 μM OmcA and 12 μM FAD, unstirred in a 1 mm cuvette (Soret region absorbance above detection limit). As prepared samples (continuous black lines) were irradiated for 5, 15, 30, 60 and 90 mins or longer at 0.4 kW m^{-2} (grey lines) prior to addition of excess dithionite (dotted lines). Inserts show extent of heme reduction during irradiation, monitored via 552 nm absorbance. For experiments containing 5 μM heme, extent of reduction; and max and min values; represent the average of two independent experiments. Stirred samples in anaerobic 50 mM HEPES, 2 mM CaCl_2 , 10 mM KCl, 50 mM TEOA, pH 7 at 20 $^\circ\text{C}$. Triton X-100, $\sim 0.06\%$ (v/v), was included for MtrCAB samples.



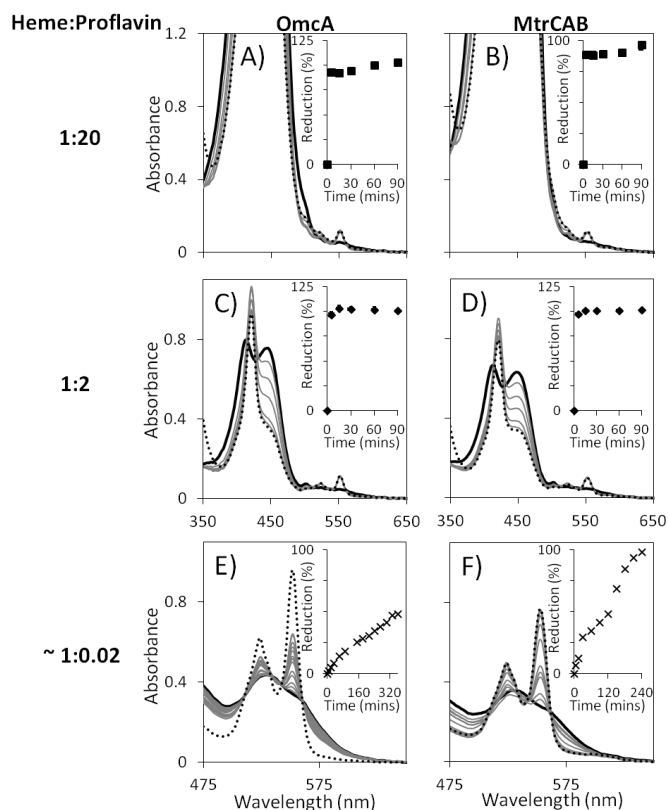
Appendix 7. OmcA and MtrCAB photoreduction with different heme:RF ratios.

A) 0.5 μM OmcA and 100 μM RF. B) 0.25 μM MtrCAB and 100 μM RF. C) 0.5 μM OmcA and 10 μM RF. D) 0.25 μM MtrCAB and 10 μM RF. E) 44 μM OmcA and 10 μM RF, unstirred in a 1 mm cuvette (Soret region absorbance above detection limit). As prepared samples (continuous black lines) were irradiated for 5, 15, 30, 60 and 90 mins or longer at 0.4 kW m^{-2} (grey lines) prior to addition of excess dithionite (dotted lines). Inserts show extent of heme reduction during irradiation, monitored via 552 nm absorbance. For experiments containing 5 μM heme, extent of reduction; and max and min values; represent the average of two independent experiments. Stirred samples in anaerobic 50 mM HEPES, 2 mM CaCl_2 , 10 mM KCl, 50 mM TEOA, pH 7 at 20 $^\circ\text{C}$. Triton X-100, $\sim 0.06\%$ (v/v), was included for MtrCAB samples.



Appendix 8. OmcA and MtrCAB photoreduction with different heme:eosin Y ratios.

A) 0.5 μM OmcA and 100 μM eosin Y. B) 0.25 μM MtrCAB and 100 μM eosin Y. C) 0.5 μM OmcA and 10 μM eosin Y. D) 0.25 μM MtrCAB and 10 μM eosin Y. E) 45 μM OmcA and 16 μM eosin Y, unstirred in a 1 mm cuvette (Soret region absorbance above detection limit). F) 14 μM MtrCAB and 12 μM eosin Y, unstirred in a 1 mm cuvette (Soret region absorbance above detection limit). As prepared samples (continuous black lines) were irradiated for 5, 15, 30, 60 and 90 mins or longer at 0.4 kW m^{-2} (grey lines) prior to addition of excess dithionite (dotted lines). Inserts show extent of heme reduction during irradiation, monitored via 420 nm absorbance for all except heme:eosin Y ratio of $\sim 1:0.05$ (552 nm). For experiments containing 5 μM heme, extent of reduction; and max and min values; represent the average of two independent experiments. Samples in 50 mM HEPES, 2 mM CaCl_2 , 10 mM KCl, 50 mM TEOA, pH 7 at 20 $^\circ\text{C}$. $\sim 0.06\%$ Triton X-100 (v/v) was included for MtrCAB samples.



Appendix 9. OmcA and MtrCAB photoreduction at different heme:proflavin ratios.

A) 0.5 μM OmcA and 100 μM proflavin. B) 0.25 μM MtrCAB and 100 μM proflavin.

C) 0.5 μM OmcA and 10 μM proflavin. D) 0.25 μM MtrCAB and 10 μM proflavin.

E) 42 μM OmcA and 8 μM proflavin, unstirred in a 1 mm cuvette (Soret region absorbance

above detection limit). F) 12 μM MtrCAB and 3 μM proflavin, unstirred in a 1 mm cuvette

(Soret region absorbance above detection limit). As prepared samples (continuous black lines),

were irradiated for 5, 15, 30, 60 and 90 mins or longer at 0.4 kW m^{-2} (grey lines) prior to

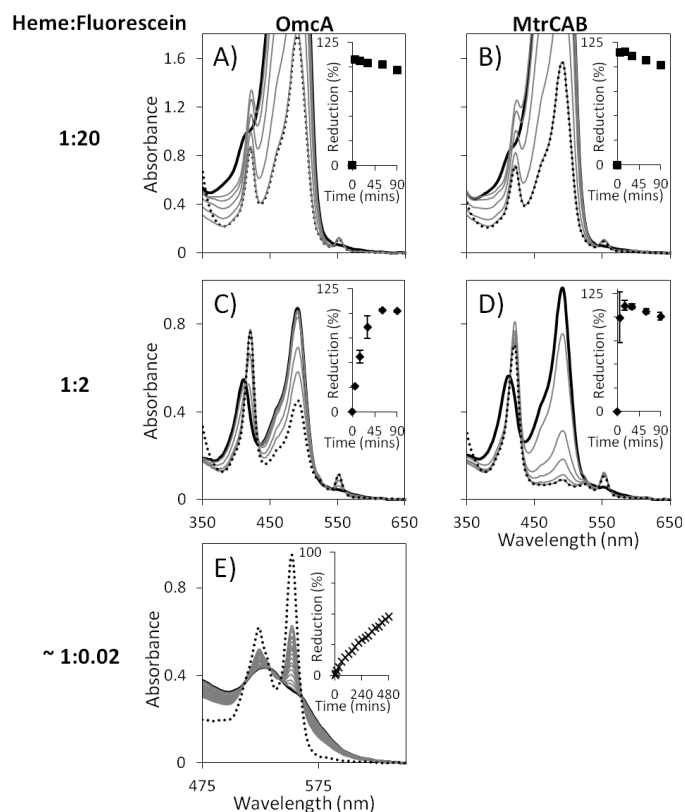
addition of excess dithionite (dotted lines). Inserts show extent of heme reduction during

irradiation, monitored via 552 nm absorbance. For experiments containing 5 μM heme, extent

of reduction; and max and min values; represent the average of two independent experiments.

Stirred samples in anaerobic 50 mM HEPES, 2 mM CaCl_2 , 10 mM KCl, 50 mM TEOA, pH 7 at

20 $^{\circ}\text{C}$. Triton X-100, $\sim 0.06\%$ (v/v), was included for MtrCAB samples.

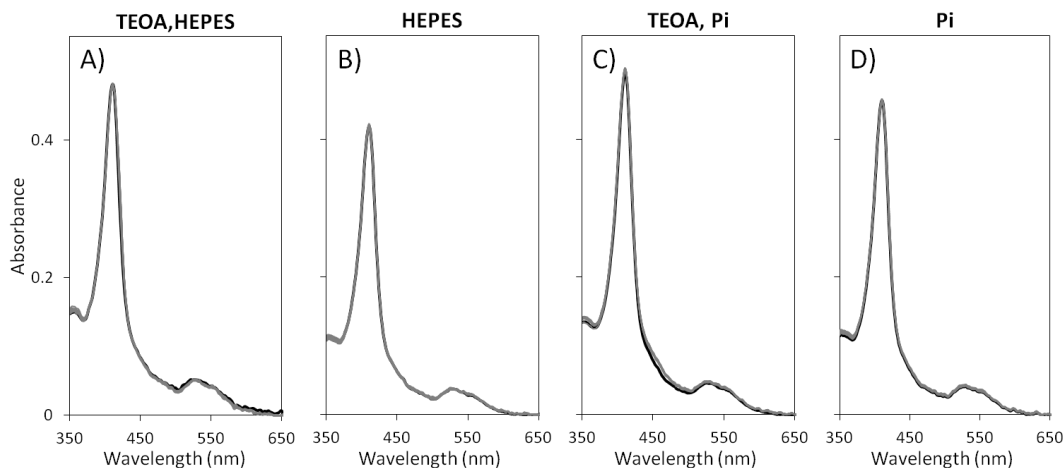


Appendix 10. OmcA and MtrCAB photoreduction at different heme:fluorescein ratios.

A) 0.5 μM OmcA and 100 μM fluorescein. B) 0.25 μM MtrCAB and 100 μM fluorescein.

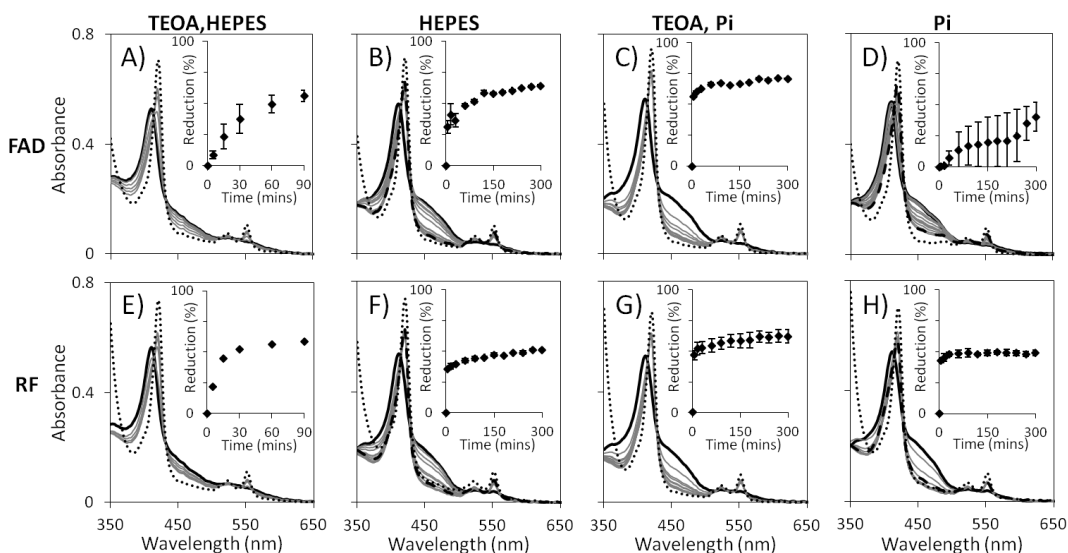
C) 0.5 μM OmcA and 10 μM fluorescein. D) 0.25 μM MtrCAB and 10 μM fluorescein.

E) 41 μM OmcA and 9 μM fluorescein, unstirred in a 1 mm cuvette (Soret region absorbance above detection limit). As prepared samples (continuous black lines) were irradiated for 5, 15, 30, 60 and 90 mins or longer at 0.4 kW m^{-2} (grey lines) prior to addition of excess dithionite (dotted lines). Inserts show extent of heme reduction during irradiation, monitored via 552 nm absorbance. For experiments containing 5 μM heme, extent of reduction; and max and min values; represent the average of two independent experiments. Stirred samples in anaerobic 50 mM HEPES, 2 mM CaCl_2 , 10 mM KCl, 50 mM TEOA, pH 7 at 20 $^\circ\text{C}$. Triton X-100, $\sim 0.06\%$ (v/v), was included for MtrCAB samples.



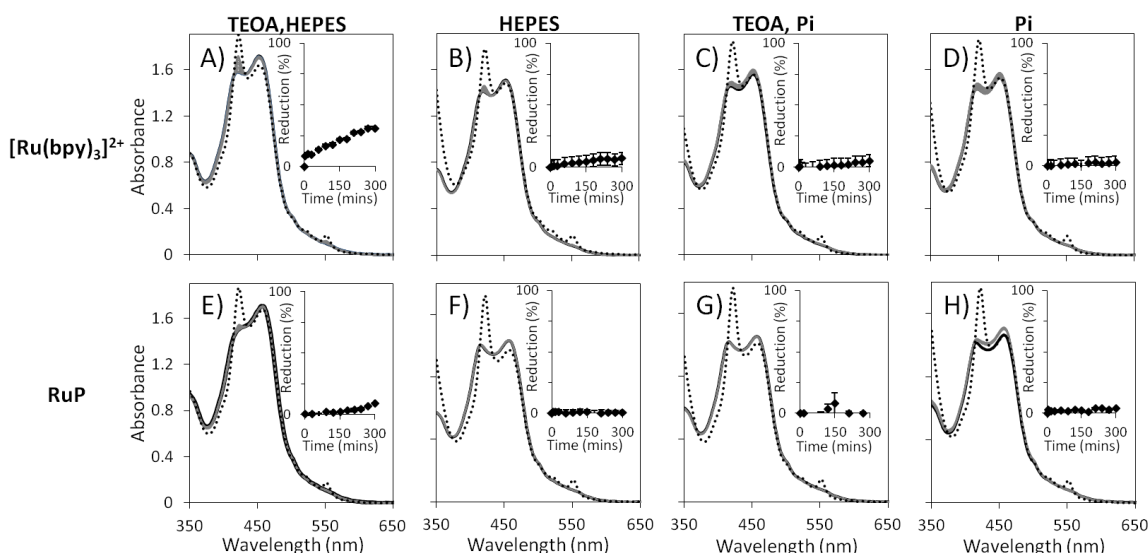
Appendix 11. OmcA spectra remains unchanged after irradiation in the absence of photosensitisers.

0.5 μM OmcA in 50 mM HEPES, 2 mM CaCl_2 , 10 mM KCl, 50 mM TEOA, pH 7 (A), 50 mM HEPES, 2 mM CaCl_2 , 10 mM KCl, pH 7 (B), 50 mM phosphate, 50 mM TEOA, pH 7 (C) or 50 mM phosphate, pH 7 (D). As prepared samples (continuous black lines) were stirred, at 20 $^\circ\text{C}$, whilst being irradiated at 0.4 kW m^{-2} over 5 hrs (grey lines) prior to addition of excess dithionite (dotted lines). Path length 1 cm.



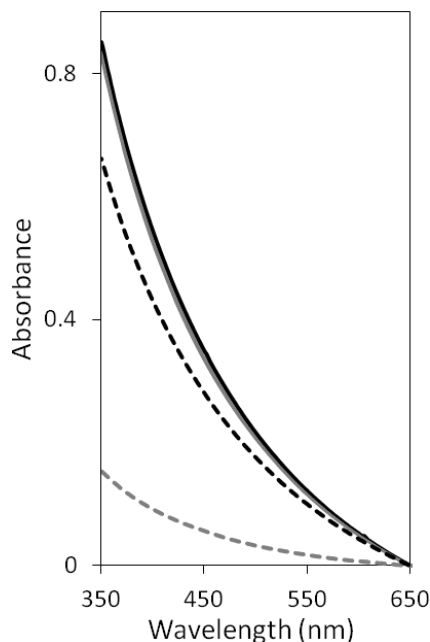
Appendix 12. OmcA photoreduction, by FAD and RF, in the presence and absence the probable electron donors TEOA and HEPES.

0.5 μM OmcA with 10 μM of FAD (A, B, C and D) or RF (E, F, G and H), in 50 mM HEPES, 2 mM CaCl_2 , 10 mM KCl, 50 mM TEOA, pH 7 (A and E), 50 mM HEPES, 2 mM CaCl_2 , 10 mM KCl, pH 7 (B and F), 50 mM phosphate, 50 mM TEOA, pH 7 (C and G) or 50 mM phosphate, pH 7 (D and H). As prepared samples (continuous black lines) were irradiated for 5, 15, 30, 60 and 90 mins or longer at 0.4 kW m^{-2} (grey lines) prior to addition of excess dithionite (dotted lines). For experiments lacking TEOA, prior to the addition of dithionite, excess TEOA was added before 15 mins irradiation at 0.4 kW m^{-2} was performed (dashed lines). Inserts show extent of heme reduction during irradiation, monitored via 552 nm absorbance. The extent of reduction; and max and min values; represent the average of two independent experiments. Stirred samples in anaerobic buffers at 20 $^\circ\text{C}$. Path length 1 cm.



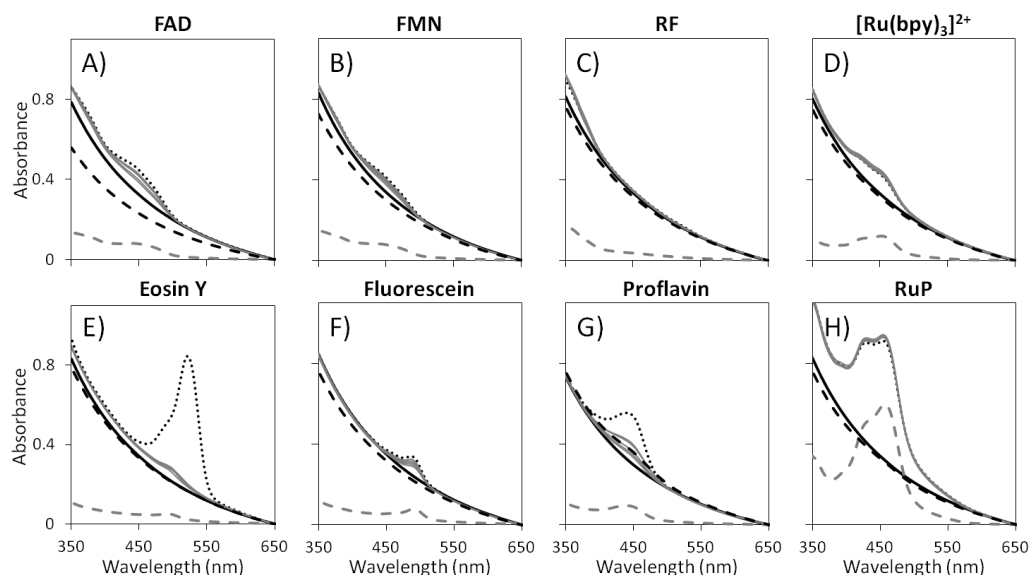
Appendix 13. OmcA photoreduction, by $[\text{Ru}(\text{bpy})_3]^{2+}$ and RuP, in the presence and absence the probable electron donors TEOA and HEPES.

0.5 μM OmcA with 100 μM of $[\text{Ru}(\text{bpy})_3]^{2+}$ (A, B, C and D) or RuP (E, F, G and H), in 50 mM HEPES, 2 mM CaCl_2 , 10 mM KCl, 50 mM TEOA, pH 7 (A and E), 50 mM HEPES, 2 mM CaCl_2 , 10 mM KCl, pH 7 (B and F), 50 mM phosphate, 50 mM TEOA, pH 7 (C and G) or 50 mM phosphate, pH 7 (D and H). As prepared samples (continuous black lines) were irradiated at 0.4 kW m^{-2} over 5 hrs (grey lines) prior to addition of excess dithionite (dotted lines). Inserts show extent of heme reduction during irradiation, monitored via 552 nm absorbance. The extent of reduction; and max and min values; represent the average of two independent experiments. Stirred samples in anaerobic buffers at 20 °C. Path length 1 cm.



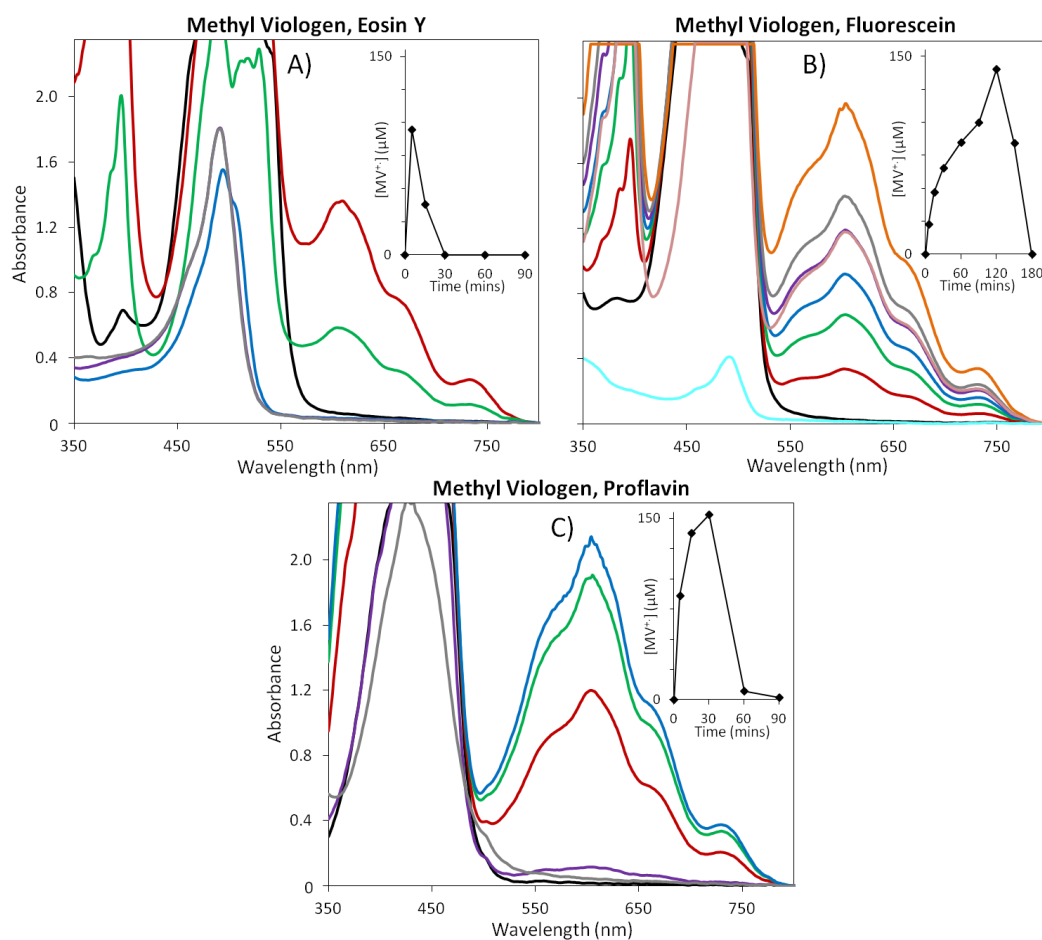
Appendix 14. Liposome absorbance spectra remains unaffected upon light incubation in the absence of photosensitisers.

1 mg mL^{-1} lipid suspension of liposomes without MV^{2+} encapsulated (continuous black line) was irradiated for 5, 15, 30, 60 and 90 mins (continuous grey lines) 2 kW m^{-2} . Irradiation was followed by ultracentrifugation to separate supernatants (dashed grey line) from liposome pellet that was resuspended in buffer (dashed black line). Stirred samples in anaerobic 50 mM HEPES, 2 mM CaCl_2 , 10 mM KCl, 50 mM TEOA, pH 7 at 20 °C. Path length 1 cm.



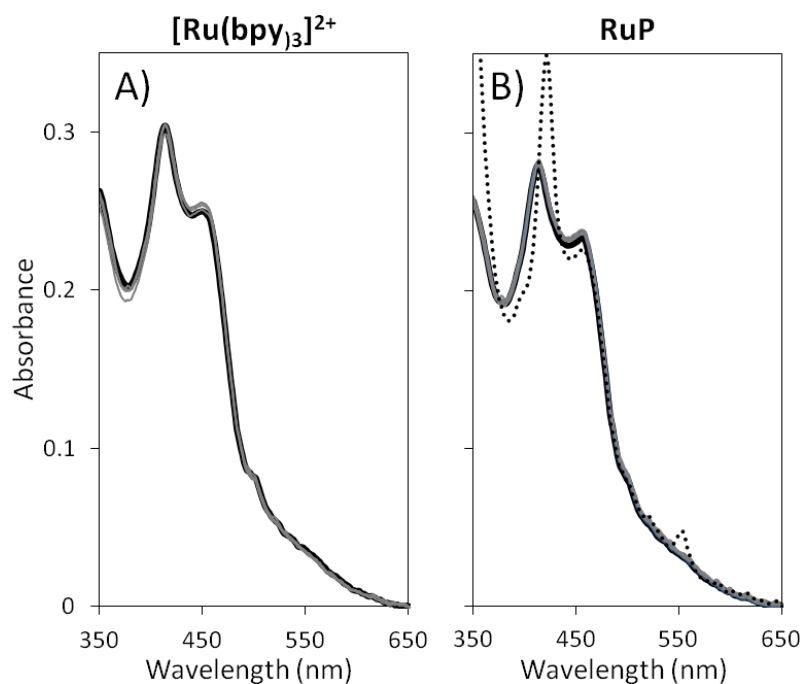
Appendix 15. Photobleaching interferes with study of interactions between liposomes and photosensitisers after irradiation.

1 mg mL⁻¹ lipid suspensions of liposomes without MV²⁺ encapsulated (continuous black lines), with either 11 μM FAD (A), 5 μM FMN (B), 9 μM RF (C), 7 μM [Ru(bpy)₃]²⁺ (D), 8 μM eosin Y (E), 1 μM fluorescein (F), 3 μM proflavin (G) or 57 μM RuP (F). As prepared samples (dotted line) were irradiated for 5, 15, 30, 60 and 90 mins at 2 kW m⁻² (continuous grey lines) prior to ultracentrifugation to separate supernatants (grey dashed lines) from liposome suspensions that were buffer resuspended (black dashed lines). Stirred samples in anaerobic 50 mM HEPES, 2 mM CaCl₂, 10 mM KCl, 50 mM TEOA, pH 7 at 20 °C. Path length 1 cm.



Appendix 16. Irradiation of methyl viologen in presence of eosin Y, fluorescein or proflavin, for cyclic voltammetry of colourless redox-inactive products.

200 μM MV^{2+} solutions in the presence of 200 μM of either eosin Y (A), fluorescein (B) or proflavin (C). As prepared samples (black lines), were irradiated at 2 kW m^{-2} until blue colour of MV^+ was obtained and subsequently lost. Spectra that followed this was recorded at 5 (red lines), 15 (green lines), 30 (blue lines), 60 (purple lines), 90 (grey lines), 120 (orange lines), 150 (pink lines) and 180 mins (cyan lines). Inserts show extent of MV^{2+} reduction during irradiation, monitored via 606 nm absorbance. Concentration of MV^+ was calculated using extinction coefficient of $13.7 \text{ mM}^{-1} \text{ cm}^{-1}$. Samples in 50 mM HEPES, 2 mM CaCl_2 , 10 mM KCl, 50 mM TEOA, pH 7 at 20°C . Path length 1 cm.



Appendix 17. Irradiation of proteoliposomes with Ru(II) dyes at higher lamp powers.

1 mg mL⁻¹ lipid suspensions of proteoliposomes, prepared via rapid dilution method, with either 12 μM $[\text{Ru}(\text{bpy})_3]^{2+}$ or 16 μM RuP (D). As prepared samples (continuous black lines) were irradiated for 5, 15, 30, 60 and 90 mins at 2 kW m⁻² (continuous grey lines) prior to addition of excess dithionite (dotted lines). Stirred samples in anaerobic 50 mM HEPES, 2 mM CaCl₂, 10 mM KCl, 50 mM TEOA, pH 7 at 20 °C. Path length 1 cm.